ज्ञान-विज्ञान विमुक्तये

ANNEXURE III

UNIVERSITY GRANT COMISSION

BAHADUR SHAH ZAFAR MARG

NEW DELHI-110 002.

Annual/Final Report of the work done on the Major/Minor Research Project.

(Report to be submitted within 6 weeks after completion of each year)

1. Project report No. 1st /2nd/3rd/final: Final
2. UGC reference no. : 36-207/2008 (SR)
3. Period of report : 01/05/2009 to 31/04/2012
4. Title of research project : "Chemically deposited superhydrophilic nanocrystalline titanium dioxide (TiO_2) films for dye sensitized solar cells".
5. (a) Name of the Principal Investigator : Prof. Lokhande Chandrakant Dnyandev

   (b) Dept. and University/ college where the work has progressed : Department of Physics, Shivaji University, Kolhapur-416004. (Maharashtra)
6. Effective date of starting of the project: 02/05/2009
7. Grant approved and expenditure incurred during the period of the report:

a. Total amount of approved Rs. 8, 89, 800/-

[Equipment: Rs.4, 00,000.00 for 3 years, Rs.50,000.00 for Contingency, Rs. 30,000.00 for travel /Field Work, Rs. 50,000.00 for Chemicals/Glassware & Rs. 30,000 for Consumable , Rs. 41,800.00 overhead Charges @ Rs.10% approved recurring Grant (Except travel & Field Work), Rs 2,88,000.00 for Project fellow @8,000.00,]

b. Total expenditure[2009-2012]= **Rs.** 8, 89, 800/-

[Equipment: Rs. 3, 96, 935, Project fellowship@ Rs. 8000/-: Rs, 2,59,544/-, chemicals/Glassware:- Rs. 53381/- & Consumable: Rs. 22120/-, Contingency: Rs. 39606/-, Travel/ Field Work: Rs.34183/, Overhead charges: Rs.41, 993/-.]

Report of the work done: (Please attach the separate sheet)

(i) Brief objective of the report:

A separate sheet is attached. Please see **Annexure A**

(ii)Work done so far and results achieved and publications, if any, resulting from the work (Give details of the papers and names of the journals in which it has been published or accepted for publication)

A separate sheet is attached. Please see **Annexure B**

(iii) Has the progress been according to original plan of work and towards achieving the objective? If not, state reasons: **Yes**

(iv) Please indicate the difficulties, if any, experienced in implementing the project: **No.**

(v) If project has not been completed, please indicate the approximate time by which it is likely to be completed. A summary of the work done for the period (Annual basis) may please be sent to the Commission a separate sheet: **Not applicable**

(vi) If the project has been completed, please enclose the summary of the findings of the study. Two bound copies of the final report of the work done may also be sent to the Commission: **Not applicable**

(vii) Any other information which would help in the evaluation of the work done on the project. At the completion of the project, the first report should indicate the output, such as (a) Manpower trained (b) Ph. D. awarded (c) Publication of the results (d)Other impact if any: **Not applicable**

SIGNATURE OF THE PRINCIPAL INVESTIGATOR

Prof. C. D. Lokhande
Principal Investigator (U.G.C. Scheme)
Thin Film Physics Lab;Department of Physics,
Shivaji University, Kolhapur - 416 004 (India)

REGISTRAR / PRINCIPAL

Registrar,
Shivaji University, Kolhapur

Annexure A

Brief objective of the report

1. Using simple and economical chemical methods, namely chemical bath deposition and successive ionic layer adsorption and reaction (SILAR) method, deposition of nanocrystalline large area (>5 cm^2) and hydrophilic titanium dioxide films will be carried out. Deposition of titanium dioxide films onto conducting substrate such as fluorine doped tin oxide coated glass and non-conducting glass substrate will be carried out.

2. Optimisation of deposition parameters such as the pH of bath, deposition temperature and dipping cycles etc and annealing temperatures etc. will be optimised to get large area and hydrophilic titanium dioxide thin films.

3. Various post deposition treatments, such as annealing in air at different temperatures will be carried out to improve film properties. Characterization of titanium dioxide thin films using physico-chemical techniques such as XRD, SEM, HRTEM, AFM, RBS, EDAX, IR, Raman etc. will be carried out.

4. The super hydrophilicity is essential for depositing TiO_2 over other materials and for making good contacts. Study of hydrophilicity of titanium dioxide films will be studied with contact angle measurement. The effect of various post preparative parameters on hydrophilicity will be found out.

5. Such hydrophilic TiO_2 films will be deposited on stainless steel substrates. These films will be dipped in rose bengal and methyl violet dyes and their photoelectrochemical performance in terms of efficiency and stability of the configuration: TiO_2/ Polysulphide/ Pt will be studied.

Annexure B

➢ Methodology

Using our 30 years research experience in deposition of various metal chalcogenide and metal oxide films by various chemical methods, it is predicted that titanium dioxide films can be prepared by chemical methods. By controlling deposition such as the pH of bath, deposition temperature and dipping cycles etc. and annealing temperatures etc compact, large area and hydrophilic titanium dioxide thin films can be obtained. Our preliminary results show that these methods will be useful for TiO_2 films. Such TiO_2 thin films deposited over substrate will have various applications: as a protective coating for photoelectrochemical solar cells, composite films such as CdSe/ TiO_2, CdS/ TiO_2, Fe_2O_3/ TiO_2, photocatalysis etc.

The thin film deposition process is conducted at relatively low temperature without the requirement of controlling atmosphere and therefore it results in to formation of nanocrystalline thin films of titanium dioxide. Slow hydrolysis of titanium tri-chloride solution process adopted for the deposition of results into formation of titanium dioxide thin films onto fluorine doped tin oxide transparent conducting glass substrate (ITO). An electro-generated base instead of alkali is used for the oxide formation. This reaction consumes H_2O and generate OH- species with increase in pH near the substrate. An energy required to hydrolyze titanium tri-chloride precursor is provided by the liquid in the bath, either by thermal collisions or by a chemical reaction between the liquid medium and the precursors, or by a combination of these two mechanisms. Reaction of titanium with oxygen is rate determining step during the titanium dioxide formation during which titanium hydroxide ions is the only reactive species as

$$Ti^{3+} + 3OH^- \text{ ------ } Ti(OH)_3 \text{ and}$$

$$Ti(OH)_3 + OH^- \text{ ----- } TiO_2 + 2H_2O$$

Hydrolysis reaction result in the accumulation of colloidal particles near the substrate and deposition is caused by the electrolyte which is depends upon the metal ion concentration, bath temperature, pH of the resultant solution etc.

The main aim of the project is to deposit good quality nanocrystalline titanium dioxide films at room temperature using chemical route. The preparative parameters will be optimised to get well adherent, nonporous, thin films of titanium dioxide material. For this purpose, various baths including aqueous and non-aqueous media, bath composition, substrates, film thickness etc. will be optimised. The physico-chemical techniques will be used to find out the relationship between crystalline size, porosity, film adherence, and preparation method of ferrite films.

Thin films TiO_2 will be chemically deposited from aqueous baths onto ITO coated glass substrate. The characterization of these films will be carried out using XRD, SEM and optical absorption techniques. TiO_2 films will be given dye treatment (rose bengal and methyl violet dye) and their

photoelectrochemical properties such as current-voltage characteristics and stability will be studied in 1 M polysulphide electrolyte.

Annexure B

➢ Work done so far (01/04/2009 to 31/03/2010)

1] Synthesis of TiO_2 thin films by SILAR method

Superhydrophilic and nanocrystalline TiO_2 thin films has been prepared by successive ionic layer adsorption and reaction (SILAR) method. The preparative parameters such as deposition temperature and dipping cycles etc and annealing temperatures are optimized to get good quality and large area deposition on non-conducting glass substrates and are listed in the following table 1.

The growth of TiO_2 thin films was carried out by the SILAR method at room temperature. The 0.1MTi(III)Cl_3, 15% HCl solution was used as a cationic and 0.1M NaOH solution was used as an anionic precursors. One SILAR cycle consists of four steps: (1) adsorption of titanium species for 20 s, (2) rinsing with distilled water for 5 s to remove excess adsorbed or loosely bounded titanium species, (3) reaction with NaOH precursor solution for 20 s to form stable TiO_2, and (4) rinsing with purified water for 5 s to remove excess or unreacted species or powdery TiO_2. The higher concentration of precursor solutions resulted in to a higher growth rate but the quality of the film was poor due to powdery deposit. In order to remove hydroxide from deposited film and to improve the crystallinity, the films were heat treated at 623 K for 2 h.

Cationic precursor	0.1 M $TiCl_3$ (15% HCl)
Anionic precursor	0.1 M NaOH
Immersion time	20 s
Rinsing time	5 s
Number of dipping cycles	75 cycles
Deposition temperature	Room temperature
Annealing temperature	623 K

➢ **Results**

1) Thickness measurment

Thickness of TiO_2 films was measured by the gravimetric weight difference method in terms of deposited weight of a TiO_2 film on the glass substrate, per unit area (g/cm^2), since the accurate measurement of TiO_2 film thickness was not possible due to the rough morphology and porosity of the film. The graph of the thickness of TiO_2 with the number of cycles is shown in Fig. 1. The rate of increase in the thickness is nonlinear, which has been attributed to the growth by nucleation and coalescence process. More nucleation sites contribute to coagulation during the growing procedure. Furthermore, slight decrease in film thickness observed could be attributed to the formation of outer porous layer and/or the film which may develop stress to cause delamination, resulting in peeling off the film after the film reaches at maximum thickness. The maximum thickness obtained for TiO_2 thin film was 1.34 μm and used for the further characterization.

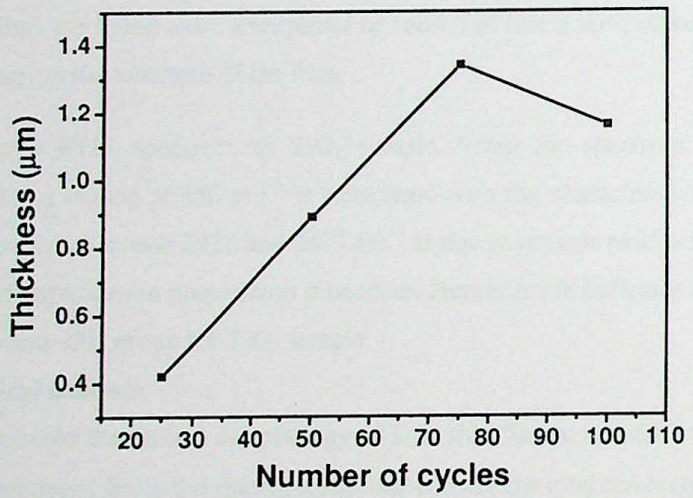


Figure.1 Variation of TiO_2 film thickness with immersion cycles.

2) Crystal structural studies (XRD and FTIR)

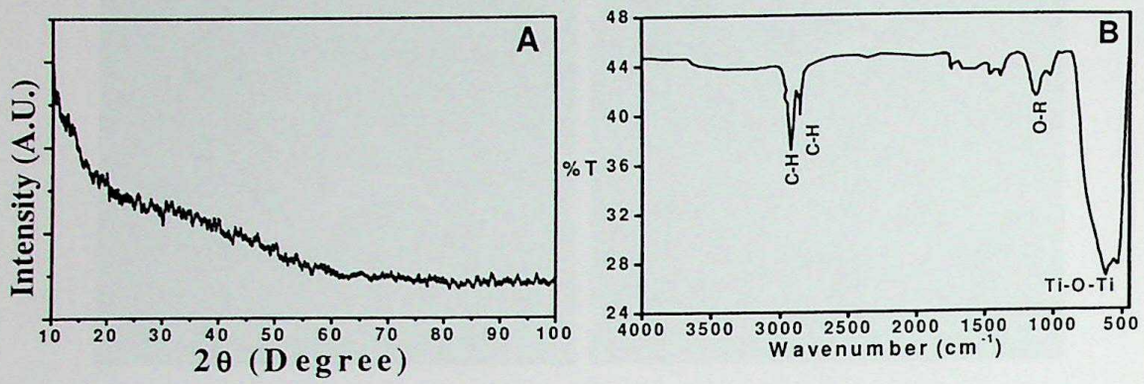


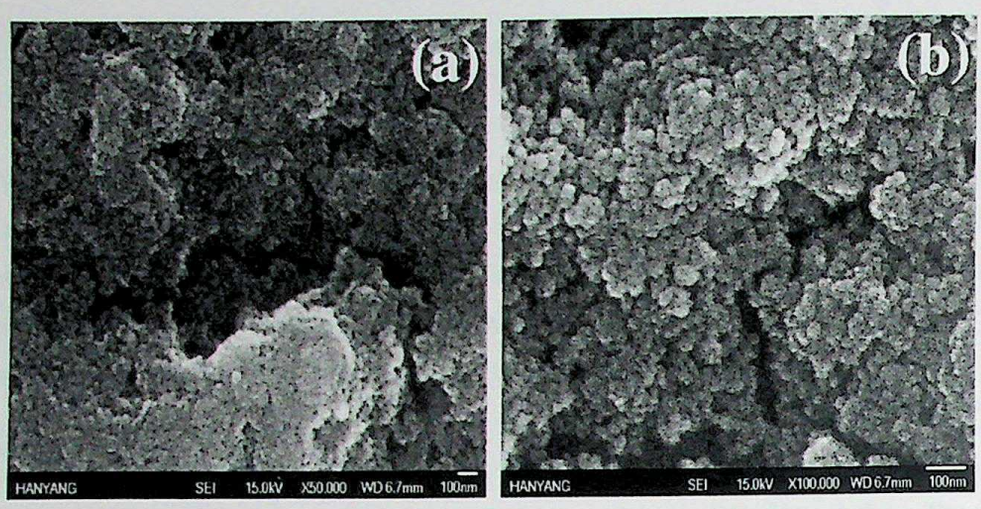
Figure 2. The (A) X-Ray diffraction pattern and (B) FTIR spectrum of TiO_2 thin film.

Fig. 2 (A) shows the X-ray diffraction (XRD) pattern TiO_2 thin film. The TiO2 films are amorphous in nature with very low crystallinity identified by X-ray diffraction analyses. In general, chemically deposited films are found to be amorphous or consist of fine grains, making it difficult to draw any conclusion regarding crystal structure of the film.

Fig. 2 (B) shows FTIR spectrum of TiO_2 sample. From the spectrum, it can be observed apparently that strong band around at 650 cm^{-1} is associated with the characteristic vibrational mode of anatase TiO_2. The narrow band around 2923 and 2873 cm^{-1} is due to organic residues originating from the sample as a result of the impurities in preparation procedure. Hence, result indicates the presence of Ti-O-Ti bonds, peroxo group and -OH group for TiO_2 sample.

3) Surface morphological analysis

Fig. 3 (a and b) shows the surface morphology of TiO_2 thin film at two different magnifications (×50 K and 100 K) respectively. From the micrographs, one can see the total coverage of the substrate with the clusters of TiO_2. The TiO_2 film shows the formation of nanosized smooth grains all over the surface containing some pits and meso-sized pores. Such type of porous structure resulted due to the film formation is based on the nucleation and coalescence.



4) Optical studies

Optical absorption spectrum of TiO_2 film is shown in inset of Fig. 4. The absorption edge was found at 330 nm. These spectra reveal that TiO_2 film has low-absorbance in the visible region, which is a characteristic of TiO_2. The optical band gap energy can be estimated by using the following equation for a semiconductor:

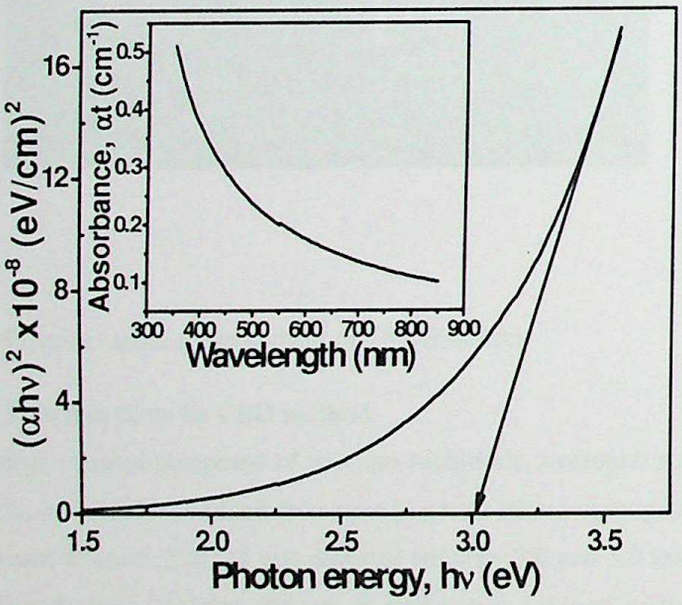


Figure 4 Plot of $(\alpha h\nu)^2$ versus $h\nu$ of TiO_2 films. Inset shows variation of absorption (αt) with wavelength (□) of TiO_2 films on glass substrate.

$$\alpha = \frac{A(Eg - h\nu)^n}{h\nu}$$

Where α is absorption coefficient, Eg is band gap, A is constant and n is equal to 1/2 for direct transition. The plot of $(\alpha h\nu)^2$ versus hν of TiO_2 film is shown in Fig. 4. From the linear nature of the plot, the direct optical transition in TiO_2 is confirmed. The band gap energy, Eg is obtained by extrapolating the linear portion of the plot $(\alpha h\upsilon)^2$ versus hνs to the energy axis at α=0. From the graph for TiO_2 thin film, band gap value of 3.01 eV which is in good agreement with the literature data.

5) Wettability test

Fig. 5 shows the image of water contact angle measurement on TiO_2 films surface. The surface of TiO_2 thin film is superhydrophilic in nature. Observed contact angles are too small to measure the contact angle because the surface of TiO_2 films is highly compact, porous and smooth. The water lies flat with contact angle on the surface of TiO_2 film instead of forming droplet. This specific property is attributed to nanocrystalline nature that is expected to possess very high surface energy.

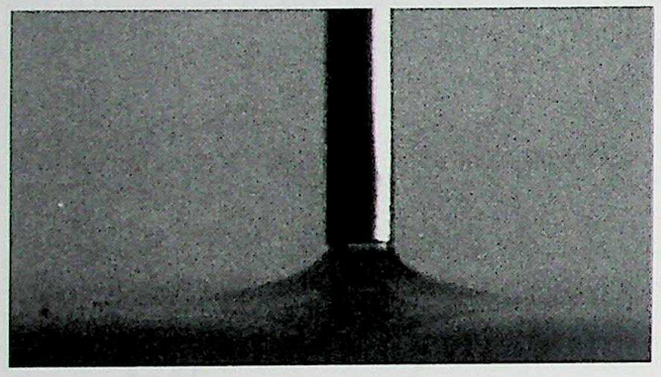


Figure 5 Contact angle measurement of TiO_2 thin film

2] Synthesis of TiO_2 thin films by CBD method

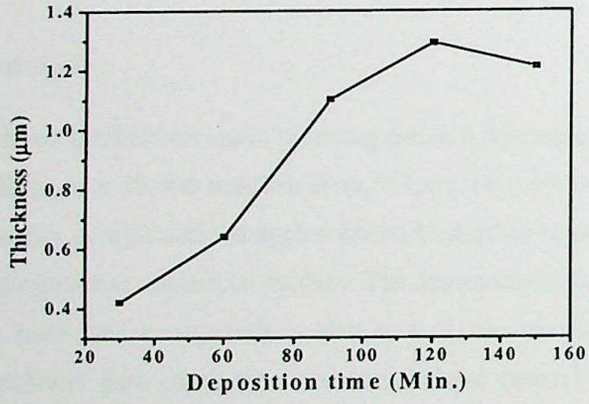
An aqueous solution composed of titanium trichloride, hydrogen peroxide was first prepared. In brief, 0.1 M $TiCl_3$, 15% HCl was added drop-wise to a well stirred hydrogen peroxide (H_2O_2, Molychem, 30 wt %) and water solution. The pH was adjusted between 2.0 and 3.0 using a mixture of 30 % liquid ammonium hydroxide with constant stirring. A transparent solution with a reddish-yellow color was obtained after vigorous stirring for 30 min at room temperature. Glass substrates were washed with chromic acid and in an ultrasonic bath at room temperature for 30 min. These cleaned substrates were

immersed in the above bath and the bath was heated. When the bath attains the temperature of 343 K, the precipitation was started in the bath. During the precipitation, heterogeneous reaction occurs on the substrate and deposition of TiO_2 took place on the substrate. The TiO_2 films were annealed in air at 623 K for 2 h. and used for further characterizations.

- **Results**

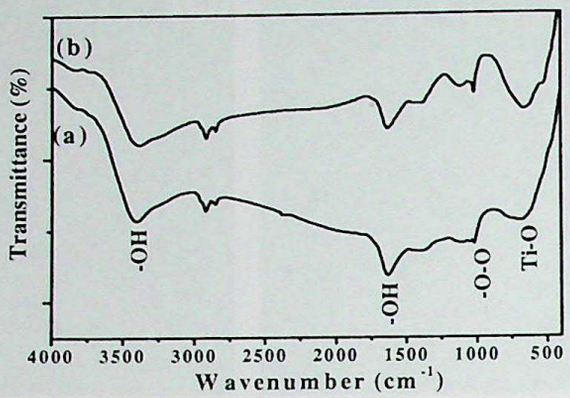
1. Thickness measurement

The thickness of the TiO_2 film was measured by a gravimetric weight difference method in terms of the weight of TiO_2 deposited on the glass substrate per unit area (mg/cm^2), since the accurate measurement of TiO_2 film thickness was not possible due to the rough morphology and porosity of the film. Fig. 1 shows the film thickness variation of TiO_2 thin film with deposition time. The rate of increase in the thickness is nonlinear, which has been attributed to the growth by nucleation and coalescence process. More nucleation sites contribute to coagulation during the growing procedure. Furthermore, slight decrease in film thickness observed could be attributed to the formation of outer porous layer and/or the film which may develop stress to cause delamination, resulting in peeling off the film after the film reaches at maximum thickness. The terminated thickness at which the highest amount of TiO_2 deposited on the substrate was 1.29 μm.



2. FTIR study

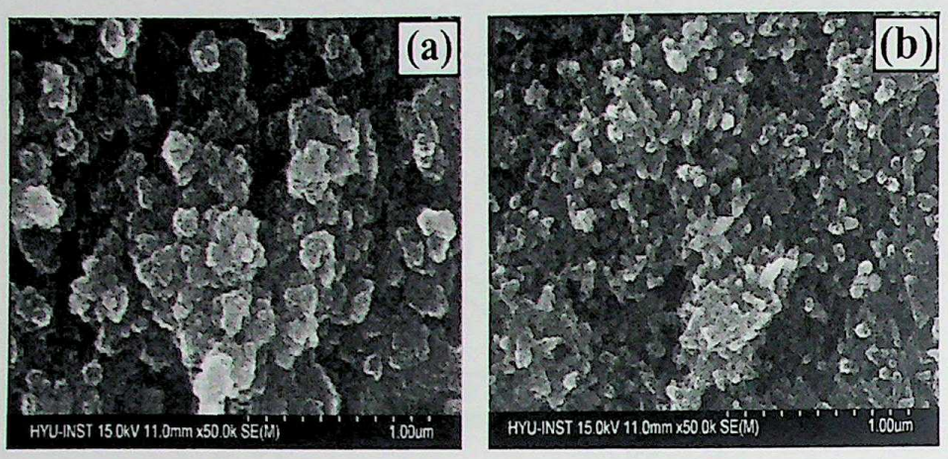
Fig. 2 shows FTIR spectra of the (a) as-deposited and (b) Annealed TiO_2 samples within the wavelength range 400 to 4000 cm^{-1}. The absorption at 3409 cm^{-1} indicates the presence of hydroxide group.



The absorption peak around at 1634 cm^{-1} may be due to the bending vibration of hydroxyl groups of molecular water. The absorption peak at around 1000 cm^{-1} is assigned to characteristic stretching vibration of peroxo groups. The strong absorption peak around at 649 cm^{-1} is associated with the characteristic vibrational mode of anatase TiO2. As-deposited TiO_2 showed the higher depth at 3409 cm^{-1} than annealed one, which attributed to removal of hydroxide after heat treatment. Hence, results indicate the presence of Ti-O bond, peroxo groups and -OH groups for as-deposited film, whereas after annealing the peaks attributed to the peroxo groups and -OH groups were almost disappeared. Less intense hydroxide and hydroxyl groups from water found in the annealed TiO_2 may be due to the fact that the spectrum was not recorded in situ and some readsorption of water from the ambient atmosphere might have occurred.

3. Surface morphological study

Fig. 3 (a and b) shows the field emission scanning electron micrographs (FESEM) of as-deposited and annealed TiO_2 thin films at x 50,000 magnification, respectively. From micrograph (Fig. 3(a)) it is seen that the deposits consists of well defined agglomerated multigrain structure having irregular shapes and sizes due to the low temperature deposition method. The approximate size of this multigrain structure is about 140 nm. Some pores and overgrowth is also seen in the micrographs. After annealing this multigrain structure completely gets converted into well defined conical nanorods. The approximate length and diameter of these nanorods is ~110 nm and 25 nm respectively (Fig. 3(b)). The barrier effect of intercrystalline TiO_2 is greatly decreased by using long nanorods instead of a porous TiO_2 thin film composed of accumulated nanosized particles. This might contribute to the easier electron transfer and decrease the ohmic loss through the TiO_2 layer in dye-sensitized solar cells.

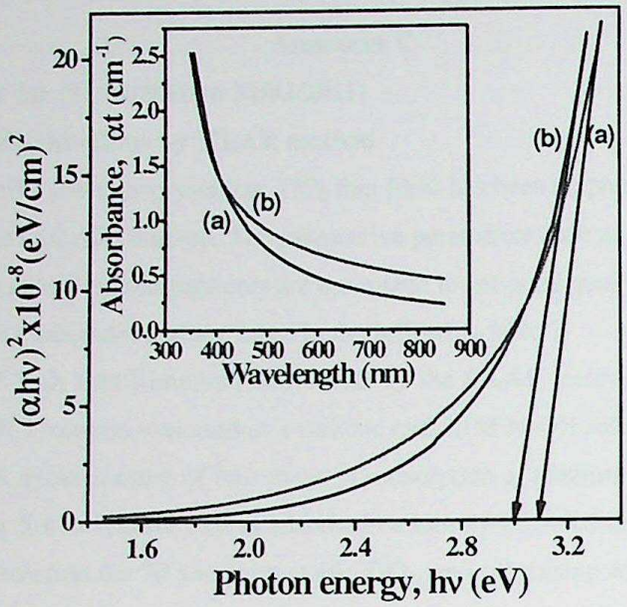


4. Optical studies

Fig. 4 (a and b) shows optical absorption spectra for as-deposited and annealed TiO_2 thin films within 350 to 850 nm wavelength range. The absorption edge was found to be 450 nm as seen from inset of Fig. 4. These spectra reveal that TiO_2 film has low-absorbance in the visible region, which is a characteristic of TiO_2. The optical band gap (Eg) for as-deposited and annealed TiO_2 film is calculated on the basis of optical absorption using the following equation,

$$\alpha = \frac{A(Eg - h\nu)^n}{h\nu}$$

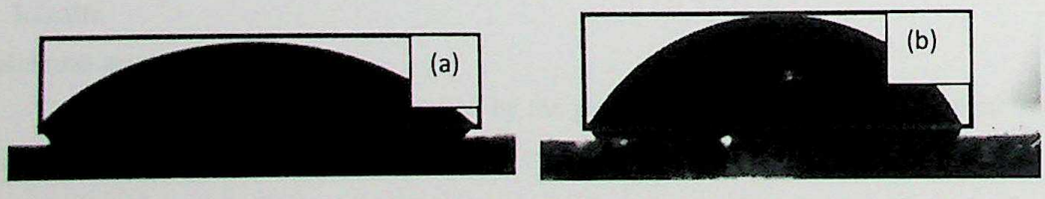
where hν is the photon energy, and A is constant. The exponent 'n' depends upon the type of transition and has values of 1/2 and 2 for direct and indirect transitions, respectively. By plotting the graph of $(\alpha h\nu)^2$ versus hν (Fig. 4), it becomes possible to determine the nature of transition involved. The extrapolation of straight-line portions of the plot (hν greater than Eg) to the zero absorption coefficient gives measurement of energy gap. Both plot show a linear dependence at h□ greater than Eg, therefore extrapolation of the straight line portions of the curves to the zero absorption coefficient gives band gap of 3.1 and 3.0 eV for as deposited and annealed TiO_2 films respectively.



Due to the improved grain size of annealed, the absorption edge showed red-shift up to some extent. The widened band gap of the TiO_2 films is attributed to the contribution of quantum size effect.

5. Wettability test

Controlling and/or modifying the surface wettability are important, which involves the interaction between a liquid and a solid in contact. Measurement of surface water contact angle is inversely proportional to the wettability and can be determined by Young's relation. Fig. 5 shows the water contact measurements for (a) as-deposited, and (b) annealed TiO_2 thin films. Interestingly, as-deposited TiO_2 exhibits hydrophilic behavior (24°), as water contact angle is less than 90°. The shape of water droplet on the film is shown in Fig. 5(a). Further, for annealed films, the water contact angle slightly increases to 32°. The droplet shape on the surface of annealed TiO_2 film was more spherical (Fig. 5(b)). Increase in water contact angle after annealing attributed to (a) non-spherical nature of the grains and (b) topographical change in structure. Due to the conversion from spherical nanograins to nanorods after annealing prevents the water from adhering to the film results into increase in water contact angle.



Annexure C

- **Work done so far (01/04/2010 to 31/03/2011)**

1] Synthesis of TiO_2 thin films by SILAR method

Superhydrophilic and nanocrystalline TiO_2 thin films has been prepared by successive ionic layer adsorption and reaction (SILAR) method. The preparative parameters such as deposition temperature and dipping cycles etc and annealing temperatures are optimized to get good quality and large area deposition on non-conducting glass substrates and are listed in the following table 1.

The growth of TiO_2 thin films was carried out by the SILAR method at room temperature. The 0.1MTi(III)Cl_3, 15% HCl solution was used as a cationic and 0.1M NaOH solution was used as an anionic precursors. One SILAR cycle consists of four steps: (1) adsorption of titanium species for 20 s, (2) rinsing with distilled water for 5 s to remove excess adsorbed or loosely bounded titanium species, (3) reaction with NaOH precursor solution for 20 s to form stable TiO_2, and (4) rinsing with purified water for 5 s to remove excess or unreacted species or powdery TiO_2. The higher concentration of precursor solutions resulted in to a higher growth rate but the quality of the film was poor due to powdery deposit. In order to remove hydroxide from deposited film and to improve the crystallinity, the films were heat treated at 623 K for 2 h.

Cationic precursor	0.1 M $TiCl_3$ (15% HCl)
Anionic precursor	0.1 M NaOH
Immersion time	20 s
Rinsing time	5 s
Number of dipping cycles	75 cycles
Deposition temperature	Room temperature
Annealing temperature	623 K

- **Results**

1) Thickness measurment

Thickness of TiO_2 films was measured by the gravimetric weight difference method in terms of deposited weight of a TiO_2 film on the glass substrate, per unit area (g/cm^2), since the accurate

measurement of TiO_2 film thickness was not possible due to the rough morphology and porosity of the film. The graph of the thickness of TiO_2 with the number of cycles is shown in Fig. 1. The rate of increase in the thickness is nonlinear, which has been attributed to the growth by nucleation and coalescence process. More nucleation sites contribute to coagulation during the growing procedure. Furthermore, slight decrease in film thickness observed could be attributed to the formation of outer porous layer and/or the film which may develop stress to cause delamination, resulting in peeling off the film after the film reaches at maximum thickness. The maximum thickness obtained for TiO_2 thin film was 1.34 μm and used for the further characterization.

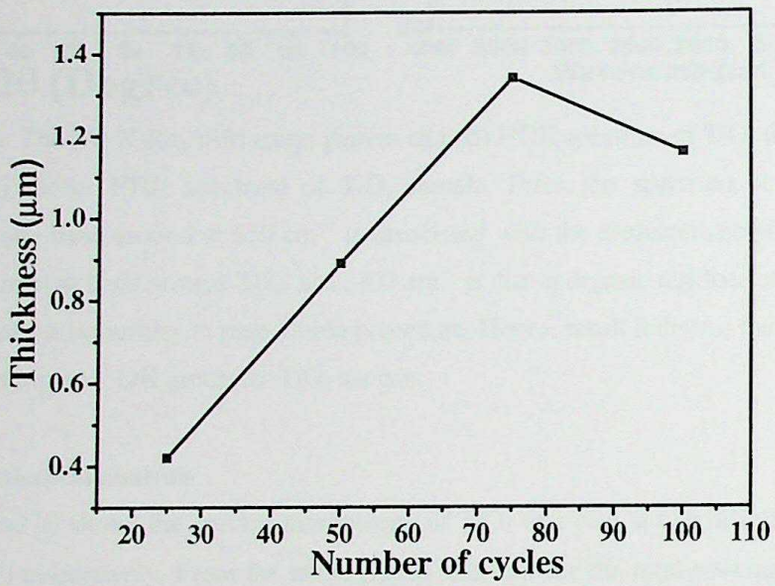


Figure.1 Variation of TiO_2 film thickness with immersion cycles.

2) Crystal structural studies (XRD and FTIR)

Fig. 2 (A) shows the X-ray diffraction (XRD) pattern TiO_2 thin film. The TiO2 films are amorphous in nature with very low crystallinity identified by X-ray diffraction analyses. In general, chemically deposited films are found to be amorphous or consist of fine grains, making it difficult to draw any conclusion regarding crystal structure of the film.

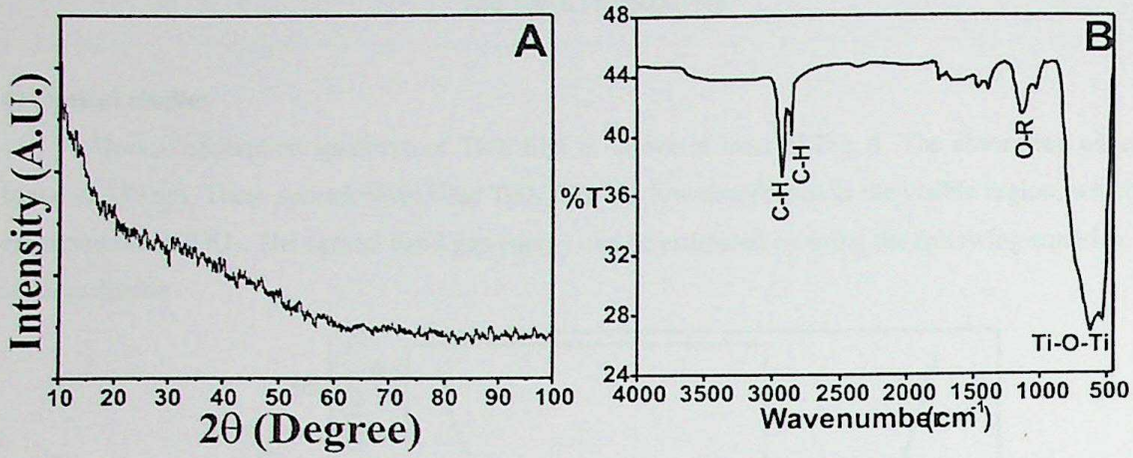


Figure 2. The (A) X-Ray diffraction pattern and (B) FTIR spectrum of TiO_2 thin film.

Fig. 2 (B) shows FTIR spectrum of TiO_2 sample. From the spectrum, it can be observed apparently that strong band around at 650 cm^{-1} is associated with the characteristic vibrational mode of anatase TiO_2. The narrow band around 2923 and 2873 cm^{-1} is due to organic residues originating from the sample as a result of the impurities in preparation procedure. Hence, result indicates the presence of Ti-O-Ti bonds, peroxo group and -OH group for TiO_2 sample.

3) Surface morphological analysis

Fig. 3 (a and b) shows the surface morphology of TiO_2 thin film at two different magnifications (×50 K and 100 K) respectively. From the micrographs, one can see the total coverage of the substrate with the clusters of TiO_2. The TiO_2 film shows the formation of nanosized smooth grains all over the surface containing some pits and meso-sized pores. Such type of porous structure resulted due to the film formation is based on the nucleation and coalescence.

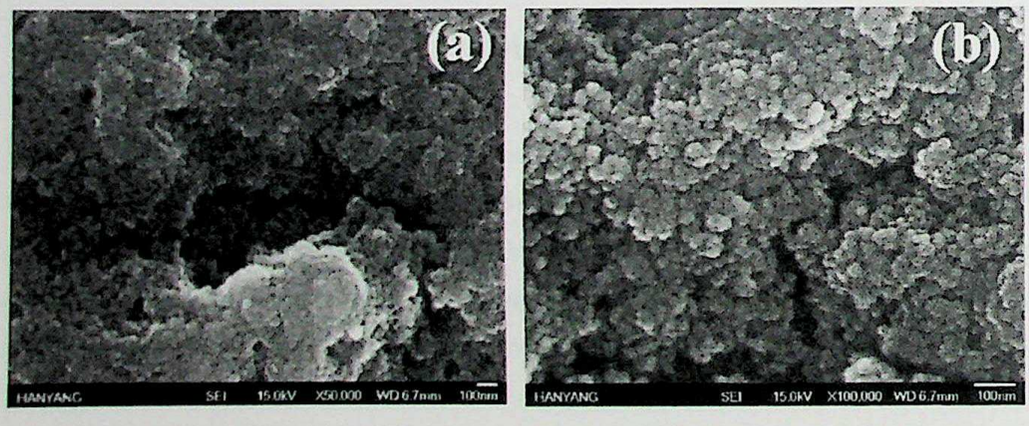


Fig. 3 (a and b) shows the surface morphology of TiO_2 thin film at two different magnifications (×50 K and 100 K) respectively

4) Optical studies

Optical absorption spectrum of TiO_2 film is shown in inset of Fig. 4. The absorption edge was found at 330 nm. These spectra reveal that TiO_2 film has low-absorbance in the visible region, which is a characteristic of TiO_2. The optical band gap energy can be estimated by using the following equation for a semiconductor:

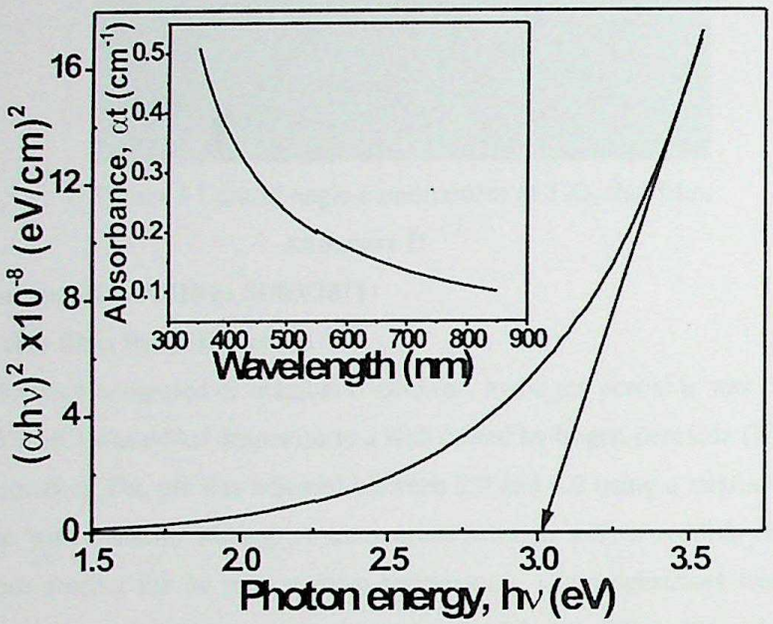


Figure 4 Plot of $(\alpha h\nu)^2$ versus hν of TiO_2 films. Inset shows variation of absorption (αt) with wavelength (λ) of TiO_2 films on glass substrate.

$$\alpha = \frac{A(Eg - h\nu)^n}{h\nu}$$

Where α is absorption coefficient, Eg is band gap, A is constant and n is equal to 1/2 for direct transition. The plot of $(\alpha h\nu)^2$ versus hν of TiO_2 film is shown in Fig. 4. From the linear nature of the plot, the direct optical transition in TiO_2 is confirmed. The band gap energy, Eg is obtained by extrapolating the linear portion of the plot $(\alpha h\upsilon)^2$ versus hν to the energy axis at α=0. From the graph for TiO_2 thin film, band gap value of 3.01 eV which is in good agreement with the literature data.

5) Wettability test

Fig. 5 shows the image of water contact angle measurement on TiO_2 films surface. The surface of TiO_2 thin film is superhydrophilic in nature. Observed contact angles are too small to measure the contact angle because the surface of TiO_2 films is highly compact, porous and smooth. The water lies flat with contact angle on the surface of TiO_2 film instead of forming droplet. This specific property is attributed to nanocrystalline nature that is expected to possess very high surface energy.

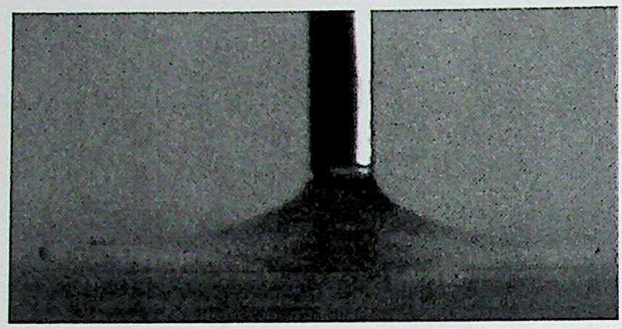


Figure 5 Contact angle measurement of TiO_2 thin film.

Annexure D

- **Work done so far (01/04/2010 to 31/03/2011)**

2] Synthesis of TiO_2 thin films by CBD method

An aqueous solution composed of titanium trichloride, hydrogen peroxide was first prepared. In brief, 0.1 M $TiCl_3$, 15% HCl was added drop-wise to a well stirred hydrogen peroxide (H_2O_2, Molychem, 30 wt %) and water solution. The pH was adjusted between 2.0 and 3.0 using a mixture of 30 % liquid ammonium hydroxide with constant stirring. A transparent solution with a reddish-yellow color was obtained after vigorous stirring for 30 min at room temperature. Glass substrates were washed with chromic acid and in an ultrasonic bath at room temperature for 30 min. These cleaned substrates were immersed in the above bath and the bath was heated. When the bath attains the temperature of 343 K, the precipitation was started in the bath. During the precipitation, heterogeneous reaction occurs on the substrate and deposition of TiO_2 took place on the substrate. The TiO_2 films were annealed in air at 623 K for 2 h. and used for further characterizations.

- **Results**

1. Thickness measurement

The thickness of the TiO_2 film was measured by a gravimetric weight difference method in terms of the weight of TiO_2 deposited on the glass substrate per unit area (mg/cm^2), since the accurate measurement of TiO_2 film thickness was not possible due to the rough morphology and porosity of the film. Fig. 1 shows the film thickness variation of TiO_2 thin film with deposition time. The rate of increase in the thickness is nonlinear, which has been attributed to the growth by nucleation and coalescence

process. More nucleation sites contribute to coagulation during the growing procedure. Furthermore, slight decrease in film thickness observed could be attributed to the formation of outer porous layer and/or the film which may develop stress to cause delamination, resulting in peeling off the film after the film reaches at maximum thickness. The terminated thickness at which the highest amount of TiO_2 deposited on the substrate was 1.29 μm.

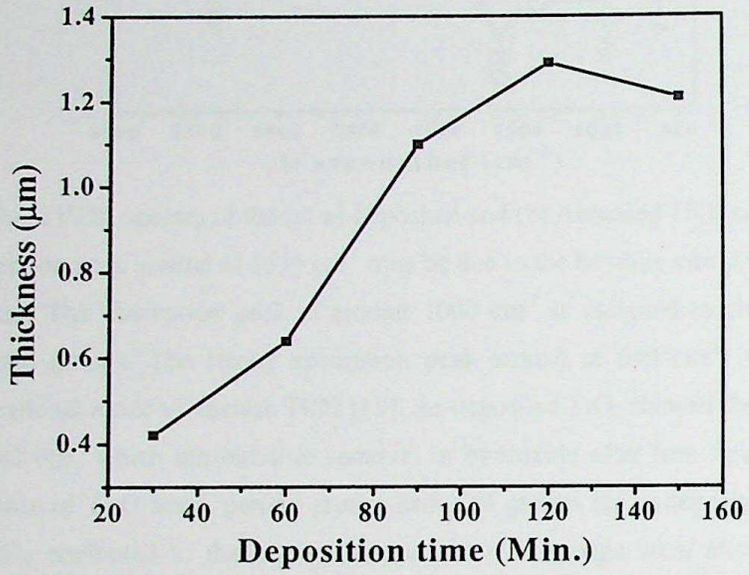


Figure.1 Variation of TiO_2 film thickness with deposition time.

2. FTIR study

Fig. 2 shows FTIR spectra of the (a) as-deposited and (b) Annealed TiO_2 samples within the wavelength range 400 to 4000 cm^{-1}. The absorption at 3409 cm^{-1} indicates the presence of hydroxide group.

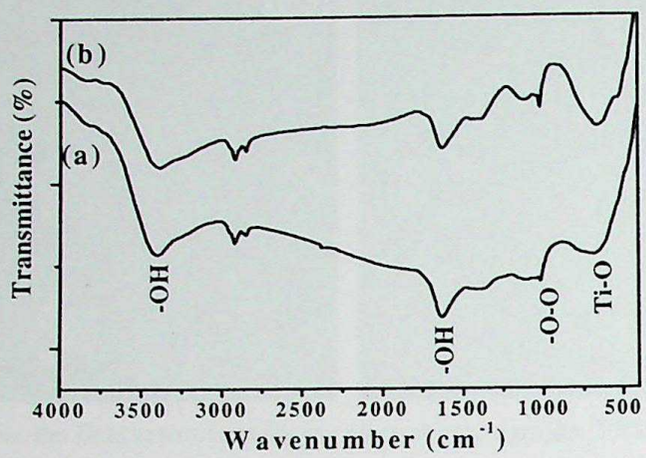


Fig. 2 FTIR spectra of the (a) as-deposited and (b) Annealed TiO_2 samples

The absorption peak around at 1634 cm^{-1} may be due to the bending vibration of hydroxyl groups of molecular water. The absorption peak at around 1000 cm^{-1} is assigned to characteristic stretching vibration of peroxo groups. The strong absorption peak around at 649 cm^{-1} is associated with the characteristic vibrational mode of anatase TiO2 [18]. As-deposited TiO_2 showed the higher depth at 3409 cm^{-1} than annealed one, which attributed to removal of hydroxide after heat treatment. Hence, results indicate the presence of Ti-O bond, peroxo groups and -OH groups for as-deposited film, whereas after annealing the peaks attributed to the peroxo groups and -OH groups were almost disappeared. Less intense hydroxide and hydroxyl groups from water found in the annealed TiO_2 may be due to the fact that the spectrum was not recorded in situ and some readsorption of water from the ambient atmosphere might have occurred.

3. Surface morphological study

Fig. 3 (a and b) shows the field emission scanning electron micrographs (FESEM) of as-deposited and annealed TiO_2 thin films at X 50,000 magnification, respectively. From micrograph (Fig. 3(a)) it is seen that the deposits consists of well defined agglomerated multigrain structure having irregular shapes and sizes due to the low temperature deposition method. The approximate size of this multigrain structure is about 140 nm. Some pores and overgrowth is also seen in the micrographs. After annealing this multigrain structure completely gets converted into well defined conical nanorods.

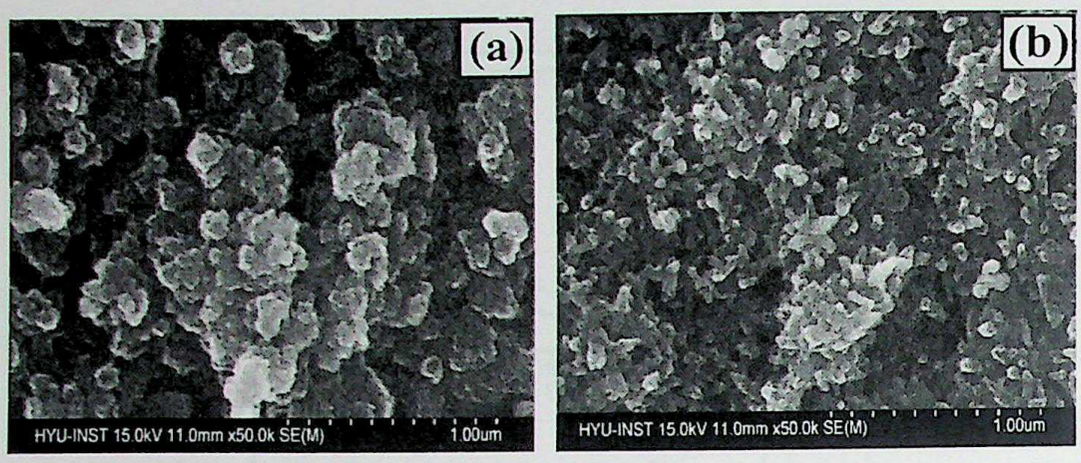


Fig. 3 (a and b) shows the field emission scanning electron micrographs (FESEM) of as-deposited and annealed TiO_2 thin films

The approximate length and diameter of these nanorods is □110 nm and 25 nm respectively (Fig. 3(b)). The barrier effect of intercrystalline TiO_2 is greatly decreased by using long nanorods instead of a porous TiO_2 thin film composed of accumulated nanosized particles. This might contribute to the easier electron transfer and decrease the ohmic loss through the TiO_2 layer in dye-sensitized solar cells.

4. Optical studies

Fig. 4 (a and b) shows optical absorption spectra for as-deposited and annealed TiO_2 thin films within 350 to 850 nm wavelength range. The absorption edge was found to be 450 nm as seen from inset of Fig. 4. These spectra reveal that TiO_2 film has low-absorbance in the visible region, which is a characteristic of TiO_2.

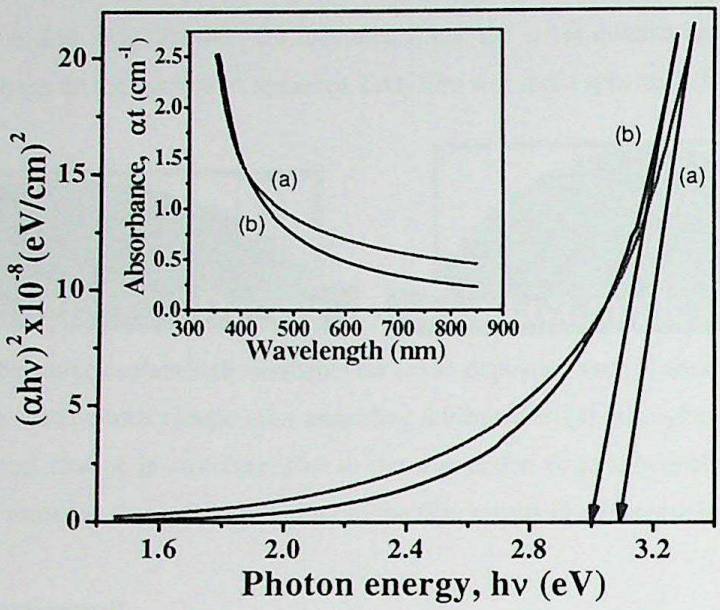


Figure 4 (a and b) Plot of $(\alpha h\acute{u})^2$ versus hν of as-deposited and annealed TiO_2 films respectively. Inset shows variation of absorption (αt) with wavelength (λ) of TiO_2 films on glass substrate.

The optical band gap (Eg) for as-deposited and annealed TiO_2 film is calculated on the basis of optical absorption using the following equation,

$$\alpha = \frac{A(Eg - h\nu)^n}{h\nu}$$

where hν is the photon energy, and A is constant. The exponent 'n' depends upon the type of transition and has values of 1/2 and 2 for direct and indirect transitions, respectively. By plotting the graph of $(\alpha h\nu)^2$ versus hν (Fig. 4), it becomes possible to determine the nature of transition involved. The extrapolation of straight-line portions of the plot (hν greater than Eg) to the zero absorption coefficient gives measurement of energy gap. Both plot show a linear dependence at hν greater than Eg, therefore extrapolation of the straight line portions of the curves to the zero absorption coefficient gives band gap of 3.1 and 3.0 eV for as deposited and annealed TiO_2 films respectively. Due to the improved grain size of annealed, the absorption edge showed red-shift up to some extent. The widened band gap of the TiO_2 films is attributed to the contribution of quantum size effect.

5. Wettability test

Controlling and/or modifying the surface wettability are important, which involves the interaction between a liquid and a solid in contact. Measurement of surface water contact angle is inversely proportional to the wettability and can be determined by Young's relation. Fig. 5 shows the water contact measurements for (a) as-deposited and (b) annealed TiO_2 thin films. Interestingly, as-deposited TiO_2

exhibits hydrophilic behavior (24°), as water contact angle is less than 90°. The shape of water droplet on the film is shown in Fig. 5(a). Further, for annealed films, the water contact angle slightly increases to 32°. The droplet shape on the surface of annealed TiO_2 film was more spherical (Fig. 5(b)).

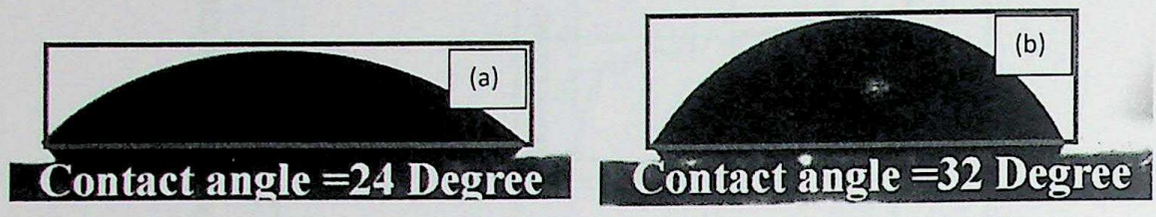


Fig. 5 shows the water contact measurements for (a) as-deposited and (b) annealed TiO_2 thin films

Increase in water contact angle after annealing attributed to (a) non-spherical nature of the grains and (b) topographical change in structure. Due to the conversion from spherical nanograins to nanorods after annealing prevents the water from adhering to the film results into increase in water contact angle.

6. Photoelectrochemical cell

A photoelectrochemical cell (PEC) is based on the junction between semiconductor and an electrolyte. The current–voltage (I–V) characteristic of a typical ITO/TiO_2/1M NaOH/graphite cell in the dark and under illumination (50mW/cm^2) is shown in Fig. 6. In the dark, the nonlinear nature of I–V curve predicts that the TiO_2 makes rectification contact with the electrolyte. Inset of Fig. 6 shows the photosensitivity under chopped light conditions carried out in order to study the response of the TiO_2 films. The photocurrent is obtained in the order of microamp/cm^2. The photoconversion efficiency 0.037% with fill factors 0.44 and flat band potential –400 mV/SCE were observed. In present investigation, low efficiency is attributed to less absorption of visible light in TiO_2 due to its wide band gap.

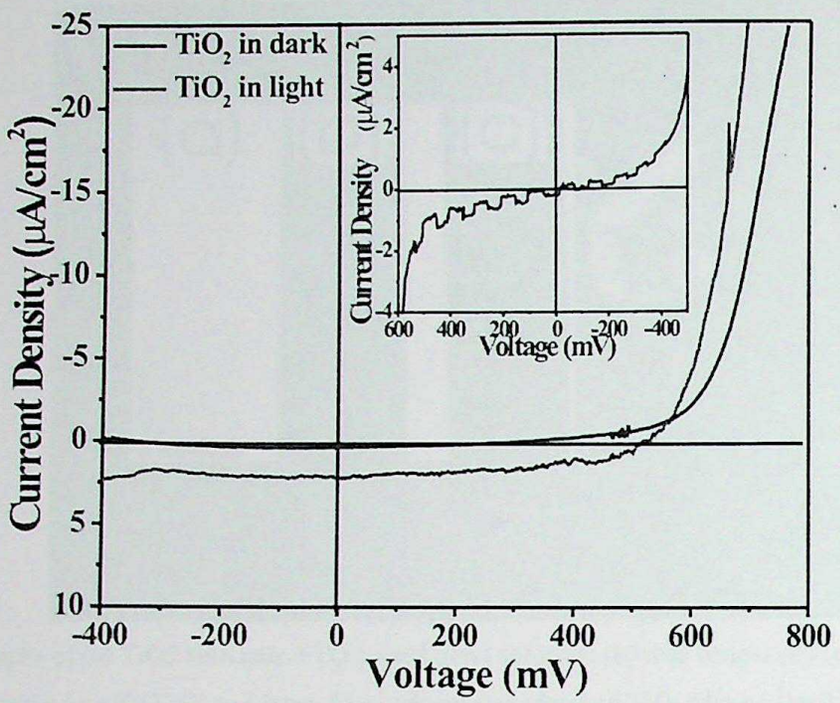


Fig. 6 I–V characteristics of annealed TiO_2 film under illumination of white light (50 mW/cm^2). Inset shows the I–V characteristic under chopped light

7. Adsorption treatment of rose bengal and methyl violet dyes on TiO_2 films.

The previously CBD deposited annealed hydrophilic TiO_2 film electrodes used for rose bengal and methyl violet dye adsorption treatment. In which, TiO_2 film electrodes were dipped into an ethanol solution of rose bengal and methyl violet dye for 24 h at room temperature. After the adsorption treatment, theTiO2 film electrodes were washed with an ethanol solution and dried. Fig.7 show the photographs of (a) TiO_2 films on FTO, (b) rose bengal and (c) methyl violet dyes are adsorbed on TiO_2 films.

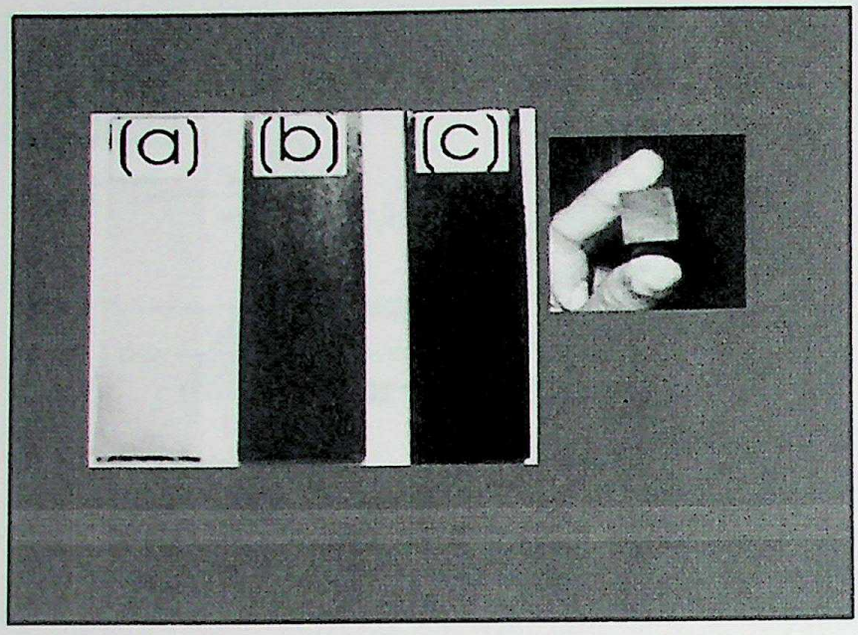


Fig.7 Photographs of (a) TiO2 film onto FTO coated glass substrate (b) rose bengal and (c) methyl violet dyes are adsorbed on TiO2 films [Inset: Rose bengal dye adsorbed TiO_2 film on flexible substrate]

Fig.8 shows the schematic experimental set-up of the dye sensitized solar cell. Maximum current and voltage output can be determined by attaching a potentiostat directly to the two sides of the cell using wires with alligator clips attached to their ends. The negative electrode is TiO_2-coated glass, and is attached to the black (-) wire, and the positive electrode (+) is connected to the counter electrode. The cell is fabricated by TCO glass substrate, photosensitizer, redox electrolyte, and counter electrode. The photograph of typical dye cell prepared with rose bengal dye inset of Fig.8.

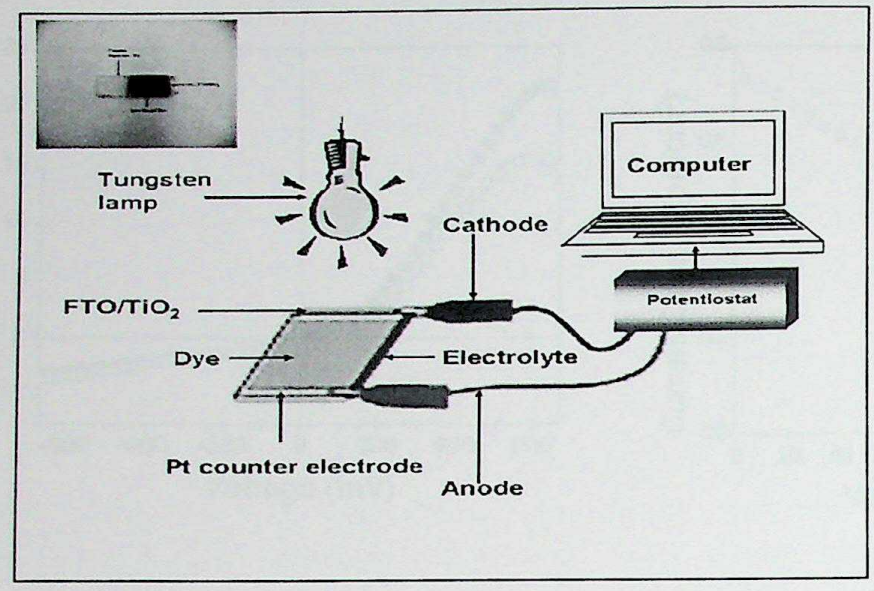
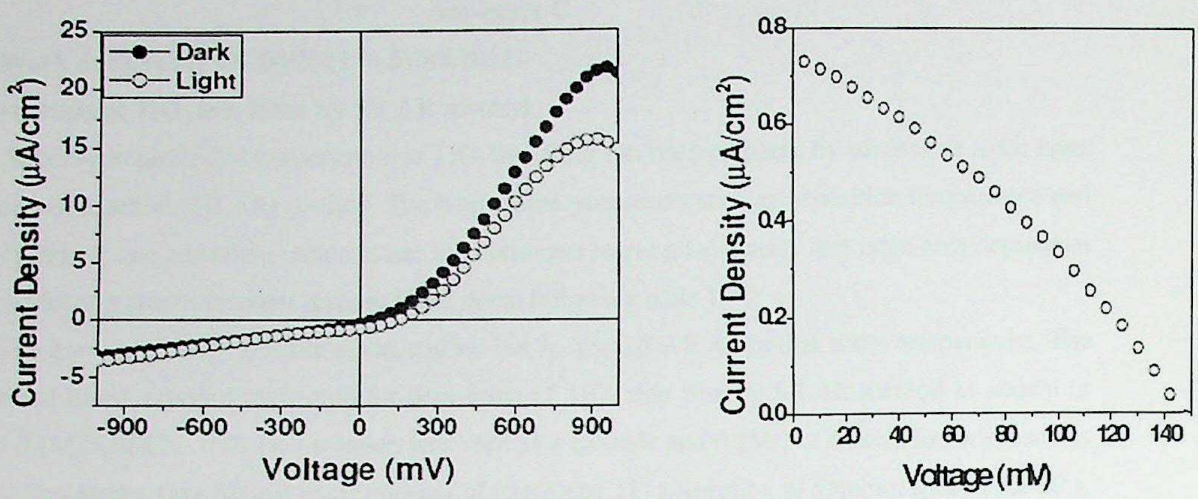


Fig.8 Schematic experimental set-up of dye sensitized solar cell [Insect: photograph of Tio_2 thin film for DSSC]

The current-voltage characteristic (I-V) in the dark and under illumination for TiO_2 film with polyiodide electrolyte for rose bengal is shown in Fig.8 (a). The I-V diode like nature of curve was shifted in the fourth quadrant indicating the cell is a generator of electricity. The junction ideality factors are calculated for dark and under illumination are shown in Table.1. The photovoltaic output characteristic under illumination intensity of $50mW/cm^2$ was studied for TiO_2 film in polyiodide electrolyte with rose bengal dye is shown in Fig.8 (b).



(a) (b)

Fig.8 (a) Current-Voltage characteristics and (b) output characteristics of TiO2 film electrode with polysulphide electrolyte for rose bengal dye under 50 mW/cm^2 tungsten filament lamp.

Table.1. Photovoltaic properties of TiO2 films deposited by CBD method with polysulphide electrolyte with rose bengal dye.

I_{sc} (μA)	0.74
V_{oc} (mV)	146
Fill Factor (FF) %	31.54
Efficiency %	0.0013
Ideality Factor (Dark)	1.90
Ideality Factor (Light)	1.87
Series Resistance (KΩ).R_s	310
Shunt Resistance (KΩ).R_{sh}	105

Annexure C

- **Work done so far (01/04/2011 to 31/03/2012)**

1] Synthesis of TiO_2 thin films by SILAR method

Superhydrophilic and nanocrystalline TiO_2 thin films has been prepared by successive ionic layer adsorption and reaction (SILAR) method. The preparative parameters such as deposition temperature and dipping cycles etc and annealing temperatures are optimized to get good quality and large area deposition on non-conducting glass substrates and are listed in the following table 1.

The growth of TiO_2 thin films was carried out by the SILAR method at room temperature. The computerized based experimental setup for deposition of TiO_2 thin film by SILAR method as shown in fig.1.The 0.1MTi(III)Cl_3, 15% HCl solution was used as a cationic and 0.1M NaOH solution was used as an anionic precursors. One SILAR cycle consists of four steps: (1) adsorption of titanium species for 20 s, (2) rinsing with distilled water for 5 s to remove excess adsorbed or loosely bounded titanium species, (3) reaction with NaOH precursor solution for 20 s to form stable TiO_2, and (4) rinsing with purified water for 5 s to remove excess or unreacted species or powdery TiO_2. The higher concentration of precursor solutions resulted in to a higher growth rate but the quality of the film was poor due to powdery deposit. In order to remove hydroxide from deposited film and o improve the crystallinity, the films were heat treated at 623 K for 2 h.

Cationic precursor	0.1 M $TiCl_3$ (15% HCl)
Anionic precursor	0.1 M NaOH
Immersion time	20 s
Rinsing time	5 s
Number of dipping cycles	75 cycles
Deposition temperature	Room temperature
Annealing temperature	623 K

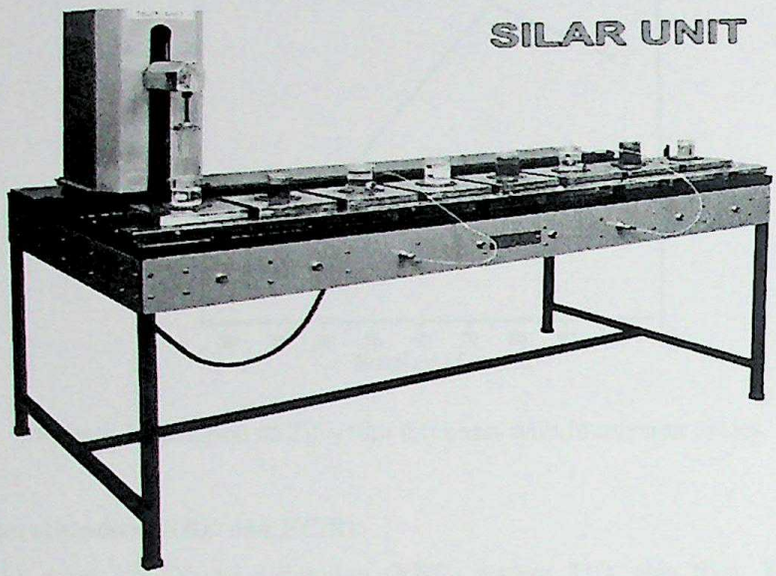


Figure.1 Experimental set-up of SILAR method.

➢ **Results**

1) Thickness measurment

Thickness of TiO_2 films was measured by the gravimetric weight difference method in terms of deposited weight of a TiO_2 film on the glass substrate, per unit area (g/cm^2), since the accurate measurement of TiO_2 film thickness was not possible due to the rough morphology and porosity of the film. The graph of the thickness of TiO_2 with the number of cycles is shown in Fig. 2. The rate of increase in the thickness is nonlinear, which has been attributed to the growth by nucleation and coalescence process. More nucleation sites contribute to coagulation during the growing procedure. Furthermore, slight decrease in film thickness observed could be attributed to the formation of outer porous layer and/or the film which may develop stress to cause delamination, resulting in peeling off the film after the film reaches at maximum thickness. The maximum thickness obtained for TiO_2 thin film was 1.34 μm and used for the further characterization.

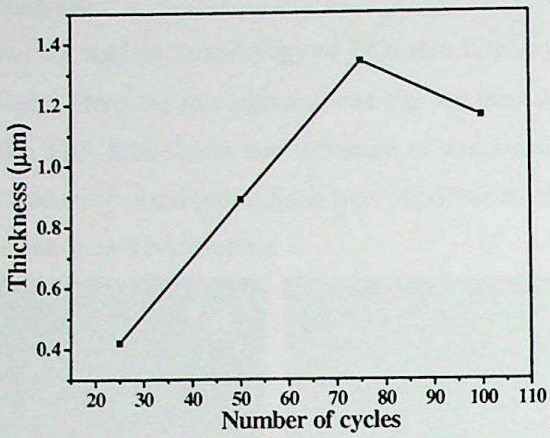


Figure.2 Variation of TiO_2 film thickness with immersion cycles.

2) Crystal structural studies (XRD and FTIR)

Fig. 3 (A) shows the X-ray diffraction (XRD) pattern TiO_2 thin film. The TiO2 films are amorphous in nature with very low crystallinity identified by X-ray diffraction analyses. In general, chemically deposited films are found to be amorphous or consist of fine grains, making it difficult to draw any conclusion regarding crystal structure of the film.

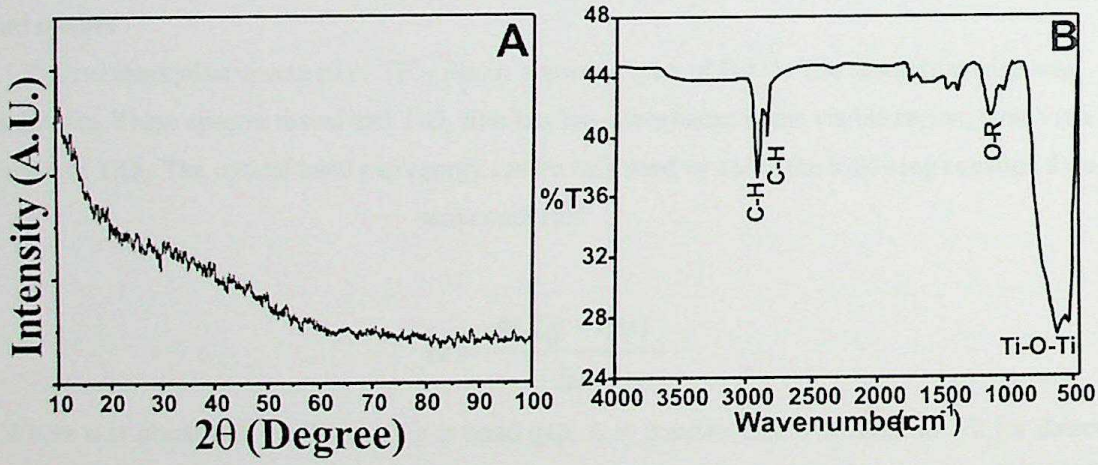


Figure 3. The (A) X-Ray diffraction pattern and (B) FTIR spectrum of TiO_2 thin film.

Fig. 3 (B) shows FTIR spectrum of TiO_2 sample. From the spectrum, it can be observed apparently that strong band around at 650 cm^{-1} is associated with the characteristic vibrational mode of anatase TiO_2. The narrow band around 2923 and 2873 cm^{-1} is due to organic residues originating from the sample as a result of the impurities in preparation procedure. Hence, result indicates the presence of Ti-O-Ti bonds, peroxo group and -OH group for TiO_2 sample.

3) Surface morphological analysis

Fig. 4 (a and b) shows the surface morphology of TiO_2 thin film at two different magnifications (×50 K and 100 K) respectively. From the micrographs, one can see the total coverage of the substrate with the clusters of TiO_2. The TiO_2 film shows the formation of nanosized smooth grains all over the surface containing some pits and meso-sized pores. Such type of porous structure resulted due to the film formation is based on the nucleation and coalescence.

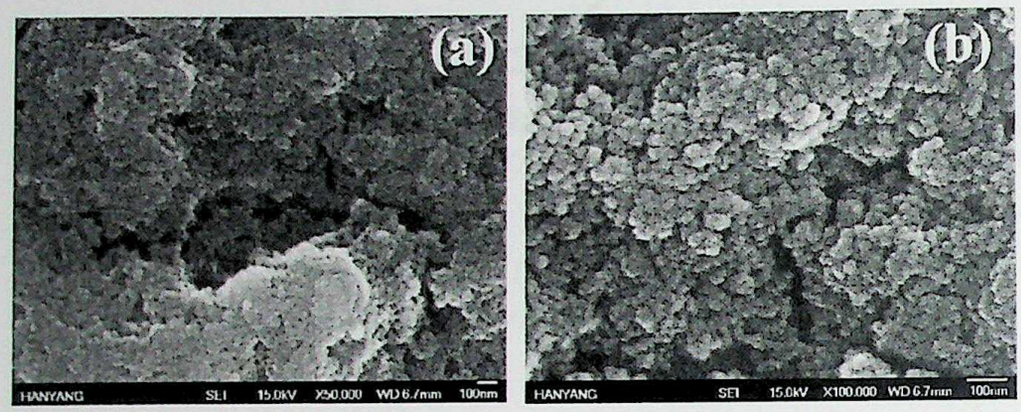


Fig. 4 (a and b) shows the surface morphology of TiO_2 thin film at two different magnifications (×50 K and 100 K) respectively

4) Optical studies

Optical absorption spectrum of TiO_2 film is shown in inset of Fig. 5. The absorption edge was found at 330 nm. These spectra reveal that TiO_2 film has low-absorbance in the visible region, which is a characteristic of TiO_2. The optical band gap energy can be estimated by using the following equation for a semiconductor:

$$\alpha = \frac{A(Eg - h\nu)^n}{h\nu}$$

Where α is absorption coefficient, Eg is band gap, A is constant and n is equal to 1/2 for direct transition. The plot of $(\alpha h\nu)^2$ versus hν of TiO_2 film is shown in Fig. 5. From the linear nature of the plot, the direct optical transition in TiO_2 is confirmed. The band gap energy, Eg is obtained by extrapolating the linear portion of the plot $(\alpha h\upsilon)^2$ versus hν to the energy axis at α=0. From the graph for TiO_2 thin film, band gap value of 3.01 eV which is in good agreement with the literature data.

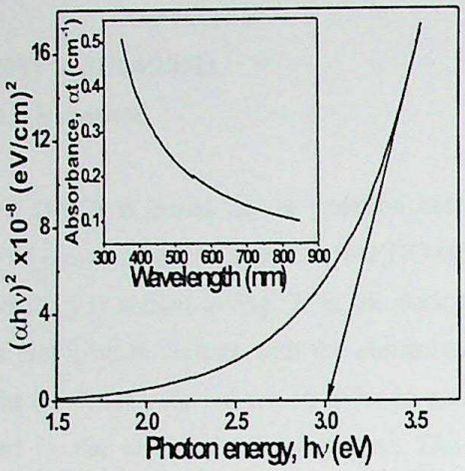


Figure 5 Plot of $(\alpha h\nu)^2$ versus hν of TiO_2 films. Inset shows variation of absorption (αt) with wavelength () of TiO_2 films on glass substrate.

Where α is absorption coefficient, Eg is band gap, A is constant and n is equal to 1/2 for direct transition. The plot of $(\alpha h\nu)^2$ versus hν of TiO_2 film is shown in Fig. 5. From the linear nature of the plot, the direct optical transition in TiO_2 is confirmed. The band gap energy, Eg is obtained by extrapolating the linear portion of the plot $(\alpha h\upsilon)^2$ versus hν to the energy axis at α=0. From the graph for TiO_2 thin film, band gap value of 3.01 eV which is in good agreement with the literature data.

5) Wettability test

Fig. 6 shows the image of water contact angle measurement on TiO_2 films surface. The surface of TiO_2 thin film is superhydrophilic in nature. Observed contact angles are too small to measure the contact angle because the surface of TiO_2 films is highly compact, porous and smooth. The water lies flat with contact angle on the surface of TiO_2 film instead of forming droplet. This specific property is attributed to nanocrystalline nature that is expected to possess very high surface energy.

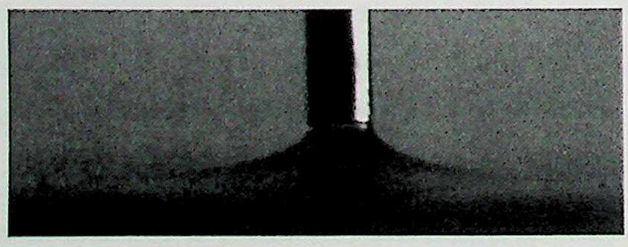


Figure 6 Contact angle measurement of TiO_2 thin film.

Annexure D

- **Work done so far (01/04/2011 to 31/04/2012)**

Synthesis of TiO_2 thin films by SILAR method

6. Photoelectrochemical cell

A photoelectrochemical cell (PEC) is based on the junction between semiconductor and an electrolyte. The current–voltage (I–V) characteristic of a typical ITO/TiO_2/1M NaOH/graphite cell in the dark and under illumination (50mW/cm^2) is shown in Fig. 7. In the dark, the nonlinear nature of I–V curve predicts that the TiO_2 makes rectification contact with the electrolyte. Inset of Fig. 7 shows the photosensitivity under chopped light conditions carried out in order to study the response of the TiO_2 films. The photocurrent is obtained in the order of microamp/cm^2. The photoconversion efficiency 0.047% with fill factors 0.42 and flat band potential –400 mV/SCE were observed. In present investigation, low efficiency is attributed to less absorption of visible light in TiO_2 due to its wide band gap.

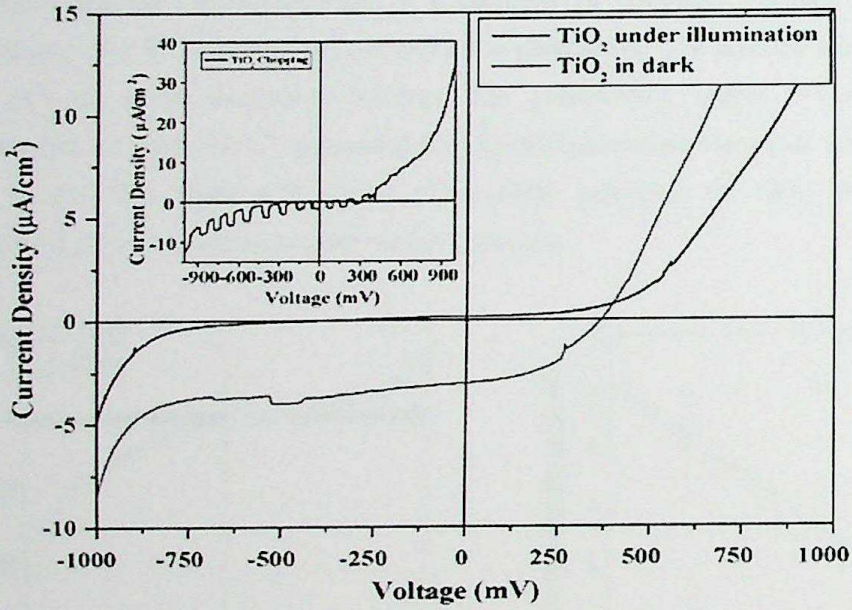


Fig. 7 I–V characteristics of annealed TiO_2 film under illumination of white light (50 mW/cm^2). Inset shows the I–V characteristic under chopped light

7. Adsorption treatment of rose bengal and methyl violet dyes on TiO_2 films.

The previously SILAR deposited hydrophilic TiO_2 film electrodes used for rose bengal and methyl violet dye adsorption treatment. In which, TiO_2 film electrodes were dipped into an ethanol

solution of rose bengal and methyl violet dye for 24 h at room temperature. After the adsorption treatment, theTiO2 film electrodes were washed with an ethanol solution and dried. Fig.8 show the photographs of Photographs of (a) as-deposited, (b) annealed at 723 K, (c) annealed TiO_2 films with rose bengal and (d) methyl violet dyes

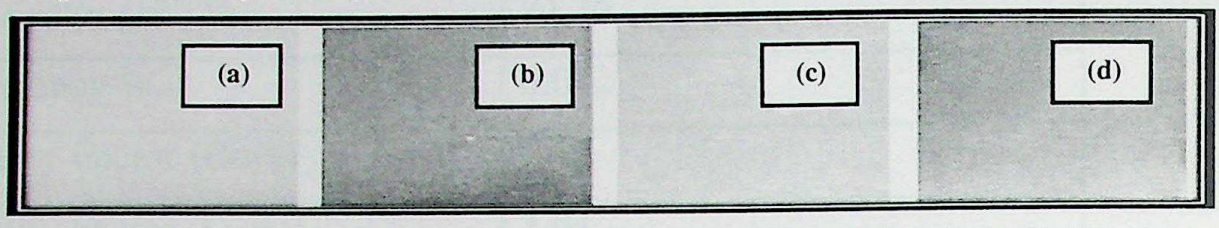
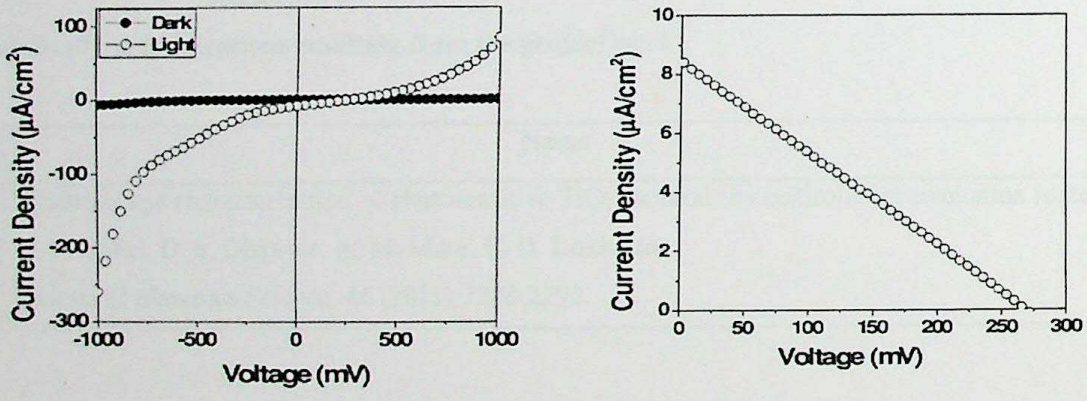


Fig.8 show the photographs of TiO_2 films (a) as-deposited, with (b) annealed at 723 K, (c) annealed rose bengal and (d) methyl violet dyes

The current-voltage characteristic (I-V) in the dark and under illumination for TiO_2 film with polyiodide electrolyte for methyl violet dye is shown in Fig 9. (a). The I-V nature of curve was shifted in the fourth quadrant indicating the cell is a generator of electricity. Increase in current under illumination indicates that TiO_2 film by SILAR method is photoactive. The junction ideality factors are calculated for dark and under illumination behavior. The photovoltaic output characteristic under illumination intensity of 50 mW/cm^2 was studied for TiO_2 film polyiodide electrolyte with methyl violet dye is shown in Fig. 9(b). Table 6.10 shows photovoltaic properties of TiO_2 film deposited by SILAR method with polyiodide electrolyte for methyl violet dye.



(a) **(b)**

Fig.9 (a) Current-Voltage characteristics and (b) output characteristics of TiO2 film electrode with polysulphide electrolyte for rose bengal dye under 50 mW/cm^2 tungsten filament lamp.

Table.1. Photovoltaic properties of TiO2 films deposited by CBD method with polysulphide electrolyte with rose bengal dye.

I_{sc} (μA)	8.46
V_{oc} (mV)	268
Fill Factor (FF) %	24.26
Efficiency %	0.022
Ideality Factor (Dark)	2.12
Ideality Factor (Light)	3.04
Series Resistance (KΩ), R_s	20
Shunt Resistance (KΩ), R_{sh}	31

- **Conclusions**

1. The hydrophilic TiO_2 films are successfully deposited by chemical bath deposition(CBD) and SILAR methods for dye sensitized solar cells application.
2. The current-voltage characteristic (I-V) of the cells checked in the dark and under illumination condition and photoactivity for chemically deposited.
3. We conclude that the chemically deposited rose bengal dye adsorbed TiO_2 film showed better performance than the unadsorbed TiO_2 film

Annexure F

- **Details of the Publications resulting from the project work**

Sr No.	Name
1.	Synthesis and characterization of photosensitive TiO_2 nanorods by controlled precipitation route D. P. Dubal, D. S. Dhawale, A. M. More, **C. D. Lokhande** Journal of Materials Science, 46 (2011) 2288-2293.

- **Papers presented in the conference during the period of project**

[1]	A novel chemical synthesis of interlocked cubes of hausmannite Mn_3O_4 thin films for supercapacitor application D. P. Dubal, D. S. Dhawale, R. R. Salunkhe, S. M. Pawar, V. J. Fulari, C. D. Lokhande, **Journal of Alloys and Compounds 484 (2009) 218–221.**

[2]	Fabrication of copper oxide multilayer nanosheets for supercapacitor application, D. P. Dubal, D. S. Dhawale, R. R. Salunkhe, V. S. Jamdade, C.D. Lokhande **Journal of Alloys and Compounds 492 (2010) 26–30.**
[3]	Conversion of interlocked cube-like Mn_3O_4 into nanoflakes of layered birnessite MnO_2 during supercapacitive studies. D. P. Dubal, D. S. Dhawale, R.R. Salunkhe, C.D. Lokhande, **Journal of Alloys and Compounds, 496 (2010) 370.**
[4]	A novel chemical synthesis and characterization of Mn_3O_4 thin films for supercapacitor application. D. P. Dubal, D. S. Dhawale, R. R. Salunkhe, S. M. Pawar, C. D. Lokhande, **Applied Surface Science 256 (2010) 4411.**
[5]	Chemical synthesis and characterization of Mn_3O_4 thin films for supercapacitor application. D. P. Dubal, D. S. Dhawale, R.R. Salunkhe, V. J. Fulari, C. D. Lokhande, **Journal of Alloys and Compounds, 497 (2010) 166.**
[6]	Systematic study of conversion of chemically prepared interlocked cube-like Mn_3O_4 to nanoflakes of birnessite MnO_2 using electrochemical cycling. D. P. Dubal, D. S. Dhawale, R. R. Salunkhe, C. D. Lokhande, **Journal of electrochemical society 150 (2010) A812-A817.**
[7]	Room temperature novel chemical synthesis of Cu_2ZnSnS_4 (CZTS) absorbing layer for photovoltaic application. N.M. Shinde , D.P. Dubal , D.S. Dhawale, C.D. Lokhande , J.H. Kim , J.H. Moon, **Materials Research Bulletin 47 (2012) 302–307**
[8]	Photosensitive Cu2ZnSnS4 (CZTS) Thin Film Grown at Room Temperature by Novel Chemical Method, C.D. Lokhande , N.M. Shinde, J.H. Kim , J.H. Moon **Invertis Journal of Renewable Energy, 3(2011)142-149**
[9]	Low cost and large area novel chemical synthesis of Cu_2ZnSnS_4 (CZTS) thin films, N. M. Shinde, C.D. Lokhande, J.H. Kim , J.H. Moon **Journal of Photochemistry and Photobiology A: Chemistry 235 (2012) 14– 20.**
[10]	Aqueous chemical growth of Cu_2ZnSnS_4 (CZTS) thin films: air annealing and photoelectrochemical properties, N. M. Shinde,P. R. Deshmukh, S. V. Patil, C. D. Lokhande, J. H. Kim , J. H. Moon, **Journal of Photochemistry and Photobiology B: Chemistry(Submitted)**
[11]	Properties of spray deposited nearly stoichiometric Cu_2ZnSnS_4 (CZTS) thin films. N. M. Shinde, R. J. Deokate, C .D. Lokhande, J.H. Kim, **Journal of Photochemistry and Photobiology A: Chemistry(Submitted)**
[12]	Development of polyaniline/Cu_2ZnSnS_4(CZTS) thin film based heterostructure as room temperature LPG, **sensor Sensors and Actuators B N.M. Shinde, S. V. Patil, P. R. Deshmukh, C.D. Lokhande, J.H. Kim , J.H. Moon (Revision submitted)**

➢ **Other papers presented in the conference during the period of project**

1	Recent developments in metal oxide based supercapacitors D. P. Dubal, D. S. Dhawale, C. D. Lokhande 4th Asian Conference on Electrochemical Power Sources (ACEPS-4) Taipei, Taiwan November 8-12, 2009.
2	Electrochemical synthesis of MnO_2 nano-nests like architecture for supercapacitor application, D. P. Dubal, D. S. Dhawale, S. V. Patil, C. D. Lokhande NSAM 2010, Kolhapur (India).
3	Chemical synthesis of nanosheet structured copper oxide thin films for supercapacitor application, S. K. Shinde, K. R. Gayakvad, D. P. Dubal, C. D. Lokhande, V. J. Fulari Abasaheb Garware Collage Pune 2010.
4	Potentiodynamically Deposited Polypyrrole Electrodes for Supercapacitor Application D. P. Dubal, S. V. Patil, D. S. Dhawale, N. M. Shinde, C. D. Lokhande International Conference on "Physics of Emerging Functional Materials" (PEFM-2010).
5	Large area novel chemical synthesis of Cu_2ZnSnS_4 (CZTS) thin films for Photovoltaic application N. M. Shinde, D. P. Dubal, C. D. Lokhande, J. H. Kim, J. H. Moon, International Conference on Solar Energy Materials, Solar Cells and Solar Energy (2011).
6	Chemical synthesis of Cu_2ZnSnS_4 (CZTS) absorbing layer for photovoltaic application N. M. Shinde, D. P. Dubal, A. D. Jagadale, C. D. Lokhande International Conference on Solar Energy Materials, Solar Cells and Solar Energy (2011).
7	Photosensitive CZTS thin film grown at room temperature by novel Chemical method, N. M. Shinde ,C. D. Lokhande ,NS-NMAT 2011 at Pandharpur
8	Low cost and large area novel chemical synthesis of Cu_2ZnSnS_4 (CZTS) thin films for Photovoltaic applicationN.M. Shinde, P.R. Deshmukh, A.D. Jagadale, R.N. Bulakhe, S.B. Jambure, C.D. Lokhande (ICPM-MDF-2012)

ज्ञान-विज्ञान विमुक्तये

ANNEXURE -V

UNIVERSITY GRANT COMISSION

BAHADUR SHAH ZAFAR MARG

NEW DELHI-110 002.

STATEMENT OF EXPENDITURE IN RESPECT OF MAJOR/MINOR RESEARCH PROJECT

1. Name of the Principal Investigator: Prof. Lokhande Chandrakant Dnyandev
2. Dept. of University/ College: Shivaji University, Kolhapur (Maharashtra)
3. UGC approval No. and date: 36-207/2008 (SR) dated 26 March 2009
4. Title of the Research Project: "**Chemically deposited superhydrophilic nanocrystalline titanium dioxide (TiO_2) films for dye sensitized solar cells".**
5. Effective date of the starting of the project: 02/05/2009
6. (a) Period of the expenditure from 01/05/2011 to 31/04/2012
7. Details of the expenditure

S. No.	Item	Amount Approved Rs.	1st years	2nd year	3rd year	Toatal amount Expenditure	Toatal amount recived	Out standing balance
i.	Books and Journals	Nil/-	Nil/-	Nil/-	Nil/-	8,47,702/-	665800/-	204000/-
ii.	Equipment	4, 00, 000.00 (For 3 years)	1, 28, 992 [+ 2, 03, 130 Tender placed]	64,813/-	203130/-			
iii.	Contingency	50, 000.00	29,412.00	9,444/-	750/-			
iv.	Field Work/ Travel (Give details in the perform at the Annexure IV)	30, 000.00	23,996.00	10,187/-	--------			
v.	Hiring Services/consumable	30,000.00	13,477.00	7,143/-	1500/-			
vi.	Chemicals and Glassware	50,000.00	27,872.00	21,597/-	3912/-			
vii.	Overhead @ 10% approved recurring Grant (Except travel/ Field Work)	41,800.00	14,000	14,000/-	13,933/-			
viii.	Project Fellowship @8, 000/-p.m	2,88,000.00	62,193.00	93,351/-	104000/-			
	Total=	8, 89, 800.00	2, 99, 942.00	2,20,535	3,27225/-			

Prof. C. D. Lokhande
Principal Investigator (U.G.C. Scheme)
Thin Film Physics Lab;Department of Physics,
Shivaji University, Kolhapur - 416 004 (India)

ज्ञान-विज्ञान विमुक्तये

ANNEXURE -VI

UNIVERSITY GRANT COMISSION
BAHADUR SHAH ZAFAR MARG
NEW DELHI-110 002.

STATEMENT OF THE EXPENDITURE INCURRED ON FIELD WORK

01/04/2011 to 31/04/2012

Name of the Principal Investigator: Prof. Lokhande Chandrakant Dnyandev

Name of the Place visited	Duration of the visit		Mode of Journey	Expenditure incurred (Rs)
	From	to		
No	No	No	-	No

Certified that the no expenditure is in accordance with the UGC norms for the Major Research Projects.

SIGNATURE OF PRINCIPAL INVESTIGATOR

REGISTRAR
Registrar,
Shivaji University, Kolhapur.

Prof. C. D. Lokhande
Principal Investigator (U.G.C. Scheme)
Thin Film Physics Lab;Department of Physics,
Shivaji University, Kolhapur - 416 004 (India)

ज्ञान-विज्ञान विमुक्तये

ANNEXURE -VII

UNIVERSITY GRANT COMISSION
BAHADUR SHAH ZAFAR MARG
NEW DELHI-110 002.

ACCEPTANCE CERTIFICATE FOR RESEARCH PROJECT

Name - Prof. Lokhande Chandrakant Dnyandev

No. F. 36-207/2008 (SR) dated 26 March 2009

Title of the Project - **Chemically deposited superhydrophilic nanocrystalline titanium dioxide (TiO2) films for dye sensitized solar cells**

1. The research project is not being supported by any other funding agency.
2. The terms and conditions related to the grant are acceptable to the Principal Investigator and University/College/Institution.
3. At present, I have no research project approved by UGC and the accounts for the previous project, if any have been settled.
4. The College/University is fit to receive financial assistance from UGC and is Included in the list prepared by the UGC.
5. The Principal Investigator is a retired teacher and eligible to receive honorarium as he/she is neither getting any honorarium from any agency nor is he/she gainfully employed anywhere.
6. His/her date of birth is 01/06/1956
7. The date of implementation of the project is 26 March 2009

SIGNATURE OF PRINCIPAL INVESTIGATOR

Prof. C. D. Lokhande
Principal Investigator (U.G.C. Scheme)
Thin Film Physics Lab;Department of Physics,
Shivaji University, Kolhapur - 416 004 (India)

REGISTRAR

Registrar,
Shivaji University, Kolhapur

ज्ञान-विज्ञान विमुक्तये

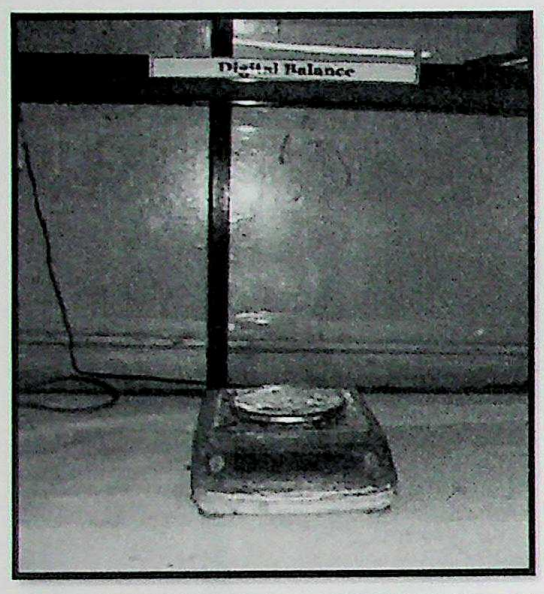
ANNEXURE -VIII

UNIVERSITY GRANT COMISSION
BAHADUR SHAH ZAFAR MARG
NEW DELHI-110 002.

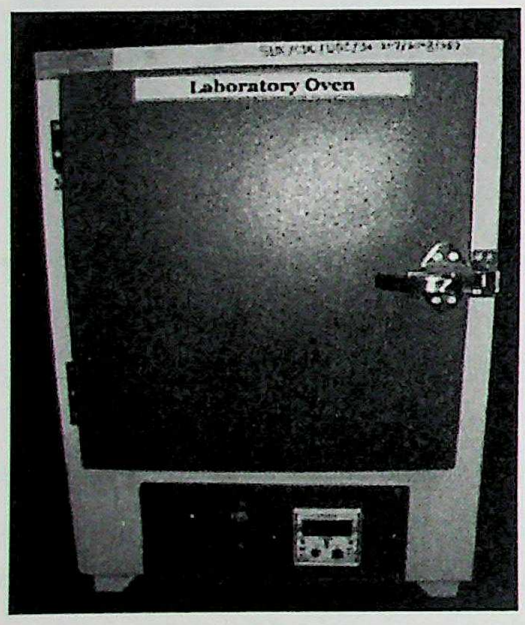
PROFORMA FOR SUBMISSION OF INFORMATION AT THE TIME OF SENDING THE FINAL REPORT OF THE WORK DONE ON THE PROJECT

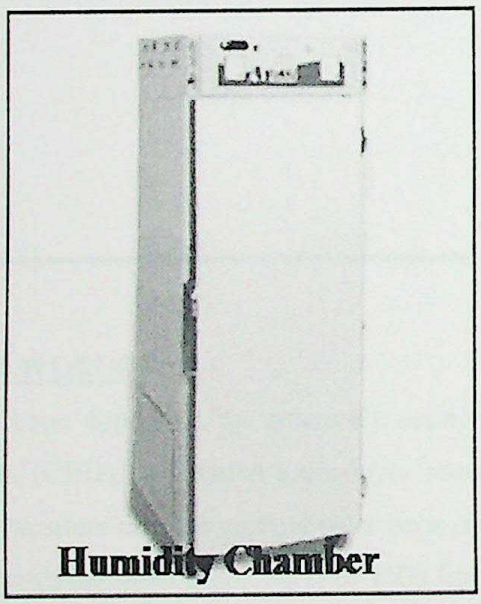
1. NAME AND ADDRESS OF THE PRINCIPAL INVESTIGATOR - Prof. Lokhande Chandrakant Dnyandev
2. NAME AND ADDRESS OF THE INSTITUTION -Shivaji University, Kolhapur (Maharashtra)
3. UGC APPROVAL NO. AND DATE-36-207/2008 (SR) dated 26 March 2009
4. DATE OF IMPLEMENTATION 6 March 2009
5. TENURE OF THE PROJECT .....
6. TOTAL GRANT ALLOCATED - 8, 89, 800/-
7. TOTAL GRANT RECEIVED - 665800/-
8. FINAL EXPENDITURE- 8,47,702/-
9. TITLE OF THE PROJECT- Chemically deposited super hydrophilic nanocrystalline titanium dioxide (TiO_2) films for dye sensitized solar cells
10. OBJECTIVES OF THE PROJECT - Annexure A
11. WHETHER OBJECTIVES WERE ACHIEVED- Yes
12. ACHIEVEMENTS FROM THE PROJECT

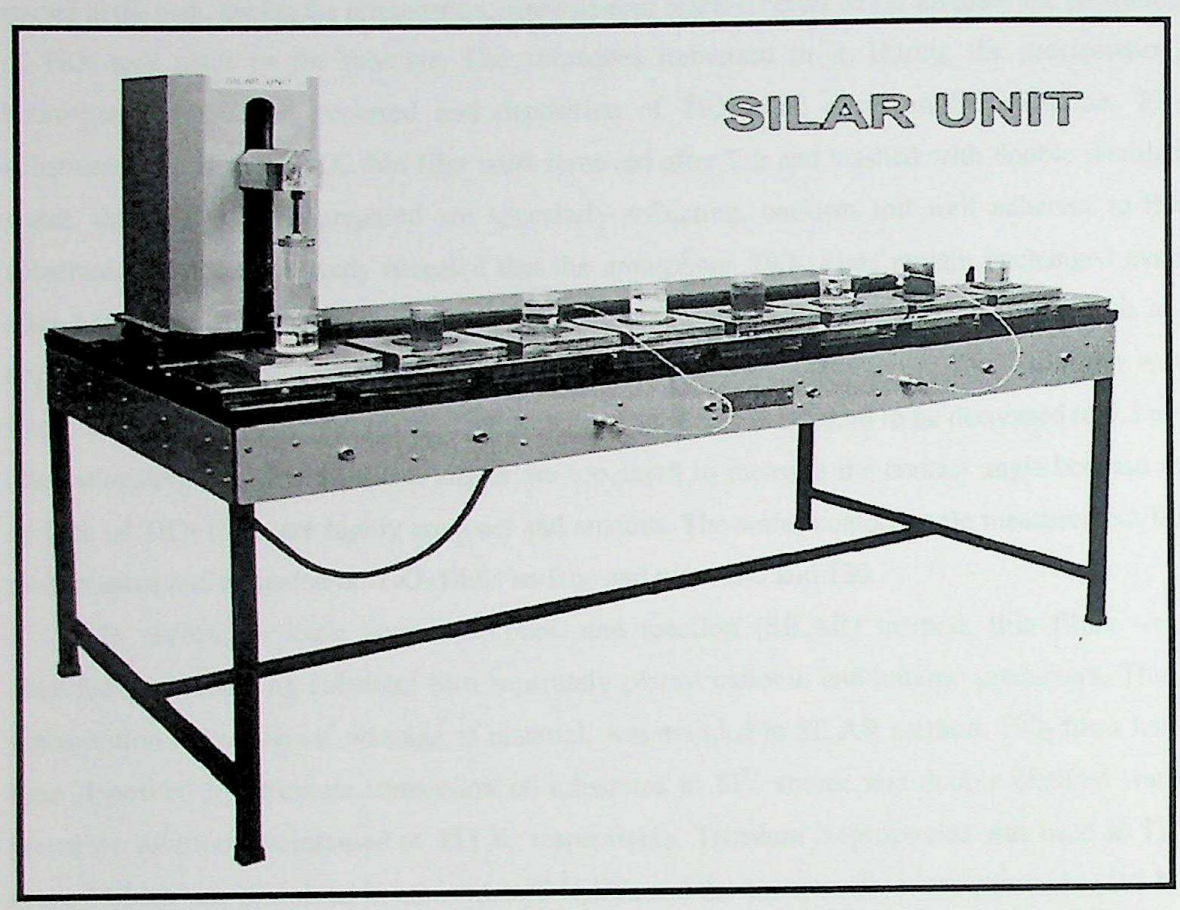
The major equipments/instruments purchased:











13. SUMMARY OF THE FINDINGS (IN 500 WORDS)

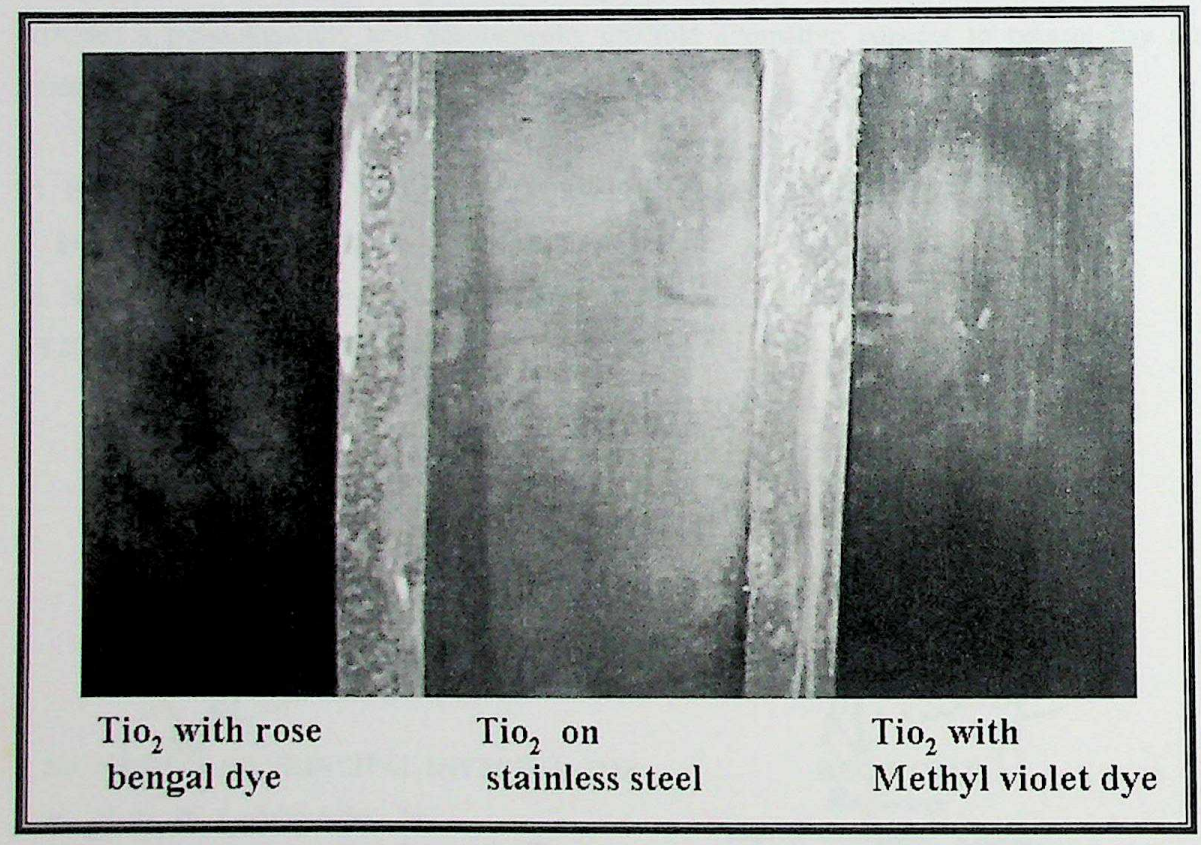
In the present work, TiO_2 films have been deposited by, relatively economical; two chemical methods i.e. chemical bath deposition (CBD), successive ionic layer adsorption and reaction (SILAR), methods. The preparative parameters of each method have been optimized to achieve maximum efficiency for DSSC's. The work has been preparation of TiO_2 films by CBD method is based on the heating of acidic solution of titanium(III) chloride containing an aqueous solution composed of titanium trichloride, hydrogen peroxide was first prepared. In brief, 0.1 M $TiCl_3$, 15% HCl was added drop-wise to a well stirred hydrogen peroxide (H_2O_2, Molychem, 30 wt %) and water solution. The pH was adjusted between 2.0 and 3.0 using a mixture of 30 % liquid ammonium hydroxide with constant stirring. A transparent solution with a reddish-yellow color was obtained after vigorous stirring for 30 min at room temperature. Glass substrates were washed with chromic acid and in an

ultrasonic bath at room temperature for 30 min. These cleaned substrates were immersed in the above bath and the bath was heated. When the bath attains the temperature of 343 K, the precipitation was started in the bath. During the precipitation, heterogeneous reaction occurs on the substrate and deposition of TiO_2 took place on the substrate. The substrates immersed in it. During the precipitation, heterogeneous reaction occurred and deposition of TiO_2 took place on the substrate. The substrates coated with TiO_2 thin film were removed after 2 h and washed with double distilled water, dried. The films prepared are specularly reflecting, uniform and well adherent to the substrates. A structural study revealed that the amorphous TiO_2 films remain unchanged even after annealing. A SEM study shows good coverage that consists of TiO_2 nanorods. Both as-deposited and annealed TiO2 films exhibit n-type electrical conductivity. The band gap was found to be 3.4 eV for as-deposited TiO_2 film. The band gap was found to be decreased to 3.3 eV after annealing. Observed contact angles are too small to measure the contact angle because of surface of TiO_2 films are highly compact and smooth. The water contact angle measurement for as-deposited and annealed on TiO_2 films surface and were 100 and 120.

In successive ionic layer adsorption and reaction (SILAR) method, thin films were obtained by immersing substrate into separately placed cationic and anionic precursors. Thus, precipitation formation i.e. wastage of material, was avoided in SILAR method. TiO_2 films have been deposited by alternate immersion of substrates in Ti^{4+} source and double distilled water precursor solutions maintained at 353 K, respectively. Titanium isopropoxide was used as Ti^{4+} source, which was dissolved in concentrated H_2SO_4 and the concentration was adjusted to 0.5 M. The pH of the solution was adjusted at ~ 0.5–1.0 by addition of aqueous ammonia (NH_4OH) solution. The oxygen precursor was the hot double distilled water maintained at temperature of 353 K. In initial process step, the substrate was immersed in titanium isopropoxide solution for 20 s which will adsorbed (TiOH) ions on the substrate. After immersion of the substrate in hot H_2O for 40 s, the reaction occurred at substrate surface to form TiO_2. This cycle was repeated for several times in order to increase the thickness of film. The second bath served the additional purpose of removal of loosely bound particles from the substrate. The period for which the substrate was kept in titanium bath was referred as adsorption

period and that for which substrate was kept in hot H_2O was referred as reaction period, since the reaction to form TiO_2 takes place in second bath. The adsorption and reaction period was 20 and 40 s, respectively for TiO_2 film formation. The as deposited and annealed TiO_2 films have been

characterized for structural, surface morphological, electrical and optical properties. The XRD analysis declares the absence of any sharp diffraction lines, indicating that the amorphous nature of TiO_2 films. The scanning electron micrographs revealed films are smooth, irregular shaped spherical grains of random size and well covered to the FTO coated glass substrate with some cracks. The thermo-emf developed between two ends showed that the TiO_2 was an n-type electrical conductivity material. The band gap decreased after annealing from 3.6 to 3.5 eV which is attributed to increase in grain size. As-deposited and annealed TiO2 films were superhydrophobic as the water contact angles greater than 90^0. The water droplet forming on the surface of TiO2 film instead of the water lies flat with contact angle because of irregular shaped spherical grains. Such type of surface morphology might have caused for higher water contact angle value instead of forming the nanorods or web-like morphology. SILAR deposited TiO2 films with polysulphide electrolyte for rose bengal dye showed good efficiency of 0.0237 % as compared to other deposition methods.



Actual photograph of large area deposition Tio_2 thin film on stainless steel substrate with rose bengal and methyl violet dye.

14. CONTRIBUTION TO THE SOCIETY

The project work undertaken and completed itself may contribute to society by avoiding light energy problem in rural area. Among the renewable energy sources solar energy has a great importance. Sun has always been the most powerful energy source on earth. It is clean, environmentally friendly and is for free. Sunlight can be transformed into electricity using solar cells. Solar cells found applications in many different fields such as in calculators, solar lamps and even on spacecraft and satellites. The use of silicon crystals in the solar cells makes it expensive. Silicon crystals are moduled together manually. On the other hand, silicon purification is difficult and a lot of silicon is wasted. In addition, since the performance of silicon cells degrades as the temperature increases, the long lasting concentrated operation of silicon cells require a cooling system. A lot of effort is put on the research for new fabrication techniques. In contrast, the novel dye sensitized nanocrystalline TiO_2 based solar cells (DSSC's) provides a technologically and economically credible alternative concept to present day pn junction photovoltaic system.

15. WHETHER ANY PH.D. ENROLLED/PRODUCED OUT OF THE PROJECT- Yes

1) Dr. D. P. Dubal 2) Mr. N. M. Shinde

16. NO. OF PUBLICATIONS OUT OF THE PROJECT .....9.....

(PLEASE ATTACH RE-PRINTS)

SIGNATURE OF PRINCIPAL INVESTIGATOR

Prof. C. D. Lokhande
Principal Investigator (U.G.C. Scheme)
Thin Film Physics Lab;Department of Physics,
Shivaji University, Kolhapur - 416 004 (India)

REGISTRAR

Registrar,
Shivaji University, Kolhapur

UGC Project Fellow Salary

Period May 2009 t0 April 2012

Month – wise and year – wise detailed statement of expenditure of Project Fellow Salary

Sr. no	Name of project student	Date	Amount Recived
		I year(2009-010)	
1)	Mr. D. P. Dubal	23/07/2009	6193/-
2)	Mr. D.P. Dubal	24/08/2009	8000/-
3)	Mr. D. P.Dubal	23/09/2009	8000/-
4)	Mr. D. P.Dubal	26/10/2009	8000/-
5)	Mr. D. P.Dubal	19/11/2009	8000/-
6)	Mr. D. P.Dubal	28/12/2009	8000/-
7)	Mr. D. P.Dubal	25/01/2010	8000/-
8)	Mr. D. P.Dubal	24/02/2010	8000/-
		Total	**62193/-**
		II year(2010-011)	
9)	Mr. D. P.Dubal	22/03/2010	8000/-
10)	Mr. D. P.Dubal	26/04/2010	8000/-
11)	Mr. D. P.Dubal	25/05/2010	8000/-
12)	Mr. D. P.Dubal	29/06/2010	8000/-
13)	Mr. D. P.Dubal	28/07/2010	516/-
14)	Mr. N. M.Shinde	18/08/2010	6968/-
15)	Mr. N . M. Shinde	7/10/2010	8000/-
16)	Mr. N . M. Shinde	26/10/210	8000/-
17)	Mr. N . M. Shinde	30/11/2010	5867/-
18)	Mr. N . M. Shinde	29/12/2010	8000/-
19)	Mr. N . M. Shinde	31/01/2011	8000/-
20)	Mr. N . M. Shinde	27/02/2011	8000/-
21)	Mr. N . M. Shinde	28/03/2011	8000/-
		Total	**93,351/-**
		II year(2010-012)	
22)	Mr. N . M. Shinde	27/04/2011	8000/-
23)	Mr. N . M. Shinde	07/06/2011	8000/-
24)	Mr. N . M. Shinde	02/07/2011	8000/-
25)	Mr. N . M. Shinde	22/08/2011	16000/-
26)	Mr. N . M. Shinde	29/09/2011	8000/-
27)	Mr. N . M. Shinde	08/11/2011	8000/-
28)	Mr. N . M. Shinde	08/12/2011	8000/-
29)	Mr. N . M. Shinde	03/01/2012	8000/-
30)	Mr. N . M. Shinde	08/02/2012	8000/-
31)	Mr. N . M. Shinde	29/02/2012	8000/-
32)	Mr. N . M. Shinde	27/03/2012	8000/-
33)	Mr. N . M. Shinde	30/04/2012	8000/-
		Total	**1,04,000/-**

Applied Surface Science 256 (2010) 4411–4416

Contents lists available at ScienceDirect

Applied Surface Science

journal homepage: www.elsevier.com/locate/apsusc

A novel chemical synthesis and characterization of Mn_3O_4 thin films for supercapacitor application

D.P. Dubal [a], D.S. Dhawale [a], R.R. Salunkhe [a], S.M. Pawar [b], C.D. Lokhande [a,*]

[a] Thin Film Physics Laboratory, Department of Physics, Shivaji University, Kolhapur 416004 (M.S), India
[b] Photonic and Electronic Thin Film Laboratory, Department of Materials Science and Engineering, Chonnam National University, 300 Yongbong-Dong, Puk-Gu, Gwangju 500-757, South Korea

ARTICLE INFO

Article history:
Received 19 November 2009
Received in revised form 11 December 2009
Accepted 14 December 2009
Available online 23 December 2009

Keywords:
Mn_3O_4 thin films
SILAR
Surface morphology
Supercapacitor

ABSTRACT

Mn_3O_4 thin films have been prepared by novel chemical successive ionic layer adsorption and reaction (SILAR) method. Further these films were characterized for their structural, morphological and optical properties by means of X-ray diffraction (XRD), Fourier transform infrared spectrum (FTIR), field emission scanning electron microscopy (FESEM), wettability test and optical absorption studies. The XRD pattern showed that the Mn_3O_4 films exhibit tetragonal hausmannite structure. Formation of manganese oxide compound was confirmed from FTIR studies. The optical absorption showed existence of direct optical band gap of energy 2.30 eV. Mn_3O_4 film surface showed hydrophilic nature with water contact angle of 55°. The supercapacitive properties of Mn_3O_4 thin film investigated in 1 M Na_2SO_4 electrolyte showed maximum supercapacitance of 314 F g^{-1} at scan rate 5 mV s^{-1}.

© 2009 Elsevier B.V. All rights reserved.

1. Introduction

Hausmannite Mn_3O_4 is one of the most stable oxides of manganese, and it has a variety of important applications such as electrochemical materials, high density magnetic storage medium, catalyst, ion-exchange, molecular adsorption etc. [1–3]. An emerging application of manganese oxide is an electrode material for electrochemical supercapacitors. In a pure form it is used to manufacture ferrites for electronic applications [4]. It is also used as a starting material for fabrication of Li–Mn–O rechargeable batteries [5]. This material is an active catalyst for oxidation of methane and CO [6] and the combustion of organic compounds between 373 and 773 K, which is of interest for solving air-pollution problems [7]. Hausmannite Mn_3O_4 is known to have a normal spinel structure with tetragonal distortion elongated along the *c*-axis due to Jahn-Teller effect on the Mn^{3+} ion. Manganese ions occupy the octahedral B-site (Mn^{3+}) and tetrahedral A-site (Mn^{2+}) corresponding to a normal spinel structure. There are 32 oxygens and 24 cations in the unit cell [8].

Recently, conducting polymers, activated carbon and transition metal oxides are widely used for supercapacitor electrode material. Manganese oxide thin films which belong to third category show excellent pseudocapacitive behavior with the large specific capacitance as high as 698 F g^{-1} [9]. As a supercapacitor, the manganese oxide electrode has been found to have good efficiency, long term performance and good corrosion stability which make it most promising new electrode material for fabrication of commercial supercapacitor [10]. Mn_3O_4 thin films have been prepared using various synthetic methods, such as sol–gel dip- or drop-coating [9], solution based chemical routes [11], electrostatic spray deposition [12], physical vapor deposition followed by electrochemical oxidation [13] and electrochemical deposition [14]. Among these chemical methods, successive ionic layer absorption and reaction (SILAR) is low cost and low temperature soft chemical solution method. The SILAR method is relatively a new and less investigated method, which is based on sequential reaction on the substrate surface. Rinsing follows each reaction, which enables heterogeneous reaction between the solid phase and the solvated ions in the solution. SILAR method has its own advantages such as layer-by-layer growing mode, excellent material utilization efficiency, and good control over the deposition process along with the film thickness and large-scale deposition capability on any type of substrate [15].

In the present investigation, we report the synthesis of Mn_3O_4 thin films by SILAR method. These films were characterized by X-ray diffraction (XRD), Fourier transform infrared spectrum (FTIR), field emission scanning electron microscope (FESEM), wettability test and optical absorbance studies. The supercapacitive behavior of Mn_3O_4 thin film was investigated by cyclic voltammetry in 1 M Na_2SO_4 electrolyte.

* Corresponding author. Tel.: +91 231 2609225; fax: +91 231 2609233.
E-mail address: l_chandrakant@yahoo.com (C.D. Lokhande).

0169-4332/$ - see front matter © 2009 Elsevier B.V. All rights reserved.
doi:10.1016/j.apsusc.2009.12.057

2. Experimental details

2.1. Synthesis of Mn_3O_4 thin films

For the deposition of Mn_3O_4 thin films, 100 mM manganese sulphate was used as the cationic precursor solution and anionic precursor solution was 1 M sodium hydroxide. The well cleaned glass/stainless steel substrate was immersed in a cationic precursor solution ($MnSO_4$) for 10 s for the adsorption of manganese species on the substrate surface. The substrate was rinsed in double distilled water for 5 s to remove loosely bound species of Mn^{2+} species. Then, the substrate was immersed in anionic precursor solution (NaOH) which was kept at 333 K for 10 s to form a layer of manganese oxide material. Rinsing the substrate again in double distilled water for 10 s to separates out the excess or unreacted species. Thus one SILAR cycle of Mn_3O_4 deposition was completed. 100 such deposition cycles were repeated at room temperature (300 K) to get a terminal thickness. The maximum thickness obtained for Mn_3O_4 thin film was 1.23 μm and used for the further characterization.

2.2. Characterization techniques

For thickness measurement, gravimetric weight difference method with the relation $t = m/(\rho \times A)$ where, m is the mass of the film deposited on the substrate in gm; A is the area of the deposited film in cm^2 and ρ is the density of the deposited material (Mn_3O_4 = 7.21 g cm^{-3}) in bulk form. The crystal structure of the film material was identified by X-ray diffraction analysis with Philips (PW 3710) diffractometer. The Fourier transform infrared (FTIR) spectrum of the samples were collected using a 'Perkin Elmer, FTIR Spectrum one' unit. The film morphology was observed by field emission scanning electron microscopy (FESEM, Model: JSM-6160). To study the wettability of the films, contact angle measurement was carried out by Rame-hart USA equipment with CCD camera. The optical absorption studies were carried out within the wavelength range 350–850 nm for Mn_3O_4 films using Systronics spectrophotometer-119, with glass substrate as reference. The supercapacitor formation and its studies were carried out using the 263A EG &G Princeton Applied Research Potentiostat forming an electrochemical cell comprising Mn_3O_4 film as a working electrode, platinum as a counter electrode and saturated calomel electrode (SCE) as a reference electrode in 1 M Na_2SO_4 electrolyte.

3. Results and discussion

3.1. Film formation mechanism

Mn_3O_4 thin films were prepared by immersing substrate in separately placed cationic and anionic precursors with rinsing between every immersion. The growth kinetics of a thin film deposition process is ion-by-ion growth mechanism, which involves the ion-by-ion deposition at nucleation sites on the immersed surfaces. The mechanism of Mn_3O_4 film formation by SILAR method is explained as follows. The hydrolysis of manganese sulphate takes place with pH ~5 which gives manganese hydroxyl $Mn(OH)^{2+}$ ions.

$$MnSO_4 + 2H_2O \rightarrow Mn(OH)^{2+} + H_2SO_4 \quad (1)$$

When substrate is immersed in this solution, $Mn(OH)^{2+}$ ions gets adsorbed onto the substrate due to attraction between ions in the solution and surface of the substrate. These forces may be cohesive forces or van der Waals forces or chemical attractive forces. Further reaction is followed by the immersion of substrate in NaOH anionic solution, where the chemical reaction between OH^- and $Mn(OH)^{2+}$ ions leads to the deposition of adherent Mn_3O_4 layer. In basic media Mn^{2+} is oxidized to Mn^{3+} and the reaction is as follows:

$$3Mn(OH)^{2+} + 2OH^- \rightarrow Mn_3O_4 + 4H_2O \quad (2)$$

Here the NaOH is base and in basic medium Mn^{2+} is unstable state hence Mn^{2+} is oxidized to Mn^{3+} and leads to the formation of Mn_3O_4 thin films. Mn_3O_4 thin films are uniform and well adherent to the substrate surface. Here, for the deposition of Mn_3O_4 thin films the adsorption period was 10 s and reaction period was 10 s. The optimized preparative parameters are summarized in Table 1.

Table 1
Optimized preparative parameters for deposition of Mn_3O_4 thin films.

Precursors	$MnSO_4$	NaOH
Concentrations	0.1 M	1 M
Immersion time	10 s	10 s
Number of immersions	100	100
Thickness (μm)	1.23	–
Deposition temperature	300 K	343 K

3.2. Thickness measurement

Thickness of Mn_3O_4 films was measured by the gravimetric weight difference method in terms of deposited weight of a Mn_3O_4 film on the glass substrate, per unit area (g cm^{-2}), since the accurate measurement of Mn_3O_4 film thickness was not possible due to the rough morphology and porosity of the film. The graph of the deposited weight of Mn_3O_4 with the number of cycles is shown in Fig. 1. In the process of deposition of Mn_3O_4 films by SILAR method, Mn_3O_4 thin films were prepared by immersing substrate in separately placed cationic and anionic precursors with rinsing between every immersion. The weight of Mn_3O_4 film was found to increase with number of cycles. After 100 cycles, the thickness of the film decreases. Inset of Fig. 1 shows the photographs of films having thickness 0.57, 0.94, 1.23 μm after 25, 50 and 100 cycles respectively. The maximum thickness obtained for Mn_3O_4 thin film was 1.23 μm and used for the further characterization.

3.3. Structural studies

Manganese oxides crystallize in several different structures with varied proportions of Mn ions (Mn^{2+}, Mn^{3+}, and Mn^{4+}). The

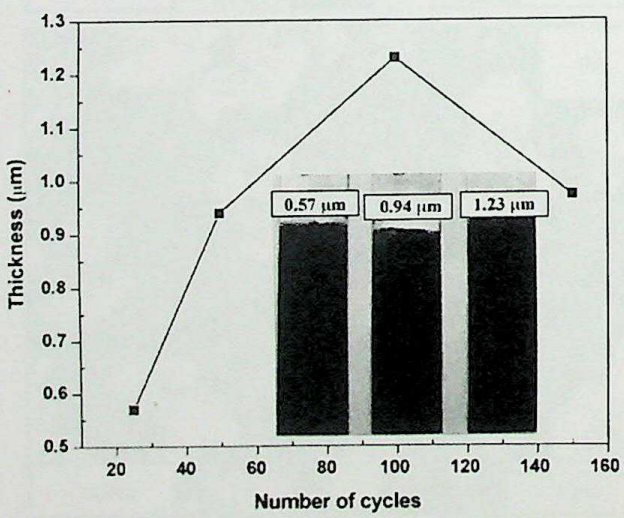


Fig. 1. Variation of Mn_3O_4 film thickness with number of cycles. Inset shows photographs of Mn_3O_4 thin films at different thicknesses.

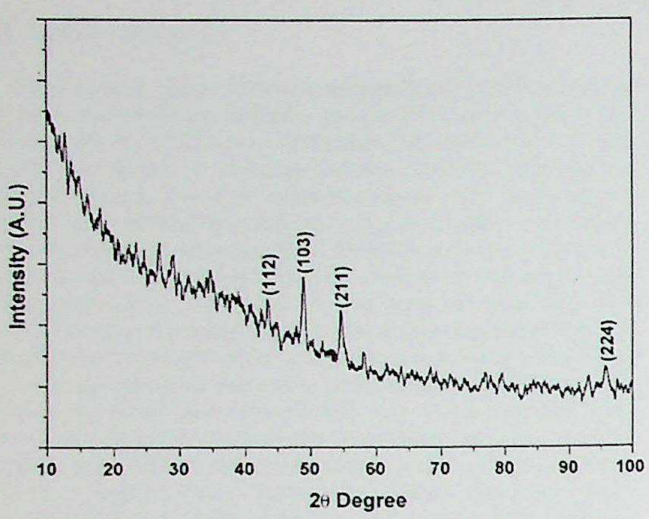


Fig. 2. XRD pattern of Mn_3O_4 thin film onto the glass substrate.

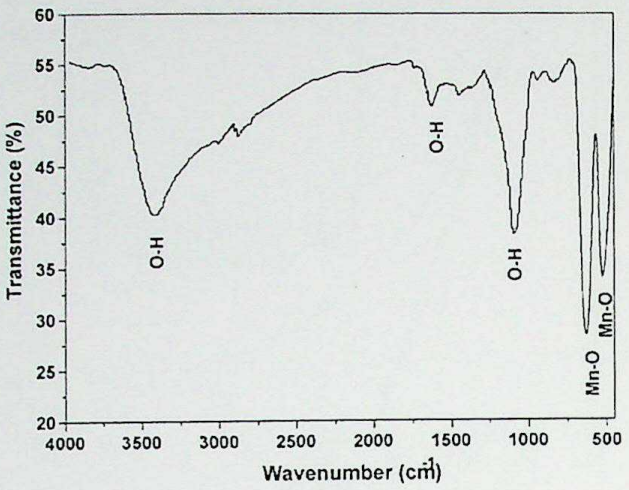


Fig. 3. FTIR spectrum of Mn_3O_4 compound.

stable and well-known manganese oxides are MnO, Mn_3O_4, Mn_2O_3 and MnO_2. From these structures, Mn_3O_4 is normal spinel oxide which is room temperature stable structure with Mn^{3+} in the octahedral positions and Mn^{2+} in the tetrahedral positions of the spinel structure. Fig. 2 shows XRD pattern of Mn_3O_4 thin film onto the glass substrate. The planes corresponding to (1 1 2), (1 0 3), (2 1 1) and (2 2 4) and calculated lattice constants $a = b = 5.7336$ Å and $c = 9.4696$ Å are in good agreement [JCPDS 24-0734, $a = b = 5.7621$ Å and $c = 9.4696$ Å], confirming the formation of Mn_3O_4 compound. The small peak intensities in XRD pattern revealed the existence of nanocrystalline crystallites. The average crystallite size was calculated according to the full width at half maxima (FWHM) of the diffraction peaks using the Scherrer equation,

$$D = \frac{0.9\lambda}{\beta \cos\theta} \tag{3}$$

where β is the broadening of diffraction line measured at half maximum intensity (radians) and $\lambda = 2.2897$ Å, the wavelength of the Cr Kα X-ray. The average crystallite size was found to be 29 nm. The observed '*d*' values and standard '*d*' values taken from JCPDS standard data card are in good agreement with each other and are listed in Table 2.

3.4. FTIR studies

In order to know the chemical bonds present in the Mn_3O_4 compound, the sample was characterized by FTIR within the wavelength range 400–4000 cm^{-1}. Fig. 3 displays the FTIR spectrum of Mn_3O_4. The absorption at 3412 cm^{-1} indicates the presence of hydroxide group [16]. The absorption peaks around at 1634 and 1108 cm^{-1} may be attributed to O–H bending vibrations combined with Mn atoms. The two broad absorption bands at 632 and 522 cm^{-1} are associated with the coupling mode between Mn–O stretching modes of tetrahedral and octahedral sites [17].

Table 2
Comparison of observed and standard '*d*' values of Mn_3O_4 thin films.

Sr. No.	Observed '*d*' (Å)	Standard '*d*' (Å)	(*hkl*)
1	3.0895	3.0890	(1 1 2)
2	2.7652	2.7680	(1 0 3)
3	2.4930	2.4870	(2 1 1)
4	1.5433	1.5443	(2 2 4)

Thus, the FTIR result suggests the presence of Mn–O bonds and some constitutional water incorporated in the Mn_3O_4 structure. This hydrous nature of Mn_3O_4 is responsible for enhanced supercapacitance.

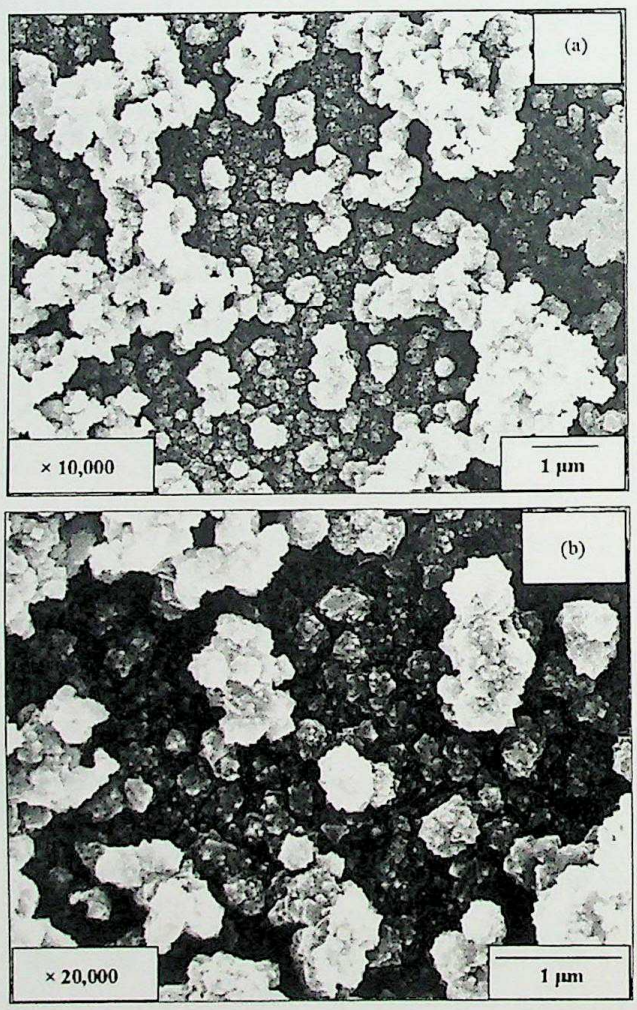


Fig. 4. FESEM micrographs of Mn_3O_4 thin films at two different magnifications (a) 10,000× and (b) 20,000×.

3.5. Surface morphology

Fig. 4(a and b) shows FESEM images of Mn_3O_4 thin films at two different magnifications (10,000× and 20,000×) respectively. From low magnification (10,000×) SEM image (Fig. 4(a)), it is seen that Mn_3O_4 film surface is compact and well covered with smooth, irregular shaped grains of random size. At high magnification (20,000×), we clearly observed the triangular shaped grains which are interconnected with each other. These interconnected triangular shaped grains form clusters with some clusters of overgrowth. Such overgrowth can be explained on the basis of nucleation and coalescence process. Initially grown nanograins may have increased their size by further deposition and come closer to each other. Thus, the larger grains appear to grow by coalescence of smaller ones. The grains were small with non-uniform and no well-defined grain boundaries; hence it was difficult to calculate the exact average value of grain size. It was nearly equal to 125–140 nm. The film surface is well covered without any pinholes and cracks. Such surface morphology with nanosized grains may offer increased surface area feasible for supercapacitor application [18].

3.6. Wettability test

Wettability test is carried out in order to investigate the interaction between liquid and Mn_3O_4 thin films. If the wettability is high, contact angle (θ), will be small and the surface is hydrophilic. On the contrary, if the wettability is low, θ will be large and the surface is hydrophobic. A contact angle of 0° means complete wetting and a contact angle of 180° corresponds to complete non-wetting. Both super-hydrophilic and super-hydrophobic surfaces are important for practical applications [19]. From Fig. 5 we observed that, the Mn_3O_4 thin films are hydrophilic as water contact angle is 55° (less than 90°) means high wettability. Similar type of behavior has been reported in our earlier report on Mn_3O_4 by chemical bath deposition method [20]. This may be due to the strong cohesive force between the water droplet and hydroxide present in the manganese oxide compound. Due to which the water is attracted rather repelled by the Mn_3O_4 film. This specific property is useful for making intimate contact of aqueous electrolyte with electrode surface in supercapacitor application. We believed this specific property will tentatively demonstrate the feasibility of Mn_3O_4 film surface useful in electrolyte/electrode interface for better performances. It is well known that in the electrochemical capacitors, hydrophilic surface of the electrode is an essential factor for better performance [21]. Kandalkar et al. [22] reported a contact angle of 60° for chemically deposited cobalt oxide thin films for supercapacitor application.

3.7. Optical absorption study

The optical absorption spectrum of Mn_3O_4 thin film in the wavelength range 350–850 nm has been investigated. Fig. 6 shows

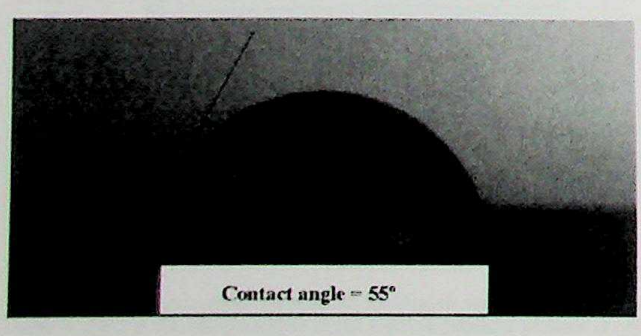


Fig. 5. Water contact angle measurement of Mn_3O_4 thin film.

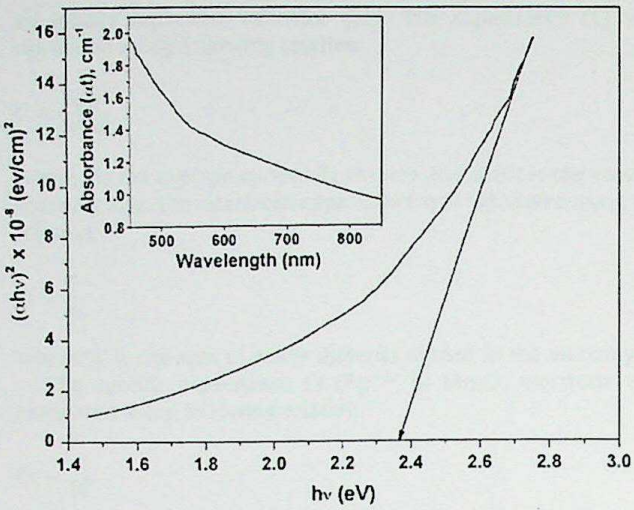


Fig. 6. Plot of $(\alpha h\nu)^2$ vs. photon energy $h\nu$ of Mn_3O_4 film (Inset shows variation of absorption (αt) with wavelength (λ) of Mn_3O_4 films on glass substrate).

the variation of $(\alpha h\upsilon)^2$ vs. $h\upsilon$ which is a straight line in the domain of higher energies, indicating a direct optical transition. Inset of Fig. 6 shows the variation of absorbance (αt) of the film with wavelength (λ). This spectrum reveals that Mn_3O_4 thin film has high absorbance of light in the visible region, indicating applicability as an absorbing material. The absorption edge was found at 516 nm due to optical band gap absorption which is in good agreement with the literature data [23]. The theory of optical absorption gives the relationship between the absorption coefficient α and the photon energy ($h\nu$),

$$\alpha = \frac{A(Eg - h\nu)^n}{h\nu} \tag{4}$$

where A, n are constants, for direct allowed transition $n = 1/2$ and for allowed indirect transition $n = 2$. The above Eq. (4) gives the band gap (Eg) when straight portion of $(\alpha h\nu)^2$ against $h\nu$ plot is extrapolated to the point $\alpha = 0$. From the graph, for Mn_3O_4 thin film the band gap value of 2.30 eV was obtained. The optical band gap of 2.50 eV was reported for chemical bath deposited Mn_3O_4 film [23]. The low band gap value obtained in the present work may be attributed to the hydrous content in the material [24].

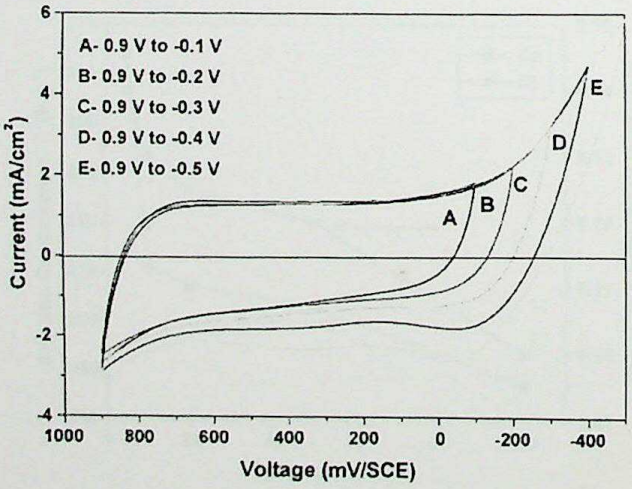


Fig. 7. The Cyclic voltammograms of Mn_3O_4 thin film in different working potential windows at the scan rate of 20 mV s^{-1}.

3.8. Supercapacitive studies

The chemically deposited nanocrystalline Mn_3O_4 electrodes were used in the supercapacitor and their performances were tested using cyclic voltammogram (CV) technique. For finding the suitable electrolyte, the cyclic voltammograms of the Mn_3O_4 electrode in the different aqueous electrolytes viz. 1.0 M solutions of NaOH, KOH, Na_2SO_4, NaCl and KCl in the voltage range of −0.1 to +0.9 V were studied. In all the cases, the Mn_3O_4 electrode exhibited symmetric CV characteristics in forward and reverse sweeps. However, in Na_2SO_4 electrolyte better performance compared to others was noticed.

3.8.1. Effect of different working potential windows on the specific capacitance

The electrochemical properties of Mn_3O_4 thin films are carried out onto the stainless steel substrate. The electrochemical reversibility of Mn_3O_4 electrode was examined systematically in different working potential windows at the scan rate of 20 mV s^{-1} in 1 M Na_2SO_4 (see Fig. 7), since the electrochemical reversibility is the prime factor influencing the power property of electrochemical supercapacitors. The currents on all CV curves reaching the plateau values are very fast when the direction of potential sweep is just changed. This shows typical capacitive-like characteristics. This part of the capacitance could be largely due to faradaic pseudocapacitance contributions. These results indicate good electrochemical reversibility of the Mn_3O_4 thin films in 1 M Na_2SO_4. The specific capacitance in the working potential window of 0.9 to −0.5 V is greater than in 0.9 to −0.1 V, but the charging and discharging voltammograms are mirror images of one another in potential window of 0.9 to −0.1 V. Hence further supercapacitive properties were tested in this potential window.

3.8.2. Cyclic voltammograms of Mn_3O_4 electrode

The chemically deposited Mn_3O_4 thin films were used in the formation of electrochemical supercapacitors and their performance was tested studying CV curves. Fig. 8 shows the CV curves of Mn_3O_4 electrode with different scan rates in 1 M Na_2SO_4 electrolyte. It was found that the current under curve was slowly increased with scan rate. This shows that the voltammetric currents are directly proportional to the scan rates of CV, indicating an ideally capacitive behavior [25]. The capacitance (C) was calculated using following relation,

$$C = \frac{I_{max}}{dV/dt} \tag{5}$$

where I is the average current in ampere and dV/dt is the voltage scanning rate. The interfacial capacitance was calculated using the relation,

$$Ci = \frac{C}{A} \tag{6}$$

where 'A' is the area of active material dipped in the electrolyte.

The specific capacitance Cs (F g^{-1}) of Mn_3O_4 electrode was calculated using following relation:

$$Cs = \frac{C}{W} \tag{7}$$

where W is the weight of Mn_3O_4 film dipped in electrolyte. The Mn_3O_4 electrode exhibited the interfacial capacitance of 0.14 F cm^{-2} and the supercapacitance of 314 F g^{-1} which is greater than our earlier reported value i.e. 193 F g^{-1} [20]. The large value in this case is attributed to the nanocrystalline and porous nature of Mn_3O_4 thin films.

3.8.3. Effect of scan rate

The high or pulse-power property of Mn_3O_4 electrode is examined using cyclic voltammetry at different scan rates. Fig. 8 shows the CV curves of Mn_3O_4 electrode in 1 M Na_2SO_4 electrolyte for different scan rates within voltage range of 0.9 to −0.1 V. Fig. 9 shows the variation of specific capacitance and interfacial capacitance with scan rate. From Fig. 9 it is seen that, specific and interfacial capacitance values are decreased from 314 to 245 F g^{-1} and 0.14 to 0.10 F cm^{-2}, respectively. The maximum specific capacitance of 314 F g^{-1} was obtained at 5 mV s^{-1}. The decrease in capacitance has been attributed to the presence of inner active sites that cannot sustain the redox transitions completely at higher scan rates. This is probably due to the diffusion effect of protons within the electrode. The decreasing trend of the capacitance suggests that parts of the surface of the electrode are inaccessible at high charging–discharging rates [26].

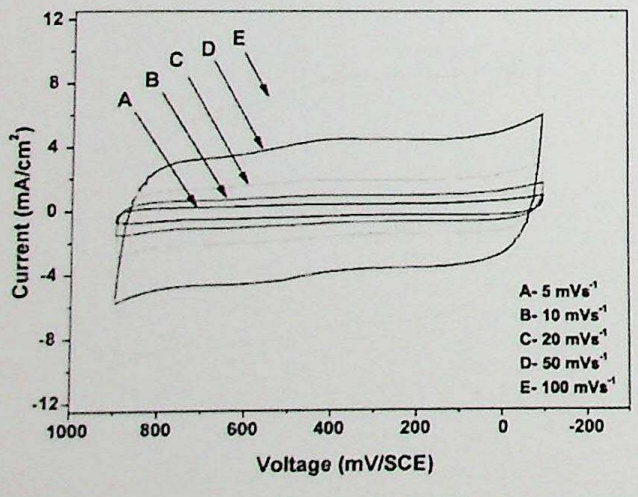


Fig. 8. The Cyclic voltammograms of Mn_3O_4 thin film electrode at different scanning rates in the 1 M Na_2SO_4 electrolyte in the working potential window of −0.1 to +0.9 V (vs. SCE).

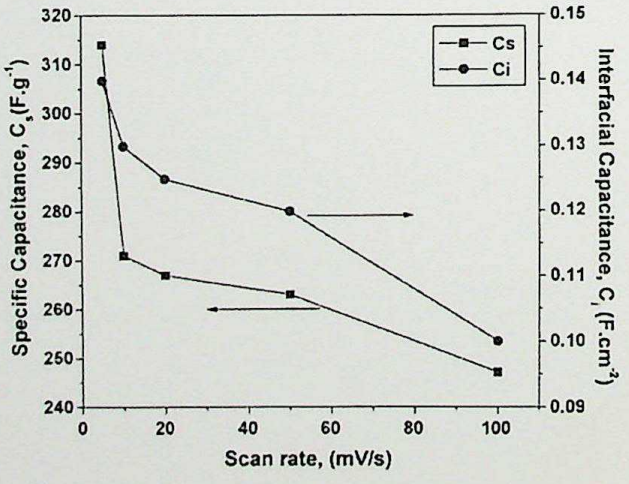


Fig. 9. Variation of specific and interfacial capacitances of Mn_3O_4 electrode at different scan rates. Concentration of Na_2SO_4 electrolyte was 1.0 M.

4. Conclusions

In summary, Mn_3O_4 thin films have been prepared by simple and inexpensive successive ionic layer adsorption and reaction (SILAR) method. XRD pattern revealed that the Mn_3O_4 thin film exhibits tetragonal hausmannite structure. From scanning electron micrograph images it is seen that Mn_3O_4 film surface was well covered with triangular shaped grains. Contact angle measurement showed Mn_3O_4 surface was hydrophilic with contact angle 55°. The optical studies showed direct band gap energy of 2.36 eV. The Mn_3O_4 electrode exhibited the interfacial capacitance of 0.14 F cm^{-2} and the supercapacitance of 314 F g^{-1} which is high as compared to Mn_3O_4 films prepared by chemical bath deposition method. These results demonstrate that chemically deposited Mn_3O_4 thin film is a good candidate as electrode material for electrochemical capacitor.

Acknowledgement

Authors are grateful to the University Grants Commission (UGC), New Delhi for financial support through the scheme no. 36-207/2008 (SR).

References

[1] M.C. Bernard, H.L. Goff, B.V. Thi, J. Electrochem. Soc. 140 (1993) 3065.
[2] A.H. De Vries, L. Hozoi, R. Broer, Phys. Rev. 66 (2002) 35108.
[3] Y. Yamashita, K. Mukai, J. Yoshinobu, M. Lippmaa, T. Kinoshita, M. Kawasaki, Surf. Sci. 514 (2002) 54.
[4] R.C. Hughes, R.C. Sweet, R. Mavrodineanu, Ferrites, Encyclopedia of Industrial Chemical Analysis, vol. 12, Interscience, New York, 1971, p. 514.
[5] F. Jiao, P.G. Bruce, Adv. Mater. 19 (2007) 657.
[6] E.R. Stobhe, B.A.D. Boer, J.W. Geus, Catal. Today 47 (1999) 161.
[7] M. Baldi, E. Finocchio, F. Milella, Appl. Catal. B: Environ. 16 (1998) 43.
[8] A.S. Fritsch, J. Sarrias, A. Rousset, G.U. Kulkarni, Mater. Res. Bull. 33 (1998) 1185.
[9] S.C. Pang, M.A. Anderson, T.W. Chapman, J. Electrochem. Soc. 147 (2000) 444.
[10] M.T. Lee, J.K. Chang, W.T. Tsai, J. Electrochem. Soc. 154 (2007) 875.
[11] Y.U. Jeong, A. Manthiram, J. Electrochem. Soc. 149 (2002) 1419.
[12] Y. Dai, K. Wang, J. Zhao, J. Xie, J. Power Sources 161 (2006) 737.
[13] B. Djurfors, J.N. Broughton, M.J. Brett, D.G. Ivey, J. Power Sources 156 (2006) 741.
[14] C.C. Hu, T.W. Tsou, Electrochem. Commun. 4 (2002) 105.
[15] H.M. Pathan, C.D. Lokhande, Bull. Mater. Sci. 27 (2004) 85.
[16] S. Karuppuchamy, J.M. Jeong, J. Oleo Sci. 55 (2006) 263.
[17] M. Ocana, Colloid Polym. Sci. 278 (2000) 443.
[18] V.R. Shinde, C.D. Lokhande, R.S. Mane, S.H. Han, Appl. Surf. Sci. 245 (2005) 407.
[19] R.D. Sun, A. Nakajima, A. Fujushima, T. Watanabe, K. Hashimoto, J. Phys. Chem. B 105 (2001) 1984.
[20] D.P. Dubal, D.S. Dhawale, R.R. Salunkhe, S.M. Pawar, V.J. Fulari, C.D. Lokhande, J. Alloys Compd. 484 (2009) 218.
[21] O. Bockman, T. Ostvold, G.A. Voyiatzis, G.N. Papatheodorou, Hydrometallurgy 55 (2000) 93.
[22] S.G. Kandalkar, C.D. Lokhande, R.S. Mane, S.H. Han, Appl. Surf. Sci. 253 (2006) 3952.
[23] H.Y. Xu, S.L. Xu, X.D. Li, H. Wang, H. Yan, Appl. Surf. Sci. 252 (2006) 4091.
[24] V.D. Patake, C.D. Lokhande, Appl. Surf. Sci. 254 (2008) 2820.
[25] T.P. Gujar, V.R. Shinde, C.D. Lokhande, W.Y. Kim, K.D. Jung, O.S. Joo, Electrochem. Commun. 9 (2007) 504.
[26] T.P. Gujar, W. Kim, I. Puspitasari, K.D. Jung, O.S. Joo, Int. J. Electrochem. Sci. 22 (2007) 666.

Journal of The Electrochemical Society, 157 (7) A812-A817 (2010)
0013-4651/2010/157(7)/A812/6/$28.00 © The Electrochemical Society

Conversion of Chemically Prepared Interlocked Cubelike Mn_3O_4 to Birnessite MnO_2 Using Electrochemical Cycling

Deepak P. Dubal,[z] Dattatray S. Dhawale, Rahul R. Salunkhe, and Chandrakant D. Lokhande[z]

Thin Film Physics Laboratory, Department of Physics, Shivaji University, Kolhapur, Maharashtra 416004, India

Interlocked cubelike Mn_3O_4 thin films have been prepared by a simple and low temperature chemical bath deposition method. These interlocked cubelike Mn_3O_4 thin films are further converted into nanoflakes of birnessite MnO_2 using voltammetric cycling in aqueous Na_2SO_4 electrolyte. The process is dynamic potential activated, which causes the formation of sheet-shaped nanoflakes. The films are characterized by X-ray diffraction, field-emission-scanning electron microscopy, X-ray photoelectron spectroscopy, Fourier transform IR spectrum, and wettability test. Impedance spectroscopy studies revealed that charge-transfer resistance of the birnessite MnO_2 structure has a lower value than that of the Mn_3O_4 structure. The effect of different numbers of potential cycles on structure, surface morphology, valence states, and contact angles has been investigated. During the cycling process, the supercapacitance of manganese oxide increased by more than 10 times. The maximum supercapacitance achieved at 5 mV s^{-1} is 223 F g^{-1}. The effect of scan rate on the specific capacitance of birnessite MnO_2 electrode has been studied.
© 2010 The Electrochemical Society. [DOI: 10.1149/1.3428675] All rights reserved.

Manuscript submitted January 25, 2010; revised manuscript received March 31, 2010. Published May 18, 2010.

A supercapacitor is an energy storage device storing the energy by accumulation of charges at the electrode/electrolyte interface. Because the capacitance is proportional to the surface area of the electrode, porous MnO_2 has attracted much attention for this application. Due to the lower point of zero charge, large surface area, strong acid sites, and easily changeable valence states, MnO_2 participates readily in a variety of oxidation-reduction and cation-exchange reactions or catalysis.[1,2] Various transition-metal oxides, such as RuO_2, Co_3O_4, NiO, Fe_2O_3, IrO_2, SnO_2, MnO_2, etc., are being studied for the supercapacitor applications. Among these metal oxides for supercapacitor electrodes, amorphous hydrous RuO_2 is the most promising material for supercapacitors because of its high specific capacitance, excellent reversibility, and long cycle life.[3,4] However, RuO_2 is expensive, toxic, and naturally less abundant, which limits their commercial use. Also RuO_2 requires the use of a strong acidic electrolyte such as sulfuric acid. The acidic media can dissolve the metal oxide over extended cycling leading to fade in the specific capacitance with cycle life. As a result, numerous metal oxides have also been tested as possible candidates for electrochemical supercapacitor devices. Candidate systems include IrO_2 [5] or CoO_x,[6] but they suffer from limitations similar to RuO_2, that is, they are expensive and require strong acidic or alkaline electrolyte. In addition, the potential window over which they operate reversibly is significantly smaller than that for RuO_2. However, MnO_2 [7] is a potential supercapacitor material due to its low cost, large natural abundance, and it is environmentally friendlier than other transition-metal oxides. Also, MnO_2 has specific capacitance of as high as 698 F/g, and it operates in ~1 V potential window; both the values are comparable with RuO_2.[8] MnO_2 does not require acidic or alkaline electrolytes; it shows high capacitance in neutral Na_2SO_4 electrolyte, hence, there is no problem of dissolution of metal oxide. Due to all these advantages, MnO_2 is an attractive candidate for supercapacitor as compared to other metal oxides.

Among manganese compounds, birnessite is a major Mn mineral phase in many soils and an important component in desert varnishes and other coatings and in ocean Mn nodules.[9] Birnessite-type compounds correspond to a class of nonstoichiometric oxides due to the substitution of some Mn(IV) by Mn(III) or Mn(II). Birnessite has a layered structure formed by MnO_6 octahedral sharing edges, with hydrated alkaline cations (Na^+, K^+, Ca^{2+},...) in the interlayers that compensate the small overall negative charge.[10,11] Moreover, birnessite-type compounds readily participate in oxidation–reduction reactions and, hence, attract considerable scientific interest as inexpensive and nontoxic materials for potential applications in hazardous waste remediation,[12,13] rechargeable battery technology,[14,15] or chemical sensors.[16,17]

The majority of papers report the formation of birnessite in powder form by oxidation of Mn(II) cations by $KMnO_4$, H_2O_2, or O_2,[18,19] by reduction of $KMnO_4$ by aqueous or nonaqueous sol–gel processes,[10,20] and by high temperature decomposition of $KMnO_4$.[21] However, little information is accessible about the conversion of spinel Mn_3O_4 to layered birnessite MnO_2 by electrochemical method. Dai et al.[22] reported the transformation of spinel Mn_3O_4 into layered birnessite MnO_2 by electrochemical cycling. The specific capacitance obtained after cycling was 133 F g^{-1}. The value obtained in our investigation is 183 F g^{-1}, which is high enough. Nam and Kim[23] also reported the structure transformation from crystalline Mn_3O_4 to amorphous birnessite MnO_2 thin films. In both above cases, the films are prepared by spray pyrolysis technique. As compared to the spray pyrolysis method, chemical bath deposition (CBD) is the attractive one because of its own advantages such as simplicity, reproducibility, nonhazardous, cost effectiveness, etc. It is well suited for producing large area thin films at low temperature and, hence, avoids oxidation or corrosion of metallic substrate. Recently, Brett et al.[24] synthesized pseudocapacitive manganese oxide films by anodic oxidation of a metallic film deposited by sputtering. They showed that very thin films of manganese deposited in a metallic form by sputtering can be converted to the capacitive oxide form by applying an anodic current in an unbuffered 1 M Na_2SO_4 electrolyte.

The present investigation describes the synthesis of interlocked cubelike Mn_3O_4 thin films by low temperature CBD method and stepwise conversion of these interlocked cubelike Mn_3O_4 to nanoflakes of birnessite MnO_2 using potential cycling. The effect of different numbers of potential cycles on structure, surface morphology, valence state, and wettability has been investigated. The effect of scan rate on the specific capacitance of birnessite MnO_2 has been studied.

Experimental

CBD of Mn_3O_4 thin films.— Interlocked cubelike Mn_3O_4 thin films were prepared by low temperature CBD method. Briefly, fresh aqueous solutions of manganese sulfate (0.05 M) and urea (1 M) were mixed at pH ~ 8. The solution was transparent and free from any precipitate. The well-cleaned stainless steel substrates were immersed in the bath at room temperature, and the bath was heated to 353 K without stirring for 12 h. After about 4 h, the solution became blurred and within 12 h, the brown precipitate was formed in the bath. During the precipitation, the heterogeneous reaction occurred

[z] E-mail: dubal_deepak@yahoo.co.in; l_chandrakant@yahoo.com

Downloaded 19 May 2010 to 166.104.138.56. Redistribution subject to ECS license or copyright; see http://www.ecsdl.org/terms_use.jsp

and the deposition of Mn_3O_4 took place on the substrate. The substrates coated with Mn_3O_4 were removed from the bath, washed with double distilled water, dried in air, and preserved in an air tight container for further characterization.

Conversion of hausmannite Mn_3O_4 into birnessite MnO_2.— The interlocked cubelike Mn_3O_4 thin films were converted into nanoflakes of birnessite MnO_2 using cyclic voltammetry (CV). The voltammetric cycling was carried out in 1 M Na_2SO_4 electrolyte at 100 mV s^{-1} scan rate within the potential window of −0.1 to +0.9 V. These Mn_3O_4 thin films were electrochemically oxidized to birnessite MnO_2 for 1000, 2000, and 3000 cycles. The as-prepared Mn_3O_4 thin films were brownish, which turned slightly black after 1000 cycles, and after 3000 cycles it became completely black. Finally, after 3000 cycles the birnessite MnO_2 thin films were cleaned with double distilled water and used for further characterizations.

Characterization techniques.— The manganese oxide films were analyzed by X-ray diffraction with a Philips (PW 3710) diffractometer using Cr Kα radiation (λ = 2.2897 Å) to determine the crystal structures. The surface morphologies of the manganese oxides were observed by a field-emission-scanning electron microscope (model JSM-6160). To analyze the valance states of elements present in the manganese oxide thin film, X-ray photoelectron spectroscopy (XPS) was carried out using electron spectroscopy for chemical analysis (VG Multilab 2000, Thermo VG Scientific, U.K.). Fourier transform IR (FTIR) spectra of the samples were collected using a Perkin Elmer, FTIR Spectrum One unit. To study the interaction between the electrolyte and electrode surface, contact angle measurement was carried out by a Rame-hart equipment with a charge-coupled device camera. The supercapacitor formation and its studies were carried out using a 263A EG&G Princeton Applied Research potentiostat forming an electrochemical cell comprising manganese oxide film as a working electrode, platinum as a counter electrode, and saturated calomel electrode (SCE) as a reference electrode in 1 M Na_2SO_4 electrolyte. Impedance study was carried out using a CHI 660D electrochemical workstation forming an electrochemical cell comprising manganese oxide film as a working electrode, platinum as a counter electrode, and SCE as a reference electrode in 1 M Na_2SO_4 electrolyte.

Results and Discussion

Film formation and reaction mechanism.— CBD method involves the hydrolysis of metal ions in aqueous solutions, followed by their controlled heterogeneous precipitation on a substrate. Two processes can take place during CBD film growth: (*i*) Ionic species in solution adsorb on the substrate and lead to heterogeneous nucleation, and (*ii*) colloidal particles first nucleate in the solution and then adsorb on the substrate surface. In a former case, reactions are based on the combination of a manganese precursor (manganese sulfate) and urea to promote Mn_3O_4 precipitation. The primary role of urea is to provide a slowly controlled supply of OH^- ions through slow thermal decomposition.[25] This includes the hydrolysis of urea and reaction of ammonia with water as follows

$$(NH_2)_2CO + H_2O \rightarrow 2NH_3 + CO_2 \quad [1]$$

$$NH_3 + H_2O \rightleftharpoons NH_4OH \quad [2]$$

In the present investigation, the low reaction temperature and unstirred chemical bath slowly releases free Mn^{2+} cations, which forms ammine complexes of $Mn(NH_3)_n^{2+}$ (n = 1–4) with NH_3(aq) in moderately basic media (pH ~ 8). In heating condition, this ammine complex is unstable and the following reaction takes place

$$Mn(NH_3)_n^{2+} \rightleftharpoons Mn^{2+} + nNH_3 \quad [3]$$

Finally, oxidation of Mn^{2+} to Mn^{3+} takes places as

$$6Mn^{3+} + O_2 + 12OH^- \rightarrow 2Mn_3O_4 + 6H_2O \quad [4]$$

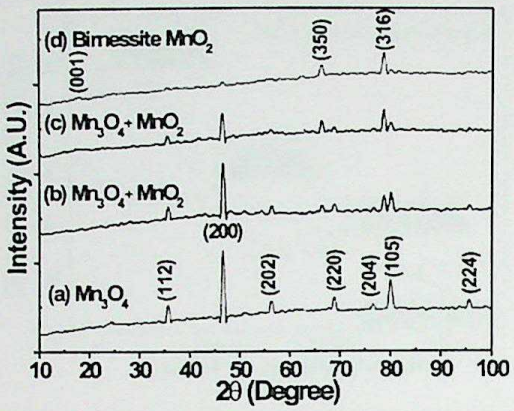


Figure 1. (Color online) The XRD patterns at different cycling stages (a) before cycling (Mn_3O_4), (b) after 1000 (Mn_3O_4 and MnO_2), (c) after 2000 (Mn_3O_4 and MnO_2), and (d) after 3000 (birnessite MnO_2) cycles.

Mn_3O_4 has a normal spinel structure with tetragonal distortion elongated along the c-axis due to the Jahn–Teller effect on the Mn^{3+} ion. Manganese ions occupy the octahedral B site (Mn^{3+}) and the tetrahedral A site (Mn^{2+}) corresponding to a normal spinel structure. These Mn_3O_4 thin films are mirror reflecting and are bright brown. A similar type of behavior has been reported by Xu et al.[26] by using NH_4Cl as a complexing agent.

Electrochemical oxidation of Mn_3O_4 to birnessite MnO_2.— The interlocked cubelike Mn_3O_4 thin films are electrochemically oxidized to nanoflakes of layered birnessite MnO_2 using potential cycling in an aqueous Na_2SO_4 electrolyte at 100 mV s^{-1} scan rate. We assume that the electrochemical cycling includes two processes, which can be expressed as follows. Reaction 5 represents the transformation of spinel Mn_3O_4 to a layered birnessite. It is a complex and irreversible process. Potential cycling

$$Mn_3O_4(\text{spinel}) \xrightarrow{\text{Potential cycling}} Na_\delta MnO_x{\cdot}nH_2O(\text{birnessite}) \quad [5]$$

During the cycling, the area under the curve goes on increasing and after 3000 cycles it becomes stable because there is formation of birnessite MnO_2. After 3000 cycles, the charge storing mechanism starts according to following reaction

$$Na_\delta MnO_x{\cdot}nH_2O + yH^+ + zNa^+(y + z)e^- \rightleftharpoons Na_{\delta+z}MnO_x{\cdot}nH_2O \quad [6]$$

Reaction 6 is the reversible cycling of the latter material. A similar type of behavior has been reported by Dai et al.[22] After 3000 cycles, bright brown Mn_3O_4 thin films turns into entirely black birnessite MnO_2 thin films.

Structural studies.— X-ray diffraction is one of the most important techniques for characterizing the structural confirmation of crystalline materials. Figure 1 shows the XRD patterns of Mn_3O_4 thin films at different cycling stages. The changes in the XRD patterns of the Mn_3O_4 film obtained after cycling within the potential window from −0.1 to +0.9 V (vs SCE) are clearly noticed in the XRD patterns. The XRD pattern of the as-prepared film (Fig. 1a) agrees well with that of the tetragonal hausmannite Mn_3O_4 structure (JCPDS card no. 24-0734). However, the intensity of (112), (200), (202), (220), (204), (105), and (224) planes corresponding to the tetragonal Mn_3O_4 structure in the XRD patterns clearly decreased after 1000 and 2000 cycles; at the same instance, the intensity of (305) and (316) planes corresponding to birnessite-type MnO_2 increased (Fig. 1b and c). Thus, the phases obtained after 1000 and 2000 cycles are mixtures of hausmannite Mn_3O_4 and birnessite

Downloaded 19 May 2010 to 166.104.138.56. Redistribution subject to ECS license or copyright; see http://www.ecsdl.org/terms_use.jsp

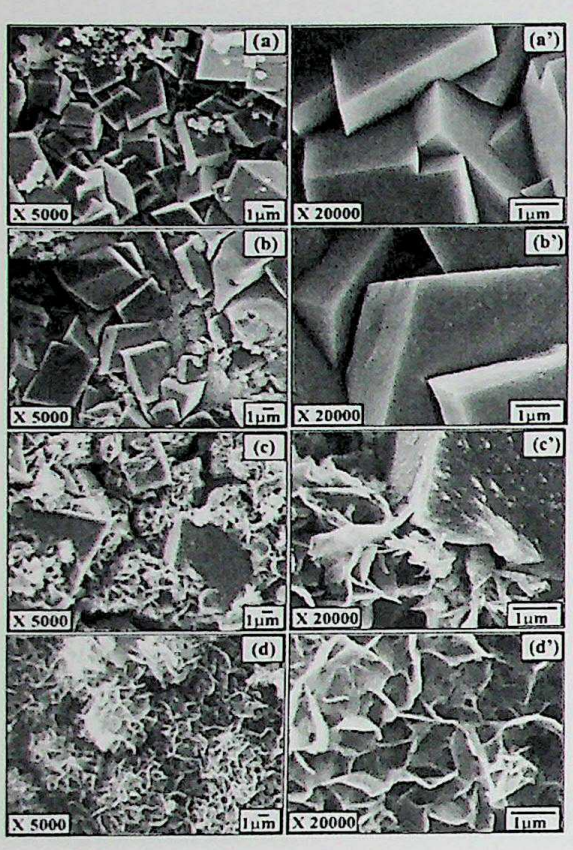


Figure 2. (Color online) The SEM images of Mn_3O_4 thin films for different cycling stages [(a) and (a')] before cycling, [(b) and (b')] after 1000, [(c) and (c')] after 2000, [(d) and (d')] after 3000 cycles at ×5000 and ×20,000 magnifications, respectively.

MnO_2 structures. Finally, after 3000 cycles, the peaks corresponding to the tetragonal Mn_3O_4 structure disappeared [some small intensities such as at (200) is observed in XRD pattern but due to limitations of XRD are not detectable], and only peaks that are recognized as layered birnessite-type MnO_2 (JCPDS card no. 23-1046) appeared in the XRD pattern (Fig. 1d). Thus, the result indicates that the as-prepared films are gradually converted from crystalline Mn_3O_4 to nanostructured birnessite MnO_2 by electrochemical oxidation using potential cycling. A similar type of behavior has been reported by Nam et al.[25] using Mn_3O_4 thin films prepared by electrostatic spray deposition technique.

Surface morphological study.— The change in the surface morphology of Mn_3O_4 thin film with potential cycling at ×10,000 magnification is shown in Fig. 2a-d. From the scanning electron microscopy (SEM) image in Fig. 2a, we observed the three-dimensional growth of interlocked cubes of Mn_3O_4 film. These interlocked cubes seem to be well covered with substrate surface and act like a flat rough surface. The approximate size of the interlocked cubes is between 5 and 10 μm. As we go on cycling up to 1000 cycles (Fig. 2b), these interlocked cubes slowly diffused like ice. Further cycling to 2000 cycles causes the partial diffusion of the interlocked cubes in such a way that they gradually get converted into highly porous nanoflakes. Thus, the micrographs Fig. 2c reveal the mixture of interlocked cubes and porous nanoflakes, which supports the XRD patterns. After 3000 cycles (Fig. 2d), we clearly observed that the interlocked cubes were totally converted into nanoflakes and the substrate surface was well covered with nanoflakes. The inset of Fig. 2d shows a high magnified image (×30,000) of the same. These porous nanoflakes provide a large surface area, which is feasible for supercapacitor application. The diameter of these flakes is about 20 nm. Thus, the potential cycling causes the interlocked cubical shaped surface to convert into highly porous nanoflakes.

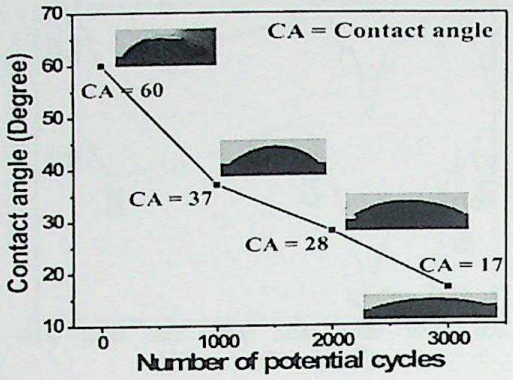


Figure 3. Contact angles for different cycling stages (a) before cycling, (b) after 1000, (c) after 2000, and (d) after 3000 cycles of manganese oxide thin films.

Wettability test.— Wettability test is carried out to investigate the interaction between the electrolyte and manganese oxide electrode. If the wettability is high, contact angle (θ) is small and the surface is hydrophilic. On the contrary, if the wettability is low, θ is large and the surface is hydrophobic. Figure 3a-d shows the water contact angles of manganese oxide films for different cycling stages. For the Mn_3O_4 thin film, the water lies slightly flat on the interlocked cubes with contact angle of 60°, as seen from Fig. 3a. As the number of potential cycles increases, the water contact angles of manganese oxide thin films decreases. The contact angles were 37, 28, and 17° after 1000, 2000, and 3000 cycles, respectively (Fig. 3b-d). This indicates that with increasing potential cycling, the contact angle decreases and finally the film surface becomes more hydrophilic. Hydrophilicity is attributed to nanocrystalline nature. Nanocrystalline material with hydrophilic nature is one of the prime requirements for a supercapacitor electrode material. The contact angle is expected to depend upon local in homogeneity, chemical composition, and the surface morphology of the electrode.[27] From the SEM images, it is confirmed that due to potential cycling interlocked cubes gets converted into highly porous nanoflakes and these nanoflakes are porous and insert deep inside the surface. Thus, water placed on the surface of the film goes inside the pores of nanoflakes due to which the contact angle decreases with increase in the number of cycles. This is useful for making the intimate contact of aqueous electrolyte with manganese oxide thin film (electrode). Thus, Na^+/H^+ ions in aqueous electrolyte can easily intercalate or deintercalate, i.e., ionic conductivity increases and hence the supercapacitance increases with number of potential cycles.

XPS.— The XPS analyses were carried out to investigate the oxidation state of Mn in Mn_3O_4 and birnessite MnO_2 thin films. Figure 4a and b displays the XPS spectra of Mn_3O_4 and birnessite MnO_2 thin films. From Fig. 4a, the Mn $2p_{3/2}$ peak centered at 641.48 eV and the Mn $2p_{1/2}$ peak at 653.3 eV, indicating that the element Mn is in the state of Mn^{2+}. The spin-orbit splitting is the difference between the binding energy values of Mn $2p_{3/2}$ and Mn $2p_{1/2}$ levels. The observed spin-orbit splitting is 11.82 eV. These results are in accordance with the reported data of Mn $2p_{3/2}$ and Mn $2p_{1/2}$ in Mn_3O_4,[28,29] which further confirms that the oxide particles before CV cycling are Mn_3O_4. Further, after potential cycling, the detected peak at the binding energy of 642.4 eV, corresponds to Mn $2p_{3/2}$, indicating that the element Mn is present in the

Downloaded 19 May 2010 to 166.104.138.56. Redistribution subject to ECS license or copyright; see http://www.ecsdl.org/terms_use.jsp

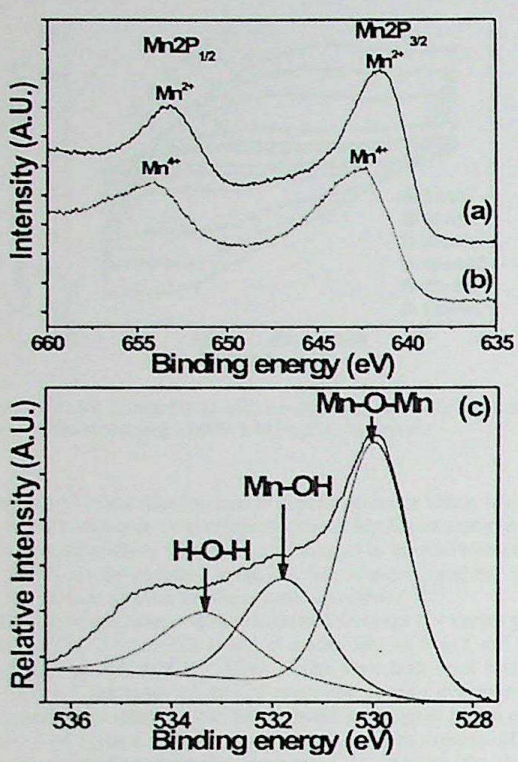


Figure 4. (Color online) XPS spectra of Mn 2p and O 1s; (a) Mn 2p spectra for Mn_3O_4 and (b) birnessite MnO_2 thin films and (c) O 1s spectrum and curve fitting for Birnessite MnO_2 film.

chemical state of Mn^{4+}. The peak appearing at the binding energy of 654 eV, which can be assigned to Mn $2p_{1/2}$, further confirms the sole existence of Mn^{4+}. So the XPS results demonstrated the solitary existence of MnO_2 after potential cycling.[30] The O 1s spectrum of the layered birnessite MnO_2 was analyzed by curve-fitting, as shown in Fig. 4c. The spectrum can be fitted with three components related to the Mn–O–Mn bond (529.98 eV) for the tetravalent oxide, the Mn–OH bond (531.80 eV) for hydrated trivalent oxide, and the H–O–H bond (533.36 eV) for residual water.[31] Thus, the state of manganese oxide obtained after cycling was hydrated, which is realistic for good supercapacitive properties.

FTIR study.— Figure 5a and b shows the FTIR spectra of Mn_3O_4 and birnessite MnO_2 thin films, respectively. The region below 1400 cm^{-1} contains peaks due to fundamental vibrations of octahedral MnO_6 and the region above 1400 cm^{-1} contains peaks primarily corresponding to OH vibrations.[32] The regions from 750–600 and 600–450 cm^{-1} correspond to the Mn–O stretching and bending vibrations. The absorption of the Mn–O lattice vibrations around 724 and 525 cm^{-1} in the spectrum is indicative of a tetragonally distorted cubic lattice. These absorption peaks may be associated with the coupling mode between Mn–O stretching modes of tetrahedral and octahedral sites.[33,34] The absorption peak at around 900 cm^{-1} is assigned to characteristic stretching vibration of peroxyl groups. The absorption bands obtained in the region of 1750–1800 and 1400–1390 cm^{-1} mainly correspond to the C–O group.[35] The broad R absorption in the 3600–2800 cm^{-1} range with a maximum at 3360 cm^{-1} arises from the –OH mode of the interacting hydroxyl groups.[36] The narrow band around 2923 and 2853 cm^{-1} are due to organic residues originating from the sample as a result of the preparation procedure.[37] From the FTIR spectra of Mn_3O_4 and birnessite MnO_2, we have clearly seen that the absorption band corresponding to hydroxyl groups are less intense in Mn_3O_4 while it becomes more intense in birnessite MnO_2. Thus, there is no significant difference between the spectra except, the stretching peak of the –OH group is slightly intensified in birnessite MnO_2 because the electrochemical cycling is carried out in the aqueous Na_2SO_4 electrolyte, which may form the tunnel structure during the reaction process; thus, a small amount of H_2O molecules is intercalated in the tunnel.

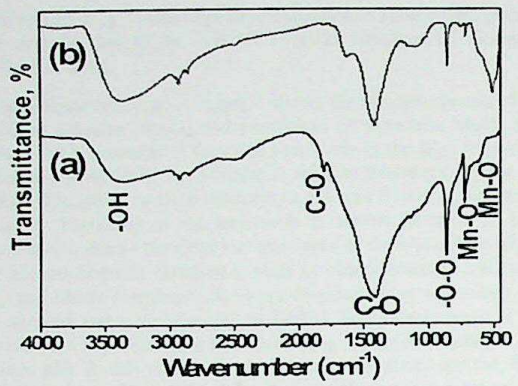


Figure 5. (Color online) FTIR spectra of (a) Mn_3O_4 and (b) birnessite MnO_2 thin films.

Supercapacitive studies.— Figure 6 shows the CVs for the Mn_3O_4 thin films at different numbers of electrochemical cycles. At the initial two cycles, the curves have no significant changes. An increase in the anodic and cathodic currents is clearly observed in the CVs over the whole potential range with cycling. The enhanced electrochemical reversibility of the films with increasing cycling is also supported by the fact that the voltammetric charges integrated from the positive and negative sweeps of the CVs increased and came closer to each other in magnitude with increasing cycle number. After 1000 cycles, the CV curves are symmetric, which indicate good capacitance behavior. The shape of the CVs becomes more symmetric after 2000 cycles and this indicates that the electrochemical reversibility and reactivity of the manganese oxide films increased during cycling in this potential window. The supercapacitive values calculated from CV curves are 11.8 F g^{-1} at the second cycle, 74.3 F g^{-1} at 1000 cycles, 95 F g^{-1} at 2000 cycles, and 139.3 F g^{-1} at 3000 cycles. The supercapacitance values increased from 11.8 F g^{-1} at the second cycle to 139.3 F g^{-1} at 3000 cycles

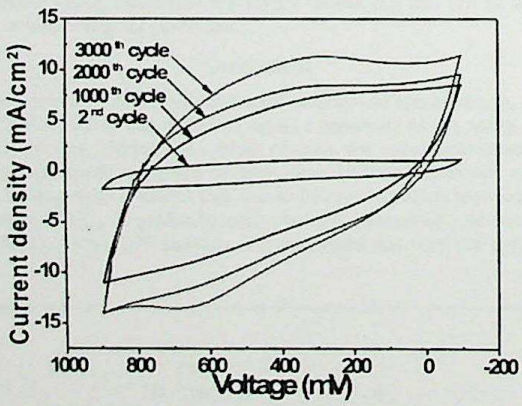


Figure 6. (Color online) Cyclic voltammograms of Mn_3O_4 electrode at different cycling stages in 1 M Na_2SO_4 electrolyte at scan rate of 100 mV s^{-1}.

Downloaded 19 May 2010 to 166.104.138.56. Redistribution subject to ECS license or copyright; see http://www.ecsdl.org/terms_use.jsp

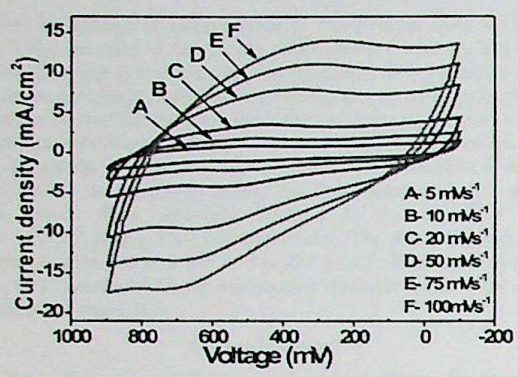


Figure 7. (Color online) Cyclic voltammograms of birnessite MnO_2 electrode at different scanning rates in 1 M Na_2SO_4 electrolyte.

more than 10 times. The increase in supercapacitance values may be due to the conversion of interlocked cubical Mn_3O_4 into nanostructured birnessite MnO_2. The pseudocapacitance of layered birnessite-type MnO_2 can be attributed to the insertion of protons and Na^+ ions and the surface sorption of above ions also existed.[38,39]

The supercapacitance values calculated from the CV curves presented in Fig. 7 were 223 F g^{-1} at a scan rate of 5 mV s^{-1} and 139 F g^{-1} at 100 mV s^{-1}. Even at the very high scan rate of 100 mV s^{-1}, the shape of the CV curve still appears symmetrical. The good power character can be attributed to the good proton conductivity of layered birnessite-typed MnO_2, which consists of an electron conducting crystalline network.[40] In addition, the flake, nanoparticles, and nanorod-like morphologies lead to a high specific surface area and porous volume, which provide the structural foundation for the high specific capacitance.[41,42] Jiang et al.[43] prepared MnO_2 by coprecipitation method using a surfactant and a reported supercapacitance of 177 F g^{-1}. Nakayama et al.[44] reported 163 F g^{-1} supercapacitance for an anodically deposited MnO_2 with polystyrene template. Also, Wang et al.[45] prepared MnO_2 nanowire arrays by sol–gel templating method and reported a supercapacitance of 165 F g^{-1}. The high supercapacitance value in the present case may be due to the layered hydrated structure of birnessite MnO_2 thin films.

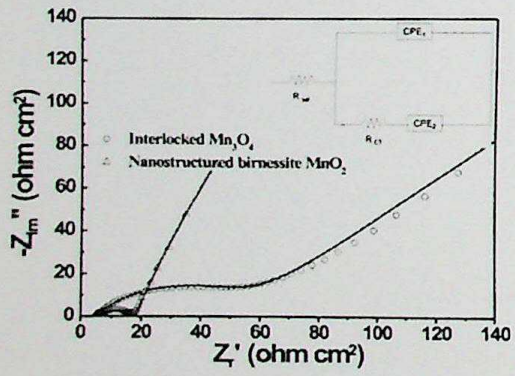


Figure 8. (Color online) Nyquist plots obtained at (a) Mn_3O_4 and (b) nanostructured birnessite MnO_2 electrodes at 0.8 V over the frequency range 1 mHz–100 MHz.

Impedance analysis.— Figure 8 shows the Nyquist spectra of interlocked cubelike Mn_3O_4 and nanoflakes of birnessite MnO_2 thin films at 0.8 V potential. A distorted semicircle in the high frequency region and a vertically linear spike in the low frequency regime are noticed. The initial nonzero intercept in the high frequency regime at Z' at the beginning of the semicircle is almost identical in both curves and is due to the electrical resistance of the electrolyte (R_{ele}), The electrochemical parameters such as charge-transfer resistance (R_{ct}) and ohmic resistance (R_s) were obtained using equivalent circuit analysis and is summarized in Table I. Equivalent circuit of the current work is presented in the inset of Fig. 8, which consists of the Nyquist plot. In this model, the double-layer capacitor and the Warburg impedance for semi-infinite linear diffusion are replaced by two constant phase elements (CPEs). The impedances of two CPEs are defined as

$$Z_{CPE1} = [Q(j\omega)^{n1}]^{-1} \quad [7]$$

and

$$Z_{CPE2} = [Q(j\omega)^{n2}]^{-1} \quad [8]$$

with $0 < n > 1$. The two CPEs, CPE_1 and CPE_2, correspond respectively to the double-layer capacitance and diffusion process of the cations at the interface. The literature corroborated that CPE may arise from (*i*) a distribution of the relaxation times as a result of diverse inhomogenities existing at the electrode/electrolyte interface, (*ii*) porosity, (*iii*) nature of the electrode, and (*iv*) dynamic disorder associated with diffusion.[46] Further, the constant value of Q is related to both the surface and the electroactive species; n denotes the correction factor due to the roughness of the electrode with values ranging between 0 and 1. A pure capacitance yields $n = 1$, a pure resistance yields $n = 0$, while $n = 0.5$ represents Warburg impedance.

From Table I, the nanoflake birnessite MnO_2 showed a low charge-transfer resistance (R_{ct} = 13.6 Ω cm^2) than the interlocked Mn_3O_4 electrodes (R_{ct} = 49.2 Ω cm^2), which was attributed to the morphology tuning when interlocked cubelike Mn_3O_4 is changed to nanostructured birnessite MnO_2. The enhancement of pores in the nanoflake network improves the diffusivity of the electrolyte ions in the pore surface, thus reducing the series resistance at the MnO_2/electrolyte interfaces. In addition, the increased specific surface area in the nanoflake MnO_2 sample over the bulk interlocked cubelike Mn_3O_4 is responsible for obtaining high capacitance in this system. Further, the high pores nature of the nanoflake sample can be confirmed by the observed value of $n_1 \sim 0.8$ in this system and is consistent with observed morphology in Fig. 2d. This implies that birnessite MnO_2 nanoflakes are highly conducting and can be used over a wide range of potentials.

Conclusions

In summary, chemically deposited interlocked spinel Mn_3O_4 can be transformed to nanoflakes of layered birnessite MnO_2 using potential cycling. During the cycling process, the supercapacitance of manganese oxide increased by more than 10 times. Scanning electron micrographs revealed that due to potential cycling, interlocked cubelike Mn_3O_4 is gradually converted into nanostructured birnessite MnO_2. From XPS analysis, it is confirmed that potential cycling

Table I. Electrochemical parameters.

Sample	R_s	R_{ct} (Ω cm^2)	CPE_1 (Ω^{-1} cm^{-2} s)	CPE_2 (Ω^{-1} cm^{-2} s)	n_1	n_2
Interlocked Mn_3O_4	4.8	49.2	0.0046	0.00013	0.574	0.487
Birnessite MnO_2	4.6	13.6	0.1263	0.0012	0.812	0.449

Downloaded 19 May 2010 to 166.104.138.56. Redistribution subject to ECS license or copyright; see http://www.ecsdl.org/terms_use.jsp

causes the change in valence state of Mn element from Mn^{2+} to Mn^{4+} and the state of manganese oxide obtained after cycling was hydrated, which is realistic for good supercapacitive properties. The water contact angle changed from hydrophilic to more hydrophilic because the surface morphology converted from interlocked cubes to porous nanoflakes. Impedance spectroscopy studies revealed that charge-transfer resistance of the birnessite MnO_2 structure is lower than that of the Mn_3O_4 structure. The supercapacitance of manganese oxide films increased from 11.8 to 139.3 F g^{-1} at 100 mV s^{-1} during 3000 potential cycles. The maximum supercapacitance achieved at 5 mV s^{-1} is 223 F g^{-1}. Thus nanoflakes of layered birnessite MnO_2 are a promising electrode material for electrochemical capacitors.

Acknowledgment

The authors are grateful to the University Grants Commission (UGC), New Delhi for financial support through the scheme no. 36-207/2008 (SR). One of the authors (C. D. Lokhande) is grateful to All India Council for Technical Education, New Delhi for financial support.

References

1. J. J. Morgan, in *Metal Ions in Biological Systems*, Vol. 37, A. Sigel and H. Sigel, Editors, Chap. 1, Marcel Dekker, New York (2000).
2. B. M. Tebo, J. R. Bargar, B. G. Clement, G. J. Dick, K. J. Murray, D. Parker, R. Verity, and S. M. Webb, *Annu. Rev. Earth Planet. Sci.*, **32**, 287 (2004).
3. P. Soudan, P. Lucas, H. A. Ho, D. Jobin, L. Breau, and D. Belanger, *J. Mater. Chem.*, **11**, 773 (2001).
4. Y. S. Yoon, W. I. Cho, J. H. Lim, and D. J. Choi, *J. Power Sources*, **101**, 126 (2001).
5. J. P. Zheng, *Electrochem. Solid-State Lett.*, **2**, 359 (1999).
6. B. E. Conway, V. Birss, and J. Wojtowicz, *J. Power Sources*, **66**, 1 (1997).
7. C. Lin, J. A. Ritter, and B. N. Popov, *J. Electrochem. Soc.*, **145**, 4097 (1998).
8. S. C. Pang, M. A. Anderson, and T. W. Chapman, *J. Electrochem. Soc.*, **147**, 444 (2000).
9. J. E. Post, *Proc. Natl. Acad. Sci. U.S.A.*, **96**, 3447 (1999).
10. D. Frias, S. Nousir, I. Barrio, M. Montes, T. Lopez, M. A. Centeno, and J. A. Odriozola, *Mater. Charact.*, **58**, 776 (2007).
11. A. C. Gaillot, Ph.D. Thesis, University of Grenoble, France (2002).
12. R. Han, W. Zou, Y. Wang, and L. Zhu, *J. Environ. Radioact.*, **93**, 127 (2007).
13. C.-H. Wu and C.-L. Chang, *J. Hazard. Mater.*, **128**, 265 (2006).
14. E. Machefaux, A. Verbaere, and D. Guyomard, *J. Power Sources*, **157**, 443 (2006).
15. V. Subramanian, H. Zhu, and B. Wei, *J. Power Sources*, **159**, 361 (2006).
16. J. P. Viricelle, A. Pauly, L. Mazet, J. Brunet, M. Bouvet, C. Varenne, and C. Pijolat, *Mater. Sci. Eng., C*, **26**, 186 (2006).
17. J. Eikenberg, A. Tricca, G. Vezzu, S. Bajo, M. Ruethi, and H. Surbeck, *J. Environ. Radioact.*, **54**, 109 (2001).
18. O. Prieto, M. Del Arco, and V. Rives, *J. Mater. Sci.*, **38**, 2815 (2003).
19. J. Cai and S. L. Suib, *Inorg. Chem. Commun.*, **4**, 493 (2001).
20. L. X. Yang, Y. J. Zhu, and G. F. Cheng, *Mater. Res. Bull.*, **42**, 159 (2007).
21. A. C. Gaillot, V. A. Drits, A. Plancon, and B. Lanson, *Chem. Mater.*, **16**, 1890 (2004).
22. Y. Dai, K. Wang, and J. Xie, *Appl. Phys. Lett.*, **90**, 104102 (2007).
23. K.-W. Nam and K.-B. Kim, *J. Electrochem. Soc.*, **153**, A81 (2006).
24. J. N. Broughton and M. J. Brett, *Electrochim. Acta*, **49**, 4439 (2004).
25. A. M. Peiró, J. A. Ayllón, J. Peral, X. Domènech, and C. Domingo, *J. Cryst. Growth*, **285**, 6 (2005).
26. H. Y. Xu, S. L. Xu, X. D. Li, H. Wang, and H. Yan, *Appl. Surf. Sci.*, **252**, 4091 (2006).
27. A. M. More, T. P. Gujar, J. L. Gunjakar, C. D. Lokhande, and O.-S. Joo, *Appl. Surf. Sci.*, **255**, 2682 (2008).
28. P. S. Shah, J. D. Holmes, K. P. Johnston, and B. A. Korgel, *J. Phys. Chem.*, **106**, 2545 (2002).
29. R. J. Iwanowski, M. H. Heinonen, and E. Janik, *Chem. Phys. Lett.*, **387**, 110 (2004).
30. Z. P. Feng, G. R. Li, J. H. Zhong, Z. L. Wang, Y. N. Ou, and Y. X. Tong, *Electrochem. Commun.*, **11**, 706 (2009).
31. L. J. Sun and X. X. Liu, *Eur. Polym. J.*, **44**, 219 (2008).
32. M. Minakshi, P. Singh, T. B. Issa, S. Thurgate, and R. D. Marco, *J. Power Sources*, **138**, 319 (2004).
33. C. M. Julien, M. Massot, and C. Poinsignon, *Spectrochim. Acta, Part A*, **60**, 689 (2004).
34. M. Ocaña, *Colloid Polym. Sci.*, **278**, 443 (2000).
35. J. Schmitt and H. C. Flemming, *Int. Biodeter. Biodegrad.*, **41**, 1 (1998).
36. S. Karuppuchamy and J. M. Jeong, *J. Oleo Sci.*, **55**, 263 (2006).
37. A. J. Maira, J. M. Coronado, V. Augugliaro, K. L. Yeung, J. C. Conesa, and J. Soria, *J. Catal.*, **202**, 413 (2001).
38. T. Brousse, M. Toupin, R. Dugas, A. L. Athouël, O. Crosnier, and D. Bélanger, *J. Electrochem. Soc.*, **153**, A2171 (2006).
39. M. Toupin, T. Brousse, and D. Bélanger, *Chem. Mater.*, **16**, 3184 (2004).
40. W. Sugimoto, H. Iwata, Y. Yasunaga, Y. Murakami, and Y. Takasu, *Angew. Chem., Int. Ed.*, **42**, 4092 (2003).
41. Y. Li, X. Xie, J. Liu, M. Cai, J. Rogers, and W. Shen, *Chem. Eng. J.*, **136**, 398 (2008).
42. L. X. Yang, Y. J. Zhu, H. Tong, Z. H. Liang, L. Li, and L. Zhang, *J. Solid State Chem.*, **180**, 2095 (2007).
43. R. Jiang, T. Huang, J. Liu, J. Zhuang, and A. Yu, *Electrochim. Acta*, **54**, 3047 (2009).
44. M. Nakayama, T. Kanaya, and R. Inoue, *Electrochem. Commun.*, **9**, 1154 (2007).
45. X. Wang, X. Wang, W. Huang, P. J. Sebastian, and S. Gamboa, *J. Power Sources*, **140**, 211 (2005).
46. J. Gamby, P. L. Taberna, P. Simon, J. F. Fauvarque, and M. Chesneau, *J. Power Sources*, **101**, 109 (2001).

Downloaded 19 May 2010 to 166.104.138.56. Redistribution subject to ECS license or copyright; see http://www.ecsdl.org/terms_use.jsp

Journal of Alloys and Compounds 492 (2010) 26–30

Contents lists available at ScienceDirect

Journal of Alloys and Compounds

journal homepage: www.elsevier.com/locate/jallcom

Fabrication of copper oxide multilayer nanosheets for supercapacitor application

D.P. Dubal, D.S. Dhawale, R.R. Salunkhe, V.S. Jamdade, C.D. Lokhande*

Thin Film Physics Laboratory, Department of Physics, Shivaji University, Kolhapur, 416004, Maharashtra, India

ARTICLE INFO

Article history:
Received 21 October 2009
Received in revised form
11 November 2009
Accepted 17 November 2009
Available online 26 November 2009

Keywords:
Copper oxide
Thin films
Chemical deposition
Multilayer nanosheets
Supercapacitor

ABSTRACT

Copper oxide multilayer nanosheets thin films have been formed using simple and inexpensive chemical bath deposition (CBD) method. These films were characterized using X-ray diffraction (XRD), Field emission scanning electron microscope (FESEM), Fourier transform infrared spectrum (FTIR), optical absorption and wettability test. The XRD pattern revealed that the copper oxide films are amorphous. Formation of copper oxide compound was confirmed from the FTIR studies. The FESEM images revealed the development of hierarchical multilayer nanosheets which covered the substrate surface. Surface wettability with liquid interface showed hydrophilic nature with water contact angle 53°. The optical absorption showed existence of direct optical band gap of energy 2.18 eV. The supercapacitive properties of copper oxide thin film investigated in 1 M Na_2SO_4 electrolyte showed supercapacitance of 43 $F g^{-1}$ at scan rate 10 $mV s^{-1}$.

© 2009 Elsevier B.V. All rights reserved.

1. Introduction

Currently, electrochemical capacitors (ECs) are attracting wide attention, due to their high power density, excellent reversibility and long cycle life [1]. The potential applications of electrochemical capacitors include the power enhancement and cycle life improvement of primary power sources such as batteries and fuel cells. Electrochemical capacitors are also attractive for other applications such as power sources for camera flash equipment, lasers, and cellular phones [2]. According to the charge storage mechanism, ECs are categorized as electrochemical double layer capacitors (EDLCs) and pseudocapacitors. The former is based on charge separation at the electrode/solution interface, whereas the latter is based on Faradaic redox reactions occurring within the active electrode materials. $RuO_2{\cdot}xH_2O$ showed great performance as an electrode material for pesudocapacitors; however, the high cost of hydrous ruthenium oxide hindered its wide application [3]. Accordingly, there is a strong incentive to find alternative electrode materials, which are inexpensive and exhibit pseudocapacitance similar to that of amorphous $RuO_2{\cdot}xH_2O$.

To this end, much attention is now focused on the oxides of manganese [4,5], nickel [6], cobalt [7] and vanadium [8] as candidate for electrode materials. Alternately we propose the copper oxide, the transition material having low cost for use in supercapacitor. Recently, copper oxide thin films have been prepared by various methods, such as the sol–gel, chemical deposition and electrochemical deposition [9–12]. Among these methods chemical bath deposition (CBD) is low cost and low temperature soft chemical solution method. As compared to other methods, CBD has attracted much interest due to its simplicity, low cost and ease in adaptation to large-scale production. Moreover, films can be deposited at low temperatures on a variety of substrates and the thickness of the deposited layers may be readily controlled by adjusting the bath chemical composition and deposition time [13].

The present investigation reports the synthesis of amorphous copper oxide multilayer nanosheets by low temperature CBD method. The copper oxide thin films were characterized by X-ray diffraction (XRD), Field emission scanning electron microscopy (FESEM) and Fourier transform infrared spectrum (FTIR), optical absorption and wettability test. The electrochemical supercapacitive characteristics of the copper oxide films were investigated by cyclic voltammetry (CV) in 1 M Na_2SO_4 electrolyte.

2. Experimental details

2.1. Preparation of copper oxide thin films

Preparation of copper oxide thin film by CBD method is based on the heating of alkaline bath of copper salt containing the substrates immersed in it. The source of copper used was 0.1 M $CuSO_4$, and to make it alkaline, aqueous ammonia was added. Initially, precipitate of $Cu(OH)_2$ dissolved after addition of aqueous ammonia. The pH of the resultant solution was ~12. The glass and stainless steel were used as the substrates, which was cleaned with detergent and chromic acid, followed by rinsing with double-distilled water and finally treated with ultrasonic waves for 15 min. These cleaned substrates were immersed in the above bath and the bath was heated. When the bath attained the temperature of 343 K, the precipitation was started in the bath. During the precipitation, heterogeneous reaction occurred

* Corresponding author. Tel.: +91 231 2609225; fax: +91 231 2609233.
E-mail addresses: l_chandrakant@yahoo.com, dubal_deepak@yahoo.co.in (C.D. Lokhande).

0925-8388/$ – see front matter © 2009 Elsevier B.V. All rights reserved.
doi:10.1016/j.jallcom.2009.11.149

on the substrate and deposition of copper oxide took place on the substrate. The substrates coated with copper oxide thin films were removed after 1 h from the bath, washed with double-distilled water, dried in air and preserved in an airtight container.

2.2. Characterization techniques

The thickness of the copper oxide film was measured by weight difference method using sensitive microbalance. The structural analysis was carried out with Philips diffractrometer (Philips PW-3710) using chromium target of wavelength 2.2896 Å. The Fourier transform infrared (FTIR) spectrum of the sample was collected using PerkinElmer, FTIR Spectrum one' unit. The film microstructure was examined with a field emission scanning electron microscope (FE-SEM, Model: JSM-6160). The optical absorption studies were carried out within the wavelength range 350–850 nm for copper oxide films using Systronics spectrophotometer-119, with glass substrate as reference. In order to study interaction between liquid and thin film surface contact angle measurement was carried out by Rame-hart USA equipment with CCD camera. The supercapacitor formation and it's studies were carried out using the 263A EG&G Princeton Applied Research Potentiostat forming an electrochemical cell comprising copper oxide film as a working electrode, platinum as a counter electrode and saturated calomel electrode (SCE) as a reference electrode in 1 M Na_2SO_4 electrolyte.

3. Result and discussion

3.1. Film formation and reaction mechanism

The black copper oxide films deposited by CBD method were uniform and well adherent to the substrates. When the process is considered in a qualitative way, the film growth is dominated by three periods: (i) nucleation or incubation period, during which the various chemical equilibriums and reactions are established in the bath. (ii) The growth period during which the film thickness has an approximately linear variety with deposition time. At the moment, the ionic product (IP) of the solution exceeds the solubility product (SP), and the solution reaches a maximum degree of supersaturation (S = degree of supersaturation = IP/SP), which consequently leads to the growth of nuclei and deposition of the film. (iii) A terminal step where the reagent becomes depleted and the film growth begins to slow and eventually stops. For deposition of copper oxide film, $CuSO_4$ is used as source of copper ions (Cu^{2+}). When ammonia is added to it, whitish blue precipitate of $Cu(OH)_2$ occurred, which get dissolved by additional of excess ammonia. This can be represented by the following reactions:

$$CuSO_4 + 2NH_4OH \rightarrow Cu(OH)_2 + (NH_4)_2SO_4 \quad (1)$$

$$Cu(OH)_2 + NH_4OH \rightarrow (NH_4)CuO_2^- + H_2O + H^+ \quad (2)$$

When this solution was heated the ionic product exceeds the solubility product and precipitation occurred on the substrate and in the solution to form CuO nuclei and thus well adherent and uniform CuO film formed on the substrate by the following reaction:

$$(NH_4)CuO_2^- + H^+ \Rightarrow CuO + NH_4OH \quad (3)$$

The mechanism shows that, in an alkaline bath there is initially formation of $Cu(OH)_2$ finally converts into CuO.

3.2. Thickness measurement

Thickness of copper oxide films was measured by the gravimetric weight difference method in terms of deposited weight of a copper oxide film on the glass substrate, per unit area (g/cm^2), since the accurate measurement of copper oxide film thickness was not possible due to the rough morphology and porosity of the film; similar to our previous report [14]. The graph of the deposited weight of copper oxide with the deposition time is shown in Fig. 1. In the process of deposition of copper oxide films by CBD method, alkaline copper sulphate bath is heated up to 343 K. It is observed that after about 20 min precipitation starts and the deposition of copper oxide begins by heterogeneous reaction at substrate surface and the deposited weight of film increases with time. The weight of copper oxide film was found to increase with deposition time. After 100 min, almost all precipitate rested down at the bottom of the bath, indicating that the reaction is complete. Here, the copper oxide films withdrawn from the bath after 60, 80, and 100 min, respectively. The maximum thickness obtained for copper oxide thin film was 1.2 μm and used for the further characterization.

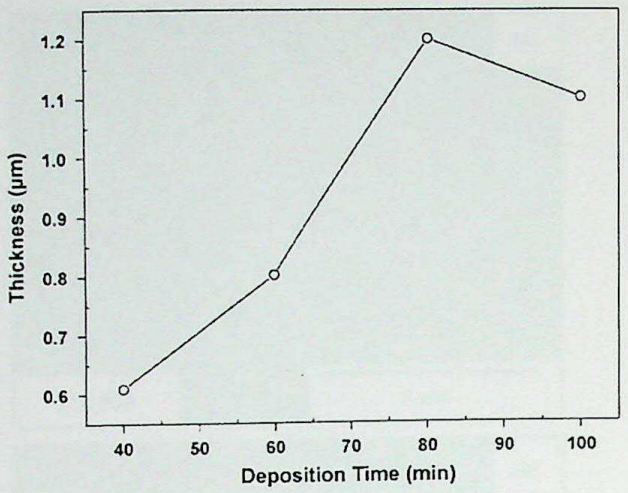


Fig. 1. Variation of copper oxide film thickness with deposition period.

3.3. Structural studies

Fig. 2 shows the XRD pattern of chemically deposited copper oxide thin film on to the stainless steel substrate. From the XRD pattern, it can be seen that there is no any significant peak corresponding to copper oxide material. This indicates that copper oxide thin films are nanocrystalline and/or amorphous in nature. Similar type of behavior has been reported by Patake et al. [15] for the copper oxide films deposited by electrodeposition method. The amorphous nature of oxide plays an important role in improvement of supercapacitor [16]. The peaks marked by triangles are due to the contribution from stainless steel substrate.

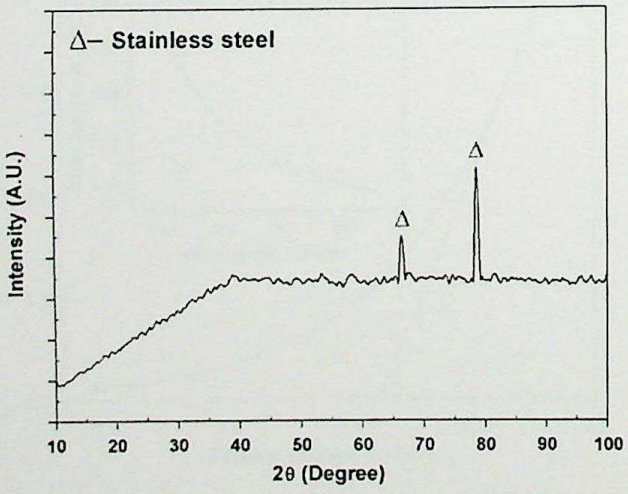


Fig. 2. The XRD pattern of copper oxide thin film on stainless steel substrate.

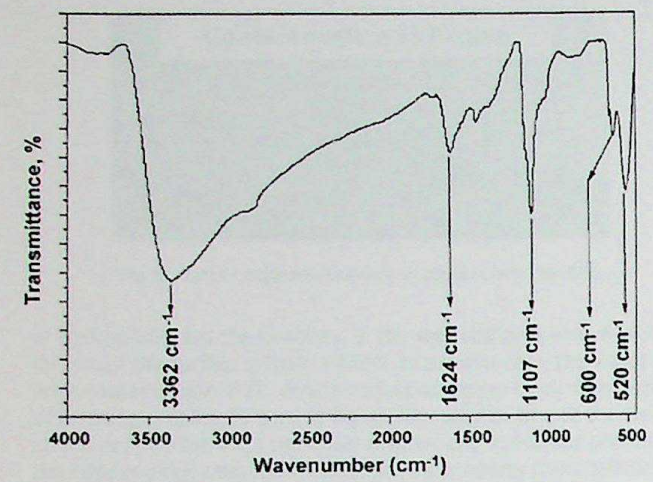


Fig. 3. FTIR spectrum of copper oxide thin film.

3.4. FTIR study

Fig. 3 displays the FTIR spectrum of copper oxide sample. The absorption at 3362 cm^{-1} indicates the presence of hydroxide group [17]. The absorption peaks around at 1624 cm^{-1} and 1107 cm^{-1} maybe attributed to O–H bending vibrations combined with copper atoms. The two broad absorption bands at 600 and 520 cm^{-1} are associated with Cu–O stretching modes [18]. Thus, the FTIR result suggests the presence of Cu–O bonds and some constitutional water incorporated in the copper oxide structure. Thus, the formation of copper oxide compound is confirmed from FTIR study.

3.5. Surface morphological study

Field emission scanning electron micrographs of copper oxide thin films at two different magnifications are presented in Fig. 4(a and b). The micrographs revealed the formation of hierarchical multilayer nanosheets clusters. At high magnification (×50,000) we clearly see that these nanosheets clusters are well covered to substrate surface (Fig. 4(b)). The width of these nanosheets is about 20–30 nm. The nanosheet, nanoparticles and nanorod-like morphologies lead to a high specific surface area and porous volume, which provide the structural foundation for the high specific capacitance [19–22].

3.6. Optical studies

The optical absorption spectrum in the range of 450–850 nm for the copper oxide film was carried out on to the glass substrate without scattering and reflection taking into account. Inset of Fig. 5 shows the optical absorption of copper oxide film; it appears that copper oxide thin film has high absorbance in the visible region. The absorption edge was found at 600 nm due to optical band gap absorption. The optical band gap (E_g) for copper oxide film is calculated on the basis of optical absorption using the following equation:

$$\alpha = \frac{A(E_g - h\nu)^n}{h\nu} \quad (4)$$

where α is absorption coefficient, E_g is band gap, A is constant and n is equal to 1/2 for direct transition. The plot of $(\alpha h\nu)^2$ vs. $h\nu$ of copper oxide film is shown in Fig. 5. From the linear nature of the plot, the direct optical transition in copper oxide is confirmed. The band gap energy, E_g is obtained by extrapolating the linear portion of the plot $(\alpha h\nu)^2$ vs. $h\nu$ to the energy axis at $\alpha = 0$. From the graph

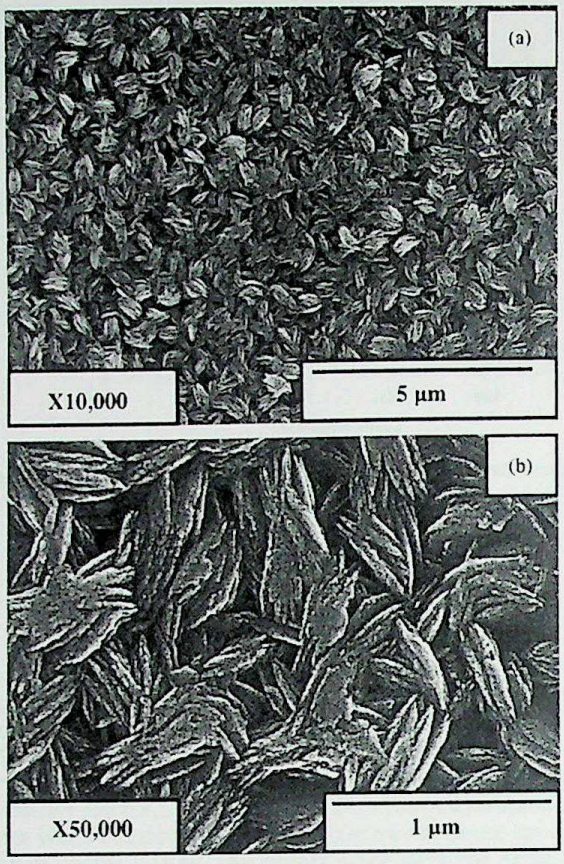


Fig. 4. The FESEM images of copper oxide thin film at (a) ×10,000 and (b) ×50,000 magnifications.

for copper oxide thin film, band gap value of 2.18 eV is observed which is similar to the other reports for copper oxide films [23,24].

3.7. Wettability test

Wettability test is carried out in order to investigate the interaction between electrolyte and copper oxide electrode. If the wettability is high, contact angle (θ), will be small and the surface

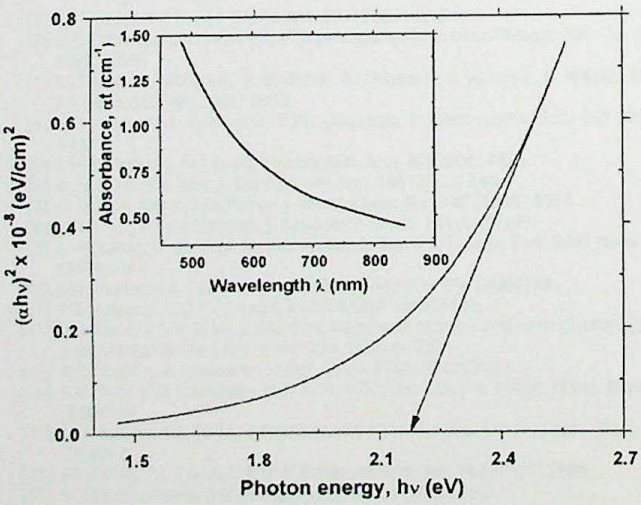


Fig. 5. The plots of $(\alpha h\nu)^2$ vs. $h\nu$ of copper oxide thin films. Inset shows variation of absorption (αt) with wavelength (λ) of copper oxide thin film on glass substrate.

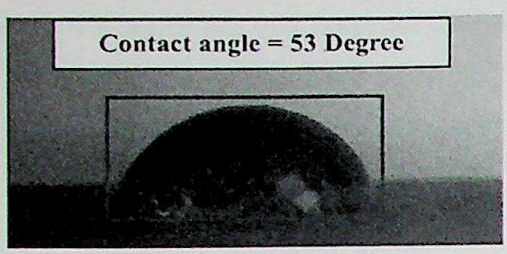


Fig. 6. Contact angle measurement of copper oxide thin film.

is hydrophilic. On the contrary, if the wettability is low, θ will be large and the surface is hydrophobic. In present case, the water lies with contact angle of 53° on the surface of copper oxide film instead of forming droplet, as seen in Fig. 6. This may be due to the strong cohesive force between the water droplet and hydroxide present in the copper oxide compound. This specific property (hydrophilicity) is attributed to nanocrystalline nature that is expected to possess very high surface energy. Nanocrystalline material with hydrophilic nature is one of the prime requirements for supercapacitor electrode material. Hydrophilicity is useful for making intimate contact of aqueous electrolyte with film surface in supercapacitor application. It is well known that in the electrochemical supercapacitor, hydrophilic surface of the electrode is an essential factor for better performance [25]. Mane et al. [26] reported a contact angle of 21° for electrochemically deposited tin oxide thin films for supercapacitor application.

3.8. Electrochemical properties

The chemically deposited copper oxide thin films were used in the formation of electrochemical supercapacitors and their performance was tested studying CV curves. The CV curve provides the measure of supercapacitors charge response with charging voltage and hence can be used to evaluate the capacitance. The pseudocapacitance of transition metal oxides have been attributed to redox transition of species at various oxidation states. The pseudocapacitance of copper oxide electrode is the result of transitions between +2 and +1 oxidation state and vice versa. The proposed redox reaction for the copper oxide electrode showing capacitance will be as follows:

$$Cu^{2+} + e^- \leftrightarrow Cu^+ (-0.08\,V/SCE)$$

In this process of reaction CuO converts into Cu_2O with changing the +2 oxidation state to +1 oxidation state and again +1 to +2 states following the same reversible process of reduction and oxidation.

The electrochemical behavior of copper oxide film was studied in 1 M Na_2SO_4 in the potential window of +0.1 to −0.7 V. Fig. 7 shows the cyclic voltammograms with different scan rates. It is found that the current under curve slowly increased with scan rate. This shows that the voltammetric current is directly proportional to the scan rates of CV, indicating an ideally capacitive behavior [27]. The capacitance was calculated using the following relation,

$$C = \frac{I}{dV/dt} \quad (5)$$

where, I is the average current in ampere and dV/dt is voltage scanning rate. Interfacial capacitance is calculated by dividing area of copper oxide electrode dipped in the electrolyte. In present case, area dipped in electrolyte is 1 cm^2. The copper oxide electrode exhibited interfacial capacitance of 0.12 mF cm^{-2} and specific capacitance of 43 F g^{-1}. Patake et al. [16] reported 37 F g^{-1} supercapacitance of copper oxide films prepared by electrodeposition method. The slightly high value may be due to hydrous nature of copper oxide in present case.

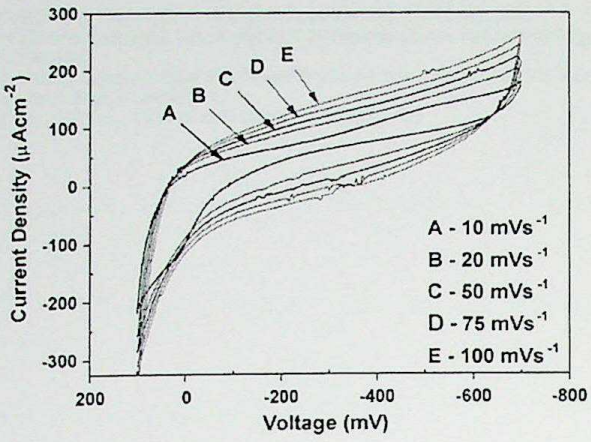


Fig. 7. The cyclic voltammograms of copper oxide electrode at different scanning rates in the 1 M Na_2SO_4 electrolyte in the +0.1 to −0.7 V vs. SCE.

4. Conclusions

In conclusion, copper oxide multilayer nanosheets have been synthesized by simple and inexpensive CBD method. The XRD pattern revealed the amorphous nature of copper oxide thin films. Formation of copper oxide compound was confirmed from the FTIR studies. The FESEM images revealed the development of hierarchical multilayer nanosheets which are well covered with the substrate surface. The copper oxide films shows hydrophilic nature with water contact angle 53° and existence of direct optical band gap of energy 2.18 eV. The copper oxide electrode exhibited the supercapacitance of 43 F g^{-1}. Thus, chemically deposited copper oxide thin films are promising electrode material for electrochemical capacitors.

Acknowledgement

Authors are grateful to the University Grants Commission (UGC), New Delhi for financial support through the scheme no. 36-207/2008 (SR).

References

[1] M. Winter, R.J. Brodd, Chem. Rev. 104 (2005) 4245.
[2] B.E. Conway, Electrochemical Supercapacitors, Kluwer-Plenum Pub. Co., New York, 1999.
[3] V. Panic, T. Vidakovic, S. Gojkovic, A. Dekanski, S. Milonjic, B. Nikolic, Electrochim. Acta 48 (2003) 3805.
[4] S.C. Pang, M.A. Anderson, T.W. Chapman, J. Electrochem. Soc. 147 (2000) 444.
[5] J.N. Broughton, M.J. Brett, Electrochim. Acta 49 (2004) 4439.
[6] K.W. Nam, K.B. Kim, J. Electrochem. Soc. 149 (2002) 346.
[7] C. Lin, J.A. Ritter, B.N. Popov, J. Electrochem. Soc. 145 (1998) 4097.
[8] H.Y. Lee, J.B. Goodenough, J. Solid State Chem. 148 (1999) 81.
[9] L. Armelao, D. Barreca, M. Bertapelle, G. Bottaro, C. Sada, Thin Solid Films 442 (2003) 48.
[10] J.M. Valtierra, S. Calixto, F. Ruiz, Thin Solid Films 460 (2004) 58.
[11] S.S. Kulkarni, C.D. Lokhande, Trans. SAEST (2003) 123.
[12] R.K. Pandey, S.N. Sahu, S. Chandra, Handbook of Semiconductor Electrodeposition, Marcel Dekker, Inc., New York, 1996, p. 237.
[13] R.S. Mane, C.D. Lokhande, Mater. Chem. Phys. 65 (2000) 1.
[14] B.O. Park, C.D. Lokhande, H.S. Park, K.D. Jung, O.S. Joo, Mater. Chem. Phys. 87 (2004) 59.
[15] V.D. Patake, S.S. Joshi, C.D. Lokhande, Oh-Shim Joo, Mater. Chem. Phys. 114 (2009) 6.
[16] J.P. Zheng, P.J. Cygan, T.R. Jow, J. Electrochem. Soc. 142 (1995) 2699.
[17] S. Karuppuchamy, J.M. Jeong, J. Oleo Sci. 55 (2006) 263.
[18] Y.Y. Xu, D.R. Chen, X.L. Jiao, J. Phys. Chem. B 109 (2005) 13561.
[19] Y. Li, X. Xie, J. Liu, M. Cai, J. Rogers, W. Shen, J. Chem. Eng. 136 (2008) 398.

[20] L.X. Yang, Y.J. Zhu, H. Tong, Z.H. Liang, L. Li, L. Zhang, J. Solid State Chem. 180 (2007) 2095.
[21] J. Sun, J. Cheng, C. Wang, X. Ma, M. Li, L. Yuan, Ind. Eng. Chem. Res. 5 (2006) 2146.
[22] W.G. Pell, B.E. Conway, J. Electro. Chem. 500 (2001) 121.
[23] A.A. Ogwu, E. Bouquerel, O. Ademosu, S. Moh, E. Crossan, F. Placido, J. Phys. D: Appl. Phys. 38 (2005) 266.
[24] J.F. Pierson, A. Thobor-Keck, A. Billard, Appl. Surf. Sci. 210 (2003) 359.
[25] O. Bockman, T. Ostvold, G.A. Voyiatzis, G.N. Papatheodorou, Hydrometallurgy 55 (2000) 93.
[26] R.S. Mane, J. Chang, D. Ham, B.N. Pawar, T. Ganesh, B.W. Cho, J.K. Lee, S.H. Han, Curr. Appl. Phys. 9 (2009) 87.
[27] C.C. Hu, T.W. Tsou, Electrochem. Commun. 4 (2002) 105.

G Model
JALCOM-19690; No. of Pages 4
ARTICLE IN PRESS

Journal of Alloys and Compounds xxx (2009) xxx–xxx

Contents lists available at ScienceDirect

Journal of Alloys and Compounds

journal homepage: www.elsevier.com/locate/jallcom

A novel chemical synthesis of interlocked cubes of hausmannite Mn_3O_4 thin films for supercapacitor application

D.P. Dubal[a], D.S. Dhawale[a], R.R. Salunkhe[a], S.M. Pawar[b], V.J. Fulari[a], C.D. Lokhande[a,*]

[a] Thin Film Physics Laboratory, Department of Physics, Shivaji University, Kolhapur, 416004 (MS), India
[b] Photonic and Electronic Thin Film Laboratory, Department of Materials Science and Engineering, Chonnam National University, 300 Yongbong-Dong, Puk-Gu, Gwangju 500-757, South Korea

ARTICLE INFO

Article history:
Received 11 December 2008
Received in revised form 17 March 2009
Accepted 24 March 2009

Keywords:
Hausmannite Mn_3O_4
Thin films
Chemical deposition
Optical properties
Supercapacitor

ABSTRACT

The interlocked cubes of hausmannite Mn_3O_4 thin films were synthesized by simple, inexpensive, and low temperature chemical route from urea containing bath. These films were characterized by using X-ray diffraction (XRD), field emission scanning electron microscope (FE-SEM), Fourier transform infrared spectra (FT-IR), optical absorption and wettability test. From the XRD patterns, polycrystalline nature of the hausmannite Mn_3O_4 films has been confirmed. Scanning electron micrographs revealed the development of three dimensional growths of interlocked cubes of Mn_3O_4 material. FT-IR spectrum bands confirmed the formation of Mn_3O_4 compound. The Mn_3O_4 film showed a direct optical band gap with energy 2.5 eV and hydrophilicity with water contact angle of 60°. Mn_3O_4 film when used in supercapacitor exhibited specific capacitance of 193 $F g^{-1}$ in 1 M Na_2SO_4 electrolyte.

© 2009 Elsevier B.V. All rights reserved.

1. Introduction

Manganese oxide thin films have potential applications in electrochemical materials, high density magnetic storage medium, catalyst, ion-exchange, molecular adsorption, etc. [1–3]. It is known to be an active catalyst for the decomposition of waste gas NO_x, selective reduction of nitrobenzene and so on. It is corrosion-inhibiting pigment for epoxy-polyamide and epoxy-ester-based primers and top coating and also a starting material for manufacturing soft magnetic materials such as manganese zinc ferrite useful for dioxymagnetic cores in transformers for power supplies. Hausmannite Mn_3O_4 is known to have a normal spinel structure with tetragonal distortion elongated along the *c*-axis due to Jahn-Teller effect on the Mn^{3+} ion. Manganese ions occupy the octahedral B-site (Mn^{3+}) and tetrahedral A-site (Mn^{2+}) corresponding to a normal spinel structure. There are 32 oxygens and 24 cations in the unit cell [4].

Recently, conducting polymers, activated carbon and transition metal oxides are widely used for supercapacitor electrode material. Manganese oxide thin films which belong to third category shows excellent pseudocapacitive behavior with the large specific capacitance as high as 698 $F g^{-1}$ [5]. Manganese oxide is a potential supercapacitor material due to its low cost, natural abundance and environmentally more friendly than other transition metal oxides. Nam and Kim [6] reported the specific capacitance of 330 $F g^{-1}$ for manganese oxide films prepared by electrostatic spray deposition method. Chang and Tsai [7] investigated the effect of heat treatment on material characteristics of anodically deposited manganese oxide films and reported the specific capacitance of 240 $F g^{-1}$.

Mn_3O_4 has been prepared by various methods viz., microwave irradiation [8], hydrothermal or solvothermal routes [9,10], reflux method [11], flash microwave method [12], metal organic chemical vapor deposition (MOCVD) [13], chemical vapor deposition, etc. Preparation of Mn_3O_4 by chemical bath deposition (CBD) method is less investigated [14] and needs further investigation. As compared to the other deposition methods, CBD is an attractive one because of its own advantages such as simplicity, reproducibility, non-hazardous, cost effectiveness, etc. It is well suited for producing large-area thin films at low temperature and hence avoids oxidation or corrosion of metallic substrate [15].

In this investigation, for the first time, we report on the synthesis and characterization of Mn_3O_4 thin film by CBD method from urea containing bath for supercapacitor application. The Mn_3O_4 films were characterized by X-ray diffraction (XRD), scanning electron microscope (SEM), Fourier transform infrared (FT-IR) spectrum, optical absorption and wettability techniques. The supercapacitive behavior of Mn_3O_4 thin films was investigated by cyclic voltammetry.

* Corresponding author. Tel.: +91 231 2609229; fax: +91 231 269233.
E-mail address: l_chandrakant@yahoo.com (C.D. Lokhande).

0925-8388/$ – see front matter © 2009 Elsevier B.V. All rights reserved.
doi:10.1016/j.jallcom.2009.03.135

2. Experimental details

2.1. Preparation of Mn_3O_4 thin films

Manganese sulphate ($MnSO_4 \cdot H_2O$) and urea ($(NH_2)_2CO$) purchased from S.D.Fine-Chem and LOBA Chemie, respectively were used without further purification. Fresh aqueous solutions of manganese sulphate (0.05 M) and urea (1 M) were prepared in double distilled water immediately before their use. The pH of the mixed solution was ~8. The solution was transparent and free from any precipitate. The commercial borosilicate glass slides were cleaned with detergent and chromic acid, followed by rinsing with double distilled water and finally treated with ultrasonic waves for 15 min. The substrates were immersed in the bath at the temperature 353 K without stirring for 12 h. After about 4 h, the solution became blurred and within 12 h the brown precipitate was formed in the bath. During the precipitation, the heterogeneous reaction occurred and the deposition of Mn_3O_4 took place on the substrate. The substrates coated with bright brown colored Mn_3O_4 thin films were removed, rinsed, dried in air and preserved in an air-tight container. The as-deposited films were uniform, specularly reflective (mirror like) and extremely adherent to the substrate.

2.2. Characterization techniques

The crystal structure of the Mn_3O_4 thin films was identified by X-ray diffraction analysis with Philips (PW 3710) diffractometer using CuK_α radiation ($\lambda = 1.5406$ Å) in 2θ ranging from 10° to 100°. The film surface morphology was observed by field emission scanning electron micrograph (FE-SEM, model: JSM-6160). The FT-IR spectrum of the sample was collected using Perkin Elmer, FT-IR spectrum one unit. The optical absorption study was carried out over the wavelength range 350–850 nm using Systronics spectrophotometer-119, with glass substrate as a reference. Contact angle measurement was carried out by Rame-Hart USA equipment with CCD camera. The cyclic voltammetry (*C–V*) studies were carried out using the 263A EG&G Princeton Applied Research Potentiostat forming an electrochemical cell comprising Mn_3O_4 thin film as a working electrode, platinum as a counter electrode and saturated calomel electrode (SCE) as a reference electrode in 1 M Na_2SO_4 electrolyte.

3. Results and discussion

3.1. Film formation mechanism

The CBD is based on the formation of solid phase from a solution, which involves two steps as nucleation and particle growth. In nucleation, the heterogeneous reaction at the substrate surface takes place when clusters of the molecules formed undergo rapid decomposition and particles combine to grow up to a certain thickness of the film. The primary role of urea is to provide a slow controlled supply of OH^- ions through slow thermal decomposition [16]. This includes hydrolysis of urea and reaction of ammonia with water as follows:

$$(NH_2)_2CO + H_2O \rightarrow 2NH_3 + CO_2 \quad (1)$$

$$NH_3 + H_2O \rightleftharpoons NH_4OH \quad (2)$$

In the present research work, the low reaction temperature and unstirred chemical bath slowly releases free Mn^{2+} cations from the stable precursor, these Mn^{2+} cations form ammine complexes of $Mn(NH_3)_n^{2+}$ ($n = 1$–4) with NH_3 (aq) in moderately basic media (pH ~ 8). Due to the formation of these complexes, the solution did not contain colloidal manganese hydroxide in the deposition solution. The reaction is as follows,

$$Mn^{2+} + nNH_3 \rightleftharpoons Mn(NH_3)_n^{2+} \quad (3)$$

In our experiment, the pH value is ~8, i.e. the solution is alkalescent. On this alkalescent and bath heating condition the $Mn(NH_3)_n^{2+}$ is unstable and the following reaction occurs as

$$Mn(NH_3)_n^{2+} \rightleftharpoons Mn^{2+} + nNH_3 \quad (4)$$

Finally, oxidation of Mn^{2+} to Mn^{3+} takes place as

$$6Mn^{2+} + O_2 + 12OH^- \rightarrow 2Mn_3O_4 + 6H_2O \quad (5)$$

Thus, nucleation and growth of Mn_3O_4 thin films take place via ion-by-ion mechanism. Many of chemically deposited thin films peel from the substrate at some stage of growth phase before reaching the terminal thickness. In the present case, Mn_3O_4 thin films are extremely adhesive to the substrate though the deposition was carried out for prolonged time intervals.

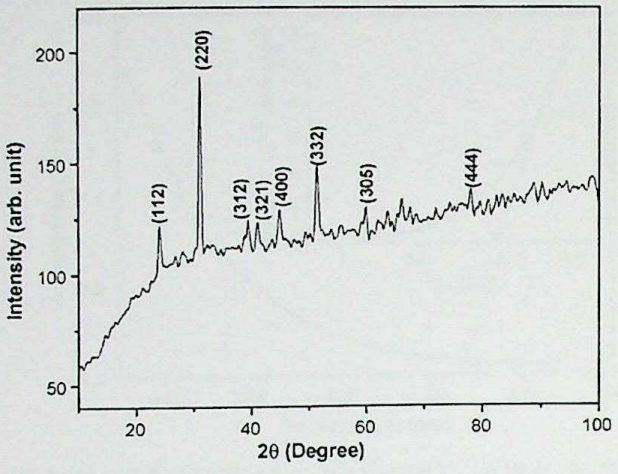


Fig. 1. The X-ray diffraction pattern of Mn_3O_4 thin film on glass substrate.

3.2. Structural studies

In order to study crystalline nature of Mn_3O_4 thin film, the XRD pattern was recorded in the 2θ range 10–100°. Fig. 1 shows XRD pattern of Mn_3O_4 thin film. It is evident from the figure that Mn_3O_4 thin film is polycrystalline and has tetragonal hausmannite structure. The calculated lattice constants $a = 5.1822$ Å, $b = 5.1822$ Å and $c = 9.4563$ Å, are in good agreement with standard lattice constants [$a = 5.7621$ Å, $b = 5.7621$ and $c = 9.4696$ Å, JCPDS card no. 75-1560]. This confirms the formation of tetragonal hausmannite Mn_3O_4 compound. Xu et al. [14] reported the hausmannite structure for Mn_3O_4 thin films by CBD method using NH_4Cl and NH_3 containing bath. Nam and Kim [6] reported the same hausmannite structure by electrostatic spray deposition method. The grain size of Mn_3O_4 thin films from XRD pattern was calculated using the Scherer's relation:

$$D = \frac{0.9\lambda}{\beta \cos\theta} \quad (6)$$

where β is the broadening of diffraction line measured at half maximum intensity (radians) and $\lambda = 1.54056$ Å, the wavelength of the Cu Kα X-ray. The grain size was found to be 20 nm for (2 2 0) plane.

3.3. Surface morphology

Fig. 2a and b shows the FE-SEM images of Mn_3O_4 thin film at two different magnifications (×2000 and ×5000). The substrate surface was covered uniformly with cube-like novel morphology. The micrograph revealed the three dimensional growth of manganese oxide cubes with some clusters of overgrowth. These cubes are interlocked with each other or aggregated. Approximate size of the cubes is in between 5 and 10 μm as seen in Fig. 2b. Xu et al. [14] reported smooth surface of film with nanosized grains for the films prepared by CBD for the deposition period of 11 h. Baykal et al. [17] prepared the Mn_3O_4 films by reflux method and reported that film consists of network formed by the particles with sizes in the submicron range.

3.4. FT-IR study

Fig. 3 shows the FT-IR spectrum of Mn_3O_4 thin film. The region below 1400 cm^{-1} contains peaks due to fundamental vibrations of

Please cite this article in press as: D.P. Dubal, et al., J. Alloys Compd. (2009), doi:10.1016/j.jallcom.2009.03.135

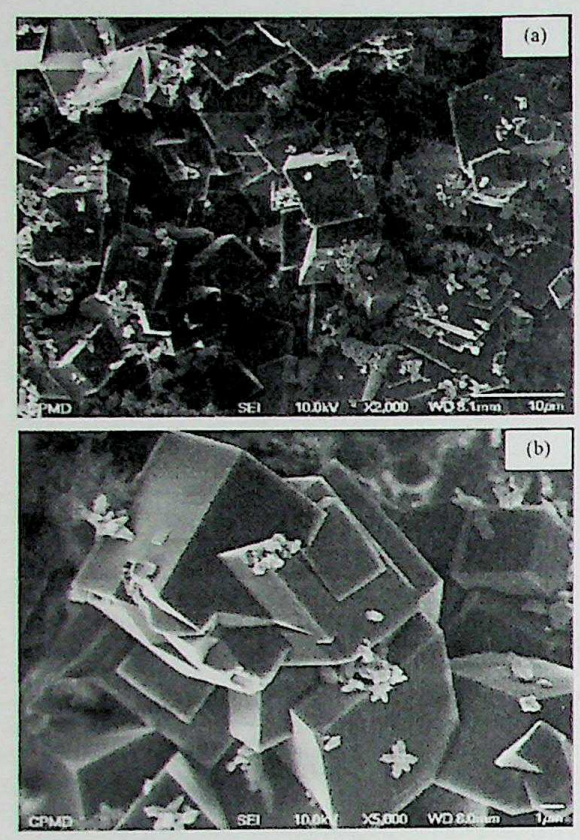


Fig. 2. The SEM images of Mn_3O_4 thin film at (a) ×2000 and (b) ×5000 magnifications.

octahedral MnO_6 and the region above 1400 cm^{-1} contains peaks primarily corresponding to OH vibrations [18]. The regions from 750 to 600 cm^{-1} and 600 to 450 cm^{-1} correspond to Mn—O stretching and bending vibrations. The absorption of the Mn—O lattice vibrations around at 724, 633 and 525 cm^{-1} in the spectrum is indicative of a tetragonally distorted cubic lattice. These absorption peaks may be associated with the coupling mode between Mn—O stretching modes of tetrahedral and octahedral sites [19,20]. This confirms the formation of manganese oxide compound. The absorption bands obtained in the region 1750–1800 cm^{-1} and 1400–1390 cm^{-1}

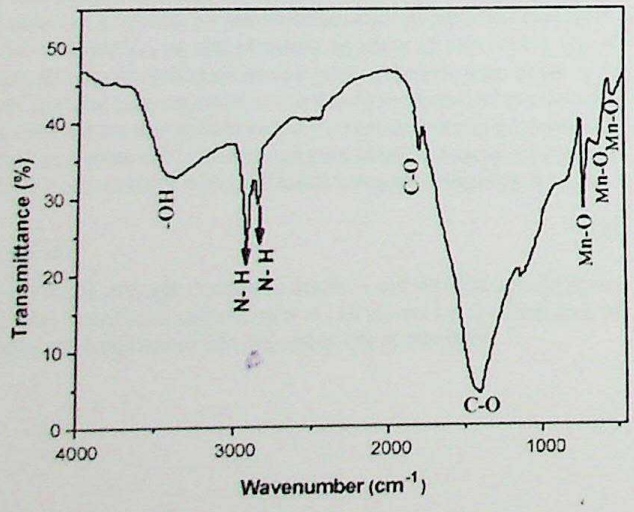


Fig. 3. FT-IR spectrum of Mn_3O_4 thin film.

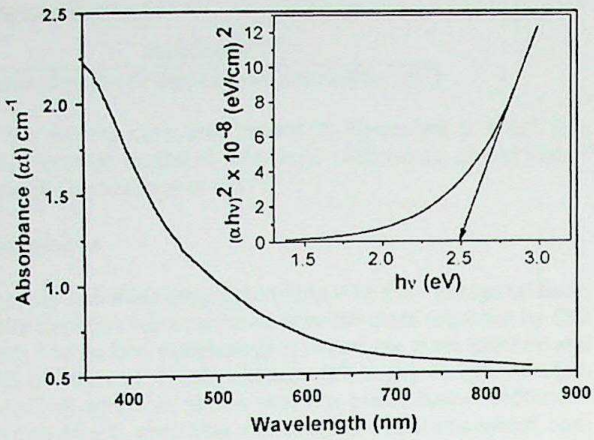


Fig. 4. The variation of absorption (αt) with wavelength (λ) of Mn_3O_4 thin film on glass substrate. Inset shows the plot of $(\alpha h\upsilon)^2$ vs. $h\upsilon$ of Mn_3O_4 thin film.

mainly correspond to C—O group [21]. The broad IR absorption in the 3600–2800 cm^{-1} range, with a maximum at 3391 cm^{-1} arises from the —OH mode of interacting hydroxyl groups [22]. The narrow bands around 2923 cm^{-1} and 2853 cm^{-1} are due to N—H bonds that is organic residues originating from the sample as a result of the preparation procedure [23]. The result indicates the presence of Mn—O bonds, carboxyl groups and —OH groups for as-deposited thin films.

3.5. Optical studies

The optical absorption of Mn_3O_4 thin films in the wavelength range 350–850 nm has been investigated. Fig. 4 shows variation of absorbance (αt) of Mn_3O_4 film with wavelength (λ). This spectrum reveals that Mn_3O_4 thin film has high absorbance of light in the visible region, indicating applicability as an absorbing material. The absorption edge was found at 500 nm due to optical band gap absorption which is in good agreement with the literature data [24]. The optical band gap energy is estimated by using the following equation for a semiconductor:

$$\alpha = \frac{A(E_g - h\upsilon)^n}{h\upsilon} \quad (7)$$

where α is absorption coefficient, E_g is band gap, A is constant and n is equal to 1/2 for direct transition. Inset of Fig. 4 shows the variation of $(\alpha h\upsilon)^2$ vs. $h\upsilon$, which is a straight line in the domain of higher energies, indicating a direct optical transition. The band gap energy, E_g is obtained by extrapolating the linear portion of the plot $(\alpha h\upsilon)^2$ vs. $h\upsilon$ to the energy axis at $\alpha = 0$. From the graph for Mn_3O_4 thin film, band gap value of 2.5 eV is observed. Xu et al. found the optical band gap of 2.54 eV for chemical bath deposition of Mn_3O_4 thin films [14].

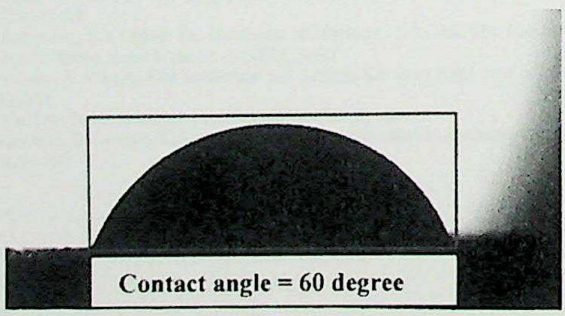


Fig. 5. Contact angle measurement of Mn_3O_4 thin film.

Please cite this article in press as: D.P. Dubal, et al., J. Alloys Compd. (2009), doi:10.1016/j.jallcom.2009.03.135

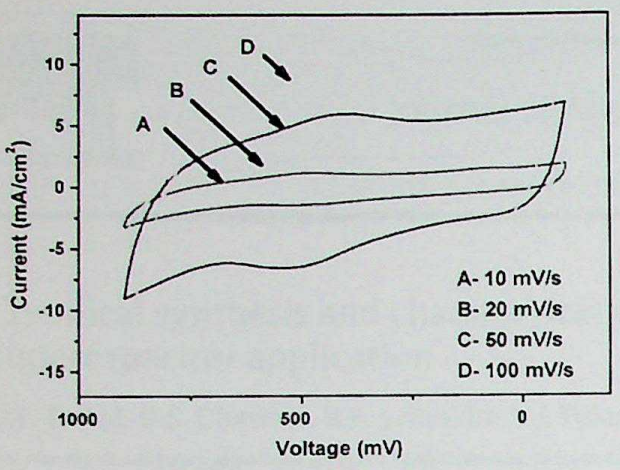


Fig. 6. The cyclic voltammograms of Mn_3O_4 electrode at different scanning rates (A–10 mV/s, B–20 mV/s, C–50 mV/s, D–100 mV/s) in the 1 M Na_2SO_4 electrolyte in the −0.1–0.9 V vs. SCE.

3.6. Wettability test

The wetting of solid with water, where air is the surrounding medium, is dependent on the relation between the interfacial tensions (water/air, water/solid and solid/air). The ratio between these tensions determines the contact angle (θ) between a water droplet on a given surface. A contact angle of 0° means complete wetting and a contact angle of 180° corresponds to complete non-wetting. The surface wettability involves the interaction between liquid and solid in contact. The wetting behavior is characterized by the value of contact angle, a microscopic parameter. Measurement of surface water contact angle is inversely proportional to the wettability and can be determined by Young's relation [25]. The contact angle is expected to depend upon local inhomogeneity, chemical composition and the surface morphology of the electrodes. In the present case, the water lies with contact angle of 60° on the surface of Mn_3O_4 thin film forming a droplet as seen in Fig. 5 indicating hydrophilic behavior. It is well known that in the electrochemical supercapacitor, hydrophilic surface of the electrode is an essential factor for better performance [27].

3.7. Supercapacitive studies

The Mn_3O_4 films were used in the electrochemical supercapacitor and its performance was tested using cyclic voltammogram. The effect of scan rate on the electrochemical capacitor was studied in 1 M Na_2SO_4 in the potential window of −0.1–0.9 V. Fig. 6 shows the cyclic voltammograms with different scan rates. It is found that the current under curve slowly increased with scan rate. This shows that the voltammetric current is directly proportional to the scan rates of *C–V*, indicating an ideally capacitive behavior [26]. The capacitance was calculated using the following relation,

$$C = \frac{I}{dV/dt} \tag{8}$$

where I is the average current in ampere and dV/dt is voltage scanning rate. Interfacial capacitance is calculated by dividing area of manganese oxide electrode dipped in the electrolyte.

Interfacial capacitance

$$= \frac{\text{capacitance (F)}}{\text{area of electrode dipped in an electrolyte (cm}^2\text{)}}$$

In the present case, area dipped in electrolyte is 1 cm^2. The Mn_3O_4 electrode exhibited interfacial capacitance of 0.11 F cm^{-2} and specific capacitance of 193 F g^{-1}.

4. Conclusions

The polycrystalline Mn_3O_4 thin films with pure tetragonal hausmannite structure were prepared onto the glass substrate by CBD method. The surface morphology revealed the three dimensional growth of interlocked cubes along with some overgrown clusters. A FT-IR spectrum shows that the bands below 1400 cm^{-1} are due to Mn—O stretching and bending vibrations which confirm the formation of Mn_3O_4 compound. The Mn_3O_4 film showed direct band gap with energy 2.5 eV and hydrophilic nature with water contact angle of 60°. The specific and interfacial capacitances of Mn_3O_4 electrode were 193 and 0.11 F cm^{-2}, respectively which persuade us to propose Mn_3O_4 as a promising supercapacitor candidate.

Acknowledgement

Authors are grateful to the Department of Science and Technology, New Delhi for financial support through the scheme no. SR/S2/CMP-82/2006.

References

[1] M.C. Bernard, H.L. Goff, B.V. Thi, J. Electrochem. Soc. 140 (1993) 3065.
[2] A.H. De Vries, L. Hozoi, R. Broer, Phys. Rev. 66 (2002) 35108.
[3] Y. Yamashita, K. Mukai, J. Yoshinobu, M. Lippmaa, T. Kinoshita, M. Kawasaki, Surf. Sci. 514 (2002) 54.
[4] A.S. Fritsch, J. Sarrias, A. Rousset, G.U. Kulkarni, Mat. Res. Bull. 33 (1998) 1185.
[5] S.C. Pang, M.A. Anderson, T.W. Chapman, J. Electrochem. Soc. 147 (2000) 444.
[6] K.W. Nam, K.B. Kim, J. Electrochem. Soc. 153 (2006) 81.
[7] J.K. Chang, W.T. Tsai, J. Electrochem. Soc. 150 (2003) 1333.
[8] S.K. Apte, S.D. Naik, R.S. Sonawane, B.B. Kale, N. Pavaskar, A.B. Mandale, B.K. Das, Mater. Res. Bull. 41 (2006) 647.
[9] Y.C. Zhang, T. Qiao, X.Y. Hu, J. Solid State Chem. 177 (2004) 4093.
[10] E. Finocchio, G. Busca, Catal. Today 70 (2001) 213.
[11] M. Anilkumar, V. Ravi, Mater. Res. Bull. 40 (2005) 605.
[12] C.B. Berthelin, D. Stuerga, J. Mater. Sci. 40 (2005) 253.
[13] O.Yu. Gorbenko, I.E. Graboy, V.A. Amelichev, A.A. Bosak, A.R. Kaul, B. Guttler, V.L. Svetchnikov, H.W. Zandbergen, Solid State Commun. 124 (2002) 15.
[14] H.Y. Xu, S.L. Xu, X.D. Li, H. Wang, H. Yan, Appl. Surf. Sci. 252 (2006) 4091.
[15] R.S. Mane, C.D. Lokhande, Mater. Chem. Phys. 65 (2000) 1.
[16] M.P. Ana, A.A. Jose, P. Jose, D. Xavier, D. Concepcion, J. Cryst. Growth 285 (2005) 6.
[17] A. Baykal, Y. Koseoglu, M. Senel, Cent. Eur. J. Chem. 5 (2007) 169.
[18] M. Minakshi, P. Singh, T.B. Issa, S. Thurgate, R.D. Marco, J. Power Sources 138 (2004) 319–322.
[19] C.M. Julien, M. Massot, C. Poinsignon, Spectrochim. Acta 60 (2004) 689.
[20] M. Ocana, Colloid Polym. Sci. 278 (2000) 443.
[21] J. Schmitt, H.C. Flemming, Int. Biodeterior. Biodegrad. 41 (1998) 1–11.
[22] S. Karuppuchamy, J.M. Jeong, J. Oleo Sci. 55 (2006) 263.
[23] A.J. Maira, J.M. Coronado, V. Augugliaro, K.L. Yeung, J.C. Conesa, J. Soria, J. Catal. 202 (2001) 413.
[24] V.S. Escribano, E.F. Lopez, P.S. Huidobro, M. Panizza, C. Resini, J.M. Gallardo-Amores, G. Busca, Solid State Sci. 5 (2003) 1481.
[25] R.S. Mane, Y.H. Hwang, C.D. Lokhande, S.D. Sartale, S.H. Han, Appl. Surf. Sci. 246 (2005) 271.
[26] C.C. Hu, T.W. Tsou, Electrochem. Commun. 4 (2002) 105.
[27] O. Bockman, T. Ostvold, G.A. Voyiatzis, G.N. Papatheodorou, Hydrometallurgy 55 (2000) 93.

Please cite this article in press as: D.P. Dubal, et al., J. Alloys Compd. (2009), doi:10.1016/j.jallcom.2009.03.135

Journal of Alloys and Compounds 497 (2010) 166–170

Contents lists available at ScienceDirect

Journal of Alloys and Compounds

journal homepage: www.elsevier.com/locate/jallcom

Chemical synthesis and characterization of Mn_3O_4 thin films for supercapacitor application

D.P. Dubal, D.S. Dhawale, R.R. Salunkhe, V.J. Fulari, C.D. Lokhande*

Thin Film Physics Laboratory, Department of Physics, Shivaji University, Kolhapur 416004 (MS), India

ARTICLE INFO

Article history:
Received 24 November 2009
Received in revised form 20 February 2010
Accepted 27 February 2010
Available online 6 March 2010

Keywords:
Thin films
Chemical synthesis
X-ray diffraction
Supercapacitor

ABSTRACT

A facile chemical bath deposition (CBD) technique has been used for the preparation of Mn_3O_4 thin films at room temperature. The structural, morphological, optical, wettability and electrical characterizations have been carried out by means of X-ray diffraction (XRD), Scanning electron micrograph (SEM), Fourier transform infrared spectrum (FTIR), optical absorption, contact angle and electrical resistivity studies of deposited films. The XRD pattern shows the tetragonal hausmannite structure of Mn_3O_4 thin film. The Mn_3O_4 formation was also confirmed from FTIR studies. SEM images showed that the substrate surface is uniformly covered with spherical beads-like architecture. The Mn_3O_4 film showed a direct optical band gap with energy 2.51 eV and hydrophilicity with water contact angle of 53°. The room temperature electrical resistivity of Mn_3O_4 thin film was found to be $1.6 \times 10^2\ \Omega$ cm. Mn_3O_4 films when used in supercapacitor exhibited specific capacitance of 284 $F g^{-1}$ in 1 M Na_2SO_4 electrolyte.

© 2010 Elsevier B.V. All rights reserved.

1. Introduction

Nanoparticulate transition-metal oxides can exhibit enhanced optical, magnetic and electrical properties when compared to their bulk counterparts, rendering such nanoparticles of interest for a variety of applications [1]. Nanometer-sized manganese oxide (Mn_3O_4), with notable increased surface area and greatly reduced size, is expected to display better performance in these aspects of application [2]. In recent years, manganese oxides have generated considerable scientific and technological interest because of their electronic and magnetic properties [3,4]. There are four crystalline phases of manganese oxides (MnO, Mn_2O_3, MnO_2, and Mn_3O_4) which have different structural and compositional properties and serve in various applications. Manganese dioxide (MnO_2) can be used as a catalyst in oxidation–reduction reactions, as electrode materials in batteries, and in energy storage devices such as ultracapacitors [5]. The dimanganese trioxide phase (Mn_2O_3) is quite attractive owing to its applications to produce soft magnetic materials [6] to catalyze the removal carbon monoxide and nitrogen oxide from waste gas [7,8] and in the catalytic combustion of methane [9]. The hausmannite phase, Mn_3O_4, has also been shown to possess electrochromic properties [10]. Furthermore, manganese oxide thin films serve as the substrate in the synthesis of magnetic oxide perovskite materials, which have important electrical and magnetic properties such as giant magnetoresistance, and metal-insulator transitions [11,12].

Recently, conducting polymers, activated carbon and transition-metal oxides are widely used for supercapacitor electrode material. Manganese oxide thin films which belongs to third category shows excellent pseudocapacitive behavior with the large specific capacitance as high as 698 $F g^{-1}$. Manganese oxide is a potential supercapacitor material due to its low cost, natural abundance and environmentally friendlier than other transition-metal oxides.

There is an extensive number study on bulk manganese oxide and little on thin manganese oxide films. Mn_3O_4 has been prepared by various methods viz., microwave irradiation [13], hydrothermal or solvothermal routes [14,15], reflux method [16], flash microwave method [17], metal organic chemical vapor deposition (MOCVD) [18], chemical vapor deposition etc. As compared to the other deposition methods, CBD is an attractive one because of its own advantages such as simplicity, reproducibility, non-hazardous, cost effectiveness etc. It is well suited for producing large-area thin films at low temperature and hence avoids oxidation or corrosion of metallic substrate [19].

Here, we present the room temperature synthesis of Mn_3O_4 thin films by simple and inexpensive chemical bath deposition (CBD) method. These films are characterized by XRD, SEM, FTIR, optical, contact angle and electrical resistivity measurement. The supercapacitive behavior of Mn_3O_4 thin films was investigated by cyclic voltammetry in 1 M Na_2SO_4 electrolyte.

2. Experimental details

2.1. Preparation of Mn_3O_4 thin films

Manganese sulphate ($MnSO_4 \cdot H_2O$) and ammonium sulphate ($(NH_4)_2\ SO_4$) were used without further purification. Fresh aqueous solution of 0.2 M $MnSO_4$ and 0.2 M

* Corresponding author. Tel.: +91 231 2609229; fax: +91 231 269233.
E-mail address: l.chandrakant@yahoo.com (C.D. Lokhande).

0925-8388/$ – see front matter © 2010 Elsevier B.V. All rights reserved.
doi:10.1016/j.jallcom.2010.02.182

$(NH_4)_2SO_4$ were prepared in double distilled water immediately before their use. The pH value of solution was adjusted with liquid ammonia to 8. After stirring, this clear and homogeneous solution was used as the precursor solution for the deposition of Mn_3O_4 thin film. Previously cleaned stainless steel substrates were immersed in the bath at room temperature. After about 3 h solution became blurred and within 8 h a brownish precipitate was formed in the bath. During the precipitation, heterogeneous reaction occurred and the deposition of Mn_3O_4 took place on the substrate. The substrates coated with Mn_3O_4 thin films were removed after 48 h from the bath, washed with double distilled water, dried in air and preserved in an airtight container. The as-deposited films were uniform, specularly reflective (mirror like) and adherent to the substrate.

2.2. Characterization techniques

The thickness of the Mn_3O_4 film was measured by weight difference method using sensitive microbalance. Structural identification of Mn_3O_4 films was carried out with an X-ray diffractometer (XRD) [chromium target ($\lambda = 2.2873$ Å)]. The film microstructure was examined with a scanning electron microscope (SEM) (JEOL-JSM 6360). The Fourier transform infrared (FT-IR) spectrum of the sample was collected using PerkinElmer, FT-IR Spectrum one' unit. The optical absorption study was carried out within a wavelength range 350–850 nm using a systronics spectrophotometer-119, with glass substrate as reference. To study the wettability of the film, contact angle measurement was carried out by Rame-hart USA equippement with CCD camera. A two-probe method was used for electrical resistivity measurement. The cyclic voltammetry (C-V) studies were carried out using the 263A EG &G Princeton Applied Research Potentiostat forming an electrochemical cell comprising Mn_3O_4 thin film as a working electrode, platinum as a counter electrode and saturated calomel electrode (SCE) as a reference electrode in 1 M Na_2SO_4 electrolyte.

3. Results and discussion

3.1. Film formation and reaction mechanism

The CBD is based on the formation of solid phase from a solution, which involves two steps as nucleation and particle growth. In nucleation, the heterogeneous reaction at the substrate surface takes place when clusters of the molecules formed undergo rapid decomposition and particles combine to grow up to a certain thickness of the film. Considering the mechanism of formation of Mn_3O_4 films, the possible chemical reaction in the solution can be speculated as follows. At the beginning of reaction, ammonium sulphate in water gets dissociated as follows,

$$(NH_4)_2SO_4 \rightarrow 2NH_4^+ + SO_4^{2-} \quad (1)$$

$$NH_4^+ + OH^- \rightleftarrows NH_3{\cdot}H_2O \quad (2)$$

In the present research work, the low reaction temperature and unstirred chemical bath slowly releases free Mn^{2+} cations from the stable precursor, these Mn^{2+} cations form ammine complexes of $Mn(NH_3)_n^{2+}$ ($n = 1$–4) with NH_3 (aq) in moderately basic media (pH ~ 8). Due to the formation of these complexes, the solution did not contain colloidal manganese hydroxide in the deposition solution. The reaction is as follows,

$$Mn^{2+} + nNH_3 \rightleftarrows Mn(NH_3)_n^{2+} \quad (3)$$

In our experiment, the pH value is ~8 i.e. the solution is alkalescent. On this alkalescent condition the $Mn(NH_3)_n^{2+}$ is unstable and the following reaction occurs as.

$$Mn(NH_3)_n^{2+} \rightleftarrows Mn^{2+} + nNH_3 \quad (4)$$

Finally, oxidation of Mn^{2+} to Mn^{3+} takes place as

$$6Mn^{2+} + O_2 + 12OH^- \rightarrow 2Mn_3O_4 + 6H_2O \quad (5)$$

Thus, nucleation and growth of Mn_3O_4 thin films take place via ion-by-ion mechanism. Many of chemically deposited thin films peel from the substrate at some stage of growth phase before reaching the terminal thickness. In present case, Mn_3O_4 thin films are adhesive to the substrate though the deposition was carried out for prolonged time intervals.

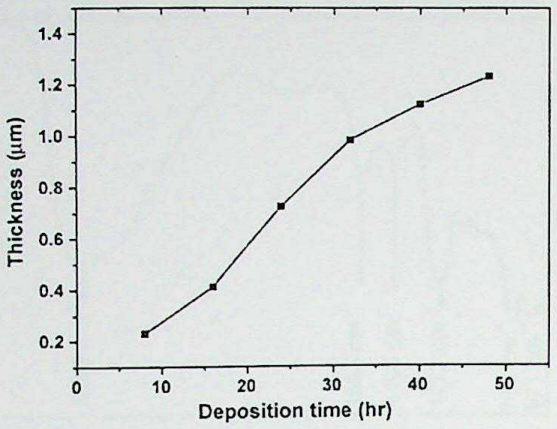


Fig. 1. Variation of film thickness of Mn_3O_4 film with deposition time.

3.2. Thickness measurement

The thickness of Mn_3O_4 thin films on stainless steel substrate was calculated using weight difference method. The density of Mn_3O_4 in bulk form (7.21 g/cm^3) [20] was used for calculation considering hydroxide phase is present in very small extent as compared to Mn_3O_4. In the process of deposition of Mn_3O_4 film by CBD method, the mixture of $MnSO_4$ and $(NH_4)_2SO_4$ was prepared in double distilled water and pH is adjusted to ~8 by using ammonia solution. It is observed that after about 3–4 h precipitation starts and deposition of Mn_3O_4 begins by heterogeneous reaction at substrate surface and the film thickness increases with time. The variation of thickness with time is shown in Fig. 1. The film thickness was found to be increased with deposition time. After about 48 h, almost all precipitate rest down at the bottom of the bath. The terminate thickness obtained was 1.23 μm.

3.3. Structural studies

Fig. 2 (a and b) shows XRD patterns of Mn_3O_4 thin film prepared by CBD method at room temperature and powder collected by scratching the film respectively. The XRD pattern of Mn_3O_4 thin film was of poor crystallinity and no well-defined peaks were observed. Hence for the material confirmation we have scratched the film and XRD was taken of the collected powder. The entire observed diffraction peaks in Fig. 2 match with those of tetragonal

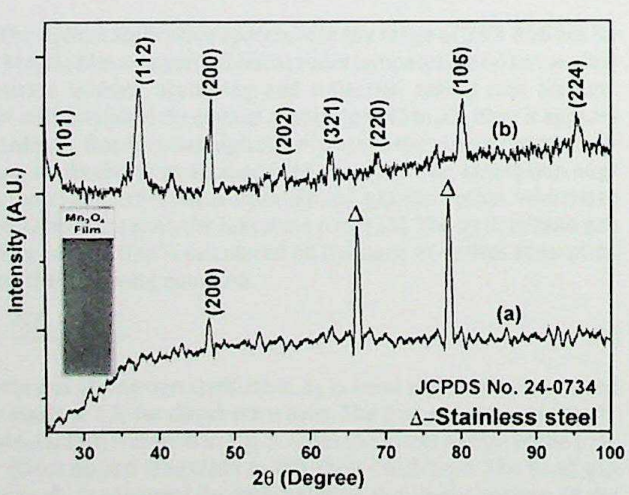


Fig. 2. The X-ray diffraction patterns of (a) Mn_3O_4 thin film on stainless steel substrate and (b) powder collected by scratching the film.

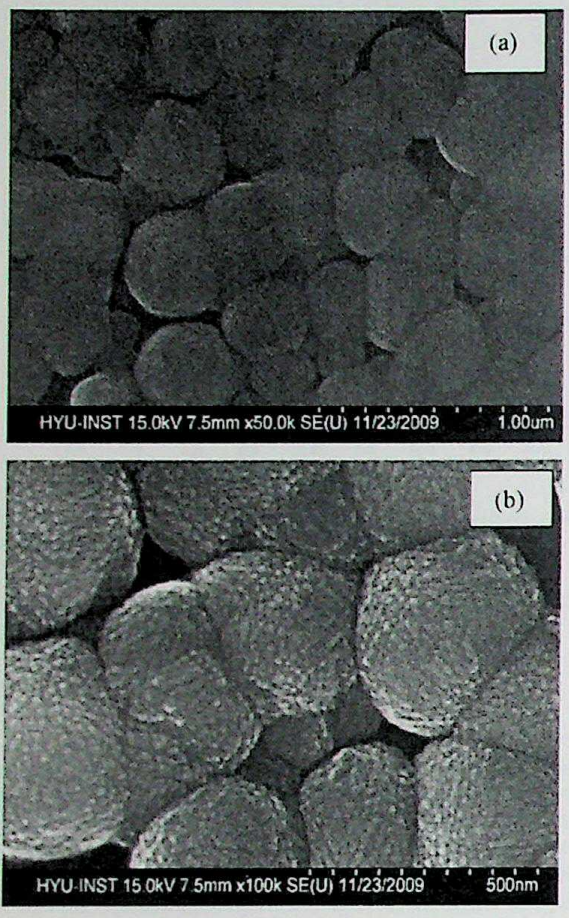


Fig. 3. The SEM images of Mn_3O_4 thin film at (a) ×50 K and (b) ×100 K magnifications.

hausmannite (JCPDS card no. 24-0734) structure. The low intensity of peak confirmed the nanocrystalline nature of hausmannite Mn_3O_4 thin film. The peaks marked by triangles are due to the contribution from stainless steel substrate. Zhang et al. [14] prepared the hausmannite Mn_3O_4 films using low temperature solvothermal method. Apte et al. [13] also reported the preparation of hausmannite Mn_3O_4 powder by microwave irradiation method. The grain size of Mn_3O_4 thin films from XRD pattern was calculated using the Scherer's relation:

$$D = \frac{0.9\lambda}{\beta \cos\theta} \tag{6}$$

where β is the broadening of diffraction line measured at half maximum intensity (radians) and $\lambda = 2.2897$ Å, the wavelength of the CrKα X-ray. The average grain size was found to be 15 nm for (2 0 0) plane. Inset of Fig. 1 shows the photograph of Mn_3O_4 thin film which demonstrates that the film is brownish in color.

3.4. Surface morphology

The SEM micrographs of Mn_3O_4 thin film at different magnifications (×50 and ×100 K) are presented in Fig. 3a and b. The SEM image shows the three-dimensional growth of the spherical beads. These spherical beads are interconnected with each other or aggregated. At high magnification (Fig. 2b) it is seen that the substrate surface was uniformly covered with beads. The boundaries of these beads get diffused. Approximate size of the single bead was about 400 nm. Such kind of morphology provides high surface area which is feasible for supercapacitor application. Shao et al. [21] prepared the Mn_3O_4 by electrospinning technique and reported that film consists of nanofibers of size about 50–200 nm.

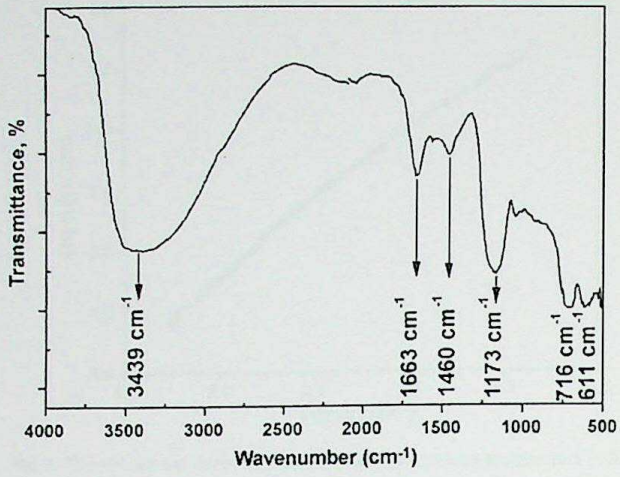


Fig. 4. FT-IR spectrum of Mn_3O_4 thin film.

3.5. FTIR study

Fig. 4 displays the FTIR spectrum of manganese oxide sample. Sample shows several small peaks in the range of 1400–1650 cm^{-1} and a broad peak at about 3439 cm^{-1}. These peaks are associated with the trace of surface-adsorbed moisture in the sample. It can be obviously observed that the stretching peak of –OH groups is much more intensified, because the manganese oxide sample is synthesized in the aqueous solution which may form the tunnel structure during the reaction process, thus a small amount of H_2O molecules is intercalated in the tunnel. Several small absorption peaks at around 1000–1500 cm^{-1} are normally attributed to the bending vibrations of O–H bonds connected with Mn atoms. The absorption peaks situated at 716 and 611 cm^{-1} as shown in Fig. 4, are attributed to the vibrations of Mn–O bonds [21]. The FTIR peaks in the range of 400–1000 cm^{-1} could reveal the existence of octahedra MnO_6 [22]. Thus presence of Mn–O bond and hydroxyl groups was confirmed from the FTIR spectrum of manganese oxide sample.

3.6. Optical studies

The optical absorption spectrum in the range of 350–850 nm for the Mn_3O_4 film was carried out at room temperature on to the glass substrate without scattering and reflection taking into account. Inset of Fig. 5 shows the optical absorption of Mn_3O_4 film; it appears that Mn_3O_4 thin film has high absorbance in the visible region, indicating applicability as an absorbing material. The absorption edge was found at 520 nm due to optical band gap absorption, which is in good agreement with the literature data [23]. The optical band gap (E_g) for Mn_3O_4 film is calculated on the basis of optical absorption using the following equation

$$\alpha = \frac{A(E_g - h\nu)^n}{h\nu} \tag{7}$$

where α is absorption coefficient, E_g is band gap, A is constant and n is equal to 1/2 for direct transition. The plot of $(\alpha h\nu)^2$ versus $h\nu$ of Mn_3O_4 film is shown in Fig. 5. From the linear nature of the plot, the direct optical transition in Mn_3O_4 is confirmed. The band gap energy, E_g is obtained by extrapolating the linear portion of the plot $(\alpha h\nu)^2$ versus $h\nu$ to the energy axis at $\alpha = 0$. From the graph for Mn_3O_4 thin film, band gap value of 2.51 eV is observed. Dubal et al.

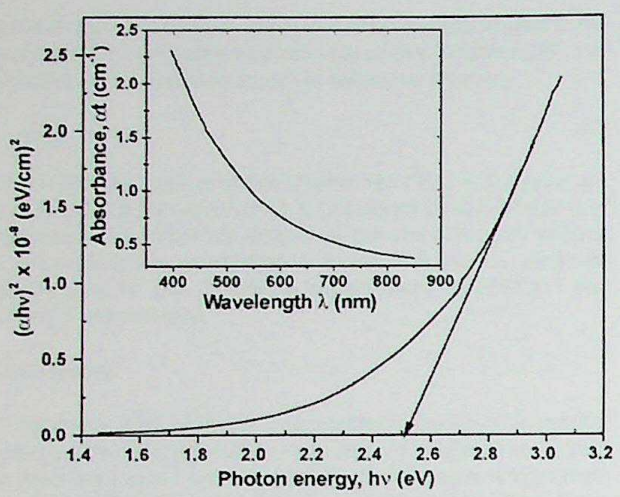


Fig. 5. The plots of $(\alpha h\nu)^2$ vs. $h\nu$ of Mn_3O_4 thin films. Inset shows variation of absorption (αt) with wavelength (λ) of Mn_3O_4 thin film on glass substrate.

found the optical band gap of 2.5 eV for chemical bath deposition of Mn_3O_4 thin films [24].

3.7. Wettability test

The wetting of solid with water, where air is the surrounding medium, is dependent on the relation between the interfacial tensions (water/air, water/solid and solid/air). The ratio between these tensions determines the contact angle (θ) between a water droplet on a given surface. A contact angle of 0° means complete wetting and a contact angle of 180° corresponds to complete non-wetting. The surface wettability involves the interaction between liquid and solid in contact. The wetting behavior is characterized by the value of contact angle, a microscopic parameter. In the present case, the water lies flat with contact angle of 53° on the surface of Mn_3O_4 film instead of forming droplet as seen in Fig. 6. This specific property is attributed to nanocrystalline nature that is expected to possess high surface energy. Nanocrystalline material with hydrophilic nature is prime requirement for supercapacitor electrode material. This is useful for making intimate contact of aqueous electrolyte with film surface in supercapacitor application. A similar type of observation has been reported for electrochemically deposited tin oxide films by Mane et al. [25].

3.8. Electrical resistivity

The D.C two point probe method was employed to understand the variation of electrical resistivity with temperature of Mn_3O_4 thin films. Fig. 7 shows the variation of log (ρ) with reciprocal of temperature (1000/T) on to the glass substrate. From figure it is clearly seen that the resistivity decreases with increase in temperature indicating that normal semiconducting behavior. The room temperature electrical resistivity of Mn_3O_4 thin film is of the order of $1.6 \times 10^2\ \Omega$ cm which is low enough to be a good supercapacitor electrode material. The activation energy was calculated using the relation

$$\rho = \rho_0 \exp\left(\frac{E_a}{KT}\right) \tag{8}$$

where 'ρ' is the resistivity at temperature T, 'ρ_0' is constant; 'K' is Boltzmann constant and 'E_a' is activation energy. The activation energy represents the location of trap levels below conduction band. From Fig. 7 for Mn_3O_4 film there is a single distinct activation energy regime indicating single mechanism involved in the conduction mechanism. The activation energy was 0.23 eV in the temperature regime 300–600 K.

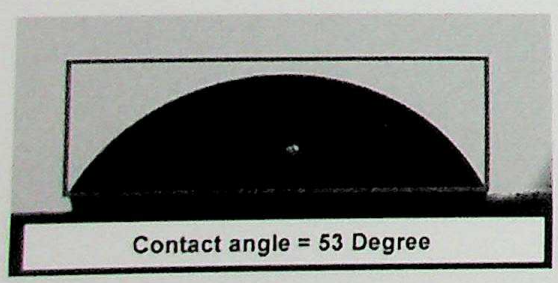


Fig. 6. Contact angle measurement of Mn_3O_4 thin film.

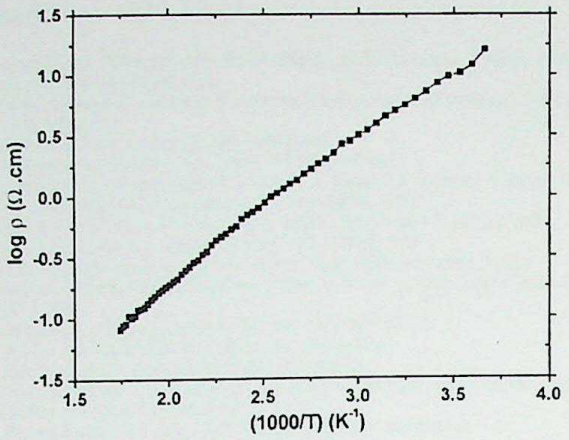


Fig. 7. The variation of dark electrical resistivity (log ρ) with temperature (1000/T) of Mn_3O_4 thin film.

3.9. Supercapacitive studies

The Mn_3O_4 films were used in the electrochemical supercapacitor and its performance was tested using cyclic voltammogramm. The effect of scan rate on the electrochemical capacitor was studied in 1 M Na_2SO_4 in the potential window of −0.1 to 0.9 V. Fig. 8 shows the cyclic voltammogramms with different scan rates. It is found that the current under curve slowly increased with scan rate. This

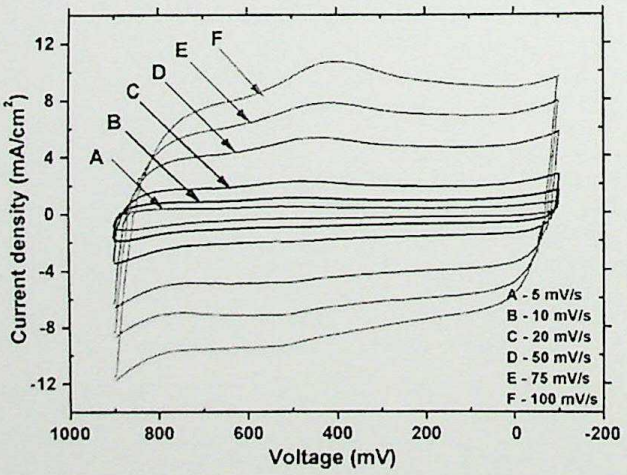


Fig. 8. The Cyclic voltammograms of Mn_3O_4 electrode at different scanning rates (A: 5 mV s^{-1}, B: 10 mV s^{-1}, C: 20 mV s^{-1}, D: 50 mV s^{-1}, E: 75 mV s^{-1}, F: 100 mV s^{-1}) in the 1 M Na_2SO_4 electrolyte in the −0.1 to 0.9 V vs. SCE.

shows that the voltammetric current is directly proportional to the scan rates of CV, indicating an ideally capacitive behavior [26]. The capacitance was calculated using the following relation,

$$C = \frac{I}{dV/dt} \quad (9)$$

where I is the average current in ampere and dV/dt is voltage scanning rate. Interfacial capacitance is calculated by dividing area of manganese oxide electrode dipped in the electrolyte. In present case, area dipped in electrolyte is 1 cm^2. The Mn_3O_4 electrode exhibited specific and interfacial capacitances of 284 $F g^{-1}$ and 0.12 $F cm^{-2}$ respectively.

4. Conclusions

In summary, XRD, FTIR and SEM results evidently indicated that the phase-pure, nanocrystalline, and size-controlled Mn_3O_4 thin films were deposited from aqueous solution at room temperature by a simple CBD method. The Mn_3O_4 film showed direct band gap with energy 2.51 eV and hydrophilic nature with water contact angle of 53°. Thus, the CBD method has proved to be a practical method for the deposition of oxide thin films at low temperatures and may be extended to fabricate other oxide thin films. The specific and interfacial capacitances of Mn_3O_4 electrode were 321 $F g^{-1}$ and 0.14 $F cm^{-2}$, respectively which persuade us to propose Mn_3O_4 as a promising supercapacitor candidate.

Acknowledgement

Authors are grateful to the University Grants Commission (UGC), New Delhi for financial support through the scheme no. 36-207/2008 (SR).

References

[1] Y. Koseoglu, F.F. Yildiz, G.S. Alvarez, M. Toprak, M. Muhammed, B. Aktas, Phys. Status Solidi (b) 42 (2005) 1712.
[2] A. Olmos, R. Redon, G. Gattorno, M. Zamora, F. Leal, A. Osorio, J. Saniger, J. Colloid Sci. 291 (2005) 175.
[3] A. Armstrong, P. Bruce, Nature 381 (1996) 499.
[4] B. Ammundsen, J. Paulsen, Adv. Mater. 13 (2001) 943.
[5] B. Ammundsen, J. Desilvestro, T. Groutso, D. Hassell, J. Metson, E. Regan, R. Steiner, P. Pickering, J. Electrochem. Soc. 147 (2000) 4078.
[6] C. Shao, H. Guan, Y. Liu, X. Li, X. Yang, J. Solid State Chem. 177 (2004) 2628.
[7] Z. Chen, J. Lai, C. Shek, J. Non-Cryst. Solids 352 (2006) 3285.
[8] P. Billik, M. Caplovicava, J. Janata, V. Fajnor, Mater. Lett. 62 (2008) 1052.
[9] K. Ramesh, L. Chen, F. Chen, Z. Zhong, J. Chin, H. Mook, Y. Han, Catal. Commun. 8 (2007) 1421.
[10] T. Maruyama, Y. Osaki, J. Electrochem. Soc 142 (1995) 3137.
[11] C.N.R. Rao, A.K. Cheetham, Adv. Mater. 9 (1997) 1009.
[12] K.J. Kim, Y.R. Park, J. Cryst. Growth 270 (2004) 162.
[13] S.K. Apte, S.D. Naik, R.S. Sonawane, B.B. Kale, N. Pavaskar, A.B. Mandale, B.K. Das, Mater. Res. Bull. 41 (2006) 647.
[14] Y.C. Zhang, T. Qiao, X.Y. Hu, J. Solid State Chem. 177 (2004) 4093.
[15] E. Finocchio, G. Busca, Catal. Today 70 (2001) 213.
[16] M. Anilkumar, V. Ravi, Mater. Res. Bull. 40 (2005) 605.
[17] C.B. Berthelin, D. Stuerga, J. Mater. Sci. 40 (2005) 253.
[18] O.Yu. Gorbenko, I.E. Graboy, V.A. Amelichev, A.A. Bosak, A.R. Kaul, B. Guttler, V.L. Svetchnikov, H.W. Zandbergen, Solid State Commun. 124 (2002) 15.
[19] R.S. Mane, C.D. Lokhande, Mater. Chem. Phys. 65 (2000) 1.
[20] D.R. Lind (Ed.), CRC Handbook of Physics and Chemistry, 79th edition, New York, 1998–1999.
[21] C.M. Julien, M. Massot, C. Poinsignon, Spectrochim. Acta A 60 (2004) 689.
[22] M.V. Ananth, S. Pethkar, K. Dakshinamurthi, J. Power Sources 75 (1998) 278.
[23] V.S. Escribano, E.F. Lopez, P.S. Huidobro, M. Panizza, C. Resini, J. Mallardo-Amores, G. Busca, Solid State Sci. 5 (2003) 1481.
[24] D.P. Dubal, D.S. Dhawale, R.R. Salunkhe, S.M. Pawar, V.J. Fulari, C.D. Lokhande, J. Alloys Compd. 484 (2009) 218.
[25] R.S. Mane, J. Chang, D. Ham, B.N. Pawar, T. Ganesh, B.W. Cho, J.K. Lee, S.H. Han, Curr. Appl. Phys. 9 (2009) 87.
[26] C.C. Hu, T.W. Tsou, Electrochem. Commun. 4 (2002) 105.

Journal of Alloys and Compounds 496 (2010) 370–375

Contents lists available at ScienceDirect

Journal of Alloys and Compounds

journal homepage: www.elsevier.com/locate/jallcom

Conversion of interlocked cube-like Mn_3O_4 into nanoflakes of layered birnessite MnO_2 during supercapacitive studies

D.P. Dubal, D.S. Dhawale, R.R. Salunkhe, C.D. Lokhande*

Thin Film Physics Laboratory, Department of Physics, Shivaji University, Kolhapur, 416 004, MS, India

ARTICLE INFO

Article history:
Received 18 November 2009
Received in revised form 30 January 2010
Accepted 5 February 2010
Available online 12 February 2010

Keywords:
Thin films
Chemical synthesis
Impedance spectroscopy
Surface properties
Energy storage

ABSTRACT

A facile route based on chemical bath deposition (CBD) from urea containing bath has been developed to deposit the interlocked cubes of hausmannite Mn_3O_4 electrode for electrochemical supercapacitor application. The as-prepared Mn_3O_4 electrode showed ideal capacitive behavior during potential cycling within the range of −0.1 to +0.9 V in 1 M Na_2SO_4 electrolyte. The X-ray diffraction (XRD), scanning electron micrograph (SEM) and Raman scattering (RS) and wettability studies during the supercapacitive stability showed that the interlocked cubes of crystalline Mn_3O_4 are electrochemically oxidized to nanoflakes of layered birnessite MnO_2 due to potential cycling. Due to potential cycling the contact angle of Mn_3O_4 thin film changed from hydrophilic to superhydrophilic nature. The effect of electrolyte concentration and scan rate on the specific capacitance of so formed MnO_2 film has been investigated. Impedance analysis shows that birnessite MnO_2 nanoflakes are good conducting than Mn_3O_4 hence can be used over a wide range of applications. It exhibited highest specific capacitance of 223 F g^{-1} in 1 M Na_2SO_4 electrolyte at 5 mV s^{-1} scan rate and 90% stability after 5000 cycles.

© 2010 Elsevier B.V. All rights reserved.

1. Introduction

Manganese oxide is known to be important transition metal oxide and is suitable for a large range of applications, namely, electrochemical materials, high density magnetic storage medium, catalyst, ion-exchange, molecular adsorption, etc. [1–3]. An emerging application of manganese oxide is an electrode material for electrochemical supercapacitors. Nowadays, considerable interest has been generated for developing electrochemical capacitors with high specific power and energy density. Since the pseudocapacitance comes mainly from the reversible redox transition of electroactive materials, transition metal oxides are considered as promising materials for supercapacitors. Hausmannite, Mn_3O_4 is known to have a normal spinel structure with tetragonal distortion elongated along the c-axis due to Jahn-Teller effect on the Mn^{3+} ion. Manganese ions occupy the octahedral B-site (Mn^{3+}) and tetrahedral A-site (Mn^{2+}) corresponding to a normal spinel structure [4].

Since manganese oxide can offer large surface area, electrochemical stability and pseudocapacitive behavior, it may take a significant contribution to the advancement of supercapacitor technology. Manganese oxide thin films show excellent pseudocapacitive behavior with the large specific capacitance as high as 698 F g^{-1} [5]. Nam and Kim [6] reported the specific capacitance of 330 F g^{-1} for Mn_3O_4 films prepared by electrostatic spray deposition method. Chang and Tsai [7] prepared manganese oxide films by anodic deposition and reported the specific capacitance of 240 F g^{-1}.

Manganese oxide has been prepared by various methods viz., microwave irradiation [8], solvothermal routes [9,10], reflux method [11], flash microwave method [12], metal organic chemical vapor deposition (MOCVD) [13], chemical vapor deposition, etc. Preparation of manganese oxide by chemical bath deposition (CBD) method is less investigated [14] and needs further investigation. Since, as compared to other methods, CBD is an attractive one because of its own advantages viz. simplicity, reproducibility, non-hazardous, cost effectiveness, etc. It is well suited for producing large-area thin films at low temperature and hence avoids oxidation of metallic substrate [15].

The interlocked cube-like Mn_3O_4 thin films are electrochemically oxidized to nanoflakes of layered birnessite MnO_2 using potential cycling. The material characteristics and electrochemical properties of these film electrodes are investigated in order to evaluate their potential use as electrode material for supercapacitor. The films are characterized by XRD, SEM and Raman scattering techniques. The effects of electrolyte concentration and scan rate on the specific capacitance of MnO_2 film are investigated.

2. Experimental details

For the deposition of interlocked cube-like Mn_3O_4 thin films, manganese sulphate ($MnSO_4 \cdot H_2O$) and urea ($(NH_2)_2CO$) were used without further purification. Fresh aqueous solutions of manganese sulphate (0.05 M) and urea (1 M) mixed at

* Corresponding author. Tel.: +91 231 2609225; fax: +91 231 2609233.
E-mail address: l_chandrakant@yahoo.com (C.D. Lokhande).

0925-8388/$ – see front matter © 2010 Elsevier B.V. All rights reserved.
doi:10.1016/j.jallcom.2010.02.014

pH ~ 8. The solution was transparent and free from any precipitate. Stainless steel substrates were immersed in the bath at room temperature (300 K) and bath was heated to 353 K. After about 4 h, the solution became blurred and within 12 h, the brown precipitate was formed in the bath. During the precipitation, the heterogeneous reaction occurred and the deposition of uniform and well-adherent Mn_3O_4 took place on stainless steel substrates.

These as-prepared Mn_3O_4 thin films are electrochemically oxidized to layered birnessite MnO_2 by voltammetric cycling in 1 M Na_2SO_4 electrolyte within potential window of −0.1 to +0.9 V.

The structural analysis of both Mn_3O_4 and birnessite MnO_2 was elucidated with Philips diffractometer (PW 3710) using CrKα target of wavelength 2.2897 Å. The microstructure of films was examined with a scanning electron microscope (SEM) (JEOL JSM-6360) which was operated at room temperature. For the surface wettability test, contact angle measurement based on the sessile-drop method consisting of the observation of water drop through a comprising microscope coupled to goniometer was preferred. 2 ml drops were sequentially deposited at different surface positions on the film using a Rame-Hart Inc. model-10 micro-syringe. Contact angles were determined after 30 s of stability period. This time is necessary for focusing and adjusting the crosshairs of the microscope on the drop. Supercapacitive performances of layered birnessite MnO_2 were tested using cyclic voltammetry (CV) in 1 M Na_2SO_4 on the 263A EG & G Princeton Applied Research Potentiostat, forming an electrochemical cell comprising MnO_2 thin film as a working electrode, platinum as a counter electrode and saturated calomel electrode (SCE) as a reference electrode. The effects of electrolyte concentration and scan rate on the supercapacitance have been studied.

3. Results and discussion

3.1. Film formation and reaction mechanism

The bright brown Mn_3O_4 films were uniform, mirror-like, and well adherent to the substrates. When the process is considered in a qualitative way, the film growth is dominated by three periods: (i) nucleation or incubation period, during which the various chemical equilibriums and reactions are established in the bath. The nuclei of the metal oxides formed on the substrate. (ii) The growth period during which the film thickness has an approximately linear variety with deposition time. At the moment, the ionic product (IP) of the solution exceeds the solubility product (SP), and the solution reaches a maximum degree of supersaturation (S = degree of supersaturation = IP/SP), which consequently leads to the growth of nuclei and deposition of the film. (iii) A terminal step where the reagent becomes depleted and the film growth begins to slow and eventually stops.

The primary role of urea is to provide a slow controlled supply of OH^- ions through slow thermal decomposition [16]. This includes hydrolysis of urea and the reaction is as follows,

$$(NH_2)_2CO + H_2O \rightarrow 2NH_3 + CO_2 \quad (1)$$

The low reaction temperature and unstirred chemical bath slowly releases free Mn^{2+} cations from the stable precursor, these Mn^{2+} cations form ammine complexes of $Mn(NH_3)_n^{2+}$ (n = 1–4) with NH_3 (aq) in moderately basic media (pH 8).

$$Mn^{2+} + nNH_3 \rightleftarrows Mn(NH_3)_n^{2+} \quad (2)$$

Finally, oxidation of Mn^{2+} to Mn^{3+} takes place as

$$6Mn^{2+} + O_2 + 12OH^- \rightarrow 2Mn_3O_4 + 6H_2O \quad (3)$$

Thus, the deposition of uniform and well-adherent Mn_3O_4 took place on stainless steel substrate. These Mn_3O_4 thin films are electrochemically oxidized to nanoflakes of layered birnessite MnO_2 using potential cycling. We assume that the electrochemical cycling includes two processes, which can be expressed below as

$$Mn_3O_4(\text{spinel}) \xrightarrow{\text{Potential cycling}} Na_\delta MnO_X \cdot nH_2O(\text{birnessite}) \quad (4)$$

$$Na_\delta MnO_X \cdot nH_2O + yH^+ + zNa^+(y+z)e^- \rightleftarrows Na_{\delta+z}MnO_X \cdot nH_2O \quad (5)$$

The reaction (4) represents the transformation of spinel Mn_3O_4 to layered birnessite. It is a complex and irreversible process. And the reaction (5) is the reversible cycling of the latter material [17].

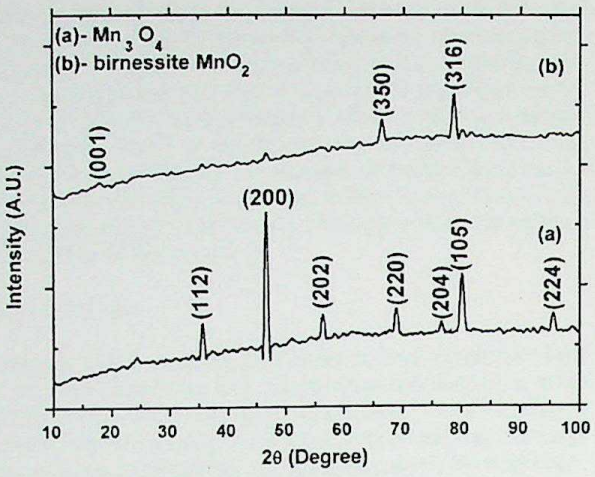


Fig. 1. The X-ray diffraction patterns of (a) Mn_3O_4 and (b) birnessite MnO_2 thin films on stainless steel substrate.

3.2. Structural studies

Fig. 1(a and b) shows XRD patterns of interlocked cube-like Mn_3O_4 and nanoflakes of layered birnessite MnO_2 thin films on to stainless steel substrate. It is evident from Fig. 1(a) the reflections at (1 1 2), (2 0 0), (2 0 2), (2 2 0), (2 0 4), (1 0 5) and (2 2 4) are indexed to the tetragonal hausmannite structure of Mn_3O_4 [JCPDS card no. 24-0734]. Similar type of results also reported by Xu et al. [14] for spinel hausmannite Mn_3O_4 films by CBD method. However, it is clear from Fig. 1(b) that the peaks corresponding to the tetragonal Mn_3O_4 structure in the XRD pattern disappeared. The XRD pattern after cycling for 3000 times shows reflections at (0 0 1), (3 5 0) and (3 1 6) which can be recognized as layered birnessite type MnO_2 [JCPDS card no.23-1046]. This result indicates that the as-prepared Mn_3O_4 film is converted from spinel Mn_3O_4 to layered birnessite MnO_2 by the electrochemical oxidation using potential cycling.

3.3. Surface morphological study

Fig. 2(a and b) shows the SEM images of spinel Mn_3O_4 and layered birnessite MnO_2 films at ×10,000 magnification, respectively. From the SEM image of Fig. 2(a), we observed the 3D growth of interlocked cubes of Mn_3O_4 material. These interlocked cubes seemed to be well covered with substrate surface and act like flat rough surface. Approximate size of these interlocked cubes is between 5 μm and 10 μm. Whereas after 3000 cycles, these interlocked cubes get totally converted into highly porous nanoflakes as seen in Fig. 2(b). Also it is seen that film surface was found to be well covered with nanoflakes. It is observed that these nanoflakes are porous and insert deep inside the surface which provides the large surface area feasible for supercapacitor application. Thus, it is obviously seen that cycling causes the interlocked cubical shaped surface to convert into porous nanoflakes.

3.4. Raman scattering study

The phase identification of the Mn_3O_4 and layered birnessite MnO_2 has been carried out using Raman spectroscopy. Fig. 3(a and b) exhibits the Raman spectra of interlocked cube-like Mn_3O_4 and layered birnessite MnO_2 thin films. In Fig. 3(a) the two peaks observed at 658 cm^{-1} and 318 cm^{-1} are in good agreement with the reported values for Mn_3O_4 [18,19] which further supports the XRD results. The peak at 658 cm^{-1} is characteristic of Mn_3O_4 with

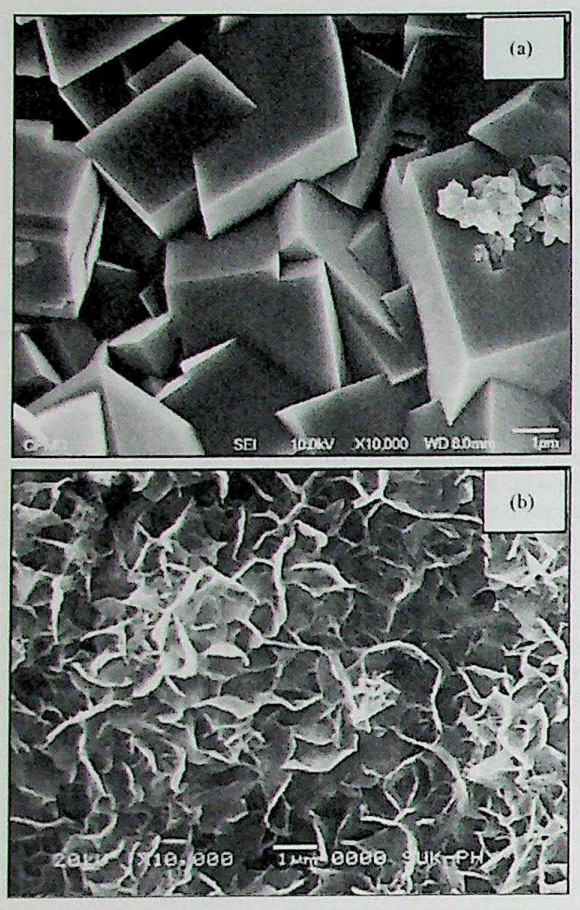


Fig. 2. The SEM images of (a) Mn_3O_4 and (b) birnessite MnO_2 thin films on stainless steel substrate.

spinel structure, similar results from Mn_3O_4 nanowires synthesized via an inverse microemulsion method were also reported [20]. In Fig. 3(b) sharp band at 646 cm^{-1} along with two weak bands at 484 cm^{-1} and 376 cm^{-1} corresponds to the skeletal vibrations. The main contributions are attributed to (Mn–O) symmetric stretching vibrations of MnO_6 octahedron in $MnO_2 \cdot nH_2O$ compounds [21,22]. The lower frequency peaks to the deformation modes of the metal oxygen chain of Mn–O–Mn in the MnO_2 octahedral lattice [23].

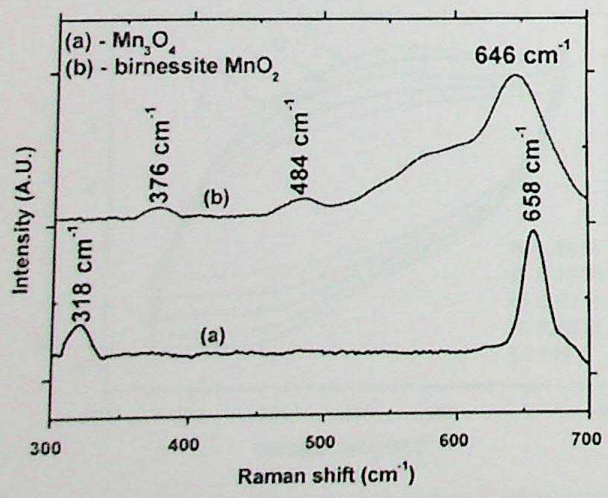


Fig. 3. Raman scattering spectra of (a) Mn_3O_4 and (b) birnessite MnO_2 thin films.

The Raman scattering spectrum of the manganese oxide film after 3000 cycles is very close to that of Na-birnessite, which has a layered structure comprised of edge-sharing MnO_6 octahedra with water molecules and/or Na^+ ions occupying the interlayer region. This suggests that the local structure is close to that of hydrated Na-birnessite [6]. Based on the similarity of the Raman scattering features of Na-birnessite and the manganese oxide film, it can be inferred that Na^+ ions may participate in the electrochemical oxidation during cycling in 1 M Na_2SO_4 within the potential window range of −0.1 to +0.9 V (vs. SCE).

3.5. Wettability test

Wettability test is carried out in order to investigate the interaction between electrolyte and manganese oxide electrode. If the wettability is high, contact angle (θ), will be small and the surface is hydrophilic. On the contrary, if the wettability is low, θ will be large and the surface is hydrophobic. Fig. 4(a and b) shows the water contact angles of manganese oxide films for different cycling stages. For Mn_3O_4 thin film, the water lies slightly flat on interlocked cubes with contact angle 60° as seen in Fig. 4(a). As the number of potential cycles increases the water contact angle of Mn_3O_4 thin films decreases and after 3000 cycles the contact angle of birnessite MnO_2 thin film was found to be 21° (Fig. 4(b)). This indicates that with increasing potential cycling the contact angle decreases and finally film surface becomes superhydrophilic. Superhydrophilicity is attributed to nanocrystalline nature. Nanocrystalline material with superhydrophilic nature is one of the prime requirements for supercapacitor electrode material. The contact angle is expected to depend upon local in homogeneity, chemical composition and the surface morphology of the electrode [24]. From SEM images it is confirmed that due to potential cycling interlocked cubes get converted into highly porous nanoflakes and these nanoflakes are porous and insert deep inside the surface. Thus water placed on the surface of film goes inside the pores of nanoflakes due to which the contact angle decreases with increase in number of cycles. This is useful for making the intimate contact of aqueous electrolyte with manganese oxide thin film (electrode). Thus, Na^+/H^+ ions in aqueous electrolyte can easily intercalate or de-intercalate, i.e. ionic conductivity increases and hence the supercapacitance increases with number of potential cycles.

3.6. Supercapacitive studies

3.6.1. Cyclic voltammetric study

The interlocked Mn_3O_4 electrodes were used in the supercapacitor and their performance was tested using cyclic voltammogram (CV) technique. The CVs were measured at a scan rate of 100 mV s^{-1} in 1 M Na_2SO_4 within a potential window ranging from −0.1 to +0.9 V (vs. SCE). Interestingly, an increase in the anodic and cathodic currents is clearly observed in the CVs over the whole potential range with cycling, particularly up to 500 cycles. This may be due to the structure conversion from spinel Mn_3O_4 to layered birnessite MnO_2. The current response in the CVs becomes stable after about 3000 cycles, and then decreases slightly upon further cycling. The shape of the CVs becomes more rectangular with increasing cycling, and this indicates that the electrochemical reversibility and reactivity of the manganese oxide films increased during cycling in this potential window. The specific capacitance of the film increased rapidly from 11 F g^{-1} to 139 F g^{-1} within the 3000 cycles. This indicates the high cycling stability of the manganese oxide film in 1 M Na_2SO_4 electrolyte.

Recently Dai et al. [17] synthesized pseudocapacitive manganese oxide films by oxidation of Mn_3O_4 thin films deposited by electrostatic spray deposition (ESD). The high temperature (1173 K) treated Mn_3O_4 is transformed from spinel to nanosheet layered

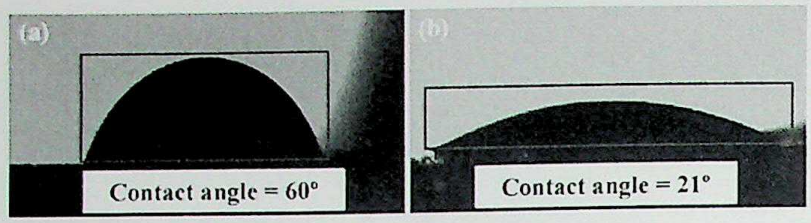


Fig. 4. Contact angles of (a) Mn_3O_4 and (b) birnessite MnO_2 thin films.

birnessite MnO_2 by electrochemical cycling in 0.2 M Na_2SO_4 electrolyte.

3.6.2. Effect of electrolyte concentration

The effect of electrolyte concentration on supercapacitance of layered birnessite MnO_2 was studied at a scan rate of 100 mV s^{-1} within the potential range of −0.1 to +0.9 V. Fig. 5 shows the CV curves of MnO_2 electrode in Na_2SO_4 electrolyte for different concentrations (i.e. from 0.1 M to 1 M). The current under the curve increases as the Na_2SO_4 concentration is increased from 0.1 M to 1 M. Thereafter the current under the curve was fairly constant. With increasing concentration of electrolyte, the supercapacitance is also increased which may be attributed to the increase in number of Na^+ ions in the electrolyte. When a potential difference is applied across the electrode in a solution, the redox reactions occur and the charge is established on the surface of the electrode. Due to electrostatic interactions, ions in the solution migrate to the electrode to counterbalance the charge on the electrode, i.e. the Na^+ ions travel from one electrode to the other through the electrolyte during charging and discharging. The movement of electrons occurs at the same time through the current source or through the external load. Thus, the current–voltage profile of the layered birnessite MnO_2 electrode is symmetric. The average capacitance was calculated using the following relation,

$$C = \frac{I}{dV/dt} \tag{6}$$

where I is average current in ampere, dV/dt is scanning rate in mV s^{-1}. The specific capacitance of the electrode was obtained dividing capacitance by the weight dipped in the electrolyte. The specific and interfacial capacitances were increased with increasing the concentration of Na_2SO_4 electrolyte.

3.6.3. Effect of scan rate

The effect of scan rate on the supercapacitance of layered birnessite MnO_2 electrode was studied in 1 M Na_2SO_4 electrolyte within wide potential window of −0.1 to +0.9 V. Fig. 6 shows the cyclic voltammograms of MnO_2 thin films at different scan rates. The current under the curve increases slowly with the scan rate. This shows that the voltammetric current is directly proportional to the scan rate of CV, indicating an ideally capacitive behavior [25]. The specific capacitance and interfacial capacitance values are decreased from 223 F g^{-1} to 139 F g^{-1}, and 0.16 F cm^{-2} to 0.10 F cm^{-2}, respectively. The maximum specific capacitance of 223 F g^{-1} was obtained at 5 mV s^{-1}. According to Conway and Pell [26] the reason for the decrease in specific capacitance depends on the amount of protons available near the surface of the electrode. When scan rate is large, the number of proton near the surface of electrode are very few during reduction and very large in number during oxidation scan. The decreasing trend of the capacitance suggests that parts of the surface of the electrode are inaccessible at high charging–discharging rates. Hence, the specific capacitance obtained at the slowest scan rates is believed to be closest to that of full utilization of the electrode material [27].

3.6.4. Stability studies

The long-term operation stability of the layered birnessite MnO_2 electrode was investigated in 1 M Na_2SO_4 electrolyte by potential cycling, and the CVs of the 1st, 4000th and 5000th cycles are shown in Fig. 7. Clearly, there are only minor changes between CVs, and the total areas/charges enclosed by the all curves, are very similar to each other, illustrating the stable nature of manganese oxide electrode in the energy storage application. The 90% stability is retained after 5000 cycles in 1 M Na_2SO_4 at 20 mV s^{-1} scan rate. The specific and interfacial capacitance values are decreased by a small amount with the number of cycles due to the loss of active material caused by the dissolution and/or detachment, during the early charging/discharging cycles in the electrolyte. It would con-

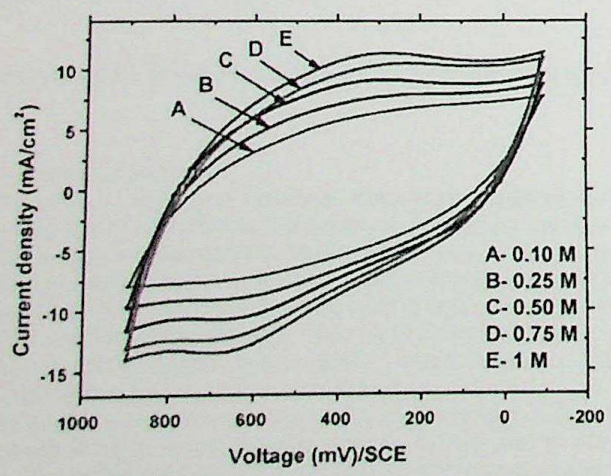


Fig. 5. Cyclic voltammograms of birnessite MnO_2 electrode in different concentrations (A–0.1 M, B–0.25 M, C–0.50 M, D–0.75 M, E–1 M) of Na_2SO_4 electrolyte.

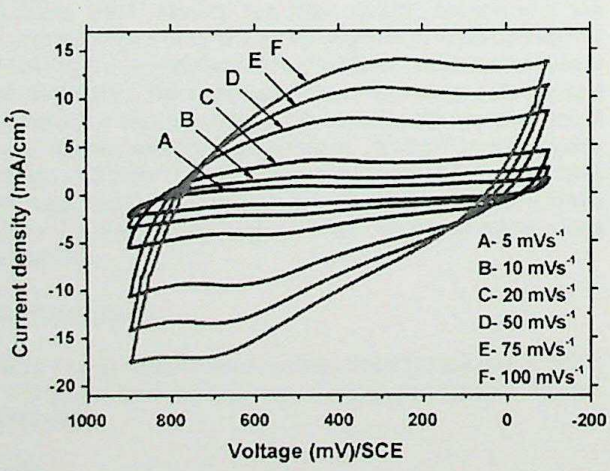


Fig. 6. Cyclic voltammograms of birnessite MnO_2 electrode at different scanning rates in 1 M Na_2SO_4 electrolyte.

Table 1
Electrochemical parameters.

Sample	R_s	R_{CT} (Ω cm^2)	CPE_1 (Ω^{-1} cm^{-2} s)	CPE_2 (Ω^{-1} cm^{-2} s)	n_1	n_2
Birnessite MnO_2	4.6	13.6	0.1263	0.0012	0.812	0.449

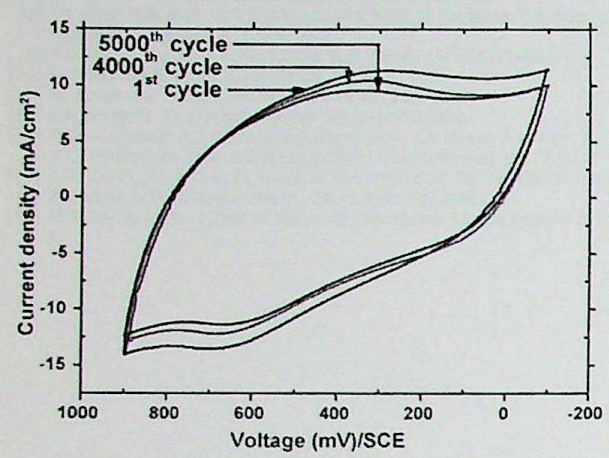


Fig. 7. Cyclic voltammograms of birnessite MnO_2 electrode at different cycles at 20 mV s^{-1} scan rate.

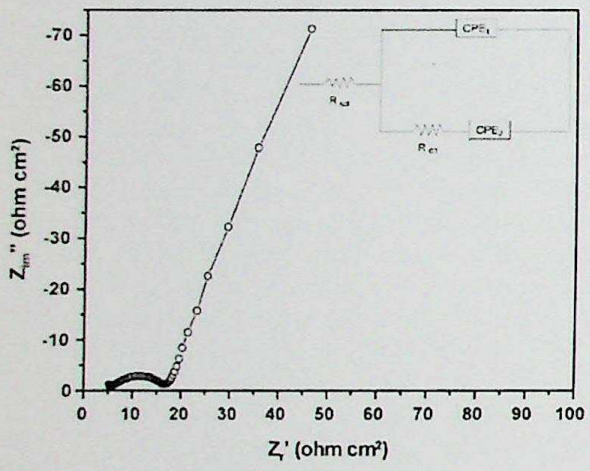


Fig. 8. Impedance spectrum of nanostructured birnessite MnO_2 in 1 M Na_2SO_4 electrolyte at 0.8 V potential. Inset of figure shows equivalent circuit for birnessite MnO_2 thin film.

sequently render the specific capacitance decay of the electrodes [28].

3.6.5. Impedance analysis

Fig. 8 shows the Nyquist spectrum of nanoflakes of birnessite MnO_2 thin film at 0.8 V potential. A distorted semicircle in the high frequency region and a vertically linear spike in the low frequency regime are noticed. The initial non-zero intercept in high frequency regime at Z′ at the beginning of the semicircle is due to the electrical resistance of the electrolyte (R_{ele}). The electrochemical parameters such as charge transfer resistance (R_{ct}), ohmic resistance (R_s) were obtained using equivalent circuit analysis and are summarized in Table 1. Equivalent circuit of the current work is presented in the inset of Fig. 8, which consists with the Nyquist plot. In this model, the double layer capacitor and the warbug impedance for semi-infinite linear diffusion are replaced by two constant phase elements (CPEs). The impedances of two constant phase elements are defined as

$$Z_{CPE1} = [Q(jw)^{n1}]^{-1} \quad (7)$$

and

$$Z_{CPE2} = [Q(jw)^{n2}]^{-1} \quad (8)$$

with $0 < n > 1$. The two constant phase elements CPE_1 and CPE_2 correspond respectively to the double layer capacitance and diffusion process of the cations at the interface. The literature corroborated that CPE may arise from (a) a distribution of the relaxation times as a result of diverse inhomogenities existing at the electrode/electrolyte interface, (b) porosity, (c) nature of the electrode and (d) dynamic disorder associated with diffusion [29]. Further, the constant value of Q is related to both the surface and the electroactive species; n denotes the correction factor due to the roughness of the electrode with values ranging between 0 and 1. A pure capacitance yields $n = 1$, a pure resistance yields $n = 0$, while $n = 0.5$ represents Warburg impedance.

From Table 1, nanoflake birnessite MnO_2 showed low charge transfer resistance ($R_{CT} = 13.6\ \Omega$ cm^2), which attributed to the morphology tuning when interlocked cube-like Mn_3O_4 is changed to nanostructured birnessite MnO_2. It is interesting to note that enhancement of pores in nanoflake network leads to improve the diffusivity of the electrolyte ions in the pore surface, thus reducing the series resistance at MnO_2/electrolyte interfaces. In addition, increased specific surface area in nanoflake MnO_2 sample over bulk interlocked cube-like Mn_3O_4 is responsible for obtaining high capacitance in this system. Further, high pores' nature of nanoflake sample can be confirmed by the observed value of $n_1 \sim 0.8$ in this system, and is consist with observed morphology in Fig. 2(b). This implies that birnessite MnO_2 nanoflakes are highly conducting and can be used over a wide range of potentials.

4. Conclusions

In this report, the interlocked cubes of crystalline Mn_3O_4 thin films are electrochemically oxidized to nanoflakes of layered birnessite MnO_2 using potential cycling. The layered birnessite MnO_2 thin film has been successfully employed as supercapacitor electrode which gives satisfactory performance, high electrochemical reversibility, good stability and high specific capacitance. The water contact angle changed from hydrophilic to superhydrophilic since the surface morphology converted from interlocked cubes to porous nanoflakes. The supercapacitance increases with increase in concentration of electrolyte and decreases with the scan rate. It exhibited highest specific capacitance of 223 F g^{-1} in 1 M Na_2SO_4 electrolyte at 5 mV s^{-1} scan rate and stability of 90% after 5000 cycles. From impedance analysis it is clear that birnessite MnO_2 nanoflakes are good conducting and can be used over a wide range of applications.

Acknowledgement

Authors are grateful to the University Grants Commission (UGC), New Delhi for financial support through the scheme no. 36-207/2008 (SR).

References

[1] M.C. Bernard, H.L. Goff, B.V. Thi, J. Electrochem. Soc. 140 (1993) 3065.

[2] A.H. De Vries, L. Hozoi, R. Broer, Phys. Rev. 66 (2002) 35108.
[3] Y. Yamashita, K. Mukai, J. Yoshinobu, M. Lippmaa, T. Kinoshita, M. Kawasaki, Surf. Sci. 514 (2002) 54.
[4] A.S. Fritsch, J. Sarrias, A. Rousset, G.U. Kulkarni, Mater. Res. Bull. 33 (1998) 1185.
[5] S.C. Pang, M.A. Anderson, T.W. Chapman, J. Electrochem. Soc. 147 (2000) 444.
[6] K.W. Nam, K.B. Kim, J. Electrochem. Soc. 153 (2006) 81.
[7] J.K. Chang, W.T. Tsai, J. Electrochem. Soc. 150 (2003) 1333.
[8] S.K. Apte, S.D. Naik, R.S. Sonawane, B.B. Kale, N. Pavaskar, A.B. Mandale, B.K. Das, Mater. Res. Bull. 41 (2006) 647.
[9] Y.C. Zhang, T. Qiao, X.Y. Hu, J. Solid State Chem. 177 (2004) 4093.
[10] E. Finocchio, G. Busca, Catal. Today 70 (2001) 213.
[11] M. Anilkumar, V. Ravi, Mater. Res. Bull. 40 (2005) 605.
[12] C.B. Berthelin, D. Stuerga, J. Mater. Sci. 40 (2005) 253.
[13] O.Yu. Gorbenko, I.E. Graboy, V.A. Amelichev, A.A. Bosak, A.R. Kaul, B. Guttler, V.L. Svetchnikov, H.W. Zandbergen, Solid State Commun. 124 (2002) 15.
[14] H.Y. Xu, S.L. Xu, X.D. Li, H. Wang, H. Yan, Appl. Surf. Sci. 252 (2006) 4091.
[15] R.S. Mane, C.D. Lokhande, Mater. Chem. Phys. 65 (2000) 1.
[16] M.P. Ana, A.A. Jose, P. Jose, D. Xavier, D. Concepcion, J. Cryst. Growth 285 (2005) 6.
[17] Y. Dai, K. Wang, J. Xie, Appl. Phys. Lett. 90 (2007) 104102.
[18] F. Buciuman, F. Patcas, R. Craciun, D.R.T. Zahn, Phys. Chem. 1 (1999) 185.
[19] F. Kapteijn, A.D. Van Langeveld, J.A. Moulijn, A. Andreini, A.M. Vuurman, A.M. Turek, J.M. Jehng, I.E. Wachs, J. Catal. 150 (1994) 94.
[20] Y. Liu, Z. Liu, G. Wang, Appl. Phys. A 76 (2003) 1117.
[21] C.M. Julien, M. Massot, R.B. Hadjean, S. Franger, S. Bach, J.P.P. Ramos, Solid State Ionics 159 (2003) 345.
[22] B. Banov, A. Momchilov, M. Massot, C.M. Julien, Mater. Sci. Eng. 100 (2003) 87.
[23] C.M. Julien, M. Massot, C. Poinsignon, Spectrochim. Acta 60 (2004) 689.
[24] A.M. More, T.P. Gujar, J.L. Gunjakar, C.D. Lokhande, Joo Oh-Shim, Appl. Surf. Sci. 255 (2008) 2682.
[25] K.H. Chang, C.C. Hu, J. Electrochem. Soc. 151 (2004) A958.
[26] B. Conway, W.G. Pell, 8th International Seminar on Double Layer Capacitors and Similar Energy Storage Devices, Deerfield Beach, FL, 1998.
[27] T.P. Gujar, W. Kim, I. puspitasari, K.D. Jung, O.S. Joo, Int. J. Electrochem. Sci. 22 (2007) 666.
[28] W.C. Chen, C.C. Hu, C.C. Wang, C.K. Min, J. Power Sources 82 (2004) 292.
[29] J. Gamby, P.L. Taberna, P. Simon, J.F. Fauvarque, M. Chesneau, J. Power Sources 101 (2001) 109.

J Mater Sci
DOI 10.1007/s10853-010-5070-7

Synthesis and characterization of photosensitive TiO_2 nanorods by controlled precipitation route

D. P. Dubal · D. S. Dhawale · A. M. More · C. D. Lokhande

Received: 3 September 2010 / Accepted: 9 November 2010
© Springer Science+Business Media, LLC 2010

Abstract Nanocrystalline TiO_2 thin films have been successfully synthesized by controlled precipitation route. These films are further annealed at 623 K for 2 h. The change in structural, morphological, optical, and wettability properties are studied by means of X-ray diffraction (XRD), Fourier transform infrared spectrum (FTIR), scanning electron microscopy (SEM), optical absorption, and contact angle measurement. From the XRD pattern it is clear that the as-grown TiO_2 films are amorphous in nature which becomes polycrystalline after annealing. The FTIR study reveals the formation of TiO_2 compound. Scanning electron micrographs shows that the as-grown TiO_2 film consists of agglomerated nanograins well covered to the substrate surface which gets converted into vertical nanorods after annealing. As-deposited and annealed TiO_2 films showed hydrophilic behavior as water contact angles were 24° and 32°, respectively. The optical absorption study reveals the small red shift due to annealing and attributed to grain size. The annealed TiO_2 film showed conversion efficiency of 0.037% in photoelectrochemical cell with 1 M NaOH electrolyte.

Introduction

Nanometer-sized materials have recently gained a considerable amount of attention of their unique physical and chemical properties, because of their large surface to volume ratio and quantum size effect. The physical and chemical properties of nano TiO_2 are dependent on the size, morphology, and crystal structure. TiO_2 nanomaterials, such as nanoparticles, nanotubes, nanorods, etc., have attracted a great deal of interest because of their unique optical, electronic, and optoelectronic properties and promising applications in solar energy conversion, photocatalysis, sensing, optoelectronic devices, and photochromic devices [1–5]. It is well known that one-dimensional architectures such as nanorods, nanowires, and nanotubes play prominent roles in functional devices due to their dimensionality and quantum confinement phenomena. The physicochemical properties of TiO_2 nanomaterials vary in their size and morphology. TiO_2 has three distinct crystalline phases in nature: brookite, rutile, and anatase, where rutile is the most stable phase and possesses field emission property, and anatase has been widely used in dye-sensitized solar cells and photodegradation due to its high photoactivity.

Zhu et al. [6] found that phase transitions from the titanate nanostructures prepared from $TiOSO_4$ to TiO_2 polymorphs took place readily in wet-chemical processes at temperatures close to ambient. Yu et al. [7] synthesized single-crystalline anatase nanorods via hydrothermal transformation of H-titanate fibers prepared by an alkaline hydrothermal reaction at 200°C. Nian et al. [8] studied the hydrothermal treatment of sodium titanate nanotube suspensions at a pH range from 2.2 to 6.9, and anatase nanorods with an aspect ratio up to 6 and a long axis along the anatase (001) were obtained at a pH slightly less than 7. Wong et al. [9] presented a size- and shape-dependent morphological transformation during the hydrothermal soft chemical transformation of H-titanate nanostructures into their anatase titania counterparts in neutral solution. Performance of TiO_2 for technical applications is strongly influenced by its morphology, crystallite size, crystalline

D. P. Dubal (✉) · D. S. Dhawale · A. M. More · C. D. Lokhande
Department of Physics, Thin Film Physics Laboratory, Shivaji University, Kolhapur 416004, Maharashtra, India
e-mail: dubal_deepak@yahoo.co.in

Journal : Large 10853 | Dispatch : 18-11-2010 | Pages : 6
Article No. : 5070 | LE | TYPESET
MS Code : JMSC19777 | CP | DISK

phase, and impurity type concentration. Porous nanocrystalline TiO_2 have attracted a great interest because; the function and performance of the material are strongly dependent on its morphology. Porosity leads to a comparatively large internal surface area, which are advantageous for many applications where a good accessibility to the film surface becomes necessary. Porous materials as electrode material exhibit good electrochemical performance because these materials possess both a high surface area and pores which are adapted to the size of ions. Accordingly, the advance of synthetic methods, in which the crystalline phase, size, and shape of the TiO_2 nanocrystals can be controlled, is of importance. In recent years, many studies related to the synthesis of anatase TiO_2 have been focused on the control of morphology as well as particle size.

TiO_2 thin films have been prepared by many growth techniques, such as RF-metal–organic chemical vapor deposition (MOCVD) [10], sol–gel process [11], electrodepositon [12], and chemical bath deposition (CBD) method [13]. As compared to the other deposition methods, controlled precipitation route is an attractive one because of its own advantages such as simplicity, reproducibility, non-hazardous, cost effectiveness, etc. It is well suited for producing large-area thin films at low temperature and hence avoids oxidation or corrosion of metallic substrate [14].

In the present work, we demonstrate the formation of controlled TiO_2 nanorods, on indium–tin-oxide (ITO) coated glass substrates in a template-free controlled precipitation route. The TiO_2 nanorods are found to be well aligned and perpendicular to the ITO substrate. X-ray diffraction, Fourier transforms infrared spectroscopy, and scanning electron microscopy techniques are used to elucidate crystal structure, chemical bonding, and surface morphology. In addition, extensive photosensitive studies of these TiO_2 nanorods have been performed.

Experimental

An aqueous solution composed of titanium trichloride, hydrogen peroxide was first prepared. In brief, 0.1 M $TiCl_3$, 15% HCl was added dropwise to a well-stirred hydrogen peroxide (H_2O_2, Molychem, 30 wt%) and water solution. The pH was adjusted between 2.0 and 3.0 using a mixture of 30% liquid ammonium hydroxide with constant stirring. A transparent solution with a reddish-yellow color was obtained after vigorous stirring for 30 min at room temperature. Glass and ITO coated glass substrates were washed with chromic acid and in an ultrasonic bath at room temperature for 30 min. These cleaned substrates were immersed in the above bath and the bath was heated. When the bath attains the temperature of 343 K, the precipitation was started in the bath. During the precipitation, heterogeneous reaction occurs on the substrate and deposition of TiO_2 took place on the substrate. The TiO_2 films were annealed in air at 623 K for 2 h and used for further characterizations.

The thickness of the TiO_2 film was measured by weight difference method using sensitive microbalance. The crystallinity of as-grown and annealed TiO_2 films was analyzed with Philips X-ray diffractometer (Philips PW 3710) with Cr K_α radiation ($\lambda = 2.2896$ Å). The Fourier transform infrared (FTIR) spectrum of the sample was collected using Perkin Elmer, FTIR Spectrum one' unit. Detailed surface images were obtained by means of field emission scanning electron microscope observation on a (FE-SEM, Model: JSM-6160) electron microscope. The optical absorption studies were carried out within the wavelength range 350–850 nm for as-grown and annealed TiO_2 films using Systronics spectrophotometer-119, with glass substrate as reference. In order to study interaction between liquid and thin film surface, contact angle measurement was carried out by Rame-hart, USA equipment with CCD camera. The photoelectrochemical properties of films were investigated using the 263A EG&G Princeton Applied Research Potentiostat forming a three-electrode system comprising TiO_2 film as working electrode, graphite as counter electrode and SCE as reference electrode in 1 M NaOH.

Results and discussion

Film formation and reaction mechanism

In controlled precipitation method, reaction takes place between the dissolve precursors generally in aqueous solution at low temperature. When the solution is saturated, the ionic product of anion and cation is equal to solubility product of metal chalcogenide/oxide and when it exceeds, precipitation occurs and ions combine on the substrate and in the solution to form nuclei. Generally metal ions are complexed and chalcogenide ions are chosen in such a way that reaction take place between slowly released metal ions to form product in powder or thin film form. Depending upon the optimized preparative conditions such as bath temperature, pH of resultant solution, deposition temperature, solution concentration, the film growth can takes place by ion-by-ion condensation on the substrate.

In present investigation, titanium (III) chloride is first hydrolyzed by H_2O in a mixture solution of H_2O and H_2O_2, which then immediately reacted with H_2O_2 to form a peroxotitanate solution. It was found that the initial pH, just after addition of H_2O and H_2O_2 to the titanium (III) trichloride solution, was ~ 1.00; this increased to ~ 3 after complete digestion of hydrolyzed titanium hydroxides. The reaction mechanism is as follows

Journal : Large 10853 | Dispatch : 18-11-2010 | Pages : 6
Article No. : 5070 | LE | TYPESET
MS Code : JMSC19777 | CP | DISK

$$Ti^{3+} + H_2O \rightarrow Ti(OH)^{2+} + H^+ \quad (1)$$

$$2H_2O_2 \rightarrow 2H_2O + O_2 \quad (2)$$

The resulting peroxotitanate solution further dissociates with increase in pH of the solution to form TiO_2 solid film onto the substrate.

$$Ti(OH)^{2+} + O_2 \rightarrow TiO_2 + 2OH^- \quad (3)$$

Thus, the uniform and well-adherent TiO_2 films are deposited on the glass substrate.

Thickness measurement

The thickness of the TiO_2 film was measured by a gravimetric weight difference method in terms of the weight of TiO_2 deposited on the glass substrate per unit area (mg/cm^2), since the accurate measurement of TiO_2 film thickness was not possible due to the rough morphology and porosity of the film [15]. Figure 1 shows the film thickness variation of TiO_2 thin film with deposition time. The rate of increase in the thickness is nonlinear, which has been attributed to the growth by nucleation and coalescence process. More nucleation sites contribute to coagulation during the growing procedure. Furthermore, slight decrease in film thickness observed could be attributed to the formation of outer porous layer and/or the film which may develop stress to cause delamination, resulting in peeling off the film after the film reaches at maximum thickness. The terminated thickness at which the highest amount of TiO_2 deposited on the substrate was 1.29 μm.

Structural study

Figure 2a and b shows typical X-ray diffraction patterns of as-deposited and annealed TiO_2 thin films on glass substrate, respectively. It is evident from XRD patterns that TiO_2 thin films are polycrystalline and has rutile phase.

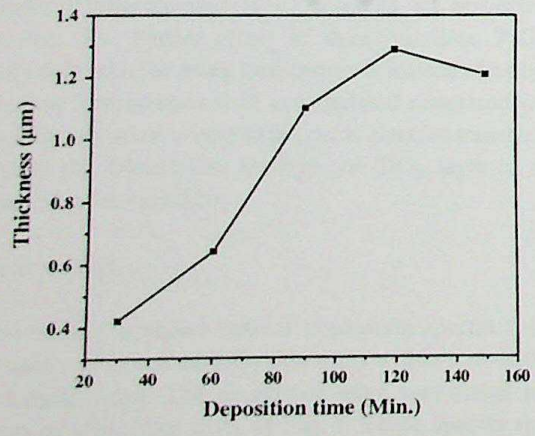


Fig. 1 Variation of TiO_2 film thickness with deposition time

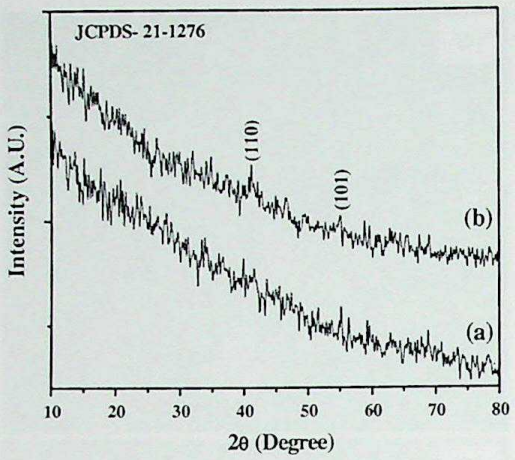


Fig. 2 XRD patterns of (*a*) as-deposited and (*b*) annealed TiO_2 thin films

The XRD pattern indicates the presence of (110), and (101) planes of TiO_2 material which is in good agreement with JCPDS cards no. 21-1276. The XRD pattern of as-deposited films probably means that the film consisted of hydrous TiO_2 colloidal particles with low crystallinity. Intensity of (110) and (101) peaks is increased as an effect of annealing, which attributed to the improvement in crystallinity. The grain size was estimated using Scherrer's formula

$$D = \frac{0.9\lambda}{\beta \cos\theta} \quad (4)$$

where, β is the broadening of diffraction line measured at half maximum intensity (radians) and $\lambda = 2.2897$ Å is the wavelength of the Cr K_α X-ray. The grain size was found to be 56 nm for (110) plane.

FTIR study

Figure 3 shows FTIR spectra of the (a) as-deposited and (b) annealed TiO_2 samples within the wavelength range 400–4000 cm^{-1}. The absorption at 3409 cm^{-1} indicates the presence of hydroxide group [16]. The absorption peak around at 1634 cm^{-1} may be due to the bending vibration of hydroxyl groups of molecular water [17]. The absorption peak at around 1000 cm^{-1} is assigned to characteristic stretching vibration of peroxo groups. The strong absorption peak around at 649 cm^{-1} is associated with the characteristic vibrational mode of anatase TiO_2 [18]. As-deposited TiO_2 showed the higher depth at 3409 cm^{-1} than annealed one, which attributed to removal of hydroxide after heat treatment. Hence, results indicate the presence of Ti–O bond, peroxo groups, and –OH groups for as-deposited film, whereas after annealing the peaks attributed to the peroxo groups and –OH groups were almost disappeared. Less

Journal : Large 10853 Dispatch : 18-11-2010 Pages : 6
Article No. : 5070 LE TYPESET
MS Code : JMSC19777 CP DISK

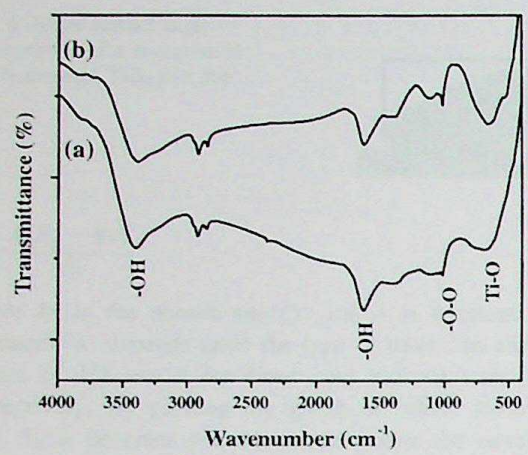


Fig. 3 FTIR spectra of (*a*) as-deposited and (*b*) annealed TiO_2 samples

intense hydroxide and hydroxyl groups from water found in the annealed TiO_2 may be due to the fact that the spectrum was not recorded in situ and some readsorption of water from the ambient atmosphere might have occurred.

Surface morphological study

Figure 4a and b shows the field emission scanning electron micrographs (FE-SEM) of as-deposited and annealed TiO_2 thin films at 50,000× magnification, respectively. From micrograph (Fig. 4a) it is seen that the deposits consists of well defined agglomerated multigrain structure having irregular shapes and sizes due to the low temperature deposition method. The approximate size of this multigrain structure is about 140 nm. Some pores and overgrowth is also seen in the micrographs. Mane et al. [19] prepared TiO_2 by CBD method and reported the formation of spherical, compact, and randomly oriented grains. After annealing this multigrain structure completely gets converted into well-defined conical nanorods. The approximate length and diameter of these nanorods is ~ 110 and 25 nm, respectively (Fig. 4b). The barrier effect of intercrystalline TiO_2 is greatly decreased by using long nanorods instead of a porous TiO_2 thin film composed of accumulated nanosized particles. This might contribute to the easier electron transfer and decrease the Ohmic loss through the TiO_2 layer in dye-sensitized solar cells [20].

Optical studies

Figure 5a and b shows optical absorption spectra for as-deposited and annealed TiO_2 thin films within 350–850 nm wavelength range. The absorption edge was found to be 450 nm as seen from inset of Fig. 5. These spectra reveal that TiO_2 film has low absorbance in the visible region,

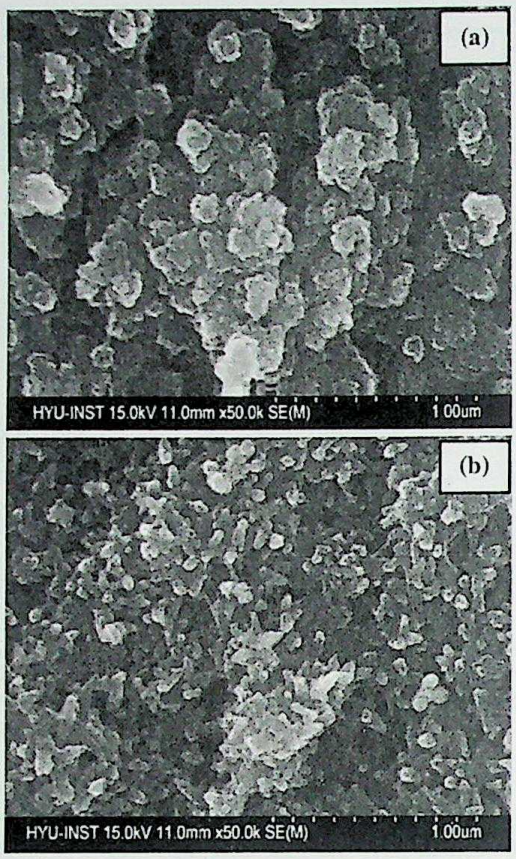


Fig. 4 Scanning electron micrographs of **a** as-deposited and **b** annealed TiO_2 thin films at ×50,000 magnification

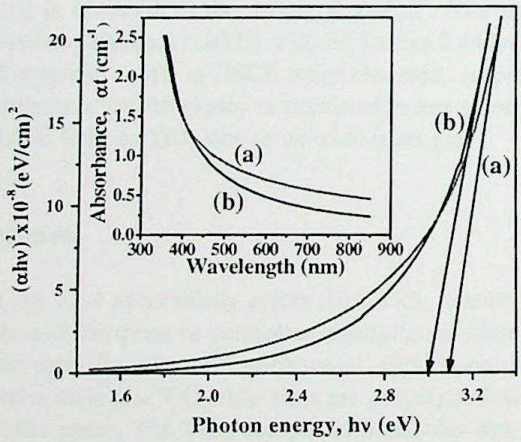


Fig. 5 Plot of $(\alpha h\nu)^2$ vs. photon energy hν of (*a*) as-deposited and (*b*) annealed TiO_2 (*inset* shows variation of absorption (αt) with wavelength (λ) of (*a*) as-deposited and (*b*) annealed TiO_2 on glass substrate)

which is a characteristic of TiO_2. The optical band gap (E_g) for as-deposited and annealed TiO_2 film is calculated on the basis of optical absorption using the following equation,

Journal : Large 10853 | Dispatch : 18-11-2010 | Pages : 6
Article No. : 5070 | LE | TYPESET
MS Code : JMSC19777 | CP | DISK

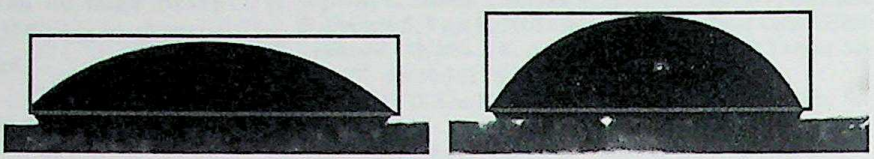


Fig. 6 Water contact angle measurement of **a** as-deposited and **b** annealed TiO_2 thin film

$$\alpha = \frac{A(E_g - h\nu)^n}{h\nu}$$

where $h\nu$ is the photon energy, and A is constant. The exponent 'n' depends upon the type of transition and has values of 1/2 and 2 for direct and indirect transitions, respectively. By plotting the graph of $(\alpha h\nu)^2$ versus $h\nu$ (Fig. 5), it becomes possible to determine the nature of transition involved. The extrapolation of straight line portions of the plot ($h\nu$ greater than E_g) to the zero absorption coefficient gives measurement of energy gap. Both plots show a linear dependence at $h\nu$ greater than E_g, therefore extrapolation of the straight line portions of the curves to the zero absorption coefficient gives band gap of 3.1 and 3.0 eV for as-deposited and annealed TiO_2 films, respectively. Due to the improved grain size of annealed, the absorption edge showed red-shift up to some extent. The widened band gap of the TiO_2 films is attributed to the contribution of quantum size effect [21].

Wettability test

Controlling and/or modifying the surface wettability are important, which involves the interaction between a liquid and a solid in contact. Measurement of surface water contact angle is inversely proportional to the wettability and can be determined by Young's relation [22]. Figure 6 shows the water contact measurements for (a) as-deposited, and (b) annealed TiO_2 thin films. Interestingly, as-deposited TiO_2 exhibits hydrophilic behavior (24°), as water contact angle is less than 90°. The shape of water droplet on the film is shown in Fig. 6a. Further, for annealed films, the water contact angle slightly increases to 32°. The droplet shape on the surface of annealed TiO_2 film was more spherical (Fig. 6b). Increase in water contact angle after annealing attributed to (a) non-spherical nature of the grains and (b) topographical change in structure. Due to the conversion from spherical nanograins to nanorods after annealing prevents the water from adhering to the film results into increase in water contact angle. Similar type of result has been reported by More et al. [23].

Photovoltaic response

A photoelectrochemical cell (PEC) is based on the junction between semiconductor and an electrolyte. The current–voltage (I–V) characteristic of a typical ITO/TiO_2/1 M NaOH/graphite cell in the dark and under illumination (50 mW/cm^2) is shown in Fig. 7. In the dark, the nonlinear nature of I–V curve predicts that the TiO_2 makes rectification contact with the electrolyte. Inset of Fig. 7 shows the photosensitivity under chopped light conditions carried out to study the response of the TiO_2 films. The photocurrent is obtained in the order of μA/cm^2. The photoconversion efficiency 0.037% with fill factors 0.44 and flat band potential −400 mV/SCE were observed. In present investigation, low efficiency is attributed to less absorption of visible light in TiO_2 due to its wide band gap.

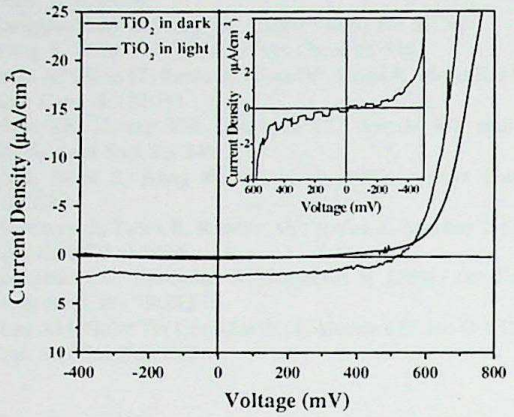


Fig. 7 I–V characteristics of annealed TiO_2 film under illumination of white light (50 mW/cm^2). *Inset* shows the I–V characteristic under chopped light

Conclusion

Here, we have successfully synthesized TiO_2 nanorods by simple and inexpensive controlled precipitation route and further used for photoelectrochemical application. XRD pattern reveals that TiO_2 thin films are polycrystalline and has rutile phase. The TiO_2 compound formation was confirmed from FTIR study. Scanning electron micrographs reveals that the multigrain structure of as-deposited TiO_2 thin films completely gets converted into well-defined conical nanorods due to annealing. The optical absorption study reveals the small red shift due to annealing and attributed to grain size. Both the as-grown and annealed TiO_2 thin films are hydrophilic in nature as water contact angle is less than 90°. The strong influence of this electrode in spite of its wide band gap and substrate resistance on

Journal : Large 10853 Dispatch : 18-11-2010 Pages : 6
Article No. : 5070 LE TYPESET
MS Code : JMSC19777 CP DISK

photoelectrochemical performance with fill factor (0.44) and device conversion efficiency (0.037%) can motivate to check its feasibility in DSSC's devices.

Acknowledgement Authors are grateful to the University Grants Commission (UGC), New Delhi for financial support through the scheme no. 36-207/2008 (SR).

References

1. Fujishima A, Honda K (1972) Nature 238:37
2. Chen X, Mao SS (2007) Chem Rev 107:2891
3. Bavykin DV, Friedrich JM, Walsh FC (2006) Adv Mater 18:2807
4. Yeredla RR, Xu H (2008) Nanotechnology 19:055706
5. Wang G, Wang Q, Lu W, Li J (2006) J Phys Chem B 110:22029
6. Zhu HY, Lan Y, Gao XP, Ringer SP, Zheng ZF, Song DY, Zhao JC (2005) J Am Chem Soc 127:6730
7. Yu Y, Xu D (2007) Appl Catal B Environ 73:166
8. Nian JN, Teng H (2006) J Phys Chem B 110:4193
9. Mao Y, Wong SS (2006) J Am Chem Soc 128:8217
10. Anpo M, Takeuchi M (2003) J Catal 216:505
11. Espinosa R, Zumeta I, Santana JL, Marinez-Luzardo F, Gonzalez B, Docteur S, Vigil E (2005) Solar Eng Mater Solid Cells 85:359
12. Lokhande CD, Min S-K, Jung K-D, Joo O-S (2004) J Mater Sci 39:6607. doi:10.1023/B:JMSC.0000044903.93296.a4
13. Lokhande CD, Lee E-H, Jung K-D, Joo O-S (2004) J Mater Sci Lett 39:2915
14. Mane RS, Lokhande CD (2000) Mater Chem Phys 65:1
15. Park BO, Lokhande CD, Park HS, Jung KD, Joo OS (2004) Mater Chem Phys 87:59
16. Karuppuchamy S, Jeong JM (2006) J Oleo Sci 55:263
17. Wang Y, Herron N (1991) J Phys Chem 95:525
18. Josea AN, Juan JT, Pablo D, Javier RP, Diana R, Marta IL (1999) Appl Catal A 178:191
19. Mane RS, Hwang YH, Lokhande CD, Sartale SD, Han S-H (2005) Appl Surf Sci 246:271
20. Jiu J, Isoda S, Wang F, Adachi M (2006) J Phys Chem B 110:2087
21. Monticone S, Tufeu R, Kanaev AV, Scolan E, Sanchez C (2000) Appl Surf Sci 162:565
22. Lokhande CD, Barkschat A, Tributsch H (2003) Sol Energy Mater Sol Cells 79:293
23. More AM, Gujar TP, Gunjakar JL, Lokhande CD, Joo O-S (2008) Appl Surf Sci 255:2682

UNCORRECTED PROOF

Journal : Large 10853 | Dispatch : 18-11-2010 | Pages : 6
Article No. : 5070 | LE | TYPESET
MS Code : JMSC19777 | CP | DISK

Invertis Journal of Renewable Energy, Vol. 1, No. 3, 2011 ; pp.142-149

Photosensitive Cu_2ZnSnS_4 (CZTS) Thin Film Grown at Room Temperature by Novel Chemical Method

C.D. LOKHANDE[1]*, N.M. SHINDE[1], J.H. KIM[2] and J.H. MOON[2]
[1]*Thin Film Physics Laboratory, Department of Physics, Shivaji University Kolhapur - 416 004 (Maharashtra)*
[2]*Department of Materials Science and Engineering, Chonnam National University, South Korea*
**E-mail: 1_chandrakant@yahoo.com*

Abstract

The current paper incorporates a novel chemical deposition method to grown Cu_2ZnSnS_4 (CZTS) thin film at room temperature on glass and FTO substrates. In order to improve the properties, CZTS thin films are annealed at 673 K for 3 h in air and the changes in structural, morphological and optical properties are studied by means of X-ray diffraction (XRD), Fourier transform infrared (FT-IR), Raman spectroscopy, Scanning electron microscopy (SEM) and UV-vis spectroscopy techniques. The photo activity of CZTS is tested by forming photoelectrochemical cell with polyiodide electrolyte. The experimental results showed that the chemicaly deposited photosensitive CZTS thin films can be a potential candidate in solar energy conversion.

Key words : Cu_2ZnSnS_4, chemical synthesis, characterization, photoresponce, photoelectrochemical cell.

1. Introduction

$CuInGaSe_2$ (CIGS) based thin film solar cells showed highest conversion efficiency of 19.9% [1]. The direct band gap (1.45 eV) of CZTS thin film is close to optimum value for PV applications. High optical absorption coefficient (10^4 cm^{-1}) and p-type conductivity are a promising material for absorber layer in thin film solar cells [2]. The CZTS thin films have been prepared by several experimental techniques such as E-Beam evaporation[3], thermal evaporation [4], sputtering and sequential evaporation [5], co-evaporation [6], multistage evaporation [7] and RF sputtered precursors[8]. Also chemical deposition methods like photo-chemical deposition [9], ionic liquids [10], electrochemical [11] and spray pyrolysis [1] have been used.

In present investigation, we report a novel chemical deposition method succesive ionic layer adsorption and reaction (SILAR) method for the deposition of CZTS thin films. This is one of the chemical method for making uniform and large area thin films, which is based on immersion of the substrate into separately placed cations and anions. The advantages of this method are described in the review by Pathan and Lokhande [12]. Here, for the ?rst time, we report synthesis of CZTS thin films using SILAR method at room temperature. As-deposited films were annealed at 673 K for 3 h to study the annealing effect on properties of CZTS films. The effect of annealing treatment on the structural, morphological, electrical, wettability and optical properties of the CZTS thin films have been investigated. Also the photoactivity of the CZTS film is tested with polyiodide electrolyte.

2. Experimental Details

2.1 Preparation of CZTS Thin Films

A novel chemical SILAR method is used for the deposition of CZTS thin films. It is based on successive immersion of the substrate into separately placed cation and anion precursor solutions and rinsing between every immersion with double distilled water to avoid precipitation. Four beakers system is used for the deposition of CZTS thin films. The 1st beaker contained mixed cationic precursor solutions of 0.1 M $CuSO_4$, 0.05 M $ZnSO_4$ and 0.05 M $SnSO_4$ in 1:1:1 ratio.

The double distilled water was placed in the 2nd beaker to remove the loosely adsorbed cations from the substrate. The 0.2 M thioacetamide (C_2H_5NS) solution in 3rd beaker was used as the anionic precursor. The 4th beaker contained double distilled water to remove the powdery deposit from the substrate. The pH values of cationic and anionic precursors were ~3 and ~6, respectively. All beakers were kept at room temperature (300 K). The schematic diagram for the deposition of CZTS thin films by SILAR method is shown in Fig.1. In order to obtain CZTS films, we used different concentrations of cationic and anionic precursors. Among different concentrations, the films obtained at 0.1 M $CuSO_4$, 0.05 M $ZnSO_4$, 0.05 M $SnSO_4$ in 1:1:1 ratio and 0.2 M C_2H_5NS solutions uniform and well adherent. The well cleaned glass and FTO substrates were dipped in 1st beaker containing cationic precursor, where Cu^+, Zn^{2+} and Sn^{4+} ions get adsorbed onto substrate surface. After immersion of the substrate into cationic precursor, substrates were rinsed with double distilled water (DDW) placed in 2nd beaker to remove loosely bounded cations. Then the substrates were immersed in 3rd beaker, where S^{2-} ions react with pre-adsorbed Cu^{2+}, Zn^{2+} and Sn^{4+} cations to form CZTS layer on the substrate. The substrate as again rinsed in double distilled water kept in the 4th beaker to remove unreacted S^{2-} ions and powdery and nonadherent CZTS material from substrate. This completed one cycle for the deposition of CZTS film. By repeating such cycle many times, the CZTS film thickness was increased. The adsorption time in cationic and reaction time in anionic solution are optimized to be 15s each. These films were used for furthrer characterization.

3. Results and Discussion

3.1 Film Formation

Thin CZTS films were obtained by immersing substrate into separately placed cationic and anionic precursors along with rinsing between every immersion with ion exchanged water. The growth kinetics of a thin film deposition process is ion-by-ion growth mechanism, which involves the ion-by-ion deposition at nucleation sites on the immersed surfaces. According to Lundin and Kitaev, nucleation takes place by adsorption of the colloidal ions and growth takes place as a result of surface coagulation of these ions, giving thin and adherent films [13]. The possible reaction mechanism for the formation of CZTS thin film is as follows,

The 1st beaker contain Cu^{2+}, Zn^{2+} and Sn^{4+} cations. When substrate is immersed in 1st beaker, Cu+, Zn^{2+} and Sn^{4+} ions are adsorbed on the substrate. Beaker 3 contains thioacetamide solution which gives sulphide ions (S^{2-}) and reaction follows,

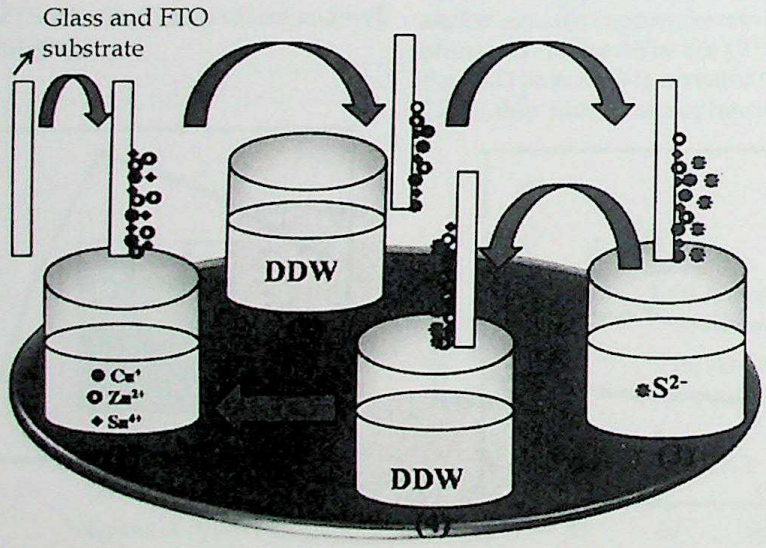


Fig. 1. The schematic diagram of SILAR method for the deposition of CZTS thin films, beaker 1 contains cationic precursors of Cu^{2+}, Zn^{+2} and Sn^{+4}, beaker 2 and 4 contain DDW and beaker 3 contains anionic precursor of C_2H_5NS

$$CH_3 - \overset{S}{\overset{\|}{C}} - NH_2 \rightleftarrows CH_3 - \overset{SH}{\overset{|}{C}} = NH \quad (1)$$

In acidic medium protonation gives

$$CH_3 - \overset{SH}{\overset{|}{C}} = NH + H^+ \rightarrow CH_3 - \overset{H\text{-}S^+\text{-}H}{\overset{|}{C}} = NH \quad (2)$$

The intermediate compound formed dissociates to give H_2S as

$$CH_3 - \overset{H\text{-}S^+\text{-}H}{\overset{|}{C}} = NH \rightarrow CH_3 - C = NH^+ + H_2S \quad (3)$$

In aqueous medium H_2S dissociates to give

$$H_2S \rightarrow H^+ + SH^- \quad (4)$$

$$SH^- \rightarrow H^+ + S^{2-} \quad (5)$$

($K = 1.2 \times 10^{-15}$) where K is dissociation constant of H_2S in aqueous medium

Finally, the following reaction takes place between pre-adsorbed Cu^+, Zn^{2+} and Sn^{4+} cations and S^{2-} anion on to the substrate to form Cu_2ZnSnS_4 thin film.

$$2Cu^{2+} + Zn^{2+} + Sn^{4+} + 4S^{2-} Cu_2ZnSnS_4 \quad (6)$$

The prepared CZTS thin films are uniform and well adherent to the substrate.

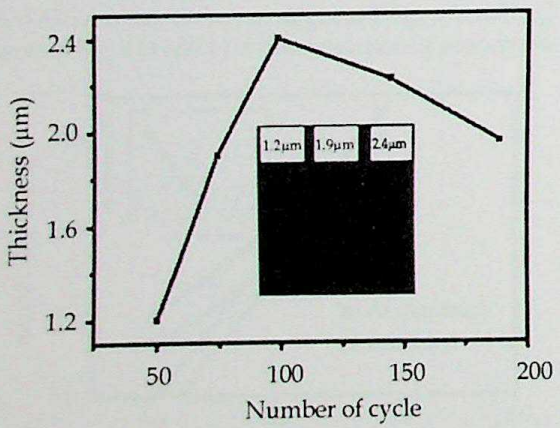


Fig. 2. The variation of CZTS film thickness with deposition cycles. Inset of fig. 2 shows the photograph of CZTS thin films for 25 (1.2 μm), 50 (1.9 μm) and 150 (2.4 μm) cycles

3.2 *Thickness Measurement*

Figure 2 shows the film thickness variation with number of deposition cycles. The rate of increase in the thickness is nonlinear, which has been attributed to the growth by nucleation and coalescence process. More nucleation sites contribute to coagulation during the growth procedure. Furthermore, slight decrease in film thickness observed after 150 cycle may be due to formation of outer porous layer and/or the film which may develop stress to cause delamination, resulting in peeling off the film after the film reaches at maximum thickness [14]. The terminated thickness, at which the highest amount of CZTS is deposited on the substrate, is 2.4 μm after 130 cycles. Inset Fig. 2 shows photograph of CZTS thin film deposited over ~21 cm^2 area confirming the feasibility of SILAR method for large area deposition.

3.3 *Structural Studies*

Figure 3 shows XRD patterns of (a) as deposited and (b) annealed CZTS thin films respectively The X-ray diffractogram of as-deposited film reveals the amorphous nature of the CZTS thin film, which is probably means that the film consisted of hydrous CZTS colloidal particles with low crystallinity. Intensity of (002), (101), (110) and (105) peak is increased as an effect of heat treatment, which attributed to the improvement in crystallinity. Kesterite phase was confirmed by the XRD pattern. Hence from the XRD pattern, it is revealed that the as deposited CZTS thin film is amorphous whereas improved

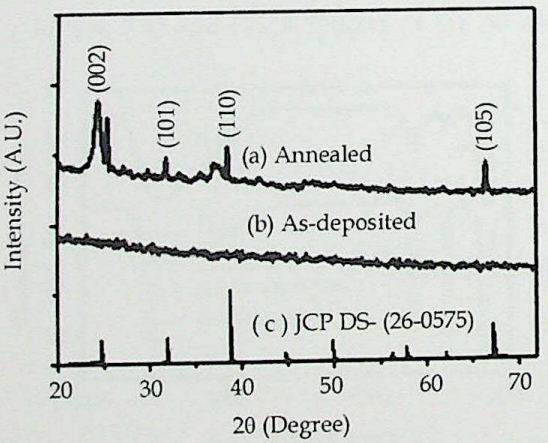


Fig. 3. The XRD patterns of (a) as deposited, (b) annealed and (c) standard JCPDS (26-0575) diffrattogram of CZTS thin films

crystalanity of the film is obsereved after air annealing. Well defined and distinct peaks along (002), (101), (110) and (105) planes are observed. The observed 'd' values are in good agreement with standard 'd' values (JCPDS card no. 26-0575). The standard XRD pattern of CZTS thin films shown in Fig. 3(c) for comparison, has a tetragonal unite cell confirmed the formation of polycrystalline CZTS films with kesterite crystal structure. From the XRD pattern Fig. 3 revealed formation of CZTS thin film with a preferential growth orientations of (002), (101), (110) and (105). A number of research groups studying CZTS thin films also obtained similar XRD pattern Fernandes et al [15] prepared dc magnetron sputtering based method to grow high quality Cu_2ZnSnS_4 (CZTS) thin films. The increase in peak intensity after air annealing may be due to the improvement in the crystallinity. The grain size of CZTS thin films from XRD pattern was calculated using the Scherer's relation:

$$D = \frac{0.9\lambda}{\beta \cos\theta} \tag{7}$$

where, β is the broadening of diffraction line measured at half maximum intensity (radians) and λ = 2.2897Å is the wavelength of the CrKα X-ray. The grain size was found to be 78 nm for (002) plane.

3.4 Optical Absorption Study

The optical absorption of as deposited and annealed CZTS thin films in the wavelength range 350-850 nm has been investigated [Fig. 4 (a and b)]. Inset of Fig. 4 (a and b) shows variation of absorbance (αt) of as deposited and annealed CZTS film with wavelength (λ). These spectra revealed that as deposited and annealed CZTS thin films have high absorbance of light in the visible region, indicating applicability as an absorbing material. The optical band gap energy is estimated by using the following equation

$$\alpha = \frac{A(Eg - h\nu)^n}{h\nu} \tag{8}$$

where α is absorption coefficient, E_g is band gap, A is constant and n is equal to 1/2 for direct transition. Fig. 4 (a and b) shows the variation of $(\alpha h\nu)^2$ ν_s. hν, which is a straight line in the domain of higher energies, indicating a direct optical transition. Extrapolation of these curves to zero absorption coefficients (α =0) gave the optical energy gap as 1.5 eV for as-deposited and 1.6 eV for annealed CZTS thin films. The decrease in band gap after annealing is a consequence of phase change from amorphous to polycrystalline nature. The decrement in the band gap energies from 1.6 to 1.5 eV after annealing has been observed which is in agreement with the earlier reported E_g value of CZTS thin film in the N_2+H_2S atmosphere at 673 K, reported by Ito and Nakazawa [16]. The band gap of the film is quite close to the optimum band gap required for a solar cell, indicates that CZTS is very promising material for thin film solar cell application.

3.5 FT-IR Study

Figure 5 shows FT-IR spectra of the (a) as-

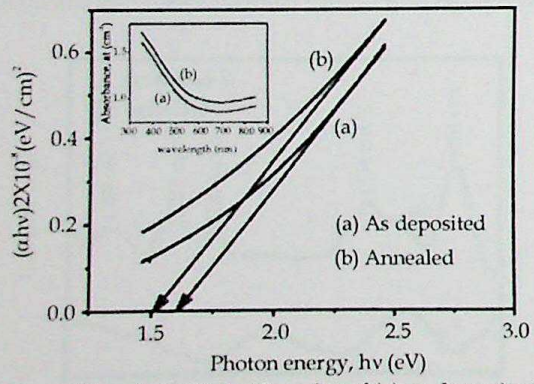


Fig. 4. The plot of (αhν)2 vs. hν of (a) as deposited and (b) annealed CZTS thin films. Inset shows variation of absorption (αt) with wavelength (λ) of CZTS thin films

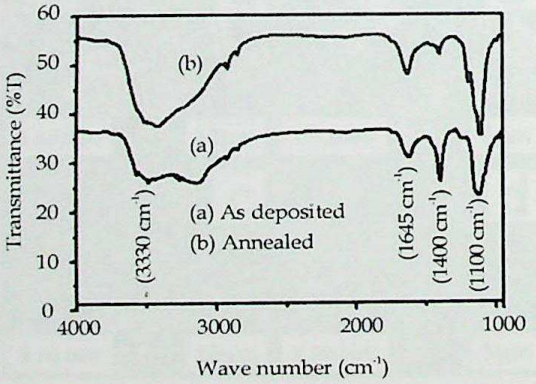


Fig. 5. The room temperature FT-Raman spectra of (a) as deposited and (b) annealed CZTS thin films on glass substrate

deposited and (b) annealed CZTS samples. From these spectra, it can be apparently observed that strong band associated with antisymmetric and symmetric vibration modes of -N-H are observed at 3300 cm^{-1} [16]. The absorption peak observed at 1645 cm^{-1}, 1400 cm^{-1}, 1100 cm^{-1} are assigned to NH_2 bending, C=S stretching vibration and NH_2 rocking vibration deformation, respectively and are in good agreement with peek observed in nanocrystaline CZTS thin film prepared by Zaberca et al [17]. This con?rms the formation of CZTS compound.

3.6 *FT-Raman Study*

The FT-Raman spectra recorded over 250-400 cm^{-1} of as-deposited and annealed CZTS thin films are shown in Fig. 6 (a and b). Raman spectra confirmed existence of the kesterite phase. Well defined peaks at 258, 283, 288, 334 and 361 cm^{-1} are in good agreement with previously reported Raman spectrum of CZTS thin films [18-19]. These peaks confirm the formation of kesterite structure of CZTS stretching mode. In addition, it is evident that there are no additional peaks related to the presence of other compounds, which means that the single phase CZTS films are obtained [20].

3.7 *Surface Morphological Analysis*

The morphology was analysed using a SEM and the results are presented in Figs. 7. Figure 7 (a, b and c, d) shows SEM images of as-deposited and annealed CZTS films onto glass substrate. It is observed from the micrographs that as-deposited CZTS films show large cracks and some overgrown nucleation centers make the film rough. Similler type of micrograph was obtained by pawar et al [21] for electrodeposited CZTS thin film. Figure 7 (b, c) show that after anneaing substrate surface become densely compact and cracks became smaller and smaller as compaired to that of as deposited of the CZTS film [15]. From micrographs, it is revealed that both films are densely packed. It is well known that the efficiency of polycrystalline thin film solar cell increases with increasing grain size of the absorber layer, and therefore, the larger grains are required for the fabrication of high efficiency solar cells [22].

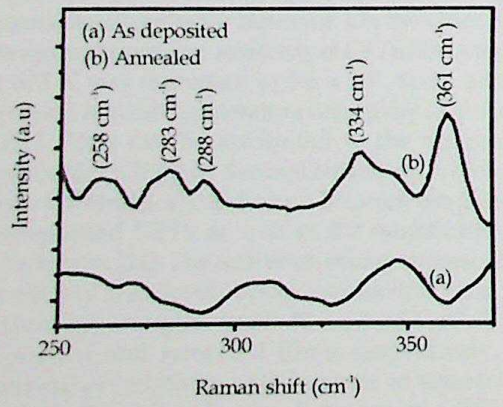


Fig. 6. The FT-IR spectrum of CZTS thin film

3.8 *Surface Wettability Study*

The contact angle is expected to depend upon local inhomogeneity, chemical composition and the surface morphology of the semiconducting electrodes [23]. In the present case, the as-deposited and annealed CZTS films showed water contact angle 34° and 56°, respectively (Fig. 8 (a, b)). Increase in contact angle after annealing is due to the little enhancement in morphology of CZTS thin film.

3.9 *Electrical Resistivity*

The electrical resistivity of CZTS films was measured by conventional d. c. two-probe method in the range of 300 to 500 K. The activation energy was calculated using the relation

$$\rho = \rho_0 \exp (Ea / KT) \quad (9)$$

Figure 9(a, b) shows variation of dark electrical resistivity (log ρ) of as-deposited and annealed CZTS

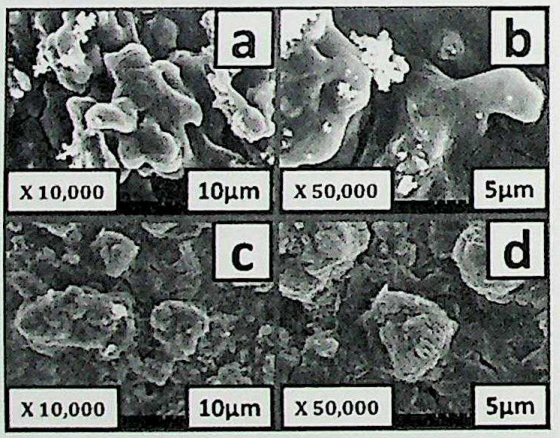


Fig. 7. The SEM images of (a, b) as deposited and (c, d) annealed CZTS thin film at X 10,000 and X 50,000 magnifications

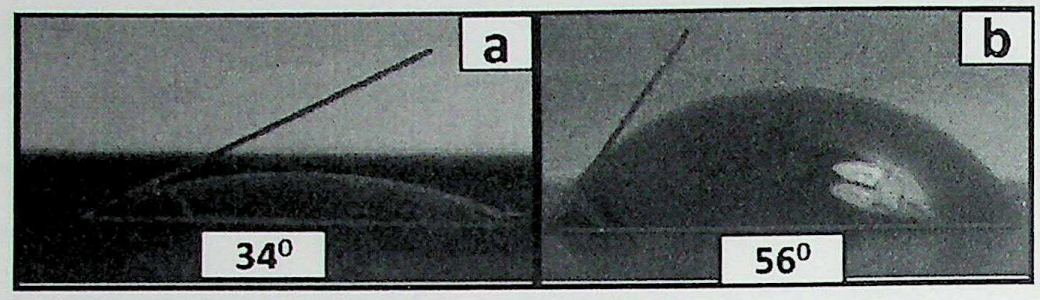


Fig. 8. The water contact angle measurement of (a) as deposited and (b) annealed CZTS thin films

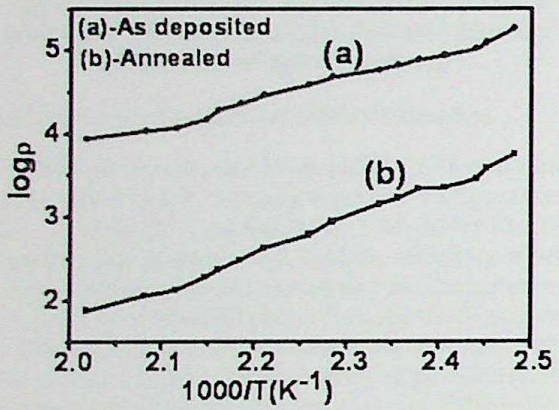


Fig. 9. The variation of dark electrical resistivity (log ρ) with reciprocal temperature (1000/T) of (a) as deposited and (b) annealed CZTS thin films

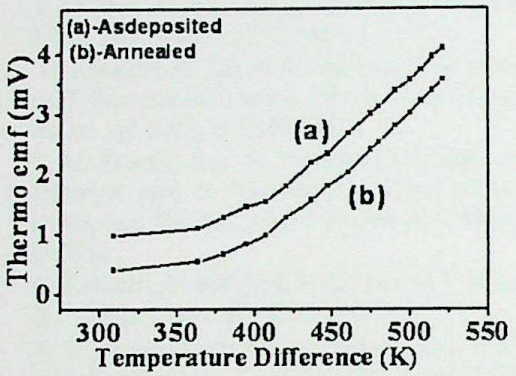


Fig. 10. Thermo emf measurement of (a) as deposited and (b) annealed CZTS thin films

films at 673 K, with reciprocal of temperature (1000/T). The room temperature electrical resistivity of as-deposited CZTS film was of the order of 1.7×10^5 Ω.cm which decreased with temperature indicating the normal semiconductor behavior. On the other hand, the room temperature resistivity of CZTS film annealed at 673 K was decreased to 5.6×10^3 Ω.cm and the decrease in room temperature resisitivity of annealed CZTS films can be attributed to the removal of hydroxide [$(OH)_2$] by thermal annealing, which may resist the electrical conduction between the grains of as-deposited CZTS as well as the modifications in defect states [24]. The activation energy represents the location of trap levels below conduction band. The activation energies are 0.32 and 0.51 eV for as-deposited and annealed films, respectively. The decrease in resistivity with increase in temperature confirmed semiconducting behavior of CZTS thin films, similler to CdTe thin film [25].

3.10 Thermo emf Measurement

The thermo-emf property of CZTS thin film was measured as a function of temperature difference and is shown in Fig. 10 (a, b) The temperature of the one end was maintained at 273 K using ice and the another end was heated. The thermo emf study showed that the CZTS is exhibits p-type electrical conductivity. The thermo-emf increased linearly with increasing temperature. The increase in thermo-emf with temperature can be attributed to the increase in carrier concentration and/or mobility of the charge carriers [26]. Induced emf of as-deposited thin film is higher than annealed film which may be due to lesser number of defect levels [27]. This result is supported p-type CZTS thin film to previously prepared by soft chemistry method, which is repoted by Todorov et al [28].

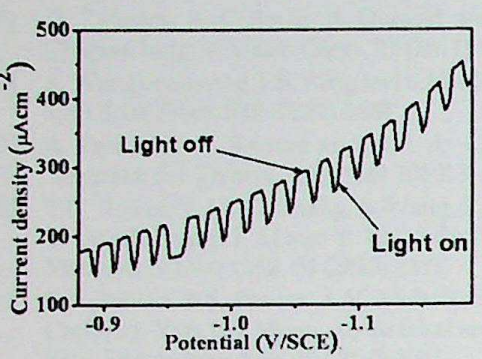


Fig. 11. The current-voltage (I-V) characteristics of annealed CZTS thin films (a) in dark and (b) under illumination of light (60 mW/cm^2)

3.11 Photo-electrochemical (PEC) Cell Studies

The photoresponse of annealed CZTS thin film was carried out by forming a typical configuration cell, p-CZTS (FTO substrate)/0.1 M (KOH-KI-I_2)/ graphite. Fig. 11 shows well defined cathodic (p-type) photosensitivity carried out under the illumination chopped light (60 mW/cm^2). When the CZTS surface is illuminated, created photoelectrons move towards the p-type CZTS electrode/ polyiodide electrolyte interface and are transferred to reduce one of the redox species. The sudden change in current indicates a transfer of electrons from the electrode to the electrolyte solution Linear scan voltammograms were photoactivity recorded (as shown in Fig.11).The photocurrent obtained is of the order of μAcm^{-2}. A conventional hot probe cathodic photoactivity identified the p-type nature of CZTS films [29, 30]. Thus the cathodic photo current response validates p-type photoactivity of the annealed CZTS thin film.

4. Conclusion

In conclusion, large area CZTS thin films have been successfully deposited by a simple and low cost novel SILAR method. Structural studies showed that as-deposited amorphous films are converted to polycrystalline CZTS after annealing at 673 K. The SEM images showed total coverage of the substrate surface. The PEC performance studies showed p-type photoactivity in polyiodide electrolyte which motivate to check its feasibility in solar cell applications. These features confirm the deposition of CZTS films using simple chemical methodology.

Acknowledgement

Authors are grateful to the University Grants Commission (UGC), New Delhi for financial support through the scheme no. 36-207/2008 (SR). One of the authors Prof. C. D. Lokhande is also grateful to the Department of Science and Technology, New Delhi for financial support through the scheme no. INT/ ROK/PROJ/34/2008.

References

[1] Y.B. Kishore Kumar, G. Suresh Babu, P. Uday Bhaskar and V. Sundara Raja, *Sol. Energy Mater. Sol. Cells*, **93** (2009) 1230.

[2] T. Teodor, K. Todorov, B. Kathleen and D. B. Mitzi, *Adv. Mater.*, **22** (2010) 1.

[3] H. Katagiri, K. Saitoh, T. Washio, H. Shinoha ra, T. Kurumadani and S. Miyajima, *Sol. Enegy Mater. Sol. Cells*, **65** (200)141.

[4] T. M. Friedlmeier, N. Wieser, Th. Walter, H. Dittrich and H. W. Schock, Proc. of 14th European PVSEC and Exhibition, P4B.10, (1997).

[5] H. Katagiri, N. Ishigaki, T. Ishida and K. Saito, *Jpn. J. Appl. phys.*, **40** (2001) 500.

[6] A. Weber, I. Kotschau, S. Schorr and H.W. Schock, *Mater. Res. Soc. Symp. Proc.* 1012 (2007).

[7] K. Moriya, K. Tanaka and H. Uchiki, *Jpn. J. Appl. Phys.*, **47** (2008) 602.

[8] K. Jimbo, R. Kimura, T. Kamimura, S. Yamada, W. Maw, H. Araki, K. Oishi and H. Katagiri, *Thin solid film*, **515** (2007) 5997.

[9] K. Moriya, J. Watabe, K. Tanaka and H. Uchiki, *phys. stat. sol.*, **8** (2006) 2852.

[10] C.P. Chan, H. Lam and C. Surya, *Sol. Energy Mater. Sol. Cells*, **94** (2010) 207.

[11] B.S. Pawar, S.M. Pawar, S.W. Shin, D.S. Choi, C. J. Park, S.S. Kolekar and J.H. Kim, *J. Appl. Phys.*, **257** (2010) 1786.

[12] H.M. Pathan and C.D. Lokhande, *Bull. Mater. Sci.*, **27** (2004) 85.

[13] G. Hodes, Chemical Solution Deposition of Semiconductor Films, Marckel Dekkar, Inc. New York , (2002) 40.

[14] J. A. Thorton, *J. Vac. Sci*, **A24** (1986) 3056.

[15] A. Farnades, P. Salome and A. F. da Chuna, *Thin Solid Films*, **517** (2009) 2519.

[16] I. Kriegel, J. Rodríguez-Fernandez, E. Como, A. Lutich, J. Szeifert and J. Feldmann, *Chem. Mater.*, **23** (2011) 1830.

[17] O. Zaberca, A. Gillorin, B. Durand and J.Y. Chane-Ching, *J. Mater. Chem.*, **21** (2011) 6483.

[18] A. Wangperawong, J. S. King and S.M. Herron, *Thin Solid Films*, **519** (2011) 2488.

[19] A. Farnades, P. Salome and A.F. da Chuna, *Semicond. Sci. Technol.*, **24** (2009) 105013.

[20] T.P. F. Liu, Y. Li, K. Zhang, B. Wang, C. Yan, Y. Lai , Z. Zhang, J. Li and Y. Liu, *Solar Energy Materials & Solar Cells*, **94** (2010) 2431.

[21] S.M. Pawar, B.S. Pawar, A.V. Moholkar, D.S. Choi, J.H. Yun, J.H. Moon, S.S. Kolekar and J.H. Kim, *Electrochem. Acta*, **55** (2010) 4057.

[22] S.M. Pawar, A.V. Moholkar, I.K. Kim, S.W. Shin, J.H. Moon, J.I. Rhee and J.H. Kim, *Curr. Appl. Phys.*, **10** (2010) 565.

[23] D. F. Li, W. Wang, H. J. Wang, X.S. Jia and J.Y. Wang, *App. Surf. Sci.*, **255** (2008) 581.

[24] V.R. Shinde, C.D. Lokhande, R.S. Mane and S.H. Han, *Appl. Sur. Sci.*, **245** (2005) 407.

[25] R.B. Kale and C.D. Lokhande, *Mater. Res. Bull.*, **39** (2004) 1829.

[26] G.D. Bagde, S.D. Sartale and C.D. Lokhande, *Mater. Chem. Phys.*, **89** (2005) 402.

[27] B.R. Sankapal, R.S. Mane and C.D. Lokhande, *Mater. Res. Bull.*, **35** (2000) 2027.

[28] T. Todorov, M. Kita, J. Carda and P. Escribano, *Thin Solid Films*, **517** (2009) 2541.

[29] P. K. Sarswat and M.L. Free, *Phys. Status Solidi.*, 10.1002/pssa.201127216

[30] J.J. Scragg, P.J. Dale, L.M. Peter, G. Zoppi and I. Forbes, *Phys. Status Solidi*, **245** (2008)1772.

Author's personal copy

Materials Research Bulletin 47 (2012) 302–307

Contents lists available at SciVerse ScienceDirect

Materials Research Bulletin

journal homepage: www.elsevier.com/locate/matresbu

Room temperature novel chemical synthesis of Cu_2ZnSnS_4 (CZTS) absorbing layer for photovoltaic application

N.M. Shinde [a], D.P. Dubal [a], D.S. Dhawale [a], C.D. Lokhande [a,*], J.H. Kim [b], J.H. Moon [b]

[a] Thin Film Physics Laboratory, Department of Physics, Shivaji University, Kolhapur 416004 (M.S), India
[b] Department of Materials Science and Engineering, Chonnam National University, South Korea

ARTICLE INFO

Article history:
Received 3 May 2011
Received in revised form 1 November 2011
Accepted 9 November 2011
Available online 19 November 2011

Keywords:
A. SILAR
B. Thin film
C. Cu_2ZnSnS_4
D. Photoelectrochemical cell

ABSTRACT

Cu_2ZnSnS_4 (CZTS) thin films have been prepared by a novel chemical successive ionic layer adsorption and reaction (SILAR) method. These films were annealed in vacuum at 673 K and further characterized by X-ray diffraction (XRD), scanning electron microscopy (SEM), UV–vis spectroscopy, electrical, and wettability studies. The X-ray diffraction studies showed the formation of kesterite structure of CZTS films. Scanning electron micrograph revealed the formation of densely packed, compact and large grained CZTS films. The CZTS films showed high optical absorption ($10^4\ cm^{-1}$) exhibiting band gap energy of 1.55 eV. Wettability test revealed the hydrophilic nature of CZTS films. The CZTS thin films showed semiconducting behavior with p-type electrical conductivity. Further photovoltaic activity of these films was studied by forming the photoelectrochemical cell.

© 2011 Elsevier Ltd. All rights reserved.

1. Introduction

Interest in the development and commercialization of thin film solar cells has been growing over the past decade because of their low cost and scalability – two key factors needed to make solar technologies competitive with carbon-based fuels [1]. Recent advances in CdTe and $CuIn_{1-x}Ga_xSe_2$ (CIGS) thin film solar cells have resulted in commercially viable photovoltaic modules. Despite having moderate efficiencies, CdTe and CIGS are not amenable for eventual terawatt-scale production due to the cost and scarcity of Te, In and Ga [1–3]. Therefore, one major challenge of thin film technology is to develop materials composed of earth abundant and non-toxic elements that can be used to manufacture efficient photovoltaic devices. Cu_2ZnSnS_4 (CZTS) is an emerging solar absorber, that is structurally similar to CIGS, but contains only earth abundant, non-toxic elements and has a near optimal direct band gap energy of 1.4–1.6 eV with absorption coefficient of $\sim 10^4\ cm^{-1}$ [3,4]. The CZTS thin films have been prepared by various chemical methods such as spray pyrolysis [7], sol–gel sulfurization [8], electro and photochemical deposition followed by sulfurization [2], liquid-precursor deposition, etc. [9]. Katagiri et al. have fabricated CZTS thin film solar cells of 6.7% efficiency using sputtering and vapor deposition methods [5]. Zou et al. fabricated a quaternary CZTS nanocrystal at temperature lower than 493 K by green synthesis method [10]. Polycrystalline CZTS films with kesterite crystal structure have been obtained by Pawar et al. [11] by pulsed laser deposited CZTS films.

To reduce fabrication cost, a novel but less investigated chemical method for CZTS film formation based on sequential reaction on the substrate surface is proposed. This method is known as successive ionic layer adsorption and reaction (SILAR) method, or simply as modified version of chemical bath deposition. In this method, thin films are obtained by immersing substrate into separately placed cationic and anionic precursors and rinsing between every immersion with ion-exchanged water. The rinsing time in ion exchange water is critical for ionic layer formation. Thus, the wastage of material is avoided in this method. The growth mechanism involves three most important steps: (i) specific adsorption of the ions of the compound to be grown by the substrate immersion in a solution of cationic precursor, (ii) water rinsing of the excess solution still adhering to the substrate, and (iii) chemical reaction between the most strongly specific adsorbed cations and the less strongly adsorbed anions by the subsequent substrate immersion in the solution [12,13].

In this paper, we are reporting the synthesis and characterization of CZTS thin films by SILAR method. The effect of vacuum annealing on structural, morphological, optical and electrical properties of CZTS thin films is investigated. The photovoltaic activity of the CZTS films is tested in 0.25 M $LiClO_4$ electrolyte.

* Corresponding author. Tel.: +91 231 2609225; fax: +91 231 2692333.
E-mail address: l_chandrakant@yahoo.com (C.D. Lokhande).

0025-5408/$ – see front matter © 2011 Elsevier Ltd. All rights reserved.
doi:10.1016/j.materresbull.2011.11.020

Author's personal copy

2. Experimental details

2.1. Synthesis of CZTS thin films

A novel chemical method, i.e. successive ionic layer adsorption and reaction (SILAR) method is used for the deposition of CZTS films. It is based on successive immersion of the substrate into separately placed cation and anion precursor solutions and rinsing between every immersion with double distilled water to avoid precipitation. Four beakers system is used for the deposition of CZTS thin films. The 1st beaker contained mixed cationic precursor solutions of 0.1 M CuCl, 0.05 M $ZnSO_4$ and 0.05 M $SnCl_4$ (1:1:1) ratio. The double distilled water was placed in the 2nd beaker to remove the loosely adsorbed cation from the substrate. The 0.2 M thioacetamide (C_2H_5NS) solution in 3rd beaker was used as the anionic precursor. The 4th beaker contained double distilled water to remove the powdery deposit from the substrate. The pH values of cationic and anionic precursors were ~3 and ~ 6, respectively. All beakers were kept at room temperature (300 K). The schematic diagram for the deposition of CZTS thin films by SILAR method is shown in Fig. 1. In order to obtain stoichiometric CZTS films, we used different concentrations of cationic and anionic precursors. Among different concentrations, the films obtained at 0.1 M CuCl, 0.05 M $ZnSO_4$, 0.05 M $SnCl_4$ (1:1:1) ratio and 0.2 M C_2H_5NS were stoichiometric, uniform and well adherent. The well cleaned glass and stainless steel (SS) substrates were dipped in 1st beaker containing cationic precursor, where Cu^+, Zn^{2+} and Sn^{4+} ions get adsorbed onto substrate surface. After immersion of the substrate into cationic precursor, substrates were rinsed with double distilled water placed in 2nd beaker to remove loosely bounded cations. Then the substrates were immersed in 3rd beaker, where S^{2-} ions react with pre-adsorbed Cu^+, Zn^{2+} and Sn^{4+} cations to form CZTS layer on the substrate. The substrates were again rinsed in double distilled water kept in the 4th beaker to remove unreacted S^{2-} ions and powdery and non adherent CZTS material from substrate. This completed one cycle for the deposition of CZTS film. By repeating such cycle many times, the CZTS film thickness was increased. The adsorption in cationic and reaction time in anionic solution are optimized to be 10 s each. Optimized rinsing time is 10 s in double distilled water.

2.2. Characterization techniques

The thickness of film is the most significant parameter and computed by using fully computerized AMBIOS Make XP-1 surface profiler with 1 Å vertical resolution. The structural properties of CZTS films were carried out using X-ray diffraction (XRD) patterns obtained with CrKα (λ = 2.2897 Å) radiation from a Philips X-ray diffractometer model PW-1710 in 20–80°. The surface morphological analysis was carried out using scanning electron microscopy (SEM) JEOL, JSM model 6360. The semi-quantitative elemental composition of the film was determined using energy dispersive X-ray (EDAX) analysis using horiba-ex-200, Japan, with spatial resolution of 134 eV. The optical absorption study was carried out within a wavelength range 350–850 nm using a UV-1800 SHIMADZU spectrophotometer. The static contact angle against water was measured using Rame-hart USA equipotent with CCD camera. The electrical properties were investigated by standard two-point probe method. The type of electrical conductivity was determined from thermoemf measurement. Photovoltaic activity of CZTS film was studied by forming a cell with CZTS as a photoelectrode, graphite as a counter electrode and saturated calomel electrode (SCE) as a reference electrode. The redox electrolyte used was 0.25 M $LiClO_4$/polypropylene carbonate (PC) solution and the cell was illuminated with a 500 W tungsten filament lamp (intensity 60 mW/cm^2).

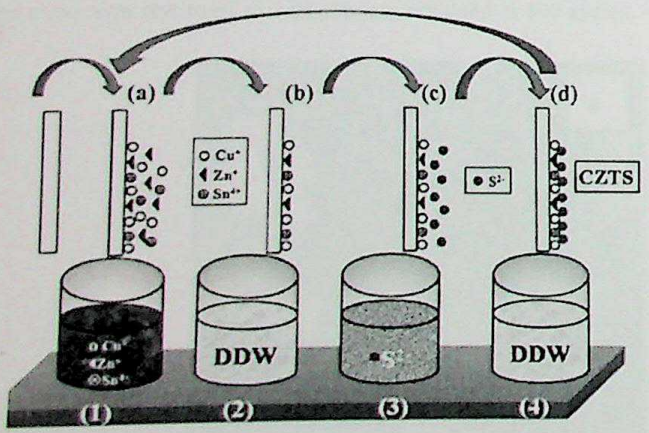


Fig. 1. Schematic diagram of SILAR method for the deposition of CZTS thin films, beaker 1 contains cationic precursors of Cu^+, Zn^{2+} and Sn^{4+}, beakers 2 and 4 contain DDW and beaker 3 contains anionic precursor of S^{2-}.

3. Results and discussion

3.1. CZTS film formation and reaction mechanism

The growth kinetics of a thin film deposition process is of the ion-by-ion type, which involves the ion-by-ion deposition at nucleation sites on the immersed surfaces. According to Lundin and Kitaev [14], nucleation takes place by adsorption of the colloidal ions and growth takes place as a result of surface coagulation of these ions, giving thin and adherent film. The possible reaction mechanism for the formation of CZTS thin film is as follows.

The first beaker contain Cu^+, Zn^{2+} and Sn^{4+} cations, when substrate is immersed in 1st beaker Cu^+, Zn^{2+} and Sn^{4+} are adsorbed on the substrate.

Beaker 3 contains thioacetamide solution which gives sulfide ions (S^{2-}) as per following reaction,

$$CH_3\text{-}\overset{\overset{S}{\|}}{C}\text{-}NH_2 \rightleftharpoons CH_3\text{-}\overset{\overset{SH}{|}}{C}{=}NH \quad (1)$$

In acidic medium protonation gives

$$CH_3\text{-}\overset{\overset{SH}{|}}{C}{=}NH + H^+ \longrightarrow CH_3\text{-}\overset{\overset{H\text{-}S^+\text{-}H}{|}}{C}{=}NH \quad (2)$$

The intermediate compound formed dissociates to give H_2S as

$$CH_3\text{-}\overset{\overset{H\text{-}S^+\text{-}H}{|}}{C}{=}NH \longrightarrow CH_3\text{-}C{=}NH^+ + H_2S \quad (3)$$

In aqueous medium H_2S dissociates to give

$$H_2S \rightarrow H^+ + SH^- \quad (4)$$

$$SH^- \rightarrow H^+ + S^{2-} \qquad (K = 1.2 \times 10^{-15}) \quad (5)$$

where K is dissociate constant of H_2S in aqueous medium.

Finally the following reaction takes place between pre-adsorbed Cu^+, Zn^{2+} and Sn^{4+} cations and S^{2-} anion to form Cu_2ZnSnS_4

$$2Cu^+ + Zn^{2+} + Sn^{4+} + 4S^{2-} \rightarrow Cu_2ZnSnS_4 \quad (6)$$

The prepared CZTS thin films are uniform and well adherent to the substrate.

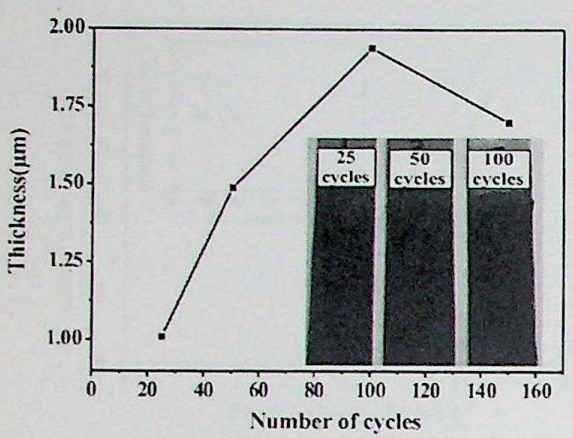


Fig. 2. Variation CZTS film thickness with deposition cycles. Inset of Fig. 2 shows the photograph of CZTS thin films for 25 (0.194 μm), 50 (1.01 μm) and 100 (1.21 μm) cycles.

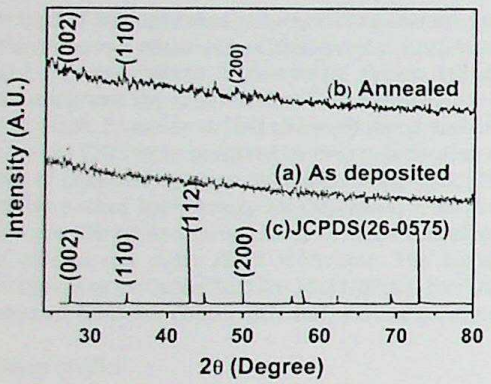


Fig. 3. The XRD patterns of (a) as deposited and (b) annealed of CZTS thin films on glass substrate and (c) standard JCPDS (26-0575) diffracttogram of CZTS thin films on glass substrate.

3.2. Thickness measurement

Thickness is the most important parameter, which alters the properties of thin film material due to surface phenomena. In order to obtain the terminal film thickness of the CZTS thin films, number of deposition cycles were repeated several times. Fig. 2 shows the variation of CZTS film thickness with number of deposition cycles. The film thickness was increased with number of deposition cycle and maximum thickness of 1.94 μm was obtained at 100 cycles. For further deposition cycles, the film material was peeled out from the surface of substrate. This can be attributed to the poor adhesion of film material to substrate [15]. Inset of Fig. 2 shows the photograph of uniform and compact CZTS thin films for 25, 50 and 100 cycles on to stainless steel substrate having area 10 cm^2, which demonstrate the feasibility of SILAR method for large area CZTS film formation.

3.3. Structural studies

In order to improve crystallinity, CZTS film were vacuum annealed at 673 K for 4 h. Fig. 3(a and b) shows the XRD patterns of as deposited and vacuum annealed CZTS thin films onto glass substrate. From Fig. 3(a), it is seen that as deposited CZTS films are amorphous since no diffraction peaks are observed. For vacuum annealed CZTS films, the major characteristic peaks along (0 0 2), (1 1 0) and (2 0 0) planes are observed (Fig. 3(b)) which correspond to kesterite structure of CZTS [JCPDS card no. 26–0575]. The standard XRD pattern of kesterite phase shown in Fig. 3(c) for comparison has a tetragonal unit cell, with sulfur atoms located in a face centered-cubic sub lattice. The Cu, Zn, and Sn atoms occupy half the tetrahedral interstitial sites within the S sub lattice with compositional order [19]. Similar type of kesterite CZTS thin films have been prepared by Chan et al. [16] using electrodeposition method. Liu et al. [17] also prepared kesterite CZTS thin films by reactive magnetron co-sputtering which are highly oriented along (1 1 2) plane. Pawar et al. [18] reported kesterite structure with major reflections along (1 1 2), (2 2 0) and (3 1 2) planes for annealed CZTS thin films obtained by electrodeposition method. The grain size was estimated according to full width at half maxima (FWHM) of diffraction peaks using Scherrer's formula,

$$D = \frac{0.9\lambda}{\beta \cos\theta} \tag{7}$$

where β is the broadening of diffraction line measured at half maximum intensity (radians) and λ = 2.2897 Å is the wavelength of the CrKα X-ray. The grain size was found to be 26 nm for (1 1 0) plane.

3.4. Surface morphology and compositional studies

Fig. 4(a and b) shows scanning electron micrographs of as deposited and vacuum annealed CZTS thin films at 10,000× magnifications. It is observed from Fig. 4(a and b) that both the films are covered with the rough surface. It is found that both films are densely packed. Large agglomoration of grains is observed, which is beneficial in photovoltaic applications, as the recombination rate of the photo-generated electron will be reduced [20,21].

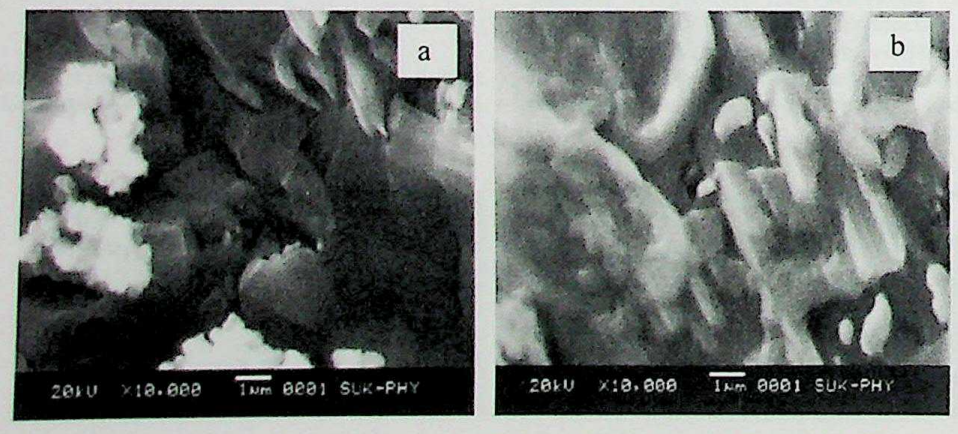


Fig. 4. The SEM images of (a) as deposited and (b) annealed CZTS thin film at 10,000× magnification.

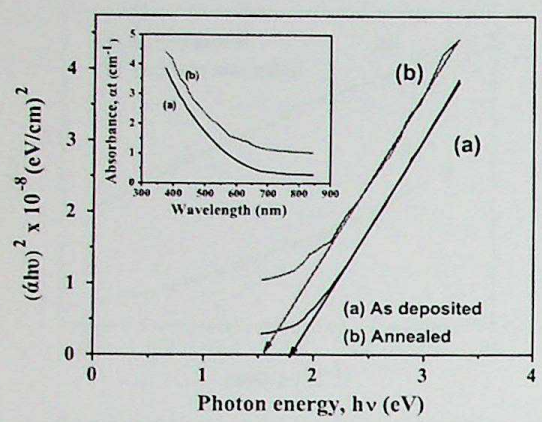


Fig. 5. The plots of $(\alpha' h\nu)^2$ vs. $h\nu$ of (a) as deposited and (b) annealed CZTS thin films. Inset shows variation of absorption ($\alpha' t$) with wavelength (λ).

Similar type of homogeneous, polycrystalline and extremely dense CZTS thin films was obtained by Caballero et al. [22]. Riha et al. [23] prepared densely packed nanocrystals, which are distributed evenly throughout the entire surface of the substrate without any cracks or voids. Pawar et al. [24] observed dense and uniform flat grains for the CZTS films prepared by electrodeposition method in presence of complexing agent. Wangperawong et al. [25] showed such dense packed morphology for Cu_2ZnSnS_4 from the aqueous bath process. The compositional analysis of the annealed CZTS thin film is carried out using EDAX technique. The atomic weight percentage ratios for Cu:Zn:Sn:S are 30:11:07:52. This showed that the annealed films are copper rich and nonstoichiometric.

3.5. Optical studies

The optical absorption studies of as deposited and vacuum annealed CZTS thin films in the wavelength range 350–850 nm has been investigated. Inset of Fig. 5(a and b) shows variation of absorbance (αt) of as deposited and annealed CZTS films with wavelength (λ). These spectra revealed that as deposited and annealed CZTS thin films have high absorbance of light in the visible region, indicating applicability as an absorbing material. The absorption coefficient is larger than $10^4\ cm^{-1}$ in the visible region, which is consistent with those reported in earlier results [2–12,15,26] and therefore, the film is considered to be a suitable material for photovoltaic solar energy conversion. The optical band gap energy is estimated using the following equation for a semiconductor,

$$\alpha = \frac{A(Eg - h\nu)^n}{h\nu} \tag{8}$$

where α is absorption coefficient, Eg is band gap, A is constant and n is equal to 1/2 for direct transition. Fig. 5(a and b) shows the variation of $(\alpha h\nu)^2$ vs $h\nu$, which is a straight line in the domain of higher energies, indicating a direct optical transition. Extrapolation of these curves to zero absorption coefficients ($\alpha = 0$) give the band gap energy 1.80 eV for as-deposited and 1.55 eV for annealed CZTS thin films which is in good agreement with band gaps reported for CZTS films by other authors [2–12,16,25,27,28]. The decrease in band gap after annealing is a consequence of phase change from amorphous to nanocrystalline. The band gap of the film is close to the optimum band gap required for a solar cell, indicating that CZTS is a promising material for thin film solar cell application [24].

3.6. Surface wettability test

Water contact angle method is an empirical diagnostic method for evaluation of thin film material useful in solar cell. The presence of local inhomogenities, chemical composition and surface morphology in thin film are directly related to the surface water contact angle [29]. Wettability test was carried in order to investigate the interaction between electrolyte and CZTS thin film. If the wettability is high, contact angle (θ), will be small and the surface is hydrophilic. On the contrary, if the wettability is low, contact angle (θ) will be large and the surface is hydrophobic. The contact angles for as deposited and annealed CZTS thin films are 45° and 60° respectively as shown in Fig. 6. This is useful for making the intimate contact of aqueous electrolyte with CZTS electrode in device formation. The increase in contact angle after heat treatment is attributed to little enhancement in grain size [30].

3.7. Electrical resistivity

The D.C. two-point probe method for dark electrical resistivity measurement showed that the CZTS films have a value $\sim 10^5\ \Omega$ cm resistivity at room temperature. The resistivity of a $10^3\ \Omega$ cm is in agreement with the CZTS films prepared by sulfurization of metallic precursors [31] and spray pyrolysis method [32]. The high value of resistivity may be attributed due to nano crystallinity or amorphous form of film, grain boundary discontinuities and presence of surface states etc. [33]. Fig. 7 shows the variation of $\log \rho$ with temperature for as-deposited and vacuum annealed CZTS thin films. The decrease in electrical resistivity with increase in temperature confirms the semiconducting nature of the CZTS material. Activation energies 'Ea' are calculated by using the relation

$$\rho = \rho_0 \exp\left(\frac{Ea}{KT}\right) \tag{9}$$

where ρ_0 is the constant, K is the Boltzman constant and T is absolute temperature. The activation energy represents the location of trap levels below conduction band. The activation energies are 0.40 and 0.45 eV for as-deposited and annealed films, respectively. This increase in the activation energy after annealing may be attributed to the modifications of defect states [30].

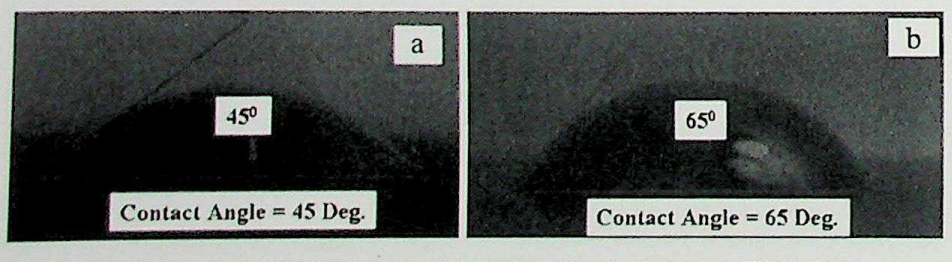


Fig. 6. Water contact angle measurement of (a) as deposited and (b) annealed CZTS thin films.

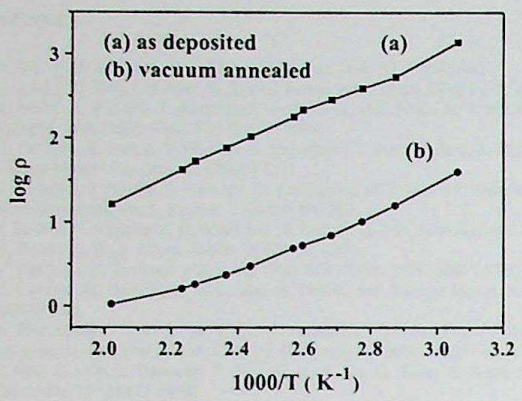


Fig. 7. Variation of dark electrical resistivity (log ρ) with reciprocal temperature (1000/T) of (a) as deposited and (b) annealed CZTS thin films.

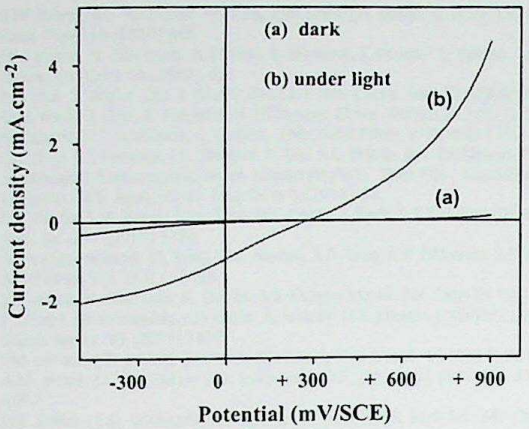


Fig. 9. The current–voltage (I–V) characteristics of annealed CZTS thin films (a) in dark and (b) under illumination of light (60 mW/cm^2).

3.8. Thermo emf measurement

The term electromotive force (emf) was measured as a function of temperature for both as deposited and annealed CZTS films. Fig. 8 shows that an increase in the temperature difference results in induced emf. The polarity of the induced emf for as deposited and vacuum annealed CZTS films indicates a p-type electrical conductivity [4]. Similar to those reported by Scragg et al. [2] and Katagiri [5]. Liu et al. [18] also reported p-type conductivity of CZTS thin films by Van der Paw method. The induced thermo-emf increases with increasing temperature, which can be attributed to the increased concentration and mobility of the charge carriers with rise in temperature [34].

3.9. Photoelectrochemical (PEC) studies

Photoelectrochemical (PEC) characterization was chosen over preparing solid-state devices as it allows for a rapid and nondestructive evaluation of photoactivity of the CZTS thin films and eliminates electrical shorting from a vapor-deposited metal back contact penetrating through the pores in the film to the front contact. These PEC cells are easy to make and many processing steps of p–n junction have been simplified or eliminated. Since the junction with liquid is formed spontaneously upon contact, irregular shaped single crystal or thin films can be used Lokhande and Pawar [35]. The solution based measurements allowed us to quickly test a quality of CZTS film electrode as a solar cell material [28].

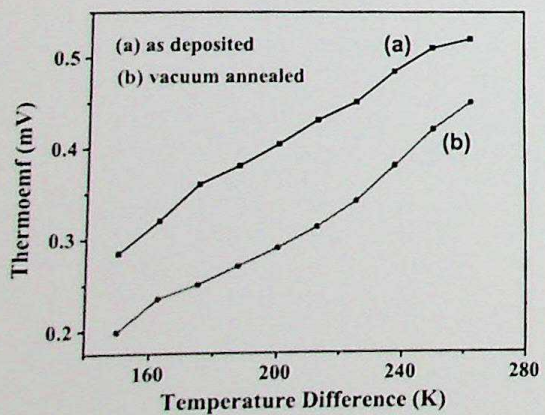


Fig. 8. Thermo emf measurement of (a) as deposited and (b) annealed CZTS thin films.

The photo-response of the vacuum annealed CZTS thin films have been studied by forming PEC Cell. The 0.25 M $LiClO_4$ electrolyte in propylene carbonate solution served as the redox mediator. The current–voltage (I–V) characteristics of vacuum annealed CZTS thin film in the dark and under illumination (60 mW/cm^2) are shown in Fig. 9(a and b). The anodic photocurrent increased gradually with increasing negative potential, indicating that the thin films were p-type [2]. As was previously displayed in the UV–vis spectra (Fig. 5), annealing the CZTS thin films at 673 K leads to better absorption properties and a more direct band gap transition. The values of short circuit current (I_{sc}) and open circuit voltage (V_{oc}) as 0.96 mA cm^{-2} and 288 mV, respectively have been obtained under the illumination intensity of 60 mW cm^{-2}. The photoconversion efficiency 0.12% with fill factors of 24% is achieved.

The photoelectrochemical measurement confirmed good photoactivity of vacuum annealed CZTS film prepared from simple SILAR method. The photocurrent obtained in the present study is not useful for a practical application; however, it is well known that conversion efficiency of such film can be considerably increased by thermal, chemical and (photo) electrochemical surface treatments [36].

4. Conclusions

In conclusion, CZTS thin films are successfully synthesized by a novel chemical successive ionic layer adsorption and reaction (SILAR) method. The X-ray diffraction studies revealed the formation of kesterite CZTS films after vacuum annealing at 673 K. The formation of homogeneous and dense surface was observed from the scanning electron micrographs. The optical study showed band gap energy of 1.55 eV. The electrical resistivity variation with temperature of CZTS thin films showed semiconducting behavior with p-type electrical conduction. Photoactivity of annealed CZTS film was confirmed from photoelectrochemical studies.

Acknowledgement

Authors are grateful to the University Grants Commission (UGC), New Delhi for financial support through the scheme no. 36-207/2008 (SR). One of the authors Prof. C.D. Lokhande is also grateful to the Department of Science and Technology, New Delhi for financial support through the scheme no. INT/ROK/PROJ/34/2008.

Author's personal copy

References

[1] D. Ginley, M.A. Green, R. Collins, Mater. Res. Bull. 33 (2008) 355.
[2] J.J. Scragg, P.J. Dale, L.M. Peter, G. Zoppi, I. Forbes, Phys. Status Solidi B 245 (2008) 1772.
[3] K. Jimbo, R. Kimura, T. Kamimura, S. Yamada, W.S. Maw, H. Araki, K. Oishi, H. Katagiri, Thin Solid Films 515 (2007) 5997.
[4] H. Katagiri, K. Saitoh, T. Washio, H. Shinohara, T. Kurumadani, S. Miyajima, Sol. Energy Mater. Sol. Cells 65 (2001) 141.
[5] H. Katagiri, K. Jimbo, S. Yamada, T. Kamimura, W.S. Maw, T. Fukano, T. Ito, T. Motohiro, Appl. Phys. Express 1 (2008) 041201.
[6] T. Tanaka, T. Nagatomo, D. Kawasaki, M. Nishio, Q. Guo, A. Wakahara, A. Yoshida, H. Ogawa, J. Phys. Chem. Solids 66 (2005) 1978.
[7] N. Kamoun, H. Bouzouita, B. Rezig, Thin Solid Films 515 (2007) 5949.
[8] K. Tanaka, M. Oonuki, N. Moritake, H. Uchiki, Sol. Energy Mater. Sol. Cells 93 (2009) 583.
[9] A. Fischereder, T. Rath, W. Haas, H. Amenitsch, J. Albering, D. Meischler, S. Larissegger, M. Edler, R. Saf, F. Hofer, G. Trimmel, Chem. Mater. 22 (2010) 3399.
[10] C. Zou, Z. Lijie, L. Deshang, Y. Yun, Q. Li, X. Xu, Xi. Chen, S. Huan, Cryst. Eng. Commun. 13 (2011) 3310.
[11] S.M. Pawar, B.S. Pawar, A.V. Moholkar, D.S. Choi, J.H. Yun, J.H. Moon, S.S. Kolekar, J.H. Kim, Electrochim. Acta 55 (2010) 4057.
[12] H.M. Pathan, C.D. Lokhande, Bull. Mater. Sci. 27 (2004) 85.
[13] R.R. Salunkhe, C.D. Lokhande, Sens. Actuators B 129 (2007) 145.
[14] G. Hodes, Chemical Solution Deposition of Semiconductor Films, Marckel Dekkar, Inc, New York, 2002, p. 40.
[15] J.A. Thornton, J. Vac. Sci. A24 (1986) 3056.
[16] C.P. Chan, H. Lam, C. Surya, Sol. Energy Mater. Sol. Cells 94 (2010) 207.
[17] F. Liu, Y. Li, K. Zhang, B. Wang, C. Yan, Y. Lai, Z. Zhang, J. Li, Y. Liu, Sol. Energy Mater. Sol. Cells 94 (2010) 2431.
[18] S.M. Pawar, A.V. Moholkar, I.K. Kim, S.W. Shin, J.H. Moon, J.I. Rhee, J.H. Kim, Curr. Appl. Phys. 10 (2010) 565.
[19] H. Katagiri, N. Sasaguchi, S. Hando, S. Hoshino, J. Ohashi, T. Yokota, Sol. Energy Mater. Sol. Cells 49 (1997) 407.
[20] Y.Z. Pan, Y. Lou, X. Qiu, J. Zhu, C. Burda, J. Am. Chem. Soc. 12 (2009) 4261.
[21] G.M. Ford, Q. Guo, R. Agrawal, H. Hillhouse, Chem. Mater. 23 (2011) 2626.
[22] R. Caballero, C. Maffiotte, C. Guillen, Thin Solid Films 474 (2005) 70.
[23] S.C. Riha, S.J. Fredrick, J.B. Sambur, Y. Liu, A.L. Prieto, B.A. Parkinson, Photoelectrochemical Characterization of Nanocrystalline Thin-Film Cu_2ZnSnS_4 Photocathodes, ACS, Appl. Mater. Interfaces 3 (2011) 66.
[24] B.S. Pawar, S.M. Pawar, S.W. Shin, D.S. Choi, C.J. Park, S.S. Kolekar, J.H. Kim, Appl. Surf. Sci. 257 (2010) 1786.
[25] A. Wangperawong, J.S. King, S.M. Herron, B.P. Tran, K.P. Okimoto, S.F. Bent, Thin Solid Films 519 (2011) 2488.
[26] K. Tanaka, N. Moritake, H. Uchiki, Sol. Energy Mater. Sol. Cells 91 (2007) 1199.
[27] I. Kriegel, J.R. Fernandez, E.D. Como, A. Andrey, M.L. Johann, J. Szeifert, J. Feldmann, Chem. Mater. 23 (2011) 1830.
[28] J.M. Luther, P.K. Jain, T. Ewers, A. Alivisatos, Nat. Mater. 10 (2011) 361.
[29] A.M. More, J.L. Gunjakar, C.D. Lokhande, O.S. Joo, Appl. Surf. Sci. 255 (2009) 6067.
[30] V.R. Shinde, C.D. Lokhande, R.S. Mane, S.H. Han, Appl. Surf. Sci. 245 (2005) 407.
[31] N. Nakayama, K. Ito, Appl. Surf. Sci. 92 (1996) 171.
[32] Y.B. Kishore Kumar, G. Suresh Babu, P. Uday Bhaskar, V. Sundara Raja, Phys. Status Solidi A 206 (2009) 1525.
[33] T.P. Gujar, V.R. Shinde, C.D. Lokhande, R.S. Mane, S.H. Han, Appl. Surf. Sci. 250 (2005) 161.
[34] B.R. Sankapal, R.S. Mane, C.D. Lokhande, Mater. Res. Bull. 35 (2000) 2027.
[35] C.D. Lokhande, S.H. Pawar, Mater. Chem. Phys. (1984) 201.
[36] V. Damodar Das, L. Damodare, Mater. Chem. Phys. 56 (1998) 45.

Journal of Photochemistry and Photobiology A: Chemistry 235 (2012) 14–20

Contents lists available at SciVerse ScienceDirect

Journal of Photochemistry and Photobiology A: Chemistry

journal homepage: www.elsevier.com/locate/jphotochem

Low cost and large area novel chemical synthesis of Cu_2ZnSnS_4 (CZTS) thin films

N.M. Shinde[a], C.D. Lokhande[a,*], J.H. Kim[b], J.H. Moon[b]

[a] Thin Film Physics Laboratory, Department of Physics, Shivaji University, Kolhapur 416004, MS, India
[b] Department of Materials Science and Engineering, Chonnam National University, South Korea

ARTICLE INFO

Article history:
Received 6 September 2011
Received in revised form
18 December 2011
Accepted 1 February 2012
Available online xxx

Keywords:
Cu_2ZnSnS_4
Thin film
Chemical synthesis
Characterization

ABSTRACT

Large area thin films of Cu_2ZnSnS_4 (CZTS) have been successfully deposited by a novel low cost chemical synthesis route. These CZTS films are characterized using X-ray diffraction (XRD), scanning electron microscopy (SEM), electrical, wettability and optical absorption techniques. The XRD analyses revealed the formation of polycrystalline CZTS thin films with tetragonal crystal structure after annealing at 673 K. The scanning electron micrographs showed total substrate coverage with randomly distributed and diffused interlocked cubes. The optical band gap was estimated to be 1.5 eV. Wettability test revealed that as deposited and annealed CZTS films are hydrophilic with water contact angles 46° and 65°, respectively. The photoactivity of CZTS is tested by forming photoelectrochemical cell in polyiodide electrolyte.

© 2012 Elsevier B.V. All rights reserved.

1. Introduction

The development of clean energy resources as an alternative to the fossil fuel has become one of the most important tasks assigned to the researchers from modern science and technology in the 21st century. Among a wide variety of renewable energy sources, solar energy is the best alternative, suitable for meeting the energy demands of the modern society. In order to promote the use of photovoltaic devices, it is necessary to develop the solar cells with low cost, high efficiency, and less environmental damaging. A quaternary Cu_2ZnSnS_4 (CZTS) is a promising candidate for low cost absorber layer in thin film solar cell due to its excellent material properties for obtaining high efficiency such as suitable band gap energy of 1.4–1.5 eV, and large absorption coefficient over 10^4 cm^{-1} [1–3]. On the other hand, in terms of material itself, CZTS solar cell has still several potential advantages. It uses more abundant Sn and Zn instead of In and Ga, which is preferable for realization of low-cost solar cell. Also CZTS contains less toxic material S rather than Se which is desirable for environment friendly applications [2]. Recently, Katagiri et al. have fabricated CZTS thin film solar cells of 6.7% efficiency using sputtering and vapor deposition methods [4]. Guo et al fabricated 7.2% efficiency CZTS solar cells using a robust, solution-based method [5]. The conversion efficiency of 9.6% has been achieved in CZTS based solar cells prepared by a non-vacuum, slurry-based coating method [6].

The CZTS thin films have been prepared by several experimental techniques such as atomic beam sputtering [1], radio frequency (RF) magnetron sputtering [7], sol–gel sulfurization methods [8], thermal evaporation [9], photochemical deposition [10], electrodeposition [11,12], spray pyrolysis [13], pulsed laser deposition [14,15], and sulfurization of electron-beam evaporated precursors [16,17]. As compared to the other deposition methods, chemical deposition is an attractive one because of its own advantages such as simplicity, reproducibility, non-hazardous, cost effectiveness. It is well suited for producing large-area thin films at low temperature and hence avoids oxidation or corrosion of metallic substrate [18].

In present investigation, we report for the first time, a novel chemical method for the deposition of CZTS thin films. This method is anticipated to have the advantages of being low cost and capable of producing large-area films. The effect of post-annealing treatment on the structural, morphological, electrical, wettability and optical properties of the CZTS thin films has been investigated. Also the photovoltaic activity of the CZTS film is tested in polyiodide electrolyte.

2. Experimental details

2.1. Preparation of CZTS thin films

The CZTS thin films have been deposited on the glass and FTO substrates using chemical method. The CuCl, $ZnCl_2$, $SnCl_4$ and $Na_2S_2O_3$ are used as sources of Cu^+, Zn^{2+}, Sn^{4+} and S^{2-} ions, respectively. The chemical bath containing 0.01 M CuCl, 0.05 M $ZnCl_2$, 0.05 M $SnCl_4$ and 0.5 M $Na_2S_2O_3$ solutions in equal volume ratio

* Corresponding author. Tel.: +91 231 2609225; fax: +91 231 2692333.
E-mail address: l.chandrakant@yahoo.com (C.D. Lokhande).

1010-6030/$ - see front matter © 2012 Elsevier B.V. All rights reserved.
doi:10.1016/j.jphotochem.2012.02.006

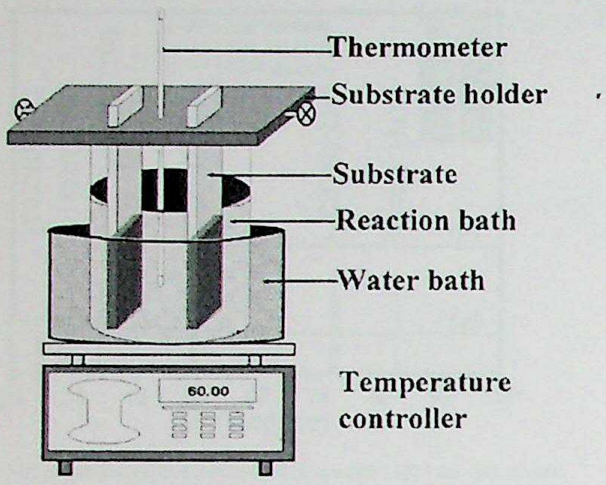


Fig. 1. The diagram of chemical method for deposition of CZTS thin films.

was prepared by mixing them in a beaker. The solutions of aqueous ammonia added to it. The final pH of the resulting solution is ~10. Previously cleaned glass and FTO substrates were immersed in the bath and then the bath was heated up to 358 K for 24 h. After about 4 h, the solution became blurred and within 24 h the dark green precipitate was formed in the bath. During the precipitation, the heterogeneous reaction occurred and the deposition of CZTS films took place on the substrates. The substrates coated with dark green colored film were removed, rinsed, dried in air and preserved in air tight container. The schematic diagram of chemical method for large area (>10 cm^2) deposition of CZTS thin film is shown in Fig. 1. The deposited film was air annealed at 673 K for 3 h and used for further characterization.

2.2. Characterization techniques

The thickness of film is the most significant parameter and computed by using fully computerized AMBIOS Make XP-1 surface profiler with 1 Å vertical resolution. The structural characterization of CZTS thin films was carried out by analyzing X-ray diffraction (XRD) patterns obtained with CrK_α (α = 2.2897 Å) radiation from a Philips X-ray diffractometer model PW-1710 in the span of angle 10–100°. The surface morphological analysis was carried out using scanning electron microscopy (SEM) JEOL JSM model 6360. The Raman spectra of the films were recorded in the spectral range of 35–4000 cm^{-1} using Raman spectrometer (Bruker MultiRAM, Germany Make). The optical absorption study was carried out within a wavelength range of 350–850 nm using a UV-1800 SHIMADZU spectrophotometer. The wettability of the film was carried out by Rame-hart USA equipment with CCD camera. A two-probe method was used for electrical resistivity measurement in the temperature range of 300–500 K. The type of electrical conductivity was determined from thermo emf measurement. Photoelectrochemical (PEC) properties were studied by forming a cell with CZTS as a photo-electrode and graphite as a counter with 0.1 M polyiodide solution. The cell was illuminated with a 500 W tungsten filament lamp (intensity 100 mW/cm^2).

3. Results and discussion

3.1. CZTS film formation

The chemical method of thin film formation is based on the formation of solid phase from a solution, which involves two steps as nucleation and particle growth. In nucleation, the heterogeneous

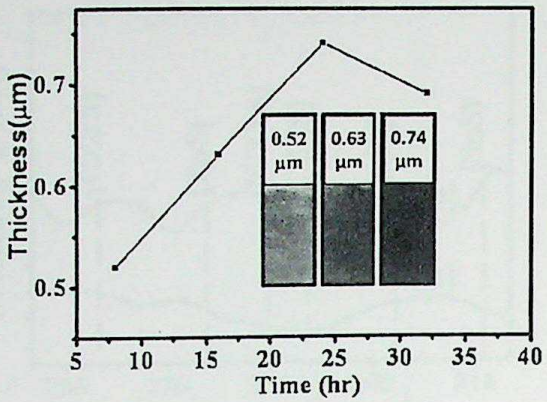


Fig. 2. Variation CZTS film thickness with deposition time. Inset of fig. 2 shows the photograph of CZTS thin films for the deposition period of 8 h (0.52 μm), 16 h (0.63 μm) and 24 h (0.74 μm).

reaction at the substrate surface takes place when clusters of the molecules formed undergo rapid decomposition and particles combine to grow up to a certain thickness of the film [19]. The possible reaction mechanism for the formation of CZTS thin films is as follows

$$2CuCl + ZnCl_2 + SnCl_4 + 8H_2O \rightarrow 2Cu^+ + Zn^{2+} + Sn^{4+} + 8HCl + 8OH^- \quad (1)$$

$Na_2S_2O_3$ is reducing agent by virtue of half cell reaction [19]

$$4S_2O_3^{2-} \rightarrow S_4O_6^{2-} + 4e^- \quad (2)$$

In acidic medium dissociation of $Na_2S_2O_3$ takes place

$$S_2O_3^{2-} + H^+ \rightarrow HSO_3^- + S \quad (3)$$

The electrons released (reaction (2)) reacts with the sulphur from reaction (3)

$$S + 2e^- \rightarrow S^{2-} \quad (4)$$

From reactions (1) and (4), the final reaction for the formation of CZTS is

$$2Cu^+ + Zn^{2+} + Sn^{4+} + 4S^{2-} \rightarrow Cu_2ZnSnS_4 \quad (5)$$

Thus, nucleation and growth of CZTS thin films take place via ion-by-ion mechanism. The CZTS thin films are extremely adhesive to the substrate though the deposition was carried out for prolonged time intervals. The maximum thickness obtained for CZTS thin film is 0.74 μm for deposition period of 24 h. In the process of deposition of CZTS film by CBD method, the mixture of CuCl, $ZnCl_2$, $SnCl_4$, and $Na_2S_2O_3$, was prepared in double distilled water and pH is adjusted to ~10 by using ammonia solution. It is observed that after about 4 h, precipitation starts and deposition of CZTS begins by heterogeneous reaction at substrate surface and the film thickness increases with time. The variation of thickness with time is shown in Fig. 2. The nonlinear rate of increase in the thickness is attributed to the growth by nucleation and coalescence process. More nucleation sites contribute to coagulation during the growing procedure. Furthermore, slight decrease in film thickness observed, after 24 h and this can be attributed to the formation of outer porous layer and/or the film may have developed stress which tends to cause delamination, resulting in peeling off the film after the film reaches at maximum thickness [20].

3.2. Structural studies

Fig. 3 shows XRD patterns of (a) as deposited and (b) annealed CZTS thin films on glass substrate. Inset of Fig. 3(a) and (b) shows the

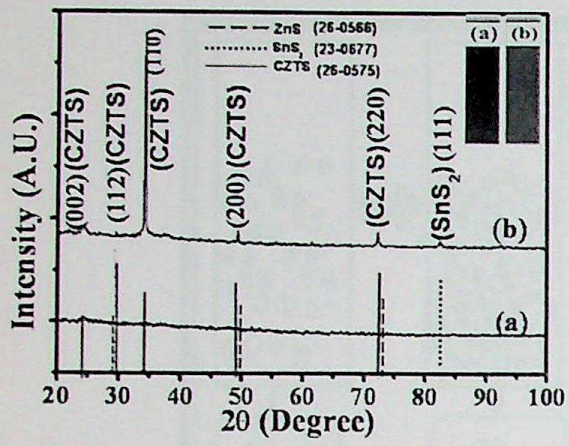


Fig. 3. The XRD patterns of (a) as deposited and (b) annealed CZTS thin film on glass substrate. (Inset of figure shows photographs of (a) as deposited and (b) annealed CZTS thin film on glass substrate). Reference XRD patterns of bulk CZTS, ZnS and SnS_2 materials are also shown for comparison.

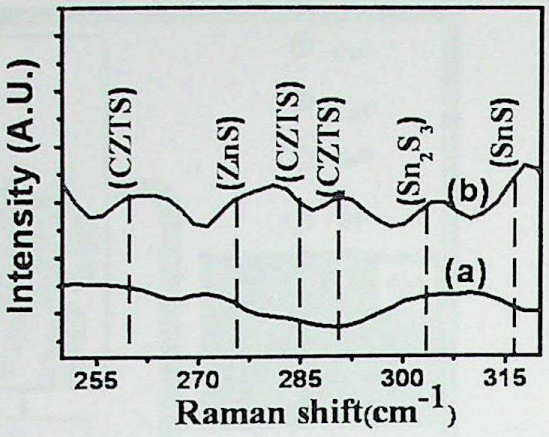


Fig. 4. The room temperature FT-Raman spectra of (a) as deposited and (b) annealed CZTS thin films on glass substrate.

actual film photograph of as-deposited and annealed CZTS thin film on glass substrate at 673 K. No distinct diffraction peak is observed in '*d*' in XRD pattern of as-deposited films, which probably means that the film consisted of hydrous CZTS colloidal particles with low crystallinity. Intensity of characteristics peaks of CZTS is increased after heat treatment and six broad XRD peaks are assignable to diffraction of (0 0 2), (1 1 2), (1 1 0), (2 0 0), (2 2 0) and (1 1 1) planes. Observed '*d*' values are in good agreement with standard '*d*' values (JCPDS card no. 26-0575) which confirmed kesterite type of CZTS thin films which attributed to the improvement in crystallinity. Also the XRD pattern, it is revealed that the as deposited CZTS thin films are amorphous while annealed CZTS thin films are polycrystalline. It should be noted that ZnS (JCPDS card no. 26-0566), having a blend structure exhibited three XRD diffraction of planes (1 1 2), (2 0 0) and (2 2 0), which are difficult to distinguish from those of kesterite type CZTS thin film. On other hand, crystal phase of SnS_2 (JCPDS card no. 26-0677) is also observed diffraction peak (1 1 1). Similar type of results has been obtained by Torimoto et al. [21] for thermal reaction deposited CZTS films. It should be noted that the relative peak intensity of the diffraction arising from (1 1 0) of CZTS plane is much stronger than other peaks which shows that CZTS films are oriented along this plane. High-temperature treatment could increase the crystallinity and grain size of CZTS films, which conduces to fabricate high efficiency solar cell because the efficiency of polycrystalline solar cell increases with an increase in grain size of the absorbed layer material [22]. The grain size of CZTS thin films from XRD pattern was calculated using the Scherer's relation:

$$D = \frac{0.9\lambda}{\beta \cos\theta} \quad (6)$$

where β is the broadening of diffraction line measured at half maximum intensity (radians) and $\lambda = 2.2897$ Å is the wavelength of the CrKα X-ray. The grain size was found to be 63 nm for (1 1 0) plane.

3.3. FT-Raman studies

The FT-Raman spectra recorded over 250–315 cm^{-1} of CZTS thin films are shown in Fig. 4. Raman spectra confirmed existence of the kesterite CZTS well defined peaks at 258, 285, and 287 cm^{-1} are in good agreement with previous reported Raman spectra of CZTS thin film [22–24]. These peaks confirm the formation of kesterite structure of CZTS stretching mode. Also FT-Raman spectra confirmed presence of ZnS with blend structure and even though SnS_2 phase has reflected in XRD, FT-Raman analysis indicate the formation of crystal phase Sn_2S_3 and SnS, SnS_2 at 274, 314, 304 cm^{-1} respectively [25,26]. From both XRD and FT-Raman analyses indicate that the formed films are kesterite CZTS along with a mixture of ZnS and SnS_2.

3.4. Surface morphological analysis

The schematic growth model for CZTS thin film is shown in Fig. 5(a). Inset photograph (a) shows actual morphology of as-deposited CZTS thin film. Chemical bath deposition is one of the "bottom-up" approach methods based on the formation of a solid phase upon transformation of a supersaturated solution to the saturated state. This transformation incorporated with various distinct steps as (a) nucleation, (b) aggregation, (c) coalescence and subsequent, (d) growth by stacking of the particles. During nucleation, clusters of metal precursor molecules likely undergo rapid decomposition. Such nucleation centers acted as foundation for the aggregation of the particles (b). Moreover, basic ground work for the nanostructure is formed by coalescence of aggregated particles (c). Subsequently, the film grows to a certain thickness on the substrate surface by stacking of the particles (d) [27]. Scanning electron micrographs of as deposited and annealed CZTS thin films at two different magnifications are presented in Fig. 5(b)[(a–a' and b–b')]. From the micrographs (Fig. 5(b)(a–a')) it is seen that the film surface of as deposited CZTS film is well covered with randomly distributed interlocked cubes. The approximate size of these cubes is in the range of 2–5 μm. After annealing, these interlocked cubes diffused each other to form compact and rough surface as shown in Fig. 5(b)[(b–b')]. The surface morphology at higher magnification [Fig. 5(b)(b')] depicts that entire surface of the substrate is covered with sharp edge cubes. Tanaka et al. [2] prepared CZTS thin films by sputtering method and reported that film consisted of the closely packed grains with sub-micron size. Round-shaped nanoparticles of about 200 nm with homogeneous size distribution are obtained by Todorov et al. [26] using soft chemistry method.

3.5. Optical absorption study

The optical absorption of as deposited and annealed CZTS thin films in the wavelength range of 350–850 nm has been investigated. Inset of Fig. 6(a) and (b) shows variation of absorbance (αt) of as deposited and annealed CZTS film with wavelength (λ). These spectra revealed that as deposited and annealed CZTS thin films have high absorbance in the visible region, indicating applicability as an

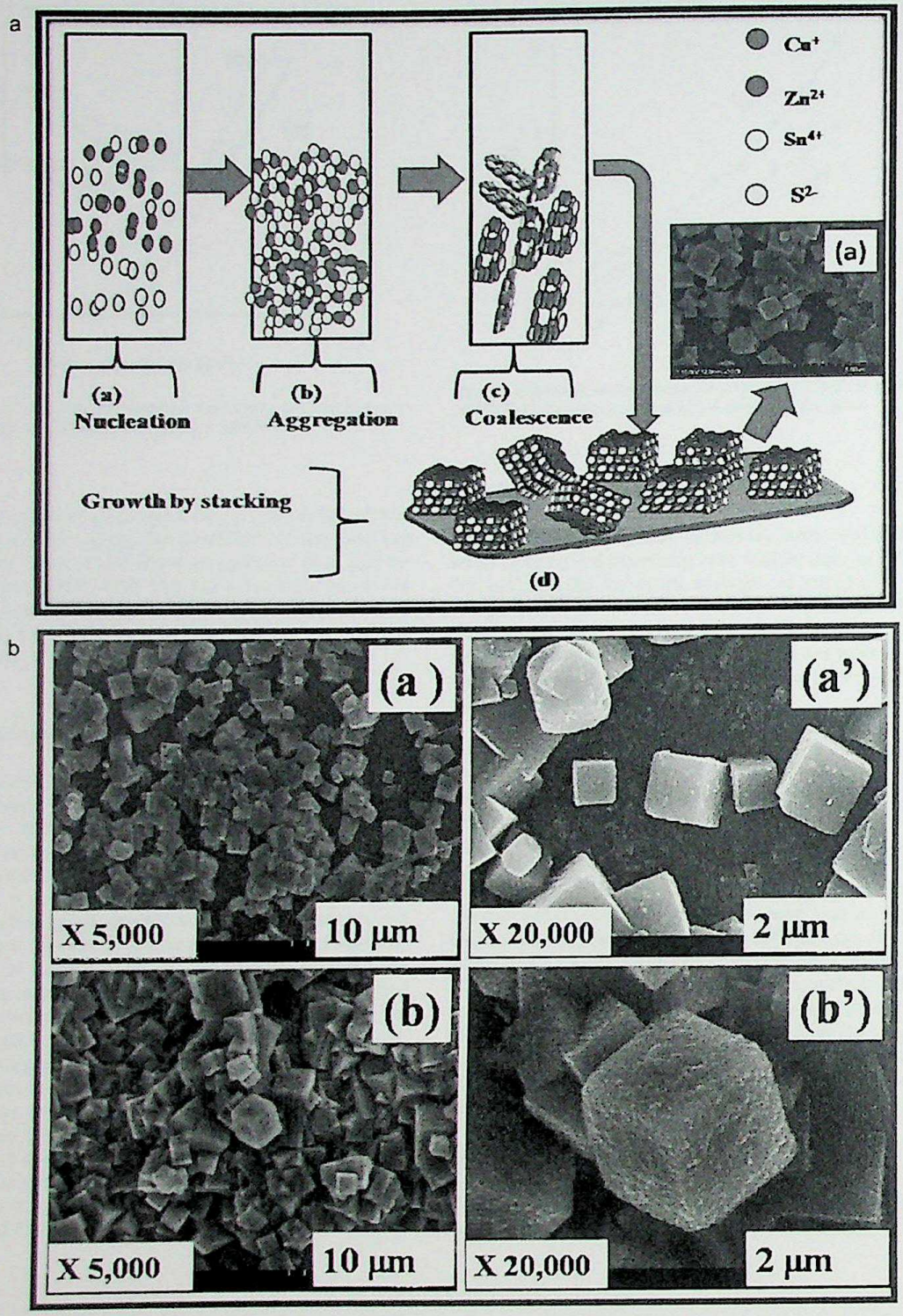


Fig. 5. (a) The schematic growth model for formation of CZTS thin films: (a) nucleation, (b) aggregation, (c) coalescence and (d) subsequent growth by stacking of the particles. (b) The SEM images of CZTS thin films at (a and a') as deposited and (b and b') at two different magnifications (×5000 and 20,000).

absorbing material. The optical band gap energy is estimated by using the following equation for a semiconductor:

$$\alpha = \frac{A(Eg - h\upsilon)^n}{h\upsilon} \quad (7)$$

where α is absorption coefficient, E_g is band gap, A is constant and n is equal to 1/2 for direct transition. Fig. 6(a) and (b) shows the variation of $(\alpha h\upsilon)^2$ versus $(h\upsilon)$, which is a straight line in the domain of higher energies, indicating a direct optical transition. Extrapolation of these curves to zero absorption coefficients ($\alpha = 0$) gave the optical energy gap as 1.7 eV for as-deposited and 1.5 eV for annealed CZTS thin films. The decrease in band gap after annealing is a consequence of phase change from amorphous to polycrystalline nature [22].

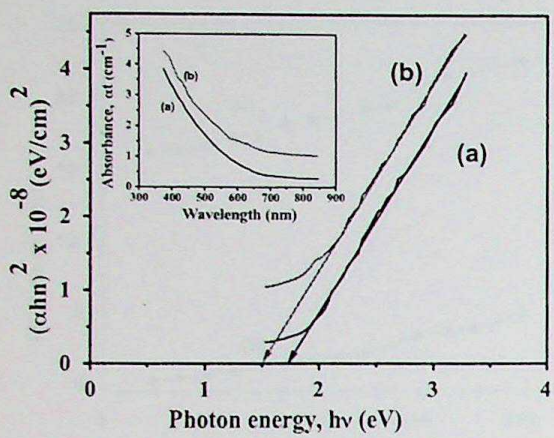


Fig. 6. The plots of $(\alpha h\upsilon)^2$ vs. $h\upsilon$ of CZTS thin films. Inset shows variation of absorption (αt) with wavelength (λ) CZTS thin films on glass substrate.

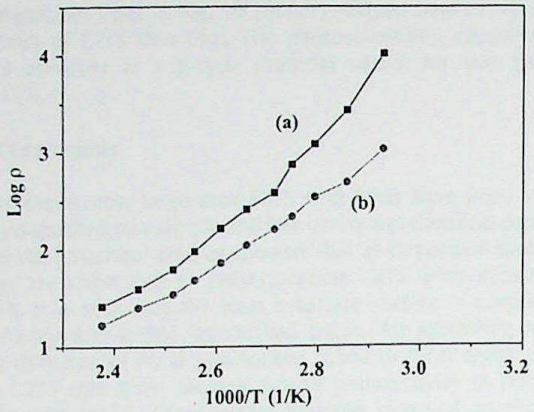


Fig. 8. Variation of dark electrical resistivity ($\log \rho$) with reciprocal temperature ($1000/T$) of (a) as-deposited and (b) annealed CZTS thin films.

Tanaka et al. [2] prepared CZTS thin films by sputtering method and reported band gap of 1.45 eV. The decrement in the band gap energies from 1.8 to 1.5 eV is also reported by Pawar et al. [22] for pulsed laser deposition (PLD) CZTS thin films. The band gap of the CZTS film is quite close to the optimum band gap required for a solar cell, indicating that CZTS is a promising material for thin film solar cell application.

3.6. Surface wettability study

In order to study the interaction between electrode and electrolyte, the wettability test is carried out. The wetting behavior is characterized by the value of the contact angle, a microscopic parameter. If the wettability is high, contact angle (θ), will be small and the surface is hydrophilic [28]. On the contrary, if the wettability is low, θ will be large and the surface is hydrophobic. The contact angle is an important parameter in surface science and its measurement provides a simple and reliable technique for the interpretation of surface energies. The method involves the measurement of contact angle between water and the thin film electrode. The contact angle is expected to depend upon local in homogeneity, chemical composition and the surface morphology of the semiconducting electrodes [29]. Fig. 7(a) and (b) shows the water contact images of as-deposited and annealed CZTS films. The contact angles for as deposited and annealed CZTS thin films are found to be 46° and 65°, respectively. Increase in water contact angle after annealing may be attributed to (i) non-spherical nature of the grains and (ii) topographical change in structure. Similar type of increase in contact angle after annealing has been reported by Shinde et al. for ZnO thin films [27].

3.7. Electrical resistivity

The DC two point probe method was employed to study the variation of electrical resistivity with temperature of CZTS thin films. Fig. 8(a) and (b) shows the variation of $\log(\rho)$ with reciprocal of temperature ($1000/T$) on to the glass substrate. From figure, it is clearly seen that the resistivity of both as deposited and annealed CZTS films was decreased with increase in temperature indicating that the normal semiconducting behavior. The activation energy was calculated using the relation

$$\rho = \rho_0 \exp\left(\frac{E_a}{KT}\right) \tag{8}$$

where ρ is the resistivity at temperature T, ρ_0 is constant, K is Boltzmann constant and E_a is activation energy. The activation energy represents the location of trap levels below conduction band. From Fig. 8 for both as deposited and annealed CZTS films, there is a single distinct activation energy regime indicating single conduction mechanism. It was found that as-deposited CZTS film exhibits a resistivity equal to 10^4 ohm-cm at room temperature, which decreases to 10^3 ohm-cm after annealing at 673 K. The activation energies were found to be 0.62 and 0.67 eV for as deposited and annealed CZTS thin films, respectively. This increase in the activation energy may be attributed to the modifications of defect states [30]. Kishore Kumar et al. [31] reported the semiconducting behavior of CZTS thin films deposited by spray pyrolysis method.

3.8. Thermo emf measurement

In the thermo emf measurement the temperature difference causes the transport of carriers from the hot end to the cold end

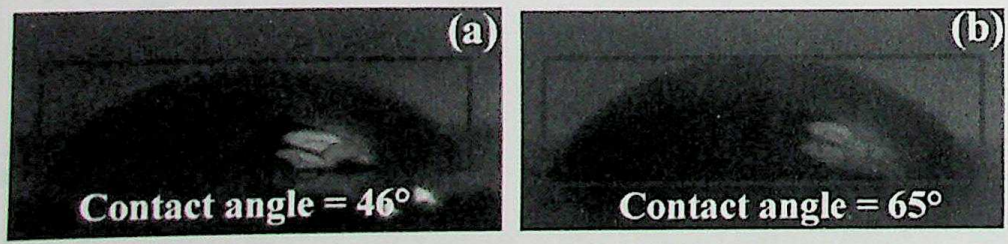


Fig. 7. Contact angle measurement of (a) as deposited and (b) annealed CZTS thin films.

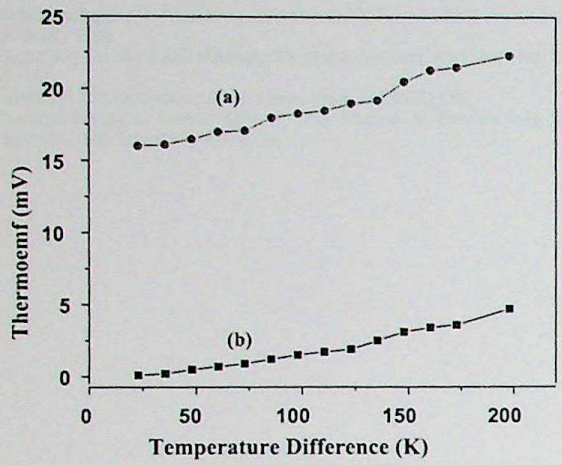


Fig. 9. Thermo emf measurement of (a) as deposited and (b) annealed CZTS thin films.

and thus creates an electric field, which gives the thermal voltage. The dependence of thermoelectric emf (induced emf) on temperature is depicted in Fig. 9. The plot shows that an increase in the temperature difference results in the decreased induced emf. Induced emfs for as deposited and annealed CZTS thin film were found to be 19.5 mV/K and 4.7 mV/K. Induced emf of as-deposited film is higher than annealed film which may be due to lesser number of defect levels [32]. The polarity of the induced emf for as deposited and annealed CZTS film indicates a p-type electrical conductivity as reported by Tanaka [2] and Kishore Kumar et al. [31].

3.9. Photoelectrochemical (PEC) cell studies

A photoelectrochemical cell (PEC) is based on the junction between semiconductor and an electrolyte. An electrolyte play an important role in PEC cell in acting as a medium for charge transfer between the photoelectrode and counter electrode [32]. The PEC response under chopped light (100 mW/cm^2) conditions was carried out in order to study the photosensitivity of the CZTS thin film. The photoresponse of annealed CZTS thin film was carried out by forming a typical configuration cell p-CZTS (FTO substrate)/0.1 M (KOH–KI–I_2)/graphite. Fig. 10 shows well defined cathodic (p-type) photoactivity under illumination. Inset of Fig. 10 shows enlarged part of *I–V* characteristics of CZTS thin film. The photosensitivity confirmed that CZTS absorber is a p-type material useful for the solar cell [32–35].

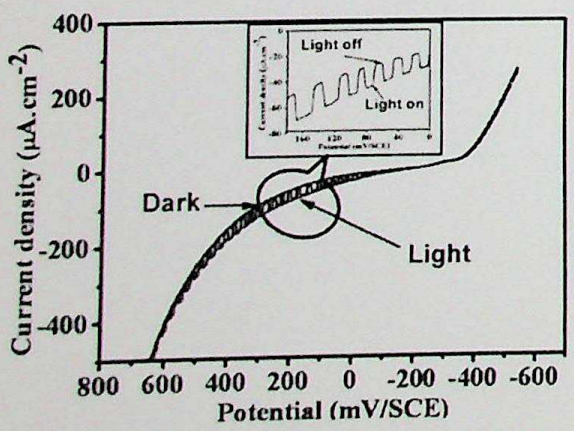


Fig. 10. The photoactivity of annealed CZTS thin film in 0.1 M polyiodide electrolyte at illuminated intensity of 100 mW/cm^2.

4. Conclusions

In conclusion, large area CZTS thin films have been successfully deposited by a simple and low cost novel chemical deposition method. Structural studies showed that as-deposited amorphous films are converted to polycrystalline CZTS after annealing at 673 K. It is seen that the total substrate surface is covered with randomly distributed interlocked cubes. Air annealing resulted into diffusion of these interlocked cubes to form rough surface. The CZTS thin films showed p-type photoactivity in polyiodide electrolyte which demonstrate that the chemical methodology is applicable to deposition of quaternary semiconductor compounds.

Acknowledgement

Authors are grateful to the University Grants Commission (UGC), New Delhi for financial support through the scheme no. 36-207/2008 (SR). One of the authors Prof. C.D. Lokhande is also grateful to the Department of Science and Technology, New Delhi for financial support through the scheme no. INT/ROK/PROJ/34/2008.

References

[1] K. Ito, T. Nakazawa, Jpn. J. Appl. Phys. 27 (1988) 2094.
[2] T. Tanaka, T. Nagatomo, D. Kawasaki, M. Nishio, Q. Guo, A. Wakahara, A. Yoshida, H. Ogawa, J. Phys. Chem. Solid 66 (2005) 1978.
[3] K.K. Jimbo, R. Kimura, T. Kamimura, S. Yamada, W. Maw, H. Araki, K. Oishi, H. Katagiri, Thin Solid Films 515 (2007) 5997.
[4] H. Katagiri, K. Jimbo, W. Shwe Maw, K. Oishi, M. Yamazaki, H. Araki, A. Takeuchi, Thin Solid Films 517 (2009) 2455.
[5] Q. Guo, G.M. Ford, W. Yang, B.C. Walker, E.A. Stach, H.W. Hillhouse, R. Agrawal, J. Am. Chem. Soc. 132 (2010) 17384.
[6] Y. Cui, S. Zuo, J. Jiang, S. Yuan, J. Chu, Sol. Energy Mater. Sol. Cells 95 (2011) 2136.
[7] J.S. Seol, S.Y. Lee, J.C. Lee, H.D. Nam, K.H. Kim, Sol. Energy Mater. Sol. Cells 75 (2003) 155.
[8] K. Tanaka, M. Oonuki, N. Moritake, H. Uchiki, Sol. Energy Mater. Sol. Cells 93 (2009) 583.
[9] K. Oishi, G. Saito, K. Ebina, M. Nagahashi, K. Jimbo, W.S. Maw, H. Katagiri, M. Yamazaki, H. Araki, A. Takeuchi, Thin Solid Films 517 (2008) 1449.
[10] K. Moriya, K. Tanaka, H. Uchiki, J. Appl. Phys. 44 (2005) 715.
[11] X. Zhang, X. Shi, W. Ye, C. Ma, C. Wang, Appl. Phys. A: Mater. Sci. Process. 94 (2008) 381.
[12] J.J. Scragg, P.J. Dale, L.M. Peter, Electrochem. Commun. 10 (2008) 639.
[13] N. Kamoun, H. Bouzouita, B. Rezig, Thin Solid Films 515 (2007) 5949.
[14] K. Moriya, K. Tanaka, H. Uchiki, J. Appl. Phys. 46 (2007) 5780.
[15] K. Moriya, K. Tanaka, H. Uchiki, Jpn. J. Appl. Phys. 47 (2008) 602.
[16] H. Katagiri, N. Sasaguchi, S. Hando, S. Hoshino, J. Ohashi, T. Yokota, Sol. Energy Mater. Sol. Cells 49 (1997) 407.
[17] H. Katagiri, K. Saitoh, T. Washio, H. Shinohara, T. Kurumadani, S. Miyajima, Sol. Energy Mater. Sol. Cells 65 (2001) 141.
[18] R.S. Mane, C.D. Lokhande, Mater. Chem. Phys. 65 (2000) 1.
[19] C.D. Lokhande, J. Phys. D: Appl. Phys. 23 (1990) 1703.
[20] J.A. Thorton, J. Vac. Sci. A 24 (1986) 3056.
[21] T. Kameyama, T. Osaki, K. Okazaki, T. Shibayama, A. Kudo, S. Kuwabatade, T. Torimoto, J. Mater. Chem. 20 (2010) 5319.
[22] S.M. Pawar, A.V. Moholkar, I.K. Kim, S.W. Shin, J.H. Moon, J.I. Rhee, J.H. Kim, Curr. Appl. Phys. 10 (2010) 565.
[23] H. Nukala, J.L. Johnson, A. Bhatia, E.A. Lund, W.M. Hlaing, M.M. Nowell, L.W. Rieth, M.A. Scarpulla, Mater. Res. Soc. Symp. Proc. 1268-EE03-04.
[24] K. Wang, O. Gunawan, T. Todorov, B. Shin, S.J. Chey, N.A. Bojarczuk, D. Mitzi, S. Guhaa, Appl. Phys. Lett. 97 (2010) 143508.
[25] C. Zou, L. Zhang, D. Lin, Y. Yang, Q. Li, X. Xu, X. Chen, S. Huang, CrystEngComm 13 (2011) 3310.
[26] A. Farnades, P. Salome, A.F. da Chuna, J. Alloys Compd. 509 (2009) 7600; T. Todorov, M. Kita, J. Carda, P. Escribano, Thin Solid Films 517 (2009) 2541.
[27] V.R. Shinde, C.D. Lokhande, R.S. Mane, S.H. Han, Appl. Surf. Sci. 245 (2005) 407.
[28] C.D. Lokhande, A. Barkschat, H. Tributsch, Sol. Energy Mater. Sol. Cells 79 (2003) 293.

[29] R.D. Sun, A. Nakajima, A. Fujushima, T. Watanabe, K. Hashimoto, J. Phys. Chem. B 105 (2001) 1984.
[30] T.P. Gujar, V.R. Shinde, C.D. Lokhande, R.S. Mane, S.H. Han, Appl. Surf. Sci. 250 (2005) 161;
B.R. Sankapal, C.D. Lokhande, Mater. Chem. Phys. 74 (2002) 126.
[31] Y.B. Kishore Kumar, G. Suresh Babu, P. Uday Bhaskar, V. Sundara Raja, Sol. Energy Mater. Sol. Cells 93 (2009) 1230.
[32] C.D. Lokhande, S.H. Pawar, Mater. Chem. Phys. 11 (1984) 201.
[33] J. Scregg, P. Dale, L. Peter, G. Zopp, L. Forbes, Phys. Status Solidi 245 (2008) 1772.
[34] S. Riha, S. Fredrick, J. Sambur, Y. Liu, A. Prieto, B. Parkinson, Appl. Mater. Interfaces 3 (2011) 58.
[35] X. Zhang, X. Shi, W. Ye, C. Ma, C. Wang, Appl. Phys. 94 (2009) 381.